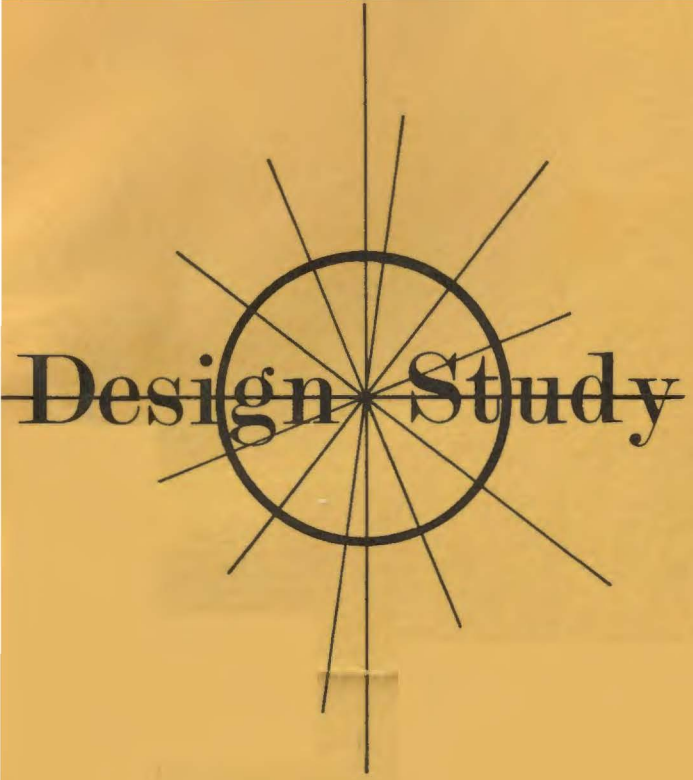

200 BEV ACCELERATOR: Studies on Experimental Use

1966
Vol. 3

Summer Study

Lawrence Radiation Laboratory
University of California

UCRL-16830

UNIVERSITY OF CALIFORNIA
Lawrence Radiation Laboratory
Berkeley, California

AEC Contract No. W-7405-eng-48

200 BeV ACCELERATOR:
STUDIES ON EXPERIMENTAL USE

1966

Volume III

Summer Study

February 1967

Editors' Preface

The reports in this volume constitute the results of the Summer Study held at Berkeley from July 11 to August 27, 1966. The major topic of the Summer Study was the experimental use of the proposed 200-BeV accelerator.

Some 30 visitors from all parts of the country and from Europe, apart from many physicists from within LRL, attended the Study. Indeed, certain physicists who did not attend submitted reports that they felt belonged in this volume, and their results are incorporated here.

Participants in the Study were hampered by the concurrence of the major national airline strike. This proved unfortunate in that several people were unable to attend but was, however, not entirely without benefit in that several attendees were unable to leave Berkeley as soon as they had planned and were therefore held as a captive work force.

The production of this volume, the third in the sequence devoted to studies in the Experimental Use of the 200-BeV Accelerator, would not have been possible without the excellent assistance of Ruth Gross, Charles Pezzotti, Billie Nash, and Nancy Schorn of the LRL Technical Information Division and Maggie O'Keefe of the LRL Mechanical Engineering Department.

Robert P. Ely, Jr.

Denis Keefe

PARTICIPANTS AND CONTRIBUTORS

A. Abashian	University of Illinois Urbana, Illinois
B. A. Barrett	Lawrence Radiation Laboratory Berkeley, California
J. P. Blewett	Brookhaven National Laboratory Upton, Long Island, New York
G. F. Chew	Lawrence Radiation Laboratory Berkeley, California
W. W. Chupp	Lawrence Radiation Laboratory Berkeley, California
G. Cocconi	CERN Geneva 23, Switzerland
F. T. Cole	Lawrence Radiation Laboratory Berkeley, California
T. Collins	Cambridge Electron Accelerator Cambridge, Massachusetts
V. Cook	University of Washington Seattle, Washington
B. Cork	Lawrence Radiation Laboratory Berkeley, California
K. K. Curtis	Lawrence Radiation Laboratory Berkeley, California
G. Domokos	University of California Berkeley, California
T. Elioff	Lawrence Radiation Laboratory Berkeley, California
R. P. Ely	Lawrence Radiation Laboratory Berkeley, California
W. B. Fowler	Brookhaven National Laboratory Upton, Long Island, New York
H. P. Hernandez	Lawrence Radiation Laboratory Berkeley, California
C. A. Heusch	California Institute of Technology Pasadena, California

J. D. Jackson	University of Illinois Urbana, Illinois
D. D. Jovanovic	Argonne National Laboratory Argonne, Illinois
J. A. Kadyk	Lawrence Radiation Laboratory Berkeley, California
G. E. Kalmus	Lawrence Radiation Laboratory Berkeley, California
R. Karplus	Lawrence Radiation Laboratory Berkeley, California
D. Keefe	Lawrence Radiation Laboratory Berkeley, California
W. J. Kernan	Iowa State University Iowa City, Iowa
J. Lach	Yale University New Haven, Connecticut
W. A. S. Lamb	Lawrence Radiation Laboratory Berkeley, California
G. R. Lambertson	Lawrence Radiation Laboratory Berkeley, California
L. Leipuner	Brookhaven National Laboratory Upton, Long Island, New York
E. J. Lofgren	Lawrence Radiation Laboratory Berkeley, California
C. E. MacDonald	Lawrence Radiation Laboratory Berkeley, California
R. B. Meuser	Lawrence Radiation Laboratory Berkeley, California
V. Perez-Mendez	Lawrence Radiation Laboratory Berkeley, California
J. M. Peterson	Lawrence Radiation Laboratory Berkeley, California
V. Z. Peterson	University of Hawaii Honolulu, Hawaii
R. J. Plano	Rutgers University New Brunswick, New Jersey
W. Rarita	University of California Berkeley, California

A. L. Read	Laboratory of Nuclear Studies Cornell University Ithaca, New York
E. Regenstreif	University of Rennes Paris, France
A. Roberts	Argonne National Laboratory Argonne, Illinois
J. Sandweiss	Yale University New Haven, Connecticut
J. R. Sanford	Brookhaven National Laboratory Upton, Long Island, New York
R. A. Schulter	Argonne National Laboratory Argonne, Illinois
G. C. Segrè	Lawrence Radiation Laboratory Berkeley, California
W. Selove	University of Pennsylvania Philadelphia, Pennsylvania
J. B. Shafer	Lawrence Radiation Laboratory Berkeley, California
L. Smith	Lawrence Radiation Laboratory Berkeley, California
V. L. Telegdi	Enrico Fermi Institute University of Chicago Chicago, Illinois
B. Thevenet	Centre d'Etudes Nucleaires de Saclay Gif-sur-Yvette, France
J. J. Thresher	Rutherford High Energy Laboratory Didcot, Berkshire, England
A. V. Tollestrup	California Institute of Technology Pasadena, California
T. E. Toohig	Woodstock College Woodstock, Maryland
W. A. Wenzel	Lawrence Radiation Laboratory Berkeley, California
R. Wilson	Harvard University Cambridge, Massachusetts
M. Wong	Harvard University Cambridge, Massachusetts
C. M. York	University of California Los Angeles, California

L. C. L. Yuan — Brookhaven National Laboratory, Upton, Long Island, New York

T. F. Zipf — Stanford Linear Accelerator Center, Stanford, California

200 BeV ACCELERATOR: STUDIES ON EXPERIMENTAL USE

VOLUME III

SUMMER STUDY - 1966

Contents

STATUS REPORT ON THE 200 BEV ACCELERATOR

E. J. Lofgren

The status of the 200-BeV accelerator project is briefly reviewed in several aspects: design study, site, University Research Association, and Congress.

DESIGN STUDY

The large-scale design study of the 200-BeV accelerator began more than three years ago, after a complicated prior history which goes back more than ten years.

In the middle of 1964, the studies converged on a particular design which became the object of an extensive Design Study Report (UCRL-16000) issued a year ago. The AEC then hired an engineering firm, DUSAF (Daniel, Urbahn, Seelye, and Fuller) to do the following:

a. An engineering and cost review of the proposed design.

b. A site cost comparison.

DUSAF started work in July 1965, and most of our effort in the last half of 1965 was directed towards transferring information to them and working with them. We also produced in that period a 200-BeV Preliminary Project Report, which essentially brought our previous report up to date.

Early this year we began a review of the major design decisions of the project. For the first time we could look at the design as a whole. We also had a coherent document to present to persons outside the project as a basis for asking their views. We could raise the question: "Did the decisions we had made 1-1/2 to 2 years ago in the heat of getting out the Design Study Report still look good?"

Our intention in this review is to consider functional adequacy and extent of technical development required, and then to explore the cost minimum.

Examples of decisions which have been under review are:

1. Injection System

Should the energy be higher or lower than 8 BeV? Should we go to a slow cycle booster? Should we consider the newer ideas of interlaced rings? This review is still in progress and has involved extensive discussion with CERN and BNL. To date we do not believe that we should change our design;

however, there are so many interesting possibilities that we continue to investigate.

2. Main Ring Magnet

Should we change to an H instead of a C magnet? The advantages of the former are mainly those of mechanical structure. The chief advantage of the C is greater accessibility; since this advantage has to do with the ability to cope with unplanned future modification to the accelerator, it is difficult to give up. The strength of the magnetic field, 15 kilogauss, is also under review. To date we have not made any major changes.

3. Experimental Facilities

The adequacy of the proposed 200-BeV accelerator and the associated equipment as an experimental instrument is, of course, the most important question of all. It is also the area where we are in most need of help, and is the central theme of this Summer Study.

In addition to the review of major decisions, work is also going on to advance the engineering designs in all areas of the project. In successive talks in this series you will find out more about these programs.

We are also carrying out development of hardware in several areas:

Model main ring magnet
Computer control of accelerator
rf Power system
Survey system
Tunnel mock-up.

SITE

The AEC issued a general solicitation for site proposals in April 1965. They received 126 proposals offering over 200 sites in 45 states. At the same time they announced that they had requested the National Academy of Sciences to form a Site Evaluation Committee to advise them in the choice of a site. The AEC made a preliminary selection in which they reduced the number of proposals to 85 from 43 states, and turned the job over to the NAS Committee. The Committee, after numerous meetings and consultations with advisers, in March 1966 issued a report in which they named six sites as best satisfying the requirements for the accelerator laboratory.

These six were:

Sierra	- near Sacramento, California
Lowry Range	- near Denver, Colorado
Stoughton	- near Madison, Wisconsin
Weston	- near Chicago, Illinois

Ann Arbor - Michigan
Brookhaven - near Patchogue, New York

Three Commissioners and the top AEC staff visited all six sites in the period April through June. Volumes of information were submitted to the AEC by the proponents of each site, and this has been digested by the staff and sent to the Commission.

The only statements that have been made about procedure or schedule are that the decision will be a Commission decision and that the decision will be made before the end of the year. There have been numerous rumors and speculations—early decision, late decision, political decision, non-political decision, and so on. These rumors are largely self-cancelling.

As for the Sierra Site—it is officially sponsored by the State of California. The Study Group backs it very strongly (it was our Site Example B in the Design Study, and chosen for excellent physical properties). Any University of California activities in support of the California site are sponsored separately from the AEC contract.

We believe that the Sierra Site is superlative in its combination of foundation conditions, size, topography, climate, and availability of power and water. In addition, we like it because many of us are committed to the project and we are already here.

UNIVERSITY RESEARCH ASSOCIATION

The National Academy of Sciences in December 1964 invited about 30 university Presidents to consider the problem of management of the accelerator.

In June 1965 they formed the University Research Association, Inc. It has 34 University members whose chief executive officers make up a Council of Presidents. The Chairman is Gaylord Hornwell.

Most of the responsibility is delegated to a Board of Trustees. The first Board was elected in November 1965. There are 15 members from the universities and 5 at large. H. D. Smyth is the Chairman of the Board of Trustees. There is also a Scientific Committee of the Trustees, of which Norman Ramsey is the Chairman.

No official recognition of the URA by the AEC has been expressed; however, it is generally accepted that URA will be the management organization. As yet URA has no permanent officers and no staff. They are looking for a president at this time.

CONGRESS

The final word, of course, rests with Congress who must authorize and provide money for the project. Congress will shortly go out of session and a new Congress will convene in January 1967. We can expect that soon after that, possibly in February or March, there will be hearings on the 200-BeV Accelerator Project before the Joint Committee on Atomic Energy. One can be hopeful that authorization will follow without too much delay.

EXPERIMENTAL FACILITIES

Denis Keefe

INTRODUCTION

The main accent of this Summer Study is intended to be on the experimental use and exploitation of the 200-BeV accelerator. We can specify the following four generic categories wherein further study would be valuable:

1. Target facilities and experimental areas
2. Worthwhile physics experiments
3. Equipment: chambers, techniques, counters, beams
4. Physics uses and capabilities of the accelerator that affect the accelerator design itself.

It is recognized that people's tastes will vary because they are more interested in tackling an individual problem in detail or in treating the grander systems problem from a broad viewpoint.

Before proceeding to a discussion of the experimental facilities described in the Design Study Report, I should point out that the description in that report refers to a facility that is feasible, would function as planned, and hangs together logically. When the final design of the 200-BeV accelerator is made, it cannot be too different in the broad sense, but may, however, differ considerably in detail. For example, the C-magnets might end up as H-magnets, or the injection system may look quite different, for the accelerator itself. In the experimental areas, analogous major changes might be the replacement of conventional secondary beam-transport magnets by superconducting magnets, or the disappearance from the design of the internal target area.

We urgently need the injection of any good ideas bearing on either the construction or the possible future development of the experimental facilities. In addition, any other ideas, good or otherwise, that might have a serious or extensive impact on the design must be considered very seriously.

In the following brief description of the possible design for experimental use, I will try to turn up and sign-post several topics that are valid topics for study during the summer.

EXPERIMENTAL FACILITIES

The basic premises we can assume for the design of the target areas are as follows:

1. Existence of long straight sections: Twelve Collins straight sections of 100 ft free drift space have been incorporated in the current design.

2. Availability of slow and fast extracted beams with > 90% efficiency into the same channel.

3. Particle production for known particles strongly collimated in the forward direction: For a secondary momentum p (BeV/c), most of the particles will be contained within a cone of half-angle of $\theta = 0.5/p$ radians. For p = 100 BeV/c, θ will be 5 milliradians, less than one-third of a degree. This strong collimation close to 0-deg production angle has led to the idea that, closely following a target, a bending magnet should be used to "fan out" the narrow cones of particles of different momenta into different secondary beam channels.

Without proceeding further towards any description of a concrete realization of a design satisfying these premises, we can immediately throw open the following questions:

What might be required to go in some of the long straight sections (other than those consumed by the functional requirements of injection and acceleration)? Some examples are sketched in Chapter XVIII of the Design Study Report (UCRL-16000); are there others?

Is the internal target area really necessary? See Chapter XIII for a fairly detailed discussion of the pros and cons. Could the estimated cost of 11 million dollars be better expended in expanding the capabilities of the external areas? Is there such a thing as a cheap, limited-scope internal-area design that would satisfy most of the unique features of internal target areas?

Regarding targetting arrangements, are there better schemes than that described in the report? There are certainly many alternatives and only a very few have been examined.

EXPERIMENTAL TOPICS

All reports referred to in this section are found in volumes 1 and 2 of UCRL-16830.

(i) Previous Work

Over two years ago, Rarita made a study of what Regge-pole theory would predict for experiments in the 200-BeV region. New data have since become available and he is currently updating this work. He should be consulted on theoretical problems connected with the high-energy regime. Toohig has examined in a recent report the feasibility of form-factor experiments by using a very-high-energy pion (kaon, antiproton ?) beam colliding with the orbital electrons of a target atom. Chinowsky and Stevenson, in their reports, have

examined interesting experiments involving neutrinos.

All of these reports have aged a little and certainly merit re-examination and criticism.

(ii) Equipment

(a) Beams: Previous work on secondary beams includes reports by Longo on counter beams at 150 BeV/c, and a novel Λ^0 hyperon beam at 100 BeV/c.

Lach has considered in detail the construction of an rf separated beam operating at 10 kMHz. In my opinion, one should assume the successful operation of superconducting deflecting cavities at the time of operation.

Toohig has been studying, and will continue to study, a possible muon facility that would be a by-product of constructing a linear strong-focusing channel primarily designed to give a "monochromatic" neutrino beam. This channel would automatically capture and trap muons.

In a report by Read are considered a variety of possible neutral beams. Chinowsky has considered the kinematics of production of quarks and other massive objects by bombardment of complex nuclei with 200-BeV protons.

Only superficial consideration has been given to the quite high fluxes of photons and electrons at energies exceeding those available at SLAC. The intensities, however, will be many orders of magnitude lower.

(b) Counters: Several types of counter exist that might be useful in the high-energy region, and quite recently certain technical advances have been made that would increase their usefulness. Murray (LRL) has been developing an rf (3-kMHz) modulated phototube, and recently high efficiencies have been achieved in secondary emission counters. Counters using coherent transition radiation (Ter-Michaelyan) may be valuable in mass-identification in, for example, short hyperon beams.

(c) Beam transport: Meuser is examining the economics and feasibility of making essentially all of the secondary beam-transport magnets superconducting. There is a choice between using fields not very different from those today and simply making a gain in power costs, or else exploiting the very-high-field capability.

(d) Detectors: There are many questions concerning the way in which spark-chamber arrays, bubble chambers, and on-line-data reduction may be used at the 200-BeV machine.

(e) Questions: What about charged hyperon beams in the 100 BeV/c region? Are there experiments in electron-photon physics that are important at high energy and modest intensity? What would be the impact of high-field transport magnets on experimental beam design? Some beams can be made shorter, but some will not change much (e.g., rf separated beams).

(iii) Items more closely connected with the accelerator

There are possibly alternative ways to accelerate antiprotons. The proposed scheme has still to be studied in more detailed layouts. Since it will not be cheap in effort and money, its importance for physics should be critically examined. Someone may wish to inquire whether one can, or might want to, accelerate deuterons.

Some preliminary consideration of 200-BeV intersecting storage rings would be useful. They would probably be superconducting because of their dc character. If some interesting threshold were to be found (e.g., in cosmic rays or at the CERN ISR) that lay beyond the reach of 200-BeV protons striking a stationary target, it might make sense to add a small tangential high-intensity ring of a few BeV at one of the long straight sections. Note that for a 1-BeV ring, the energy in the center-of-mass system would be twice that available when a 200-BeV proton struck a proton at rest. Would the interaction rates and the unusual kinematical features make this a sensible proposal?

Finally, more study of individual experiments requiring high intensity would be valuable. Intensities like 10^{13} pps sound high at this time, but in the context of the later 1970's they will not be unusual. Are there physics reasons that we might anticipate that would cause pressure for still higher intensities?

A. PARTICLE PRODUCTION

PARTICLE-PRODUCTION MEASUREMENTS AT 0-DEG BY OBSERVING THE 180-DEG LABORATORY YIELDS IN p-p COLLISIONS AT 200 BEV

D. D. Jovanovic

This note describes a simple method of measuring pion and kaon yields at or near 0 deg by observing the low-momentum particles emitted at 180 deg in the laboratory. This method was recently applied at 12.0-BeV incident proton energy at the ZGS and yielded very good information on pion production near the kinematic limit.

For the p-p system there is a complete backward-forward symmetry in the c.m. (except, of course, when protons are longitudinally polarized), and measurement of interactions products, viz π, K, e, at 0 deg or at 180 deg is equivalent. We want to stress that for some cases secondaries at 180 deg all have momenta below $\approx$ 500 MeV/c, and simple time-of-flight technique allows for easy particle separation (π, K, e). At these momenta, momentum analysis requires trivial bending magnets with minimum or no perturbation on the external proton beam. Furthermore, exploring 0 deg or very near zero production angles (0.5 - 2.0 mrad) means that backward angles are large: 10 - 50 deg, facilitating large-solid-angle geometry and making surveying and alignment trivial.

The relation between 180-deg particle momentum and the corresponding 0-deg particle momentum in p-p collisions is:

$$(P_{lab})^{0\ deg} = (P_{lab})^{180\ deg} [\bar{\gamma}\ (1 + \bar{\beta}^2)] + (E_{lab})^{180\ deg}\ 2\bar{\gamma}^2\ \bar{\beta},$$

where $\bar{\gamma}$ and $\bar{\beta}$ are the constants for the motion of c.m. For 200 BeV, $\bar{\gamma}$ = 10.372 and $(1 - \bar{\beta}) = 4.658 \times 10^{-3}$. Figure 1 is a plot of this relation for pions and kaons produced in 200-BeV p-p collisions. It is clear that forward pion momenta accessible to this method are limited to $P_\pi \geq 40$ BeV/c and for kaons $p_K \geq 120$ BeV/c. Target thickness for the 180-deg lab momenta represents a range cutoff which is non-negligible below 100 MeV/c! Figure 2 is the similar plot showing the relation between forward and backward production angles for several pion momenta. Obviously the examination of very small forward angles can be done with great precision and minimum equipment alignment problems.

The detrimental aspect in surveying the backward hemisphere is the enormous Jacobian between the forward and backward production:

$$\left(\frac{d^2\sigma}{d\Omega dp}\right)^{0\ deg} \Big/ \left(\frac{d^2\sigma}{d\Omega dp}\right)^{180\ deg} = \frac{(P)^{0\ deg}}{(P)^{180\ deg}} \approx 400\ .$$

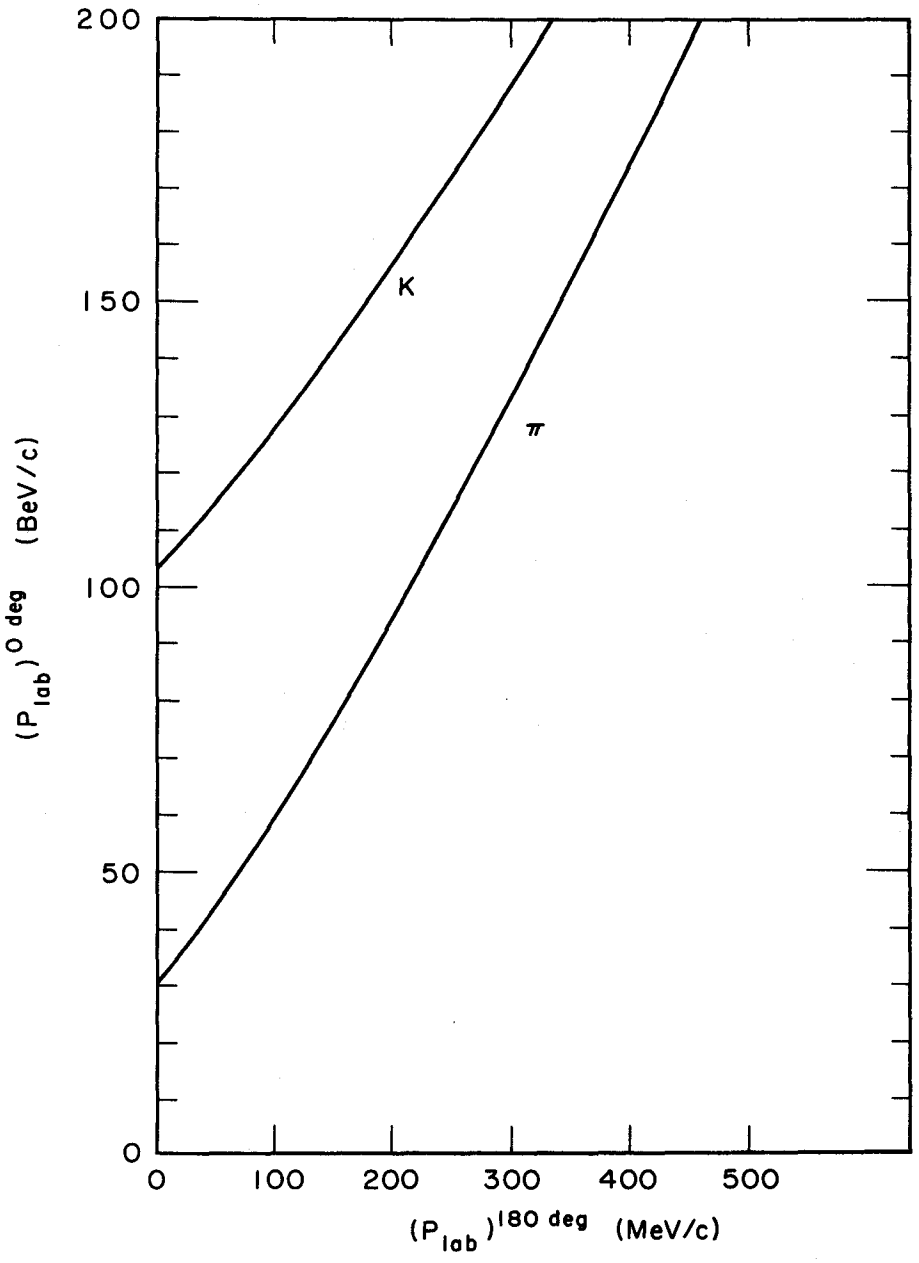

Fig. 1. Relation between particle momenta at 180 deg and particle momenta at 0 deg for pions and kaons produced in 200-BeV p-p collisions.

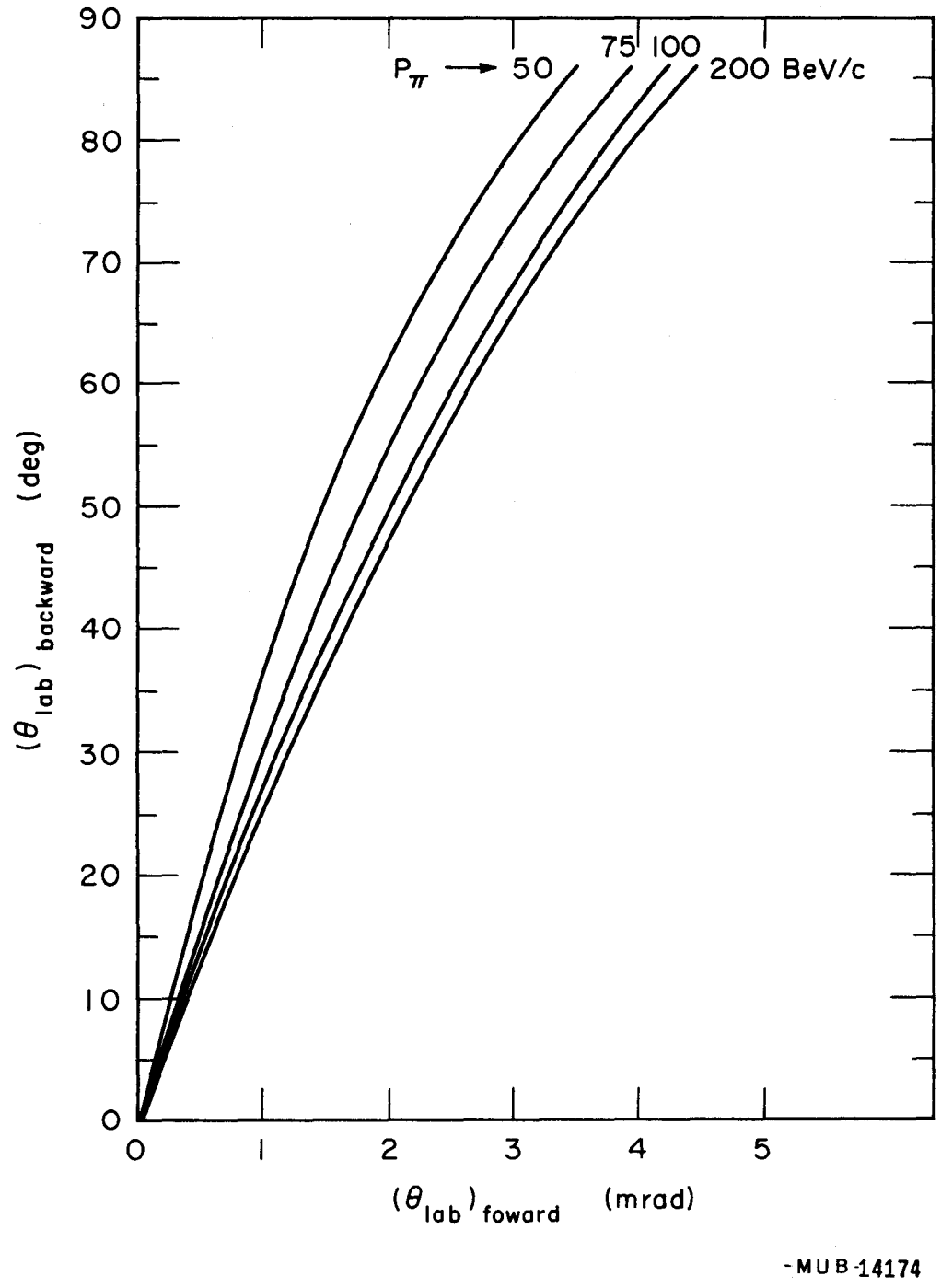

Fig. 2. Relation between forward and backward production angles for several pion momenta in symmetric p-p collisions.

However, external-proton-beam intensity easily compensates for such a drawback.

Figure 3 shows one of the many possible experimental configurations. The external beam is incident from the left on the thin (10 cm) hydrogen target. A small septum magnet 30-in. long with a 1-cm septum analyzes the backward-emitted particles. Counter A and the counter array B are the detectors with $\approx$ 2 m separation, allowing a good time-of-flight separation. Presumably the whole system has a vacuum-pipe enclosure or He-bag to minimize the multiple scattering, which is serious at these low momenta.

Typical rates for such a setup would be $\approx 10^3$ particles in $\Delta\Omega = 10^{-4}$ and $\Delta p/p \approx 1/2\%$ for a mb/sr BeV/c production cross section with 10^{12} incident proton intensity.

Finally, as an illustration of this method we present, in Fig. 4, the π^+ production spectrum at 0 deg deduced from the spectrum measured in 12 BeV p-p collisions at 180 deg in the laboratory. [Lundy, Lamb, Novey, and Yovanovic, Phys. Rev. Letters 17, 100 (1966)].

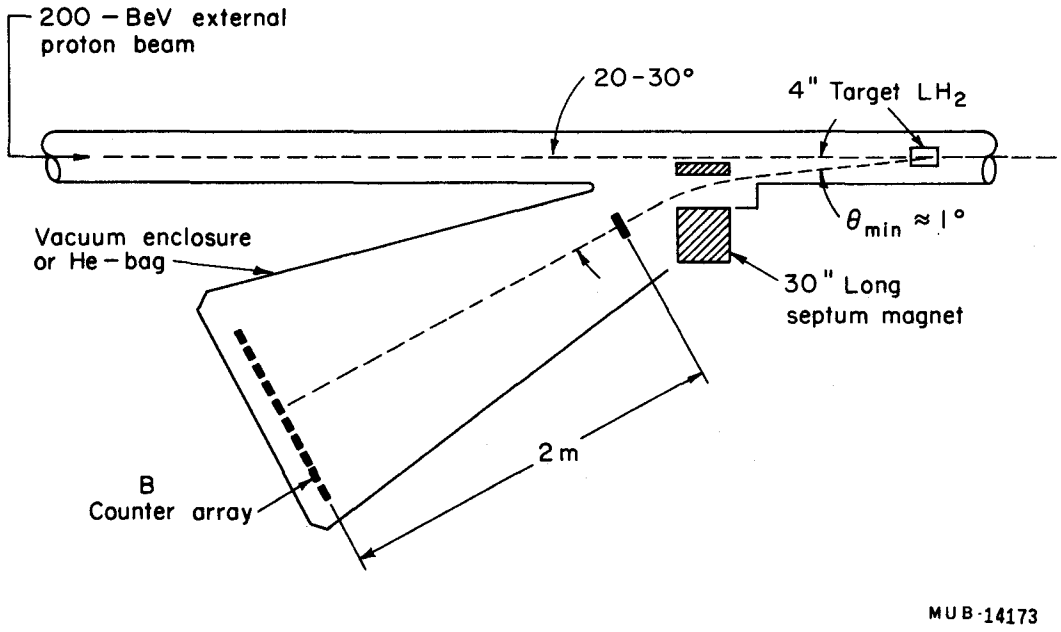

Fig. 3. A possible experimental configuration for measuring particle production at 180 deg in the laboratory system.

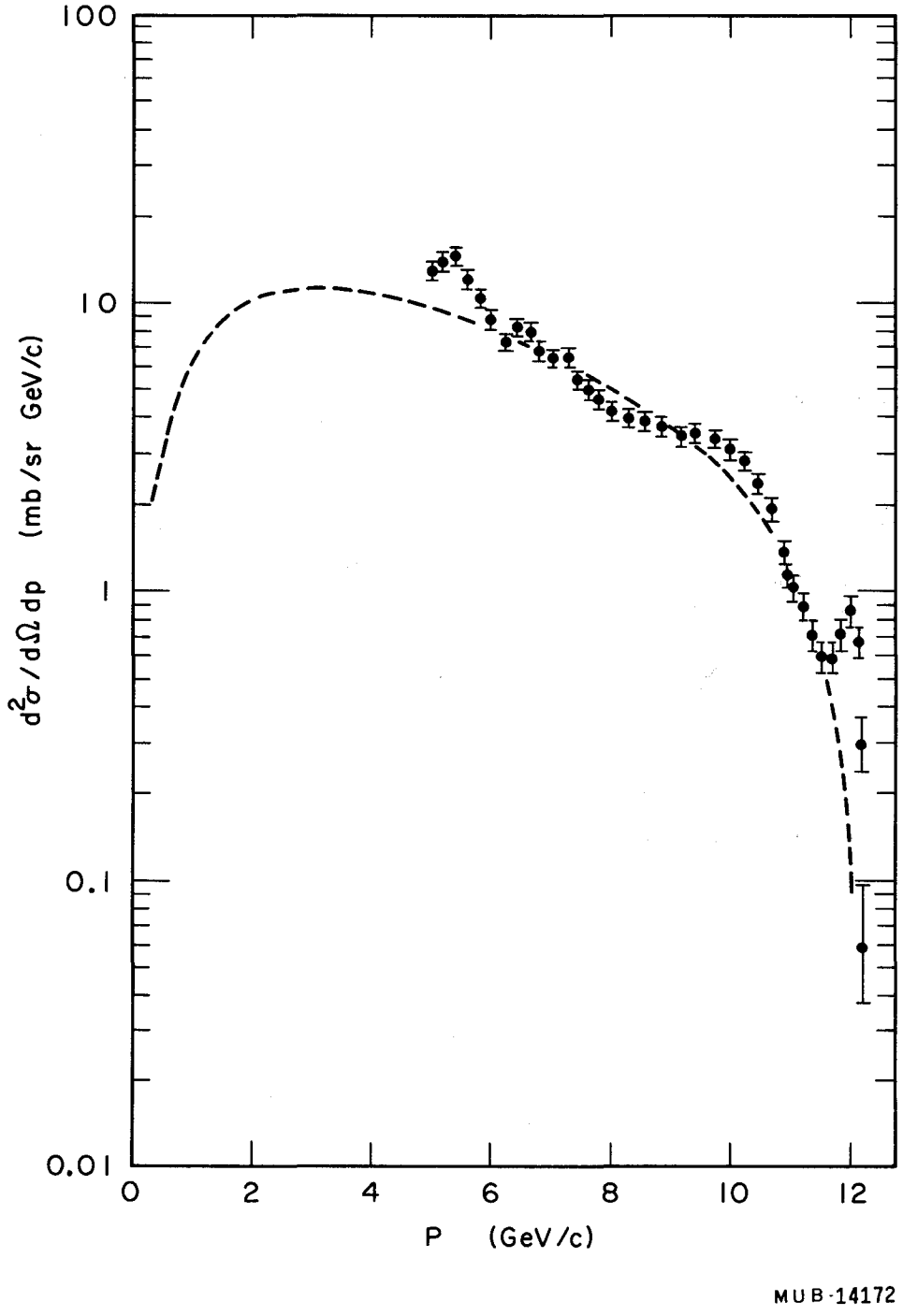

Fig. 4. The π^+ production spectrum at 0 deg from 12-BeV p-p collisions deduced from the spectrum measured at 180 deg in the laboratory. The dashed line is a calculated phase space assuming 30% three-body, 30% four-body, 25% five-body, and 15% six-body final states.

EVALUATION OF PION FLUXES PRODUCED BY 200 BEV PROTONS

G. Cocconi

In Lawrence Radiation Laboratory Report UCID 10148,* G. Trilling has examined the possibility of improving the CKP (Cocconi, Koester, and Perkins) formula for guessing the pion fluxes produced by 200-BeV protons.

In the CKP formula, repeated here for convenience,

$$\frac{d^2\sigma}{dp\, d\omega} = \frac{A\, p^2}{p_0^{1/2}}\, e^{-\frac{p}{B\, p_0^{3/4}}}\, e^{-\frac{p\theta}{C}} \qquad (1)$$

(p_0 = primary proton momentum, p = secondary pion momentum, θ = angle of emission $\ll 1$, all in the lab system), there are three independent parameters: A, relating to the multiplicity of π production; B, determining the scale of the exponential decrease of the longitudinal component of the momentum spectra; and C, giving the scale of the transverse momentum distribution ($p_\perp = p\,\theta$).

In the Trilling formula the same differential cross section is given by the sum of the two terms:

$$\frac{d^2\sigma}{d\omega\, dp} = \left(A_1\, p^2\, e^{-\frac{p}{B_1\, p_0^{1/2}}}\, e^{-\frac{p_0^{1/2}\, p^2\, \theta^2}{C_1\, p}} \right)$$

$$+ \left(A_2\, \frac{p^2}{p_0}\, e^{-\frac{p^2}{B_2\, p_0^{\,2}}}\, e^{\frac{p\theta}{C_2}} \right) . \qquad (2)$$

---

* Reprinted in 200 BeV Accelerator: Studies on Experimental Use: 1964-1965, Vol. I, Lawrence Radiation Laboratory Report UCRL-16830, April 1966, p. 25.

There is an analogy between Eq. (1) and each term in Eq. (2), and the three pairs of parameters A_1 A_2, B_1 B_2, C_1 C_2 play roles similar to those played by A, B, and C.

With Eq. (2) it is possible to fit the existing experimental data better than with Eq. (1). However, Eq. (2) should be preferred to Eq. (1) for guessing the fluxes produced by protons of energy much larger than those presently available, only if Eq. (2) describes better than Eq. (1) the dependence on p_0 and on p of the phenomena that are responsible for secondary production in high-energy collisions.

To see whether this is the case, let us start by considering the extreme energies, which are the ones we are most interested in for the new accelerators. At these energies, i.e., at π-meson energies larger than, say, one-half the proton primary energy, the first term of Eq. (2) contributes negligibly, because of the dependence on $p_0^{1/2}$ of the first exponential. The choice between Eqs. (1) and (2) must thus be based on the comparison between Eq. (1) and the second term of Eq. (2). The transverse momentum dependence (the second exponential) is the same in the two equations; the difference resides in the different distributions used for the longitudinal component (the first exponential). In Eq. (1) an exponential is proposed that has a scale increasing with proton energy as $p_0^{3/4}$; in Eq. (2), a Gaussian is proposed, with standard deviation proportional to p_0.

The justification for choice (1) was the following: the exponential law for the longitudinal component was chosen because it was the simplest law that matched reasonably well the known spectra; then the 3/4-power law came as a consequence of the fact that the multiplicity increases as $p_0^{1/4}$ and that the energy must be conserved.

In the case of Eq. (2), the Gaussian shape was proposed because it seemed to fit better the spectra near the high-energy tail. The choice of a scale proportional to p_0 was dictated by the belief that isobar formation continues to be important at high energies and that the decay of baryon isobars formed on incoming protons gives rise to high-energy pions at a scale that expands proportionally to the increasing proton energy. In fact, during the past years, evidence has been accumulated that the cross section for the formation of baryon isobars of isospin I = 1/2 (those produced by the exchange of a Pomeranchon in the Regge-pole terminology) in the reaction

$$p + p \rightarrow N^* + p$$

is, for each isobar, constant, independent of the proton energy.* Surely these isobars will generate with constant cross section pions of momenta covering, in the laboratory, the region that goes from about zero to a maximum momentum expressed, in first approximation, by the relation

$$p_{max} \approx p_0 \left[1 - (M/M^*)^2\right],$$

---

* See, e.g., E. W. Anderson et al., Phys. Rev. Letters 16, 855 (1966).

where M^* is the mass of the isobar and M is the proton mass when the isobar decays directly into a proton and a pion (two-body decay) or the mass equivalent to that of all particles, except the pion, in a many-body decay.

The maximum values of the momentum contributed by the decay of the known I = 1/2 isobars are given below, as well as the probabilities of their two-body decay.

M^* (MeV)	p_{max}/p_0	Two-body decay (%)	Production cross section, 10-30 BeV (mb)
1400	0.55	100?	≈ 0.7
1520	0.62	75	0.2
1690	0.69	85	0.6
2190	0.81	$\approx$ 20	0.1

The figures in the second column show that the lighter isobars cannot contribute to the formation of the most energetic pions. The heaviest isobar fares better, but then its two-body decay probability is smaller than that of the other isobars. It is reasonable to expect that this trend will be followed by heavier and still-undetected isobars with I = 1/2, and that the larger M^* is, the larger will be the probability of multi-body decay and of cascade decays. In these cases, M will be larger than the proton mass and p_{max}/p_0 will be correspondingly reduced.

In fact, in order to acquire an energy not far off the maximum possible energy, a pion must be produced in the forward direction, while the two nucleons must go together in the opposite direction, in the center-of-mass system. Such a process involves for the incoming nucleon a four-momentum transfer

$$-t \lesssim 2p_0 M,$$

increasing as p_0 increases. It seems very unlikely that the cross section for processes of this kind will turn out to be energy-independent.

For these reasons we believe that the linear scale used in Eq. (2) for the longitudinal momentum distribution emphasizes too much the most energetic tail of the pion spectrum, and that, in order to be consistent with the present physical intuition, the scale should expand as p_0^{α}, with $\alpha < 1$. Is $\alpha = 3/4$ the right guess? We do not know, but at the present moment this looks to us to be the best choice.

Coming now to the low-energy secondaries, those contributed especially by the first part of the equation proposed by Trilling, one must make two remarks. The first is that there is no indication in the pion spectra measured thus far of a

distinction between processes where low-energy secondaries are predominant and processes where high-energy secondaries predominate. Hence, it seems unrealistic to expect that at 200 BeV the secondaries will have spectra with two bumps, as predicted by Eq. (2); continuous spectra with a single maximum seem more appropriate. The second remark is that, in the first part of Eq. (2), the transverse momentum distribution is assumed to be Gaussian with standard deviation proportional to $(p_0^{1/2}/p)$, i.e., dependent on the momenta of both the primary proton and the secondary pion, while there is no experimental evidence for this kind of dependence. Actually, the constancy of the transverse momentum distribution is the only fact on which we are ready to bet, and is also supported by cosmic ray evidence. In leaving it out, we leave out our only "intuition."

At the expense of being called conservative, we thus reach the conclusion that for a wild extrapolation the CKP formula looks more reliable than the Trilling formula. Though the existing data on secondary spectra up to 30 BeV are not perfectly fitted by Eq. (1), it seems that when confronted with the problem of extrapolating to 200-300 BeV, the physical arguments on which this equation was built are more sound than those that led to Eq. (2).

Equation (1) can possibly be improved and made to better agree with both the existing data and our physical intuition, by introducing the modification in the transverse momentum distribution suggested by R. Hagedorn of CERN.

In the last few years* it has been observed that, at machine energies, the average transverse momentum of the secondaries depends on the mass of the secondary. For pions it is $\approx$350 MeV/c, for kaons $\approx$ 450, and for $\Sigma \approx$ 650 MeV/c. Hagedorn has incorporated this fact into Eq. (1) by modifying the second exponential as follows:

$$\frac{d^2\sigma}{dp\, d\omega} = \frac{A\, p^2}{p_0^{1/2}}\, e^{-\frac{p}{B\, p_0^{3/4}}}\, e^{-\frac{\sqrt{m^2 + p^2\theta^2}}{C}}, \qquad (3)$$

where m is the mass of the secondary particle.** For $p\theta > m$, one has $m^2 + p^2\theta^2 \rightarrow p\theta$, and Eq. (3) becomes practically identical with Eq. (1). When $p\theta < m$, then

$$\sqrt{m^2 + p^2\theta^2} \rightarrow m\left(1 - \frac{p^2\theta^2}{2m^2}\right)$$

---

*See, e.g., Bartke et al., Nuovo Cimento 29, 8 (1963).

**Here A is no more constant, but depends slightly on m and p.

and the transverse momentum distribution at small angles becomes Gaussian, with standard deviation proportional to the square of the mass of the secondary particle, thus satisfying the more sophisticated requirements. The average transverse momentum increases as m increases, in agreement with the existing evidence, thus making Eq. (3) more adaptable to the calculation of fluxes of other secondaries, besides the pions.

The fitting of Eq. (3) to the data available up to now has not yet been carried out. It can be anticipated that, as far as the fluxes produced by 200-300 BeV protons are concerned, the final result will not be very different from that obtained a few years ago utilizing Eq. (1).

ESTIMATE OF THE FLUXES OF STRONGLY INTERACTING PARTICLES PRODUCED BY AN ELECTRON BEAM

G. Cocconi

When confronted with the problem of predicting the fluxes of strongly interacting particles, typically π-mesons, produced by an electron hitting a target, two approaches are possible.

One is that followed by Y. S. Tsai in the SLAC Handbook[1] and consists in using the theoretical estimates of the photoproduction cross sections for the particles created in the various channels, and summing them, taking into account the spectrum of the photons produced in the target by the electron through bremsstrahlung.

Another approach, the one here described, is more phenomenological and rests on the assumption that, asymptotically, the general properties of strong interactions are independent of the nature of the particles producing them. Therefore, at the energies of the present accelerators one can already make use, for the evaluation of the fluxes produced by a photon, of the fluxes that other particles, e.g., the protons, are known to produce at equivalent momenta.*

Our recipe is consequently the following:

(a) The total strong interaction cross section, σ_k, of a photon of momentum k on a nucleon at rest is constant for k well above threshold momentum, as suggested by the CEA and the DESY results, and equal to

$$\sigma_k = 55\ \mu b .$$

Photons thus have a strong interaction mean free path

$$\lambda_k = \frac{1}{N\sigma_k} = 3.0 \times 10^4\ g/cm^2 .$$

(b) The π-mesons, as well as the other strongly interacting secondaries, are produced by a photon of momentum k interacting in a target, with the same multiplicity, momentum spectrum, and angular distribution as those produced by a

---

*Equivalence here refers mostly to the multiplicity of the secondary particles. For lack of better evidence, in (b) below, the momenta of photons and protons will be assumed equivalent when they are equal.

proton of momentum $P_0 = k$ interacting in the same target.* In first approximation, the spectra are given by the CKP formula,[2] i.e.,

$$\frac{d^2n}{dP\, d\omega} = A \frac{P^2}{P_0^{1/2}} e^{-\frac{P}{B P_0^{3/4}}} e^{-\frac{P\theta}{C}} \text{ (sr · BeV · interaction)}^{-1}, \qquad (1)$$

where P is the laboratory momentum, in BeV, of the secondary pion emitted at an angle θ, and A, B, C, are three constants whose values for pions of one sign have been found to be

$$A = 10 \text{ BeV}^{-5/2}, \quad B = 0.22 \text{ BeV}^{1/4}, \quad C = 0.22 \text{ BeV}.^{**}$$

(c) The bremsstrahlung spectrum produced by an electron of momentum E_0 hitting a target is given by the asymptotic expression

$$dN(k) = t\, dk/k; \quad (k < E_0,\ t \lesssim 1,\ \theta = 0), \qquad (2)$$

where $t = x/x_0$ is the target thickness in units of radiation length x_0.***

From assumptions (a), (b), and (c) it follows that the differential spectrum of the π-mesons produced by an electron of momentum E_0 hitting a target of thickness t is

$$\frac{d^2N}{dP\, d\omega} = \frac{\frac{1}{2} x}{\lambda_k} \int_{k=P}^{E_0} \frac{d^2n}{dP\, d\omega}\, dN(k),$$

---

*This is the most questionable assumption because, while in p-p interactions the inelasticity is ≈ 0.5, in the photon-neutron case the inelasticity is probably closer to 1.

**More complex expressions that fit better the existing experimental data have been proposed by Trilling[3] and by Ranft.[4] Their use could be appropriate in a computer program, but not here since our aim is to obtain for the spectra a simple analytical expression.

***The use of the more complete expression given by Tsai is again avoided so as to simplify the final result.

where the factor (1/2)x represents the average thickness of the target crossed by the photons.* After some simplifications, one obtains

$$\frac{d^2N}{dP\,d\omega} = \frac{2}{3}\,\frac{xt}{\lambda_k}\,A\,B\,E_0^{1/4}\,P\,e^{-\frac{P}{B\,E_0^{3/4}}}\left(1 - e^{-\frac{E_0^{3/4}P^{1/4}-P}{B\,E_0^{3/4}}}\right)e^{-\frac{P\theta}{C}}. \quad (3)$$

Equation (3) is used here to evaluate the π-meson fluxes (one sign only) produced by an electron of momentum $E_0 = 20$ BeV crossing a light target one radiation length thick ($t = 1$, $x = 60$ g/cm^2). The results are plotted in Fig. 1.

Compared with the fluxes predicted by Tsai, the fluxes of Fig. 1 are substantially smaller and compressed within a narrower solid angle around the forward direction. This collimation is the consequence of the assumption that also for the photo-produced secondaries the transverse momentum distribution is invariant. The measurement that will be performed at SLAC within the next year will show which set of curves is nearer the truth.

Equation (3) and Fig. 1 refer to π-meson fluxes. According to our model, the other secondary particles—K-mesons, antiprotons, etc.—should behave in the same manner. In order to evaluate their fluxes, the constant A in Eq. (3) should be multiplied by the relative abundance of the particle with respect to that of π-mesons, provided that the top momenta considered are high enough to assure that the relative abundance has reached the asymptotic value. For instance, at $E_0 \gtrsim 20$ BeV, the multiplying factor is ≈ 0.1 for K^+-mesons, and ≈ 0.01 for antiprotons.

Equations (1) and (3) can also be used to evaluate the ratio R between the fluxes produced on the same target by a proton of momentum P_0 and by an electron of momentum E_0. One obtains

$$R = \frac{\frac{x}{\lambda_p}\frac{d^2n}{dP\,d\omega}}{\frac{d^2N}{dP\,d\omega}} = \frac{3}{2}\,\frac{\lambda_k}{\lambda_p\,B\,t}\,\frac{P}{P_0^{1/2}\,E_0^{1/4}}\,\frac{\exp\left[\frac{P}{B}\left(\frac{1}{E_0^{3/4}} - \frac{1}{P_0^{3/4}}\right)\right]}{1 - \exp\left(\frac{E_0^{3/4}\,P^{1/4}-P}{B\,E_0^{3/4}}\right)}, \quad (4)$$

where $\lambda_p = 60$ g/cm^2 is the collision mean free path of protons in a light material.

---

*The self-absorption of the target is neglected.

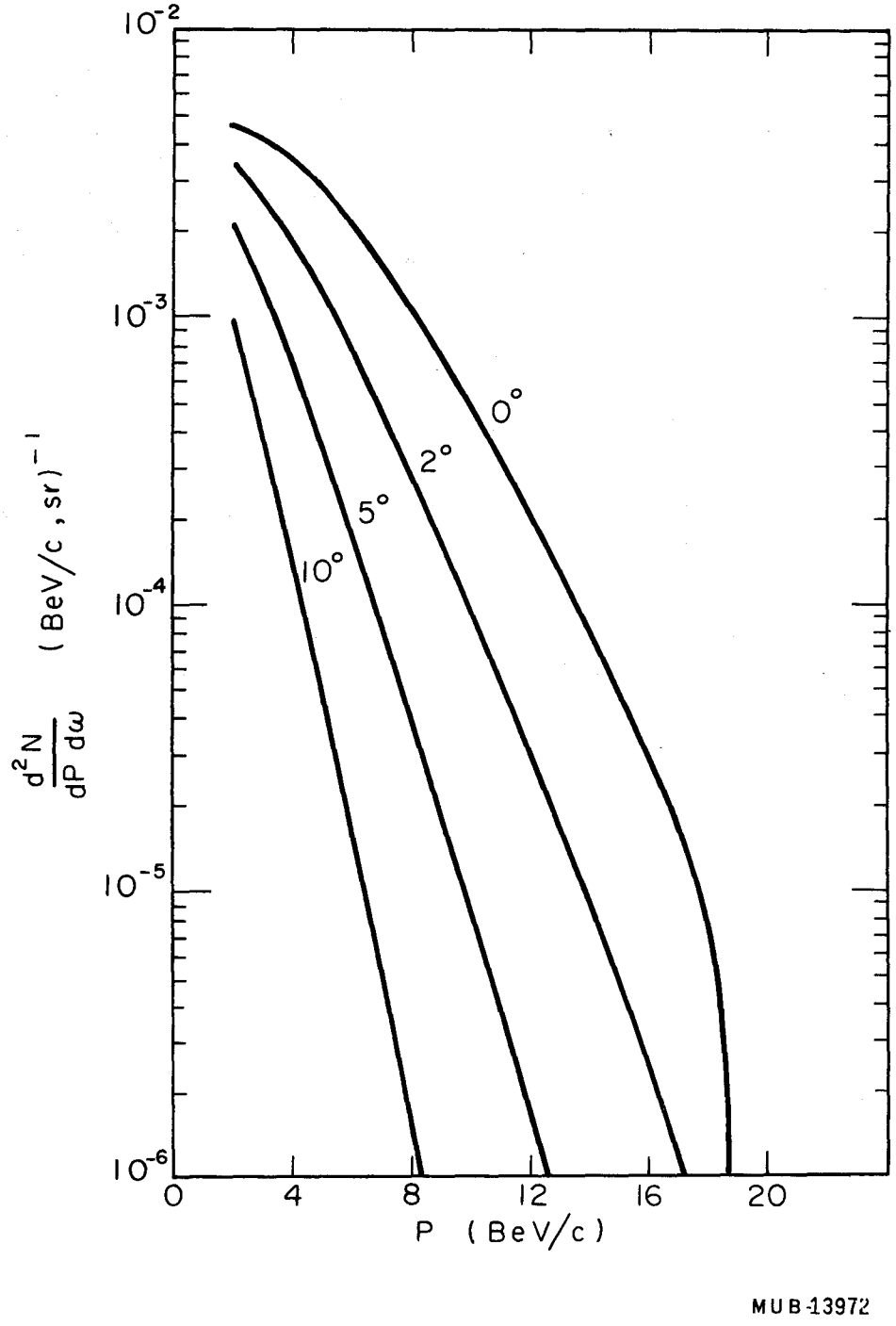

Fig. 1. π-meson fluxes (one sign) from a 20-BeV electron on t = 1 target.

In Eq. (4) the angle of emission θ does not appear, a consequence of the postulated invariance of the transverse momentum distribution of the secondaries. The ratio R thus expresses also the ratio of the fluxes integrated over the solid angle.

As an application, in Fig. 2 are plotted the ratios of the proton fluxes to the electron fluxes produced in a target one radiation length thick for two characteristic cases: one in which protons and electrons have the same momentum, $P_0 = E_0 = 20$ BeV, and the other in which the proton has 30 BeV and the electron 20 BeV. According to these curves, in order to produce comparable fluxes of secondaries with P = 10 - 15 BeV, a 20-BeV electron machine should accelerate a number of electrons $10^{4.0}$ to $10^{4.5}$ times larger than the number of protons accelerated by a 30-BeV proton accelerator.

References

1. Y. S. Tsai, Estimates of Secondary Beam Yields at SLAC, SLAC Handbook (1966).

2. G. Cocconi, L. J. Koester, D. H. Perkins, Lawrence Radiation Laboratory Report UCRL-10022 (1961), p. 167. (1961 High Energy Physics Study, Summer 1961.)

3. G. H. Trilling, Pion and Proton Fluxes from High Energy Proton Collisions, in 200 BeV Accelerator: Studies on Experimental Use, Vol. I, Lawrence Radiation Laboratory Report UCRL-16830, April 1966.

4. J. Ranft, CERN Report MPS/EP 66-4 (1966).

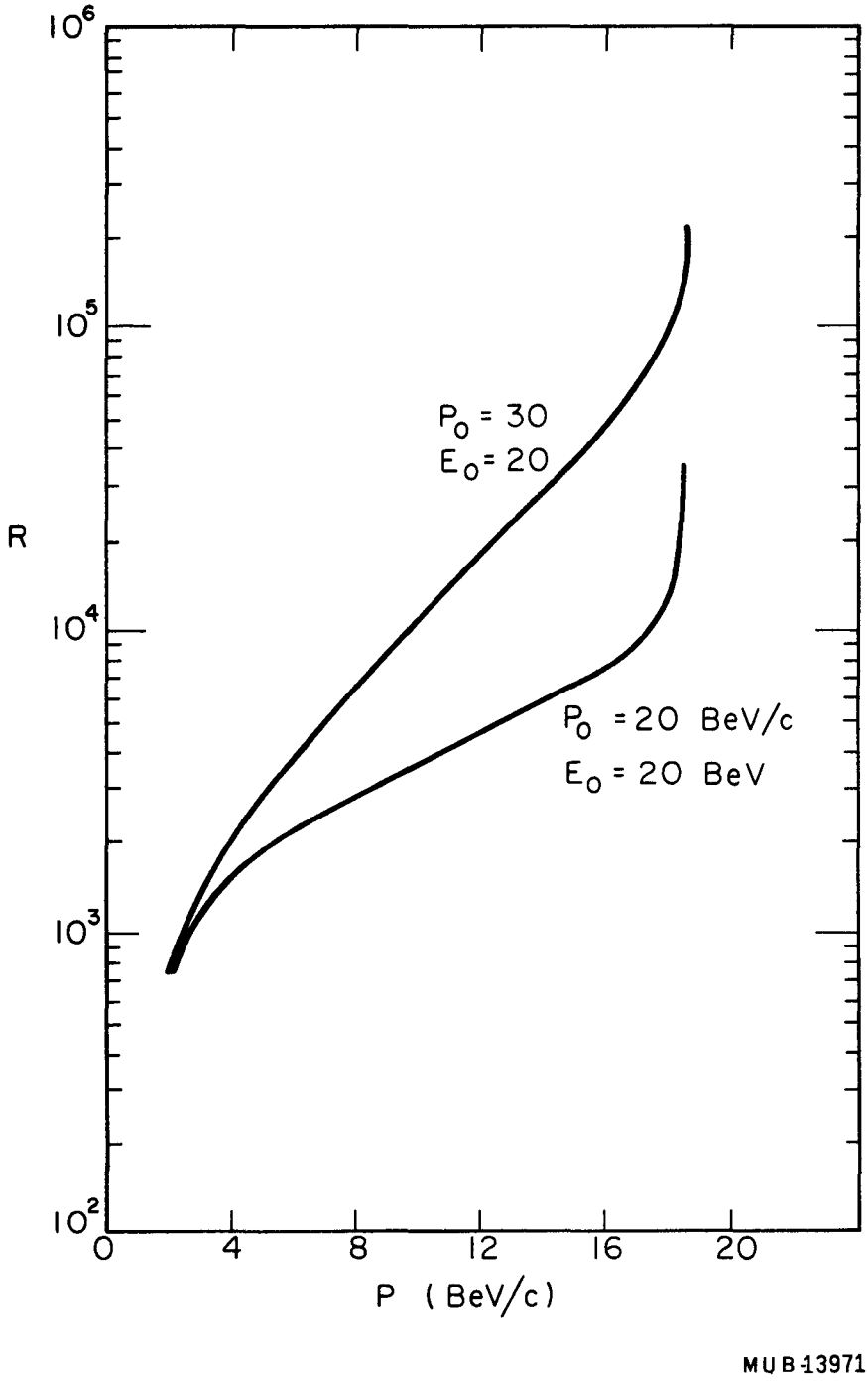

Fig. 2. Ratio, R, of fluxes produced by one proton and one electron on t = 1 target.

B. TARGETING AND EXPERIMENTAL FACILITIES

TARGETING COMPATIBILITY OF BEAMS FOR COUNTER AND BUBBLE-CHAMBER EXPERIMENTS

J. R. Sanford

This brief note will outline certain questions that interest me concerning the utilization of the 200-BeV accelerator. These questions generally concern the ability of the accelerator facility to share the proton intensity among many experiments simultaneously.

Targeting for counter experiments usually consists of providing a steady stream of particles at constant energy for a half second or more every pulse. Bubble chambers need a fast burst of particles within less than 0.001 sec. The goal of targeting compatibility must be to provide beams under such different conditions in an efficient way on every pulse of the accelerator.

Recent developments in bubble-chamber technology have made possible the operation of multiple-pulsing bubble chambers. In a few years these chambers may be able to expand several times every pulse and may even become a resonant system and be capable of taking pictures every 50 msec or so.

Generally speaking, the usual fast external proton beam (EPB) would not be suitable as a source of particles for such a chamber. The usual fast EPB ejects one or a few of the bunches of circulating protons within the machine. In order to be efficient, and not lose protons during the ejection, the beam would be kept bunched for each such fast burst in the EPB. Such a bunched beam is not useful for counter experiments in between fast bursts for a multiple-pulsing bubble chamber. In fact, since the internal beam has to be positioned before fast ejection, and in a different position for slow ejection, and since it may take 30 msec to change from one to the other, compatible external beam operation may be impossible.

One solution to this problem would consist of modulating the intensity in a basically slow EPB. The protons in the beam would usually go on to targets for counter experiments, but when the extra bursts of protons come along, the external beam would be deflected on to targets for bubble-chamber beams. This would be repeated as often as needed for the multiple-pulsing bubble chamber, and the intensity of protons in the burst would be adjusted to produce a satisfactory number of secondary particles for the bubble chamber. The counter experiments would have to gate off their electronics while the beam spill was interrupted, but they would only lose about 0.1% of the beam time. Naturally, there will be fewer protons for the counter beams, but the protons would not have been available anyway. More inefficient methods of targeting would have used the proton bubble-chamber beams.

The development of such modulated beams would mean, I hope, that other EPB's would be fast/slow beams of this type, and that no time would be lost in going from one mode of operation to another. Then counter experiments and bubble-chamber experiments could use the same external beams and extract the maximum utilization of the machine pulse and proton intensity.

Another question concerns the compatibility of simultaneous targeting in an internal targeting area, and the ejection of a fast/slow EPB. Although only about 10% of the proton intensity is expected to be targeted in the internal targeting area, it must be done while one or more EPB's are simultaneously operating. Furthermore, the proton intensity of the EPB's will be modulated by perturbing the circulating beam while it is near a half-integral resonance. All of this must be done, and in the presence of a steady slow spill on the internal target.

Maybe these conditions are too demanding, but it seems that the accelerator should be designed with such capabilities, if possible.

A TARGET FOR A 200 BEV EXTRACTED PROTON BEAM

G. Cocconi

A 200-BeV extracted proton beam (EPB) of luminosity

$$A^2 = (\pi r_o^2 \times \pi \theta_o^2) = (\pi \times 0.33 \text{ mm mrad})^2 ,$$

when found on a target, can have transverse dimensions $r_o = 0.2$ mm and angular aperture $\theta_o = 0.15$ mrad. A typical target is a transmission target made of beryllium, 10 g/cm^2 thick, in which about 15% of the beam interacts, while the 85% that emerges on the other side is practically undisturbed. The average multiple scattering angle generated by the transmission target, $\langle\theta\rangle \approx 0.04$ mrad, is in fact negligible in comparison with the natural width of the beam, θ_o.

The secondaries produced in the target by the interacting protons are concentrated in the forward direction, within a cone whose aperture is determined by the average transverse momentum, $p_\perp$, of the secondaries. There is good evidence for assuming that, in first approximation,

$$\langle p_\perp \rangle \approx 0.4 \text{ BeV/c} ,$$

independent of the momentum of the secondary particle and of its nature. Consequently, most of the secondaries of momentum p are emitted within a cone of angular aperture

$$\theta_p = \frac{\langle p_\perp \rangle}{p} = \frac{0.4 \text{ BeV/c}}{p} .$$

For the efficient utilization of the secondaries in an experimental area, it is necessary to isolate a beam ($\pm\Delta\theta$) of particles having a definite momentum $p \pm \Delta p$, and to eliminate as much as possible the background generated in the area by all other unwanted secondaries produced in the target. At the energies we are considering, the most stubborn background consists of μ-mesons produced by the decay of π-meson secondaries, and care should be taken to minimize these mesons.

At this point, as a reminder, it is worth mentioning that the decay probability of a $\pi^\pm$-meson of momentum p to a μ-meson is $L/55p$, where L is the length, in meters, of the π-meson path in the laboratory system, and p is the π-meson momentum in BeV/c. The μ-meson produced travels practically in the same direction as the π-meson, has the same charge, and has a momentum between p and 0.5 p, with uniform probability.

The fact that the number of μ-mesons is proportional to L, makes it desirable to stop as soon as possible the π-mesons not entering the useful channels, even at the expense of the flexibility in choosing the secondary beam momentum.

In conclusion, the requirements for the design of a 200-BeV EPB target are the following:

(a) Vacuum channel containing the primary proton beam emerging from the target. This beam can be used farther away on other targets.

(b) Secondary beam extraction from the forward direction.

(c) Angular aperture of the secondary beams accepted in the channels not much smaller than θ_p.

(d) Maximum reduction of the free path of all secondaries not entering the channels.

(e) Elimination of the secondary μ-mesons from the experimental area.

The target system here proposed is illustrated in Figs. 1, 2, and 3, and has the following properties.

The primary 200-BeV proton beam, 0.4-mm wide, 0.15 mrad divergent, is focused on a beryllium target, a rod 5-cm long, 2 cm in diameter. In order to operate the target system, the position and the divergence of the beam should be kept constant within $\pm r_o$ and $\pm \theta_o$.

The target is placed at the beginning of an 18-m long, homogeneous magnetic field, B = 2 teslas, produced in the horizontal gaps of three dipole magnets: M_1, M_2, and M_3, each 6-m long [Fig. 1(a)]. These magnets are also illustrated in Fig. 2, where it can be seen that their gaps have cross sections of 10 times 100, 15 times 150, and 15 times 200 cm^2, respectively.

The characteristic feature of this system is that the 18-m long gap is filled with heavy non-magnetic material (lead, uranium, mercury), except along the secondary beams. Those beams are thus completely embedded in matter that absorbs the secondaries not entering the useful channels.

Some construction details are given in Fig. 1(b), where the transverse scale has been expanded by a factor of 10. The EPB emerging from the target is transported down the 18 meters in a 2-cm-diameter pipe that eventually continues beyond M_3 up to the next target, some hundred meters downstream (see Fig. 3). The secondary beams— positive, negative, and neutral—leave the vacuum tank through side windows, and continue in channels carved into the material filling the rest of the gap. The magnets are split horizontally (see Fig. 2) to allow the placement of the vacuum tank and of the portion of the return legs of magnets 2 and 3 that have slits for the less-energetic beams.

Since the iron of the magnets is very effective in absorbing the secondaries and in deviating the μ-mesons, the magnets should be designed with a high iron-

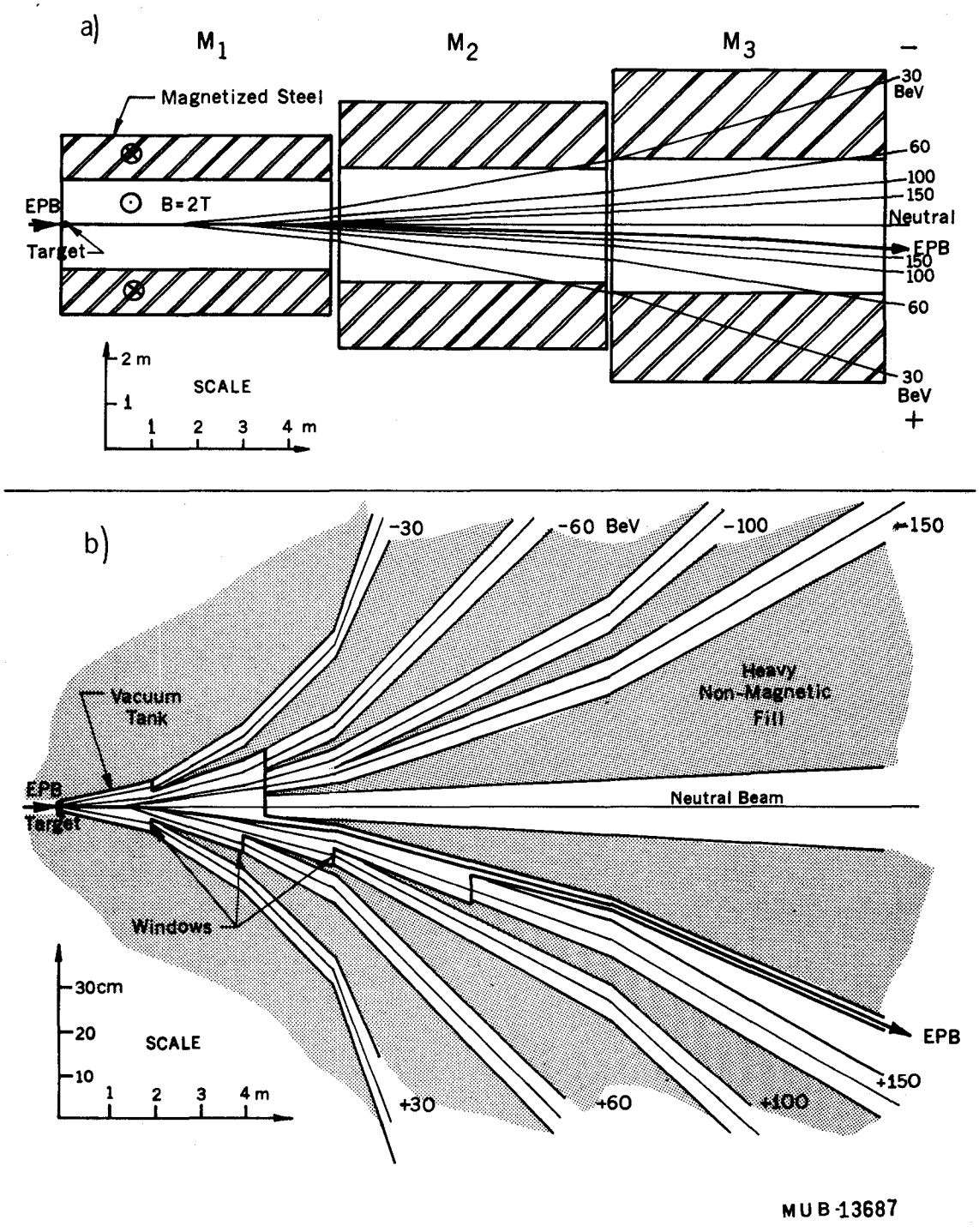

Fig. 1. (a) Plan view of EPB targeting magnets.
(b) Plan view of non-magnetic shielding to define secondary channels in the gap of the targeting magnets.

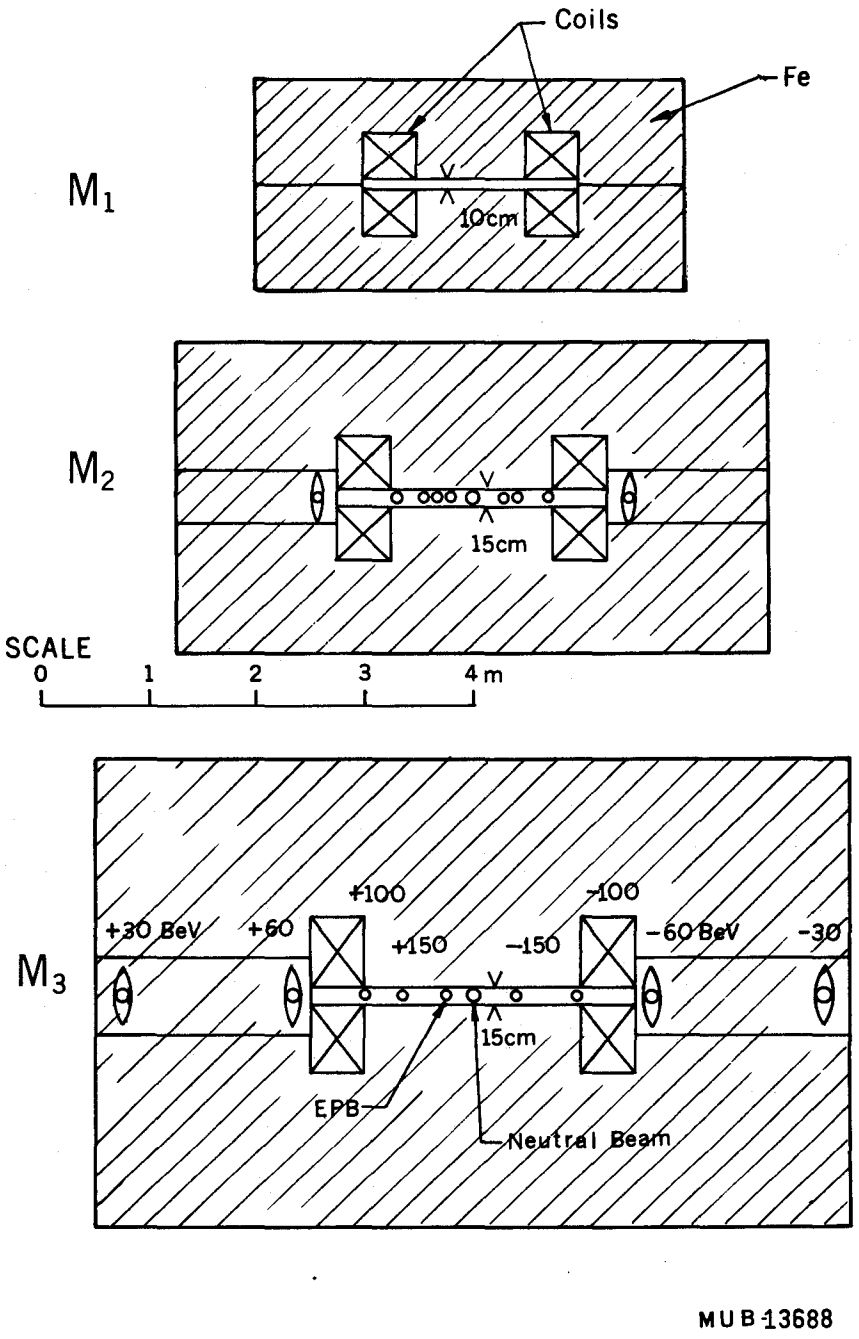

Fig. 2. Cross sections of targeting magnets M_1, M_2, and M_3.

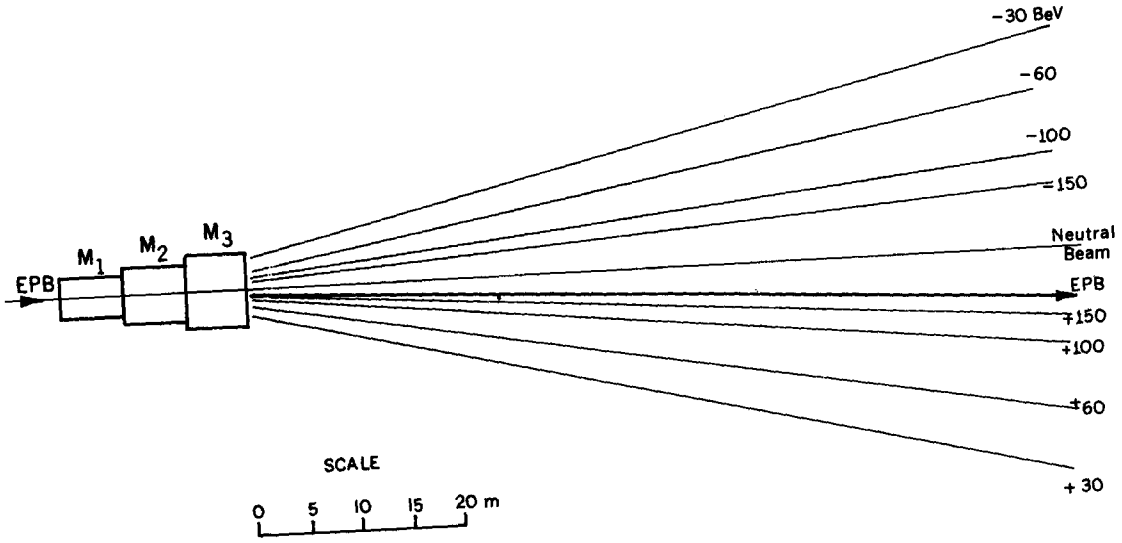

Fig. 3. Plan view of beam lines leaving targeting magnet.

to-copper ratio. The gaps are kept as narrow as possible to minimize power consumption. The system is simple enough that even a radical modification of the beam momenta should not be very difficult to carry out.

The momenta chosen for the charged secondary beams, 150, 100, 60, and 30 BeV/c, are typical. The apertures of the channels adopted in the present design, as well as the accepted transverse momenta and the momentum bites, are summarized below.

Secondary beam momentum (BeV/c)	Aperture, $\pm \Delta\theta$ (mrad)	Transverse momentum p (BeV/c)	Momentum bite, $\pm \Delta p$ (BeV/c)
$\pm$150	3	0.45	6
$\pm$100	3	0.3	3
$\pm$60	5	0.3	1.7
$\pm$30	5	0.15	1.3
Neutral	5	--	--

The most critical channel is that with +150 BeV, because it runs so close to the EPB. At the end of M_3 it diverges from the EPB by 18 mrad and is 16 cm away: this is enough to make possible the insertion in that position of a system magnet.

In order to decrease the μ-meson background around the most energetic beams, it will be necessary to pull these beams farther away from the EPB by means of additional bending magnets. Figure 3 shows that there is space for this, as well as for the shielding.

Further shielding is likely to be unnecessary for the lower-momentum channels that go through the magnetized legs of M_2 and of M_3. The vertical slots in the iron (also filled with non-magnetic material where not used by the beam) provide holes with low field that let the beams go through, while the magnetized iron "traps" the μ-mesons still present, by bending them in the forward direction.

No evaluation of the shielding necessary to protect the other channels is attempted here. However, it is believed that the amount of material that must be put around the long EPB channel for elementary safety reasons will already be adequate in most of the cases.

In comparing the "solid target" here described with other target systems, the inconvenience of the rigid channels should be weighed against the advantage of a minimum μ-meson background. When the μ-meson background must be eliminated farther away from the target, as is the case when a more flexible system is considered, then the amount of shielding becomes so large as to introduce a rigidity in the experimental area setup that can be worse than that

of the solid target. This situation becomes more evident the larger the energy of the proton beam.

The construction of a solid target becomes simpler in the case of an end target, in which the proton beam is totally absorbed. The vacuum tank is then no longer necessary, the most energetic positive secondary beam is no longer cramped near the EPB, and the filling in the gap is more efficient in stopping unwanted secondaries.

ON TARGETING STATIONS IN AN EXTERNAL PROTON BEAM AT THE PROPOSED 200 BEV ACCELERATOR

A. L. Read

In these notes we shall discuss various arrangements of targets, quadrupole and dipole magnets used for obtaining secondary particles from an extracted proton beam at the 200 BeV accelerator. Some of the schemes have already been described elsewhere[1,2] and will not be discussed in detail here.

The targeting arrangements to be discussed are the following:

(i) Scheme I: A system which is roughly equivalent to that given in the Design Study Report[1] (DSR), for the internal target area H.

(ii) Scheme II: A system similar to that shown in the DSR for external proton beam (EPB) target station I-A.

(iii) Scheme II-A: A system we described in an earlier note.[2]

(iv) Scheme III: A system similar to that shown in the DSR for EPB target station J-A.

(v) Scheme IV: A system in which the secondary beam production target is followed by, first, a quadrupole magnet lens, and then a dipole magnet. Such a scheme is presently being considered for use at the long-spill EPB at the BNL-AGS.

DISCUSSION OF SCHEME I

An example of a Scheme I targeting station for an EPB is shown in Fig. 1. Note that there is no secondary beam at 0-deg production angle. This is the outstanding special feature of this beam. The principal advantage of this is that the unscattered EPB and the various secondary beams can be independently controlled by the individual users of the beams. The major drawback is that the beams are not as intense as they could be, since the yield of secondary particles falls rapidly as the production angle increases.

Let us take an example and estimate the beam intensities. Take the 50-100 BeV/c counter-beam shown in Fig. 1. Assume (i) the particle production cross sections are given by the empirical formulas of Trilling,[3] (ii) an EPB of 10^{12} protons per second (pps), (iii) a target thickness of 0.5 interaction lengths, (iv) quadrupole magnets Q with an aperture of radius 2 in., (v) a momentum-bite of $\pm 1\%$ (HWHM). Then the π^- intensities are estimated to be $\approx 10^7$, 4×10^6, $1.5 \times 10^6 \pi^-$/sec at 50 BeV/c and $\approx 2 \times 10^7$, 3×10^6, and $5 \times 10^5 \pi^-$/sec at 100 BeV/c, for production angles of 0 deg, 5 mrad, and 10 mrad, respectively. For

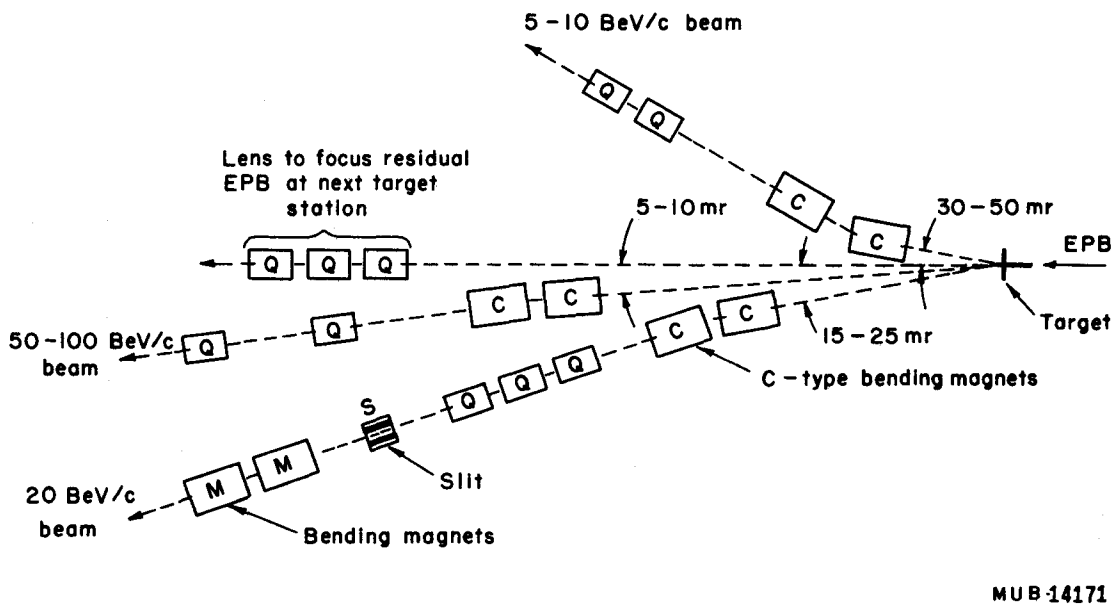

Fig. 1. Scheme I targeting station for EPB.

many experiments these fluxes of pions at 5 mrad (even 10 mrad, in many cases) are quite adequate.

Let us take a second example: for 10-20-BeV/c π^-, the number of π^- produced at angle $\approx$ 3 deg is predicted by Trilling[3] to be quite comparable with the number produced at 0 deg. For "low" energy secondary beams, then, the 0-deg production angle requirement is not necessarily important.

DISCUSSION OF SCHEMES II AND II-A

An example of a Scheme II targeting station for an EPB is shown in Fig. 2. Note the following features of such an arrangement:

(i) Secondary beams produced at 0 deg are obtained. For high-energy ($\gtrsim$ 50 BeV/c) beams, this insures the maximum possible flux of such beams attainable at the 200-BeV accelerator.

(ii) When the momentum of the "prime" beam, for example, the 150-BeV/c π^- beam in Fig. 2, is changed, then the momenta of all the other changed particle beams are scaled in direct proportion. This will often by inconvenient. One method of independently controlling at least one other secondary beam, using a correcting bending magnet M_5 and various production target positions, has been discussed previously[2] (also see Fig. 3).

(iii) When the momentum of the prime beam is changed, the trajectory of the residual EPB is also necessarily changed. In the type of experimental area shown in Fig. 2, one could construct an EPB beam-stop of large horizontal dimension, so that it could intercept the beam, regardless of the magnetic fields in the targeting magnets M_{1-4}. However, if there is to be a subsequent EPB targeting station further downstream, then the question of redirecting the proton beam, for various excitations in M_{1-4}, is quite complicated. This question is discussed further in the next section.

DISCUSSION OF SCHEME III

In Fig. 4 an example of a Scheme III targeting station for an EPB is shown. The purpose of the present discussion is to consider the question of transporting the EPB to a subsequent targeting station, while obtaining a secondary beam of variable momentum. In order to simplify the discussion, only one secondary beam is shown in Fig. 4. As in Fig. 3, there could of course be several secondary beams produced simultaneously at the target station. The fields in magnets M_1, M_2, M_3, and M_4 are adjusted so that for all secondary beam momenta, the trajectory of the residual EPB at the downstream end of the target station is always the same. Note that in the example shown in Fig. 4, the final proton-beam direction is the same as the incident-beam direction. Thus, if B_1, B_2, B_3, and B_4 are the angles of bend of the EPB in the four target magnets, we have the constraint $B_1 + B_4 = B_2 + B_3$. In addition, since the position of the residual EPB must be unchanged, a second constraint on the bending angles B_1 is necessary. For example, we could require that $B_1 = B_4$ (thus $B_2 = B_3$, also). The momentum of the secondary beam is determined by the magnetic field settings in M_2, M_3 (keeping $B_2 = B_3$) and M_1.

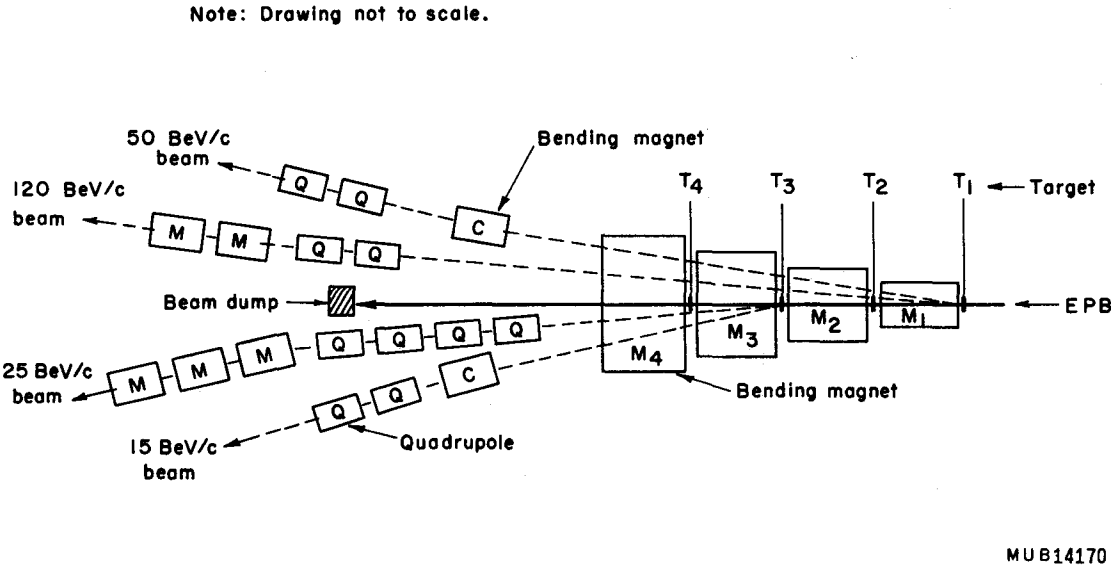

Fig. 2. Scheme II targeting station for EPB.

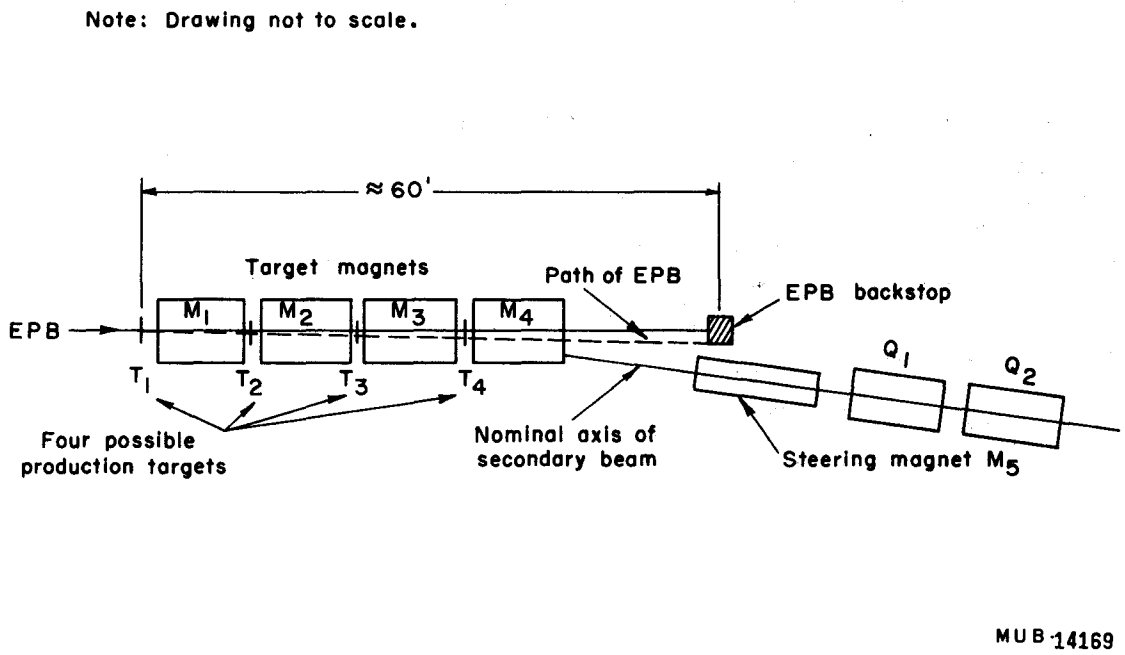

Fig. 3. Scheme IIA targeting station for EPB.

Note: Drawing not to scale.

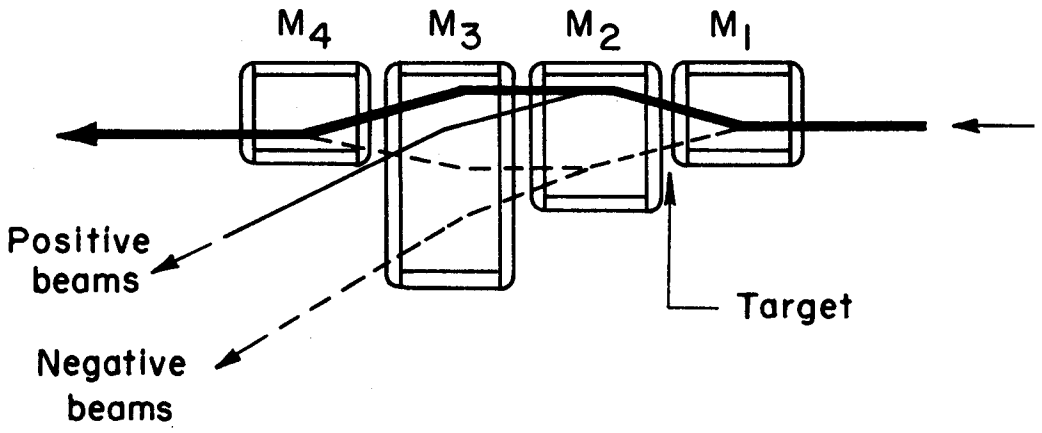

MUB-14168

Fig. 4. Scheme III targeting station for EPB.

We now ask two questions:

(i) What is the highest-momentum positive beam that can be obtained with such a system? This is determined by the width of the septum of M_4 and by the dimensions, at M_4, of the residual EPB and the secondary beam. Using the magnets just as described in the DSR,[1] and taking a separation between EPB and secondary beam lines, at M_4, of 15 in., then the highest attainable positive beam (at 0-deg production angle) has momentum 75 BeV/c, for 200-BeV EPB energy.

(ii) What size of quadrupole magnet lens is required to attain the optimum solid angle of acceptance for the secondary beam? This lens would presumably be placed immediately downstream from M_4, in the secondary particle beam. Taking a half-angle of acceptance, about 0 deg for the beam, of $\approx 0.5/p$ rad (p is the secondary beam momentum, in BeV/c), we are required to use a quadrupole lens with an aperture of radius about 10 in.: this would be an unrealistically large aperture! It must be of interest to estimate what sort of beam we can obtain with the Scheme III type of target station. Let us take the diameter of the quadrupole lens to be 8 in., then a $\Delta p/p = \pm 1\%$ HWHM 75-BeV/c π^+ beam produced by 10^{12} EPB protons/sec, produced at 0 deg in a target one-half of an interaction length long, would have an intensity of $\approx 4 \times 10^7$ π^+/sec (and $\approx 4 \times 10^6$ K^+/sec). It is clear that for the majority of applications these intensities are more than adequate. One method of raising the highest attainable positive beam momentum, for this target-station configuration, might be to replace the Fe-Cu magnets by superconducting bending magnets—with a maximum field of, say, 50 kG. In such a case, the maximum attainable 0-deg positive beam would have momentum of 140 BeV/c. However, it is perhaps premature to discuss this possibility seriously at the present time.

DISCUSSION OF SCHEME IV

An example of a possible Scheme IV-type EPB targeting station is shown in Fig. 5. The essential difference between this scheme and those discussed in the two preceding sections is that a quadrupole magnet lens is placed downstream of the secondary beam production target, but upstream of the system of bending magnets that separate the residual EPB from the high-energy secondary beams. This sort of scheme might be quite useful for obtaining very high energy ($\geq$ 150 BeV/c) charged secondary beams, since the first septum magnet, which bends the residual EPB, but not the secondaries, is placed at or near a focus of both the EPB and of the secondary beams. The steering magnets M_{S1} and M_{S2} could be used to deflect beams of various momenta in the 125-175 BeV/c range into the subsequent transport systems for the secondary beams. The slits S_1, S_2 and the quadrupole magnet lenses L_1, L_2 would have to be moved appropriately, as the selected secondary momentum was varied. For beams of momentum $\lesssim$ 125 BeV/c, this sort of system could still be used. The secondary beam would not be well "focused" in the region of M_{S1} and M_{S2}. Presumably this is not a serious difficulty since the physical separation of such "low" momentum beams from the residual EPB is quite large.

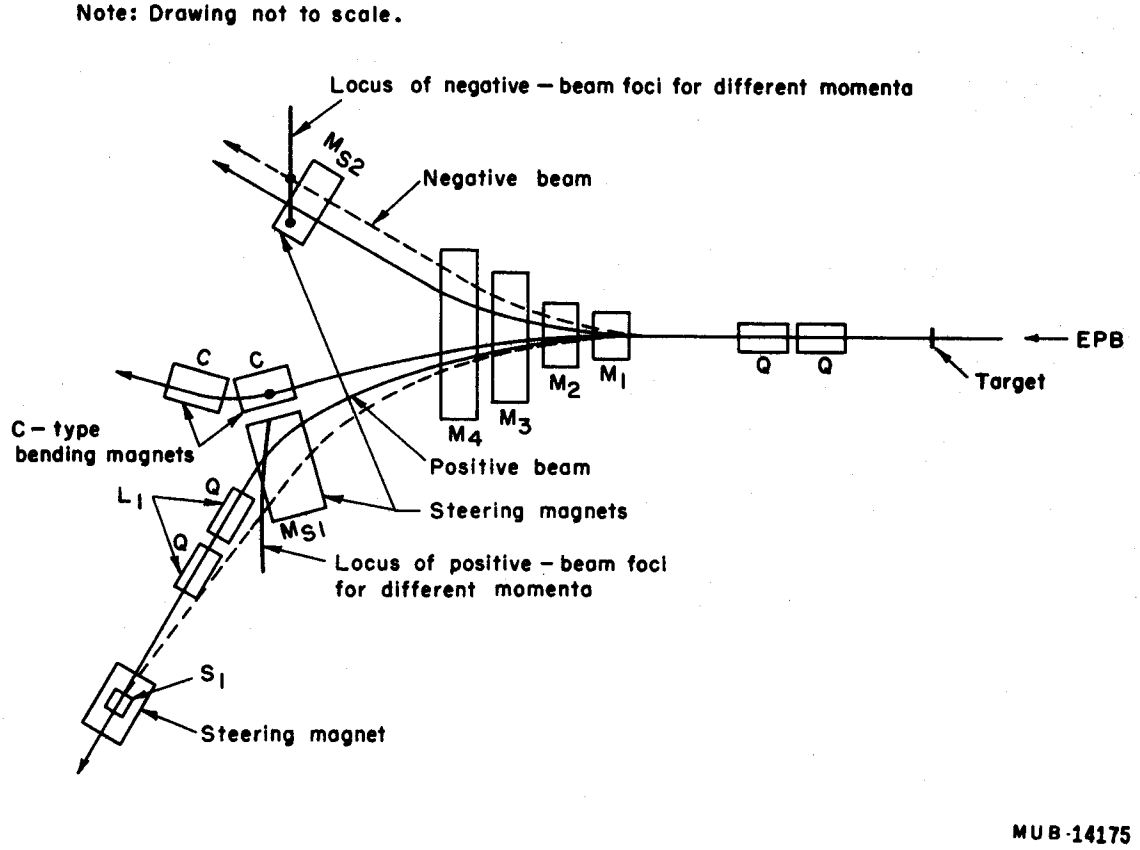

Fig. 5. Scheme IV targeting station for EPB.

SUMMARY

We have discussed above a few possible examples of EPB targeting stations for obtaining charged secondary particle beams. Such schemes would seem to be a realistic arrangement to use for many types of high-energy physics experiments. The possibility of setting up two more beams independently controllable, at any of these types of target stations, seems to be quite feasible. The question of the need to consider the possibility of more complicated systems (e.g., with many 0-deg beams from the same production target) depends strongly upon the scope and rate of performance expected of the high-energy-physics experimental program, about which only a wide spectrum of varying and probably unrealistic estimates can be made today. Let us suppose, however, that we have five targeting stations (as in the DSR), an average of 2.5 secondary beams per station, each beam containing on the average one "Y"-fork (thereby using two experiments alternately), and assume that no two experiments can run in series, using the same secondary particle beam. Then the number of experiments set up simultaneously in an area that could be served by a particle beam would be $5 \times 2.8 \times 2 = 25$. Is 25 enough? That is largely an economic question. However, assuming that we wish to increase beyond the 25, do we increase (i) the number of target stations, (ii) the number of beams per station, or (iii) the number of forks per beam? The feasibility of increasing (i) or (iii) is a matter of economics, real estate, etc. As far as (ii) is concerned, we can certainly obtain additional "secondary" beams, of either "low" momentum ("low" = less than $\approx$ 25 BeV/c) or finite production angle ($\theta_{prod} \approx$ a few degrees) in any of the target-station systems considered in this note and elsewhere.[1,2]

References

1. 200 BeV Accelerator Design Study, Lawrence Radiation Laboratory Report UCRL-16000, Chap. XIII, June 1965.

2. A. L. Read, Remarks on the Experimental Physics Program at the 200 GeV Accelerator , in 200 BeV Accelerator: Studies on Experimental Use: 1964-1965, Vol. I, Lawrence Radiation Laboratory Report UCRL-16380, April 1966, p. 256.

3. Also in the preceding reference volume: D. Keefe, G. Mealy, and G. Trilling, Antiproton Fluxes from High Energy Proton Collisions, p. 58; also see G. Trilling, Pion and Proton Fluxes from High Energy Proton Collisions, p. 25.

ROUND-TABLE DISCUSSION ON THE IMPORTANCE OF THE INTERNAL TARGET AREA AND ITS POSSIBLE CONFIGURATION

This round-table meeting was moderated by Denis Keefe, who delivered a brief introduction to establish a framework for the discussion. The group of participants included most of the summer study group in Berkeley at the time and many members of the local Design Study Group.

INTRODUCTORY REMARKS (Denis Keefe)

Before opening the discussion, I would like to make the following two points. As regards procedure, I intend to talk for about 30 minutes and to try to establish an acceptable framework. Second, we are not here to arrive at a decision, which will be the job of the group carrying out final design, but to help define the best working hypothesis that the study group ought to adopt. In the process it may become clear which alternatives are most worthy of intensive study.

The internal target area of the Design Study Report (DSR) could be considered as supplying some four, or so, experimental outlets (or secondary beams). Its estimated cost is about 11 million dollars. If we assume that the total experimental program should remain unchanged, it is germane to discuss whether this sum (or part of it) would not be better invested in adding to the external areas. For example, the full power of the external beams is realized only when three or four series targets can be utilized, and this situation is far from reached in the proposed scheme. Alternatively, among the four proposed external target areas, three (in the DSR) are identical and the fourth has some special properties. Perhaps all should have some quite different features, e.g., one be suitable only for low primary energy (maybe $\leq$ 70 BeV) to minimize the muon shielding, another be optimized for neutral beams, another for neutrinos, and so on. A cut-back on the expensive internal area could allow the release of money to enhance the variety and flexibility of the external areas. In the process, some of the disadvantages of eliminating or restricting the internal area could be compensated.

As a starting point we adopt the philosophy that the major part of the experimental program be based externally. Therefore, at most, we are considering a maximum of one fully-developed internal area and no more. At minimum, we consider none. In addition, we will specify that the predominant use of the internal target will be in a Collins straight section using a time-averaged intensity of 10% of the circulating beam, viz , 3×10^{12} ppp. For limited periods, higher beams could be allowed if the physics uses so demanded; likewise, on special occasions targets could be placed in the curved section of the machine so that the magnetic fields in the synchrotron guide field would help to deflect out the beams of lower momenta. However, in this case the muons would also be bent at steeper angles to the proposed shielding wall and could quickly become a hazard, so that this should not be considered a normal mode of operation.

For historical reasons we can recall the three usually quoted advantages of internal targets:

(a) Target Efficiency: See, for example, Chapter XIII of the DSR for a discussion of efficiency and productivity; only an extremist can argue that this is any longer important.

(b) Ease of Spilling on Multiple Internal Targets: We can rule this out because we are considering only one internal area at most.

(c) Target Optics, viz , the possibility of observing a tiny source size away from 0-deg, or the possibility of several experiments running from the same target with freedom to vary their momenta independently. These features are advantageous only at relatively low secondary momenta at which typical production angles [$\approx 0.5/p(\text{BeV}/c)$ radians] are not too small.

We now proceed to discard this list, partly for the reasons stated, and partly to set up a new list of the reasons for which an internal area seems required, as follows:

(i) Use of Very Tenuous Targets: Forget multiple traversals in connection with normal metal targets as they are not important, but consider the case of an experiment requiring a target whose tenuosity is determined by the secondary product or products. As examples that we can cite today, we list the very low momentum recoil proton in low momentum-transfer p-p scattering whose detection and measurement demands small energy loss and coulomb scattering, the production of monopoles that may have anomalously high energy loss, or the desire for secondary beams of extremely low electron contamination impossible to attain from thick targets. Who knows what new examples in this same general category may be invented in the next decade? In the event that the escape probability of the desired secondary product should determine the tenuosity of the target, then the multiple-traversal feature becomes very important. During a 600-msec flattop, some 40 000 traversals are possible with a corresponding enhancement of the data-taking rate.

(ii) "Decoupled," "Point" Optics: It is often claimed that several experimenters may view a very small internal target in a straight section at finite angles and be free to vary their secondary momenta independently. At high energies this mode of operation will be de-emphasized because of the forward collimation of the secondaries. We believe that the advantages can be recovered by inserting a target in a straight section of the EPB. If you recall the limitation on the internal target operation to only 10% of the beam, it is clear that the equivalent external straight section target (SST) need not be very thick, ≈ 1 cm. This is therefore a weak point.

(iii) Indefinitely Small Emittance: This is not relevant for bubble-chamber operation. If a very tiny target is inserted in the internal beam during a long flattop, eventually all the protons will pass through it. For a 500-msec spill and a long target (≈ 1 mfp), the minimum cross section is about 0.003 by 0.003 inch in principle. (In practice, note the problems of support and of cooling.) Externally, the theoretical minimum cross section necessary to capture the whole beam is 0.006 by 0.006 inch. Both these target sizes are comparable, therefore—also probably unrealistically small—and this point is also a weak one.

(iv) First Year or So of Operation: Causality demands that the beam be circulating within the accelerator before it becomes available in the external areas. One argument goes that useful experiments may proceed using an internal area while the extraction mechanisms are being worked on and tuned up early in the operating phase, and that even thereafter the internal area represents insurance against failure of the EPB's. The counter argument is that the extracted beams can be developed very rapidly (e.g., in 1 month), if so legislated, and the pressure for the development of the external areas (undeniably the main focus of experimentation) will be all the greater if no internal area is included.

(v) Future Modifications: The demountable shielding around the internal area may, at some later stage, provide very convenient access to a part of the main ring that includes a long straight section. One example might be the addition of a low-energy intersecting ring for clashing beam experiments. Six to twelve months shutdown could be avoided. Alternatively, an EPB could be extracted in this area at some later time when internal targeting had lost its attractions.

(vi) More Flexibility: Elioff has pointed out that the shielding design, viz, constant in cross section at the internal area, could allow fairly rapid handling. This argument, whether true or not, can be met by supplying an SST in the EPB where the shielding will have similar characteristics.

If it is agreed that no major items have been overlooked, can we agree to limit our discussion to Points (i), (iv), and (v), because the others are weak or can be satisfied in the EPB?

DISCUSSION (R. P. Ely)

(Editor's note: Much of the following discussion actually took place during the delivery of the introduction. Since no tape was made, I have summarized the remarks in my own words from my notes. Where many comments to the same point were made, I have grouped them together without attempting to capture the subtle variations in interpretation, for which I apologize to one and all.)

To initiate the discussion, Haglund presented four plans for the internal target area which had been developed in the previous two weeks in discussions with Sanford, Keefe, and Ely. These are shown in Figs. 1-5 and vary in scope from the full-scale area proposed in the Design Study Report (UCRL-16000) to a simple stub tunnel tangent to the machine similar to the EPB tunnel. The estimated costs are shown in Table I and are to be compared with the approximately one million dollars that 400 feet of normal tunnel would cost.

Before the general discussion, Jovanovic inquired: (a) Can the EPB be flattopped as successfully as the internal beam? (b) Can the internal and external beams be targeted independently in a random manner? Lambertson replied to point (a) that it was probably possible but at a greater cost in effort and expense, and to point (b) that the present vision of a flattopped EPB extraction would make it difficult, but it is perhaps possible by using horizontal excursions for the EPB extraction and vertical ones for the internal targets. Future experience at the CERN PS and the AGS will help clarify these points.

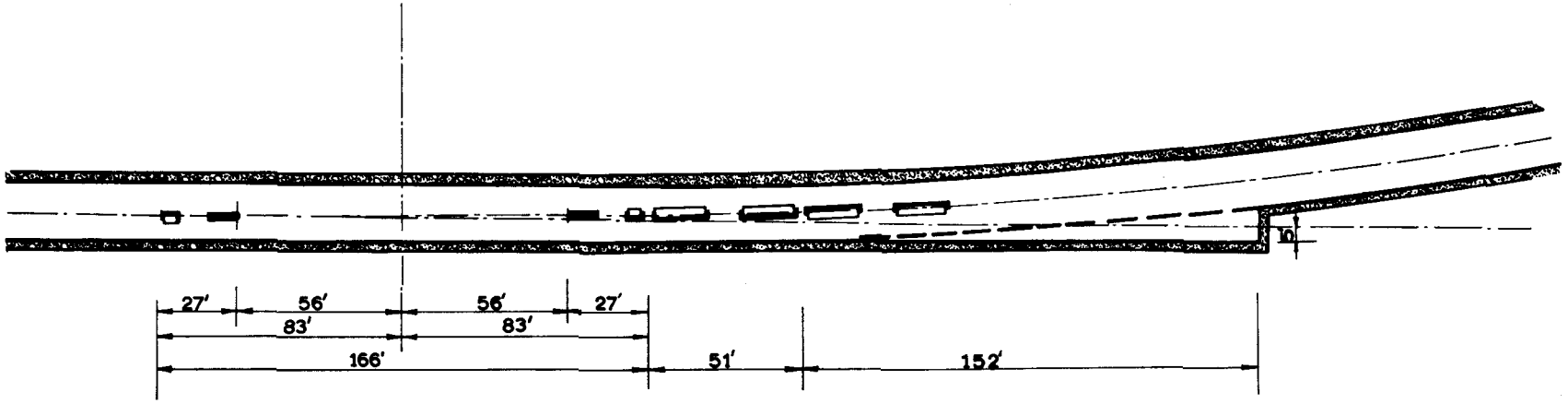

Superperiod

Fig 1

XBL 673-2029

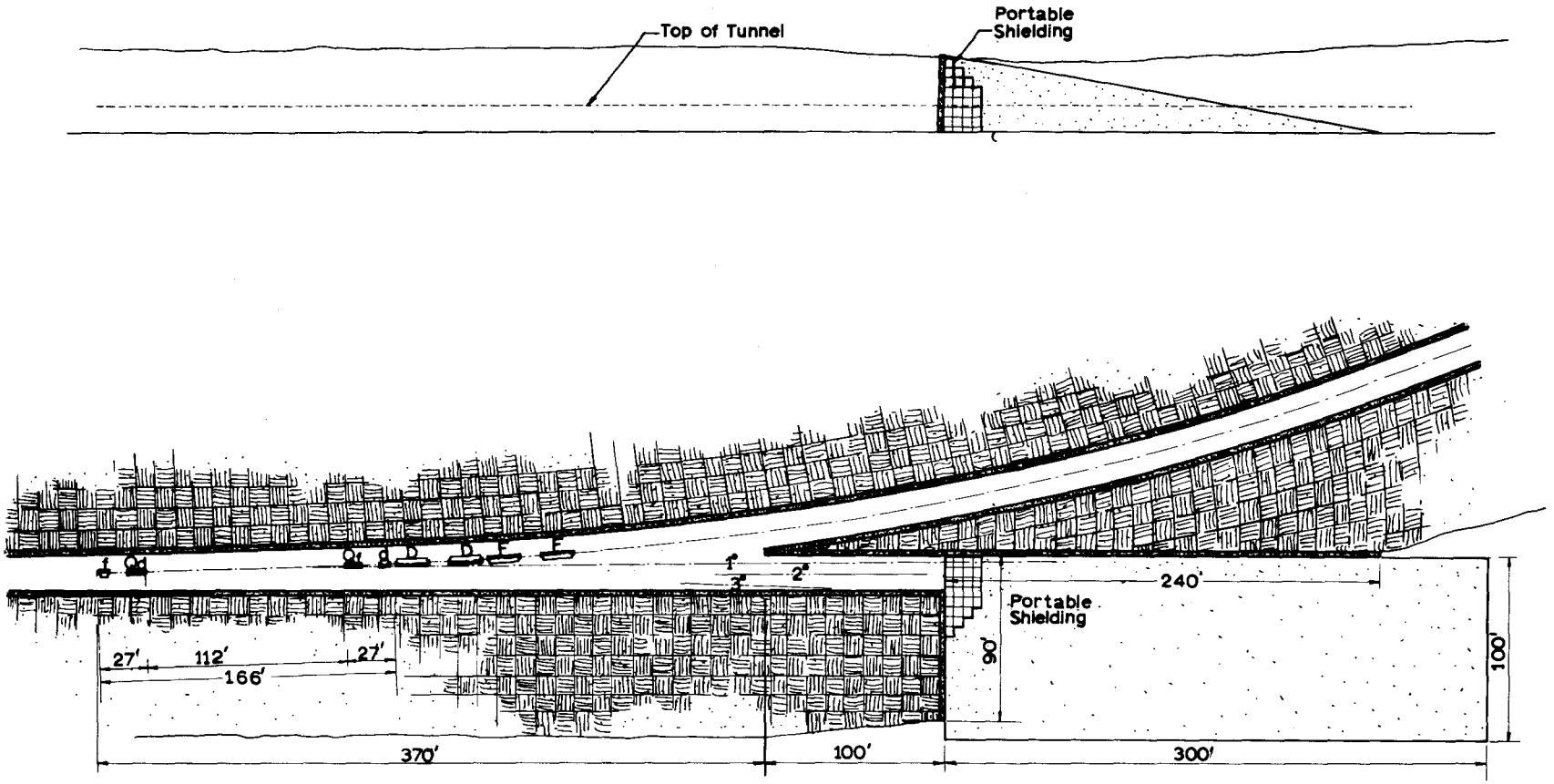

"Minimal" Internal Area

Fig. 2

XBL 673-2030

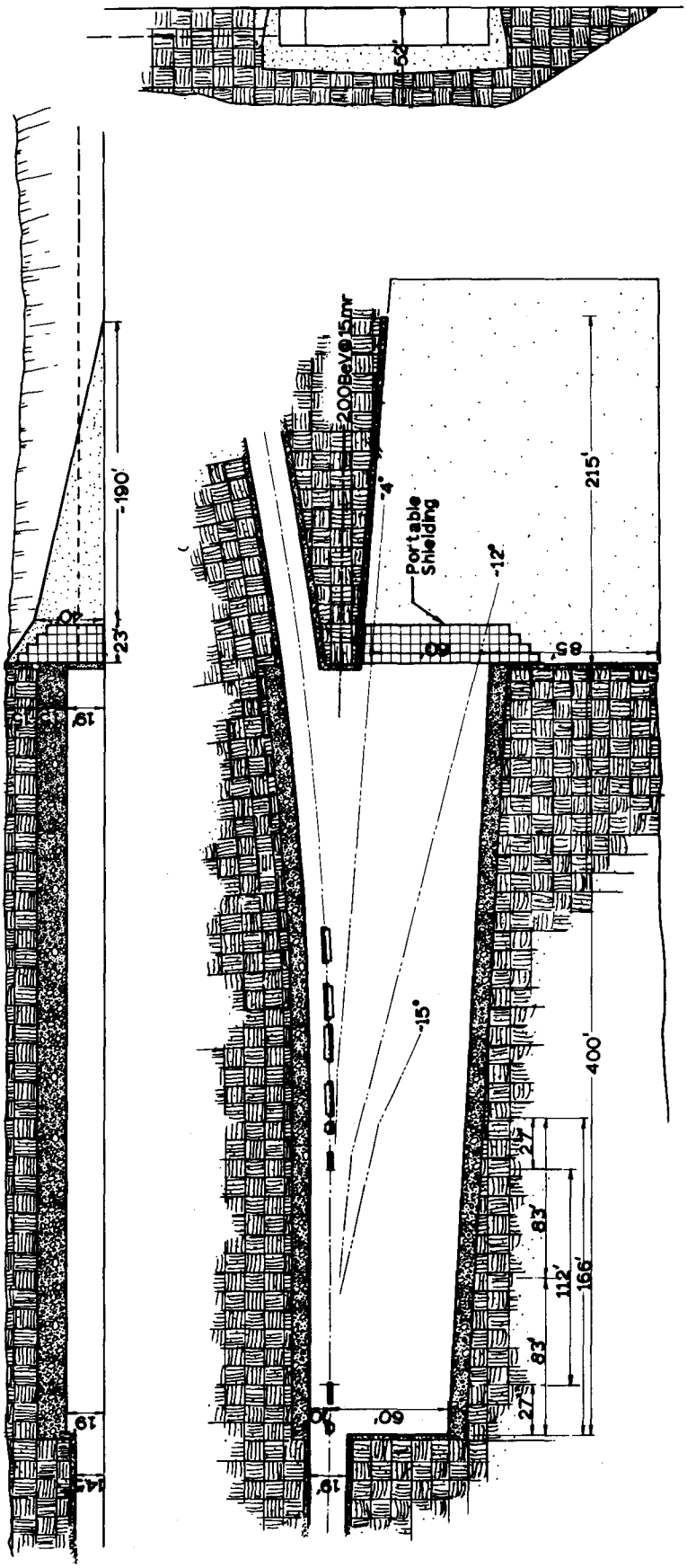

"Underground" Internal Area

Fig 3

XBL 673-2031

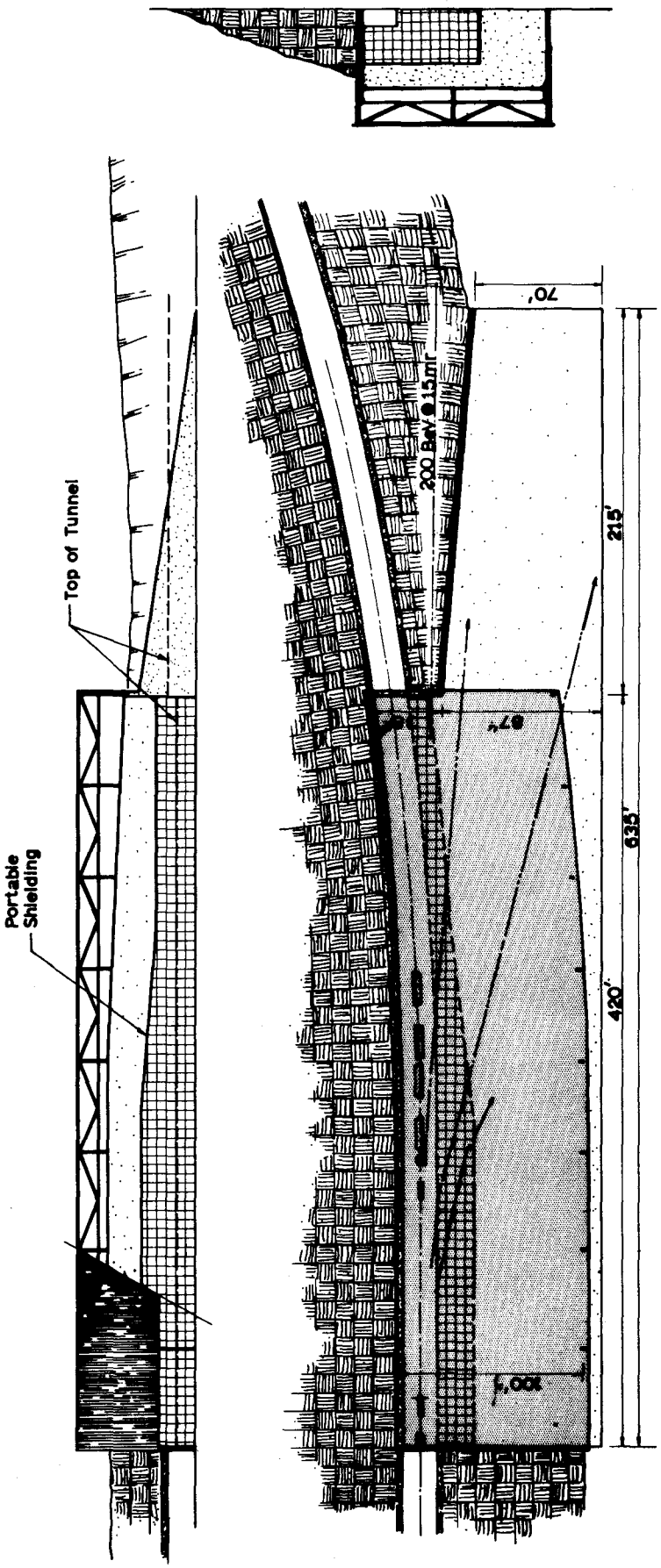

"Half" Internal Area

Fig 4

XBL 673-2032

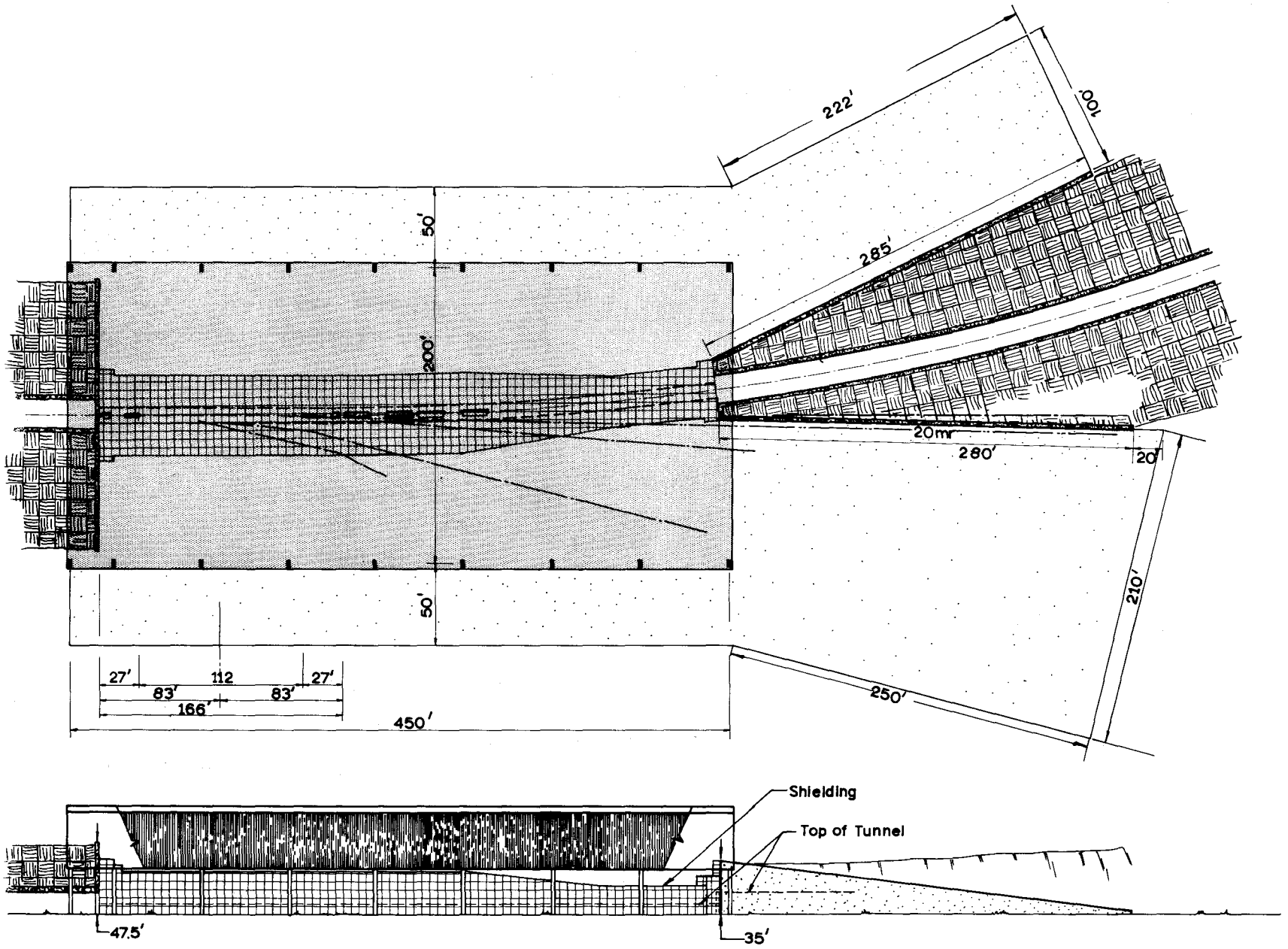

"Full" Experimental Area

Fig 5

XBL 673-2033

Elioff pointed out that even if the three main points suggested by Keefe failed to justify the area, they could well be considered as invaluable fringe benefits, since the internal area would always be of value as a normal targeting area for standard experiments. He felt it likely that set-up time would be considerably less because of the absence of the heavy muon shield which must be present in the EPB.

Several people rejoined that because of radiation problems only 10% of the beam could be dumped on the internal target, but Elioff felt many experiments would require less than 10% of the beam.

Gilbert mentioned that the presence of the internal targeting area would prevent the servicing of that section by the shielded vehicle, and hence extend maintenance problems in that area; Cocconi thought the high radiation levels might cause delays which balanced the benefits of a smaller amount of shielding.

Elioff repeated that radiation might be a more severe problem in the EPB where large targeting magnets would get hot, but Keefe pointed out that (a) these magnets could be removed bodily with a crane, and (b) if no internal area were constructed, a straight targeting section, which would be added to one of the EPB lines, would provide the same type of shielding structure as in the internal area. This latter point added two million dollars to the EPB plans in the event that no internal area is constructed. Cocconi felt strongly that experiments should be done in the EPB when possible, since all setups in the internal area would require stopping the whole machine.

Main points (i) and (v) were discussed from much the same point of view since (i) involved provision for a by-and-large unknown group of experiments. Cocconi felt the items mentioned could be done in the tunnel, but Keefe said this would preclude any piece of large apparatus such as a spectrometer at right angles to the beam. Yuan favored one of the modest areas since he didn't feel it would be necessary to use both sides of the ring simultaneously.

Abashian, Selove, and Tollestrup all argued vigorously for the necessity of the internal area to cover unknown and unanticipated situations. Since the machine is being constructed to investigate the unknown, they felt it of prime importance to include all facilities. Tollestrup mentioned as an example the possibility of utilizing the extraordinarily tight bunching of the beam at transition for time-of-flight measurements.

There was some discussion of the possibility of adding the area later if it was necessary. Keefe thought some small holes in the earth shielding of the ring could be made in a month, but that a full-scale area would need a six-month shutdown which would be very costly in machine utilization. Abashian and Selove both thought that it would be much easier to make modifications to the external area at a later date. Lambertson added further that because of the extraordinary earth loading in the internal area, it would be almost impossible to add the internal area after the machine was built at most of the possible sites.

A great deal of discussion centered around the need for an internal area in the initial experimental phases as insurance against delay or difficulties with the

EPB. Vigorous in their defense of this concept were Elioff, Sanford (in absentia), Abashian, Selove, Tollestrup, and Yuan. On the other hand, Thresher felt the mere presence of the internal area would serve to delay the completion of the EPB and hence some of the major purposes of the machine such as neutrino work. Joining him in these thoughts were Cocconi and Jovanovic. Cocconi especially felt that the machine should be designed as a device separate from the experimental areas and that the concept of an internal targeting area was bad philosophy.

Obviously, no consensus was reached, but it was felt that a broad basis for future discussion had been established. A straw vote of the various proposed schemes revealed the following alignment:

Full-scale area	Elioff, Abashian, Selove, Tollestrup
One-half area	Yuan
Vestigial area	Jovanovic
No area	Cocconi, Thresher

The meeting adjourned for lunch at 12:00 noon.

Table I. Cost breakdown of proposed internal target areas (costs in units of $1000).

	Plain superperiod (Fig. 1)	Minimal (Fig. 2)	Underground (Fig. 3)	Half (Fig. 4)	Full (Fig. 5)
Structure-enclosure slab retaining walls; access, utilities, and shielding	510	1,670	3,730	2,000	3,840
Shielding blocks	--	200	520	2,400	3,640
A and E, contingencies, and escalation	290	820	2,010	1,970	3,000
Crane	---	---	400	150	240
TOTAL (k$)	800	2,690	6,660	6,520	10,720

NOTE ON THE INTERNAL TARGET AREA

Tom Elioff

It appears that an external-beam experimental area is certainly more flexible than an internal target area. Arguments to this effect have been reiterated throughout Chapter XIII of the Design Study Report (UCRL-16000) as well as its counterpart, UCID-10138.

The remaining and perhaps more important question is whether an internal target area is important to the overall physics program of the accelerator and hence should be included with proper perspective as an integral part of the accelerator. Therefore, let us review a few factors which are true in whole or in part .

1. Chapter XIII has some of the following statements:

   a. "The unstacking and restacking of the enormous mass of shielding (time-wise)...would require one EPB area to be always operable.

   b. "The problems of setup are tedious and...will favor lengthy beam setups.

   c. "Muon shielding ≈ 100 m by ≈ 15 m of iron equivalent."

The prescription for extended beam setups is, of course, in the interest of technical efficiency. It is not in the interest of physics if the experiments do not match the area. If one does not allow frequent changes when and if they are necessary (changes without unnecessarily long and expensive set-up procedures), one may curtail the flexibility and usefulness of the accelerator. The internal target area could be the facility for such changes, at least in the initial years of operation when one has to gain some experience with the new machine.

Although statements like a, b, and c are implied in Chapter XIII for both internal and external areas, the internal area does not require a beam dump, extensive muon shielding, or a complicated conglomeration of shielding materials. In general, the inner shielding wall is of heavy concrete 20 feet thick and 20 feet high. Typical beam passages are 60 to 80 feet long within the shield, only about 4 times as long as those normally used at the Bevatron. Thus, from extrapolation of present procedures by Mr. Olsen at the Bevatron, it would seem possible to stack or unstack the roof blocks in half a day. The use of two cranes, each of 100-ton capacity, would further shorten this time. This is feasible if we establish the experimental area as one half the original design area, i.e., a building 400 feet long by about 80 feet wide. The shorter crane would make the 100-ton crane feasible for larger roof-block modules.

The main point here is that it seems possible to establish a new beam in several days in the internal area, rather than in several weeks in the EPB. Shutdown and maintenance periods of this order would be expected at least in the early years of the accelerator. In the later years, a sufficient variation of beams might be approached to reduce change-overs even in this area (assuming two or three beams can be set up here).

2. Work on an internal target area need not be initiated immediately after turn-off. A cool-off period (without targeting) can be arranged just as easily for an internal beam area as for an external beam area. In either case, one assumes the beam is utilized in an alternate area during cool-off. In general, the internal area will be less active than the beam dump areas of the EPB.

3. In this discussion, we assume that the internal target area is a minimum-intensity area which utilizes $\approx 10\%$ of the beam.

4. The crane handling in the internal area, especially with a combination of the main ring cranes and overhead crane of the experimental area, should be no worse than in the external beam area.

5. Chapter XIII implies that because plunging mechanisms must travel farther for the internal area than for the external area, they are perhaps less reliable. The single, simple, and already proven flipping mechanism for an internal target will be enormously more reliable than the total combination of plunging and pulsing magnets of the extraction system, EPB channel, and backstop, their associated power supplies, as well as EPB target actuators.

6. A list of the advantages of the EPB to the experimenters is expounded in Chapter XIII. These are zero-degree production, emittance, and targeting efficiency almost as good as those of the internal area, as well as certain geometrical and flux considerations. These are advantages only when absolutely required. They represent no advantage to the experimenter if his requirements can be fulfilled at the internal area and his experiment can be set up and executed more rapidly there.

7. There are a number of ways of utilizing the EPB, and they are experimentally flexible; we have already, however, mentioned the difficulties in changing beams. The number of experiments that utilize the same target is finite and suffers from some inflexibility with regard to individual intensity and energy control. The internal area offers another experimental area at a reasonable price which will be necessary to meet the experimental demands. Even though the area is less flexible, the very fact that it can provide for a number of experiments is its chief advantage—particularly the kind of experiments utilizing lower intensities and lower energies for secondary beams.

8. Mention has been made (Chap. XIII, UCRL-16000) of some possible experiments that might be performed only at an internal area. However, probably the most realistic advantage is the use of the internal area during the early stages of machine tuning. This would be the first area at which experiments could be performed with intermittent beam during tune up. This area could also be profitably used for machine development.

9. The internal area would provide one of the most flexible access regions to the main ring. Removal of a few roof blocks with the overhead crane provides this access. The main access tunnel could be eliminated for this section of the machine.

10. The EPB will probably be used heavily by bubble-chamber and neutrino experiments. The internal area may be more attractive for some "smaller" scale lower intensity counter experiments.

11. EPB operating areas can be expanded at a later date. It will be difficult to include an internal area "later." The internal area is logically, historically, and profitably used in the early years of an accelerator. (Actually internal areas have never been phased out in any existing accelerators even in their later years.)

12. The internal area is efficient for simultaneous beam sharing. This is of considerable importance in view of expected high experimental demands.

13. An internal area would probably be converted into an EPB area, if necessary, at less cost than some other straight section of the machine.

14. In discussing the above points, we have had in mind a flexible internal area of the "Half-Hall" type shown in Fig. 4 of the "Round-Table Discussion on the Importance of the Internal Target Area and Its Possible Configuration" (this volume). The area is approximately 400 by 80 feet on the outer machine radius only. An additional five million dollars seems a rather good price for a flexible experimental area. However, the main point in the preceding discussion is not concerned with either cost or the comparison between internal and external beam areas. It is simply that the internal area <u>together</u> with the EPB areas will provide a faster, more efficient, and more flexible physics program than the external areas alone.

THE POSSIBILITY OF USING A SMALL STORAGE RING IN CONJUNCTION WITH THE MAIN ACCELERATOR FOR COLLIDING BEAM EXPERIMENTS

J. J. Thresher

INTRODUCTION

The Design Study Report (UCRL-16000, Vol. I) discusses briefly the possibility of constructing a pair of 200-BeV intersecting storage rings to be used in conjunction with the 200-BeV accelerator. Mention is also made of a more modest facility consisting of a low-energy ring which would be arranged to intersect the main ring of the accelerator. This would give a substantial increase in the center-of-mass energy, as the following table shows:

Proton kinetic energy in small storage ring (BeV)	200	100	50	25	10	8	5	2	0
$E_{c.m.}$ (BeV)	402	285	202	144	94	85	69	48	19.5

In this report we examine the latter possibility in a little more detail, using 8 BeV for the energy of the storage ring. This gives a total center-of-mass energy of 85 BeV, and has the advantage that the ring can be filled directly from the booster. However, there is no reason why a ring capable of storing higher energy protons should not be considered.

At first sight, the simplest way to proceed would seem to be to design the small ring to intersect the main ring in one of the long straight sections, preferably the one just downstream of the booster. However, such a scheme has several undesirable features. First, any detectors that must be placed really close to the 200-BeV beam would interfere with the beam during injection. Next, the vacuum system of the accelerator in the interaction region and downstream of it would almost certainly have to be replaced by one tailored to the needs of experiments with colliding beams; the same would probably be true of the magnets downstream of the interaction region. Finally, the length of time that the accelerator would have to be out of operation during construction of the storage ring would be considerable. A more attractive, but more expensive, scheme is to build a sidetrack alongside the main accelerator. It would contain a straight section which would be used for the intersecting region, and its total length might perhaps amount to the equivalent to two superperiods. The beam would be switched into the sidetrack immediately after acceleration to full energy. The idea of using a sidetrack was first suggested by Collins as part of a scheme for beam extraction. There appears to be no reason why it could not be used for both purposes simultaneously.

INTERACTION RATES

In the scheme considered here, we assume that the accelerator runs normally at 23 pulses per minute with a 0.6-sec flattop. We examine the interaction rate during the flat-top period, assuming that the beam is being extracted uniformly during this time for use in the external target areas. If 3×10^{13} protons per pulse are accelerated to full energy, then, so far as the calculation of rates is concerned, the accelerator would be equivalent to a 200-BeV storage ring of the same circumference containing 3.5×10^{12} circulating protons. The protons would fill an area approximately 10 mm wide and 3 mm high, and would have a momentum spread $\Delta P/P \leq \pm 10^{-4}$.

The small ring would probably be stacked in synchrotron phase space. In a ring with the same circumference as the booster, it should be possible to stack about 2.5×10^{12} protons per turn, allowing for an efficiency of a little over 50% for transferring the beam from the booster to the ring. The momentum spread of the beam from the booster is expected to be $\pm 0.75\times10^{-3}$, which would lead to a spread of approximately $\pm 0.75\times10^{-4}$ in the storage ring after stacking and debunching. The storage ring could probably be designed to accept a maximum momentum spread of $\pm 1.5\times10^{-2}$. Thus the upper limit on the number of particles stored, which should be proportional to the momentum spread, would be 5×10^{14}.

The interaction rate, I, may be calculated to a good approximation from the following formula, [1]

$$I = \frac{2 N_1 N_2 c \sigma}{h \theta} \text{ /sec} , \qquad (1)$$

where N_1 and N_2 are the number of circulating protons per cm in the main ring and the storage ring, respectively, θ is the angle at which the two beams intersect, h is the height of the beam in the storage ring (which we assume to be the height of the 200-BeV beam), c is the velocity of light, and σ is the interaction cross section.

The Design Study Report suggests a circumference of 4337 m for the main ring and one of 619.6 m for the booster. We therefore obtain

$$N_1 = 0.81 \times 10^7 \text{/cm}$$

and

$$N_2 = 5.38 \times 10^{11} (\Delta P_2/P_2) \text{ /cm} ,$$

where $\pm \Delta P_2/P_2$ is the momentum spread in the small ring which within the design limit of $\pm 1.5\times10^{-2}$ will be dictated by experimental requirements. If we now choose $\theta = 0.1$ radian—a crossing angle of 5.7 deg—and h = 0.3 cm (i.e., we assume that, in the interaction region, the height of the beam in the small ring can be made equal to that of the beam in the main ring), then

$$I = 1.35 \times 10^4 \sigma \, (\Delta P_2/P_2) \text{ /sec} , \qquad (2)$$

where σ is expressed in millibarns.

The spread in the total center-of-mass energy is given approximately by $\Delta E^*/E^* = 1/2 \, ((\Delta P_1/P_1)^2 + (\Delta P_2/P_2)^2)^{1/2}$. Thus an experiment requiring $\Delta E^*/E^* = \pm 10^{-3}$ could be carried out with $\Delta P_2/P_2 = \pm 2 \times 10^{-3}$ since the effect of $\Delta P_1/P_1$ is negligible. The interaction rate would then be 1.6/min/μ barn, and a total cross section of 40 millibarns would give 1070 interactions/sec. The situation for other choices of $\Delta E^*/E^*$ is summarized in Table I.

COMPARISON OF THE PRESENT SCHEME WITH THE ISR AT CERN

The construction of a pair of intersecting storage rings at CERN is now in progress. They will provide a total energy in the c.m. system of approximately 52 BeV. The estimated time of completion is 1971. A comparison of the rates expected in the ISR with those we have just estimated is therefore relevant. We shall use the parameters given in the CERN Design Study Report[2] for this purpose.

The expression for the interaction rate is

$$I = 4.12 \times 10^7 \sigma \, (\Delta P/P)^2 \text{ /sec} , \qquad (3)$$

where σ is again in millibarns, and the momentum spread in each of the two rings is $\pm \Delta P/P$. The spread in the total c.m. energy is given approximately by $\Delta E^*/E^* = (1/\sqrt{2}) \, \Delta P/P$. The rates obtained for various choices of $\Delta E^*/E^*$ are given in Table II and should be compared with those in Table I. We should point out, however, that in predicting the rates for the ISR the CERN group assumed an intensity of about 10^{12} protons per pulse in the PS. By the time the ISR comes into operation, it is likely that an intensity of at least 3 times this figure will be available. In this case, the number of protons that can be stored in each ring for a given $\Delta P/P$ should increase substantially over the present design figure, say by a factor of two or more. Thus on the basis of counting rate alone, the case for the 200-BeV x 8-BeV scheme looks weak. However, when viewed in isolation, the rates do not seem to be prohibitively low, and it is impossible at this stage to assess the value of the substantially higher c.m. energy that the 200-BeV x 8 BeV scheme would provide. The whole scheme would, of course, be more attractive if the small ring were capable of running at a somewhat higher energy, say 25 BeV. This would give a total energy of 144 BeV in the c.m. system--almost three times that of the ISR. It would now have to be filled from the accelerator itself rather than from the booster, but this should not be a serious problem. The interaction rates would be similar to those already calculated.

COST ESTIMATE

A rough estimate of the cost of the scheme is $55 000 000. It assumes that the total cost per unit length of the storage ring and of the main ring bypass is the same as for the main accelerator--$35 000/meter. The circumference of the storage ring is 620 m, which should be suitable for storing protons up to about 25 BeV if magnets capable of running at 15 kG are used. The cost of the bypass is based on a length of 720 m, i.e., about two superperiods.

The breakdown is therefore as follows:

Bypass	$25 000 000
Storage ring	20 000 000
Experimental area	10 000 000
Total	$55 000 000

The estimated cost for the CERN storage rings is approximately $50 000 000.

CONCLUDING REMARKS

It is fairly obvious that any decision to proceed with a scheme such as that discussed here should wait until the accelerator itself has been in operation for some time. (The same is probably true of the suggestion to build a pair of 200-BeV intersecting storage rings.) By then we should have a much clearer idea about the way in which physics should be done in this new energy region; there should also be a considerable amount of information available from CERN on the problems associated with the use of storage rings, and hopefully some indication as to the value of going to c.m. energies appreciably higher than 50 BeV. If possible, therefore, one should simply ensure that at this stage nothing is done that would make it difficult for such a scheme to go ahead if the need arose.

Table I. Estimated interaction rates for the 200-BeV x 8-BeV scheme.

$\frac{\Delta E^*}{E^*}$	$\frac{\Delta P_1}{P_1}$	$\frac{\Delta P_2}{P_2}$	I_{total} $(sec^{-1})^a$	I/min/μb
$\pm 0.7 \times 10^{-4}$	$\pm 10^{-4}$	$\pm 10^{-4}$	54	0.08
$\pm 0.7 \times 10^{-3}$	$\pm 10^{-4}$	$\pm 1.4 \times 10^{-3}$	756	1.13
$\pm 0.7 \times 10^{-2}$	$\pm 10^{-4}$	$\pm 1.4 \times 10^{-2}$	7,560	11.3

a. In calculating the total interaction rate, I_{total}, we have assumed a total cross section of 40 mb.

Table II. Estimated interaction rates for the ISR at CERN.

$\frac{\Delta E^*}{E^*}$	$\frac{\Delta P}{P}$	I_{total} $(sec^{-1})^a$	I/min/μb
$\pm 0.7 \times 10^{-4}$	$\pm 10^{-4}$	16.5	0.025
$\pm 0.7 \times 10^{-3}$	$\pm 10^{-3}$	1650	2.5
$\pm 0.7 \times 10^{-2}$	$\pm 10^{-2}$	165 000	250

a. In calculating the total interaction rate, I_{total}, we have assumed a total cross section of 40 mb.

References

1. See, for example, L. W. Jones, Proc. Int. Conf. High Energy Accelerators and Instrumentation CERN 1959, (CERN, Geneva, 1959) 15.

2. Report on the Design Study of Intersecting Storage Rings for the CERN Proton Synchrotron, AR/Int SG/64-9, May 12, 1964.

ANTIPROTON FACILITIES AT THE 200 BEV ACCELERATOR

W. J. Kernan

INTRODUCTION

Any attempts at detailed predictions of how to do particular experiments on a new accelerator depend heavily on predicted particle fluxes at the accelerator. For a 200-BeV accelerator, this necessarily means extrapolation of the fluxes of secondary particles produced in 30-BeV proton interactions. For π and K mesons, this extrapolation is on a fairly firm footing. At 30 BeV, threshold effects and associated problems are not important for π's and K's. For $\bar{p}$, however, the $\bar{p}/\pi^-$ ratio is apparently still increasing as a function of energy at 30 BeV. This behavior may continue or it may level off, and at present no method of extrapolating the data at 30 BeV to fluxes at 200 BeV is well established. Keefe, Mealy, and Trilling (KMT)[1] have parameterized the low energy (< 30 BeV) data and used this to predict fluxes of $\bar{p}$ at 200 BeV. Their formula gives a good fit to the data of Dekkers et al.,[2] at 18.8 and 23.1 BeV/c. But to extrapolate from these values to 200 BeV involves a large uncertainty. In particular, this formula predicts a surprisingly large number of high-energy $\bar{p}$ secondaries.

An alternative approach is to calculate the expected pion flux and take 1% of this for the $\bar{p}$ flux. Since this assumes that the $\bar{p}/\pi$ ratio is constant from 30 to 200 BeV, it is probably too conservative an estimate of the expected $\bar{p}$ fluxes.

This uncertainty in resulting $\bar{p}$ fluxes greatly influences any attempt at deciding on a particular scheme for obtaining secondary beams of $\bar{p}$ from the 200-BeV accelerator.

ANTIPROTON FACILITIES ASSOCIATED WITH THE 8-BEV BOOSTER

It has been suggested[3] that $\bar{p}$ with $E(\bar{p}) \leq 8$ BeV could be produced by protons of 50 to 100 BeV and stored in the booster (using this as a separator), and then injected into the main ring, accelerated, and later extracted into a $\bar{p}$ experimental area near the booster. In this section the question of acceleration will not be considered.

A. Maximum $\bar{p}$ Fluxes

An attempt is made here to estimate the maximum flux of $\bar{p}$ that can be produced by 50- to 100-BeV protons and stored in the booster ring. KMT's formula for $\bar{p}$ flux is

$$\frac{d^2N}{dp\, d\Omega} = \frac{1}{32} A \frac{p^2E^*}{E} e^{-p^{*2}/B^2} e^{-3.0(p\theta)^2}, \qquad (1)$$

where p* and E* are the c.m. momentum and energy of an antiproton which has laboratory momentum p and energy E. The production angle, θ, in the laboratory system is in radians.

The dependence on the energy of the incident proton is contained in the parameters A and B. Here B is set equal to 0.18 times the total c.m. energy. KMT calculated A from the $\bar{p}$ multiplicity at 18.8 and 23.1 BeV/c and then simply guessed a value of A at 200 BeV/c. In doing this they have been "conservative" by not assuming a linear relationship between A and proton energy, but estimating A (200 BeV/c) so that

$$\frac{A\ (200\ \text{BeV/c})}{A(23.1\ \text{BeV/c})} < 2\, \frac{A\ (23.1\ \text{BeV/c})}{A\ (18.8\ \text{BeV/c})},$$

or, to express it in terms of the average change of A with proton momentum in the different ranges of proton momentum,

$$\left[\frac{\Delta A}{\Delta p}\ (18.8 < p < 23.1)\right] > 20\left[\frac{\Delta A}{\Delta p}\ (23.1 < p < 200)\right].$$

However, KMT's value of A at 200 BeV/c remains only a guess. If, however, one accepts this A at 200 BeV/c as a valid estimate, there is a very limited range of smooth curves that one can run through these three points 18.8, 23.1, and 200 BeV/c. In particular, when the requirement of smooth behavior of A with proton momentum is combined with requiring a smooth behavior of the antiproton multiplicity $N(\bar{p})$ with proton momentum [where $N(\bar{p}) = 2AB$], the band of choice narrows, and typical consistent curves of A and $N(\bar{p})$ are shown in Figs. 1 and 2, respectively. Within these assumptions, the freedom to vary the curves is $\lesssim 20\%$ of their value at a point. However, one should always keep in mind that these curves are tied to a pure guess of the value A at 200 BeV/c.

Using the values of A from Fig. 1, taking B to be 0.18 (c.m. energy), Eq.(1) has been calculated for θ = 0-deg for incident proton energies of 50, 100, 150, and 200 BeV. The results are shown in Fig. 3. From this curve $\frac{d^2N}{dp\, d\Omega}$ $(\text{sr})^{-1}(\text{BeV/c})^{-1}$ (interacting proton)$^{-1}$ has been taken as 3.4×10^{-2} for 8-BeV $\bar{p}$ and for incident protons in the range 50 to 100 BeV.

If one wishes to match the emittance of the target to the acceptance of the booster ring, and assumes a target size of 1 x 1 mm, one needs a solid angle which is given by

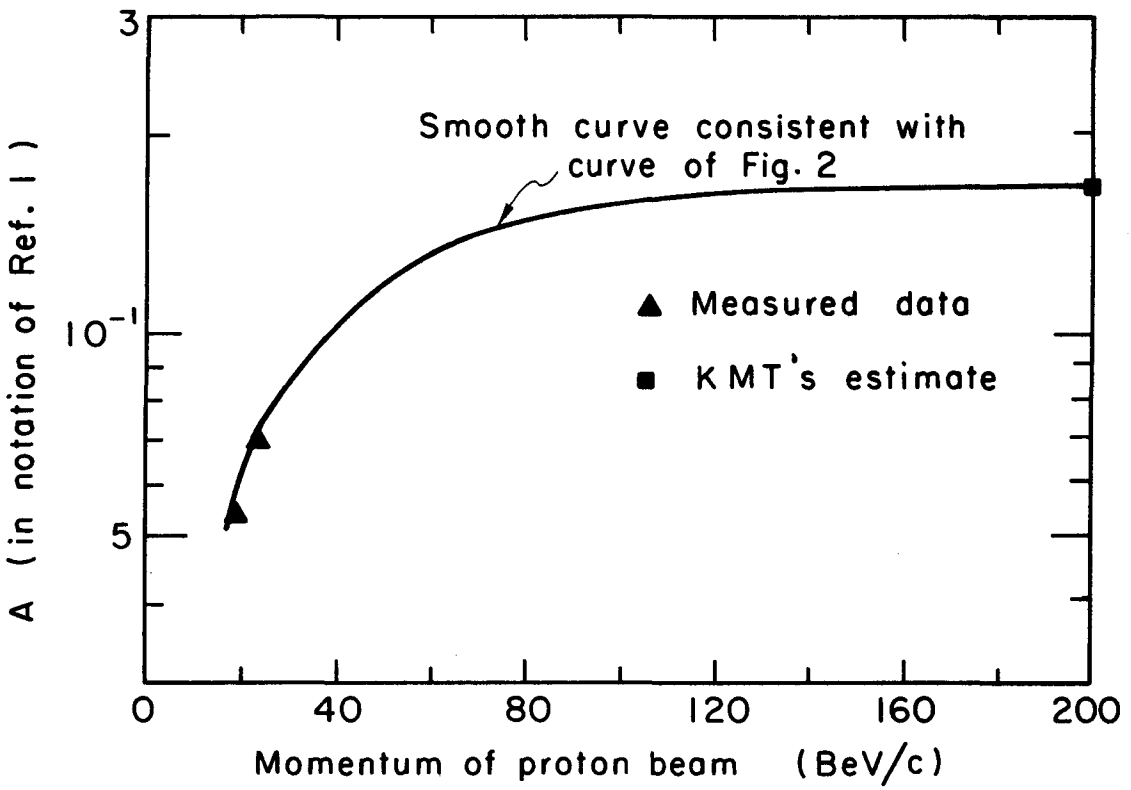

Fig. 1. A possible smooth curve for the parameter A in the formula for the antiproton flux [Eq. (1) in text]. The curve has been fitted to the two measured points shown and to the KMT estimated at an incident beam momentum of 200 BeV/c.

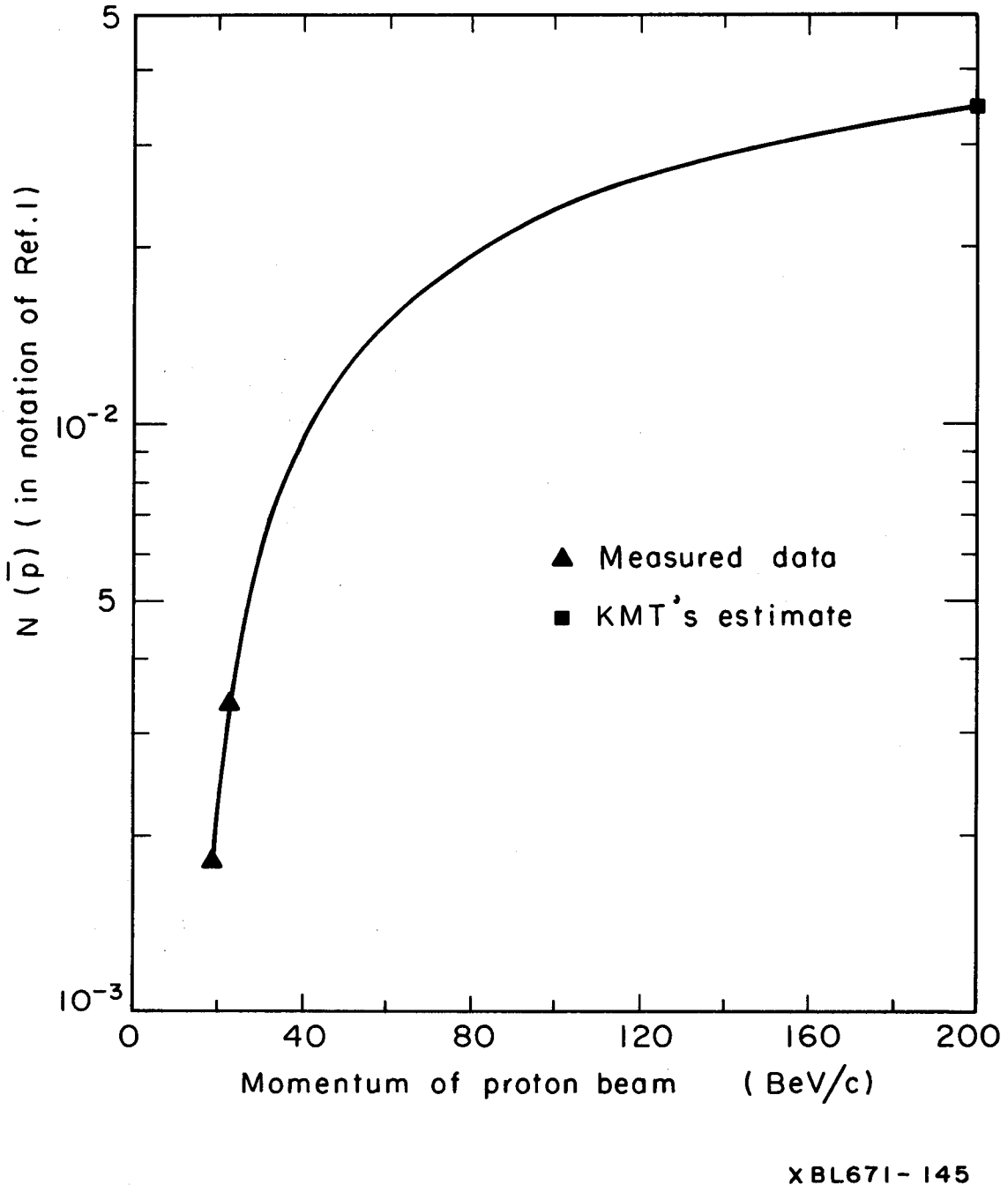

Fig. 2. A possible smooth curve for the antiproton multiplicity $N(\bar{p})$ vs incident beam momentum. The curve has been fitted to the two measured points shown and to the KMT estimate at 200 BeV/c.

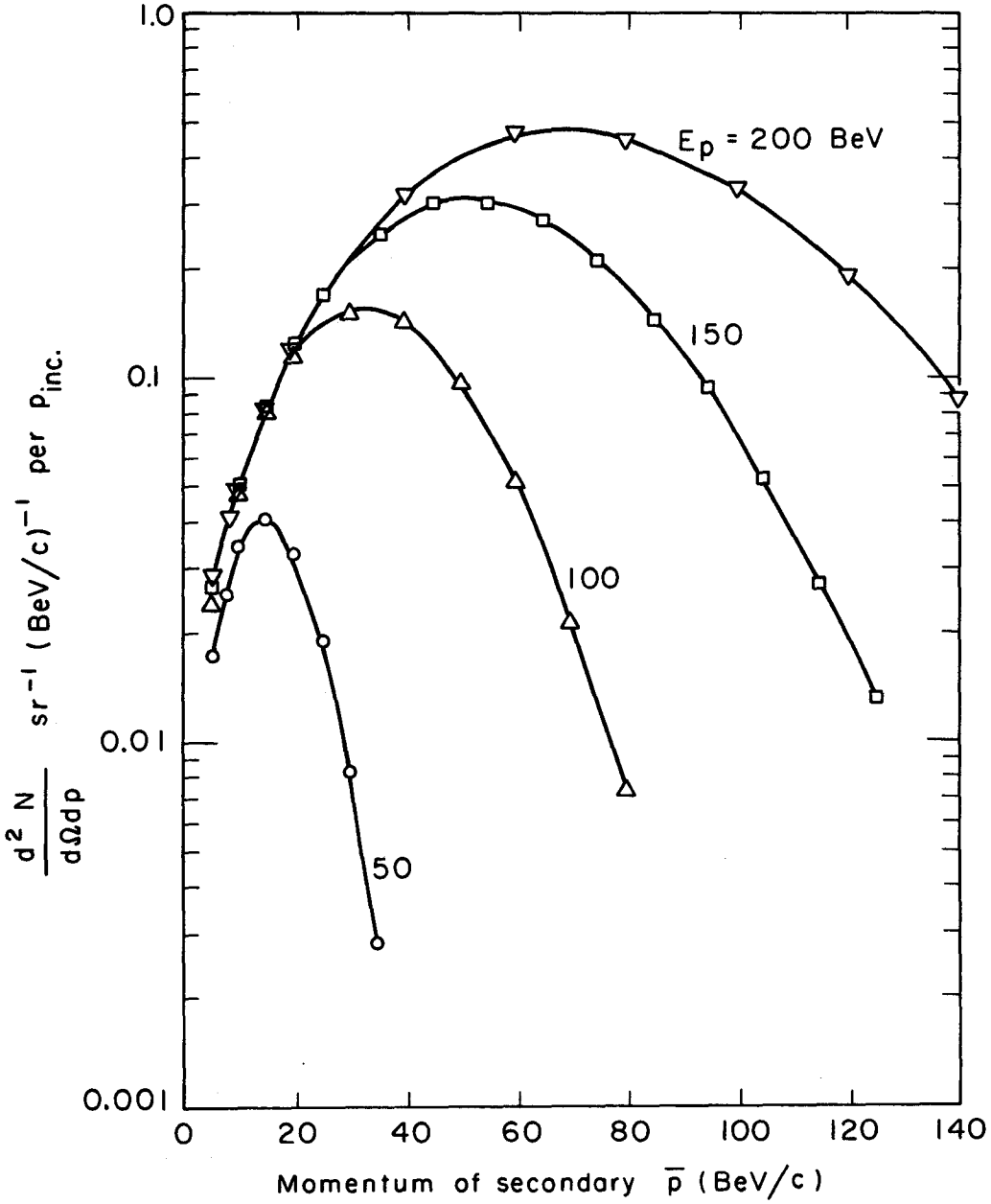

Fig. 3. The antiproton flux estimated from KMT's formula [Eq. (1) in the text], with values of the parameters A and B determined from Figs. 1 and 2 and Eq. (2) of the text.

$$\Delta\Omega = \frac{(\pi\, ab)^2}{\beta_1\, \beta_2}\ \frac{1}{t_B}\ . \qquad (2)$$

For the booster β_1 = 17.4 m, β_2 = 20.9 m, and conservative values of a and b are 6 and 2.5 cm, respectively. With these values and $t_B = 10^{-2}$ cm^2, $\Delta\Omega$ is equal to 6.1×10^{-2} steradians (sr).

In this estimate, the proton intensity is taken as one seventh of the assumed machine intensity of 3×10^{13} ppp. The remaining factor needed to calculate the intensity of $\bar{p}$ for the booster is the value of $\Delta p/p$. The maximum value for this is $\pm\, 3 \times 10^{-2}$ (Ref. 4); however, the acceptance goes to zero for the extremes of this, so an average of $\Delta p/p$ and acceptance change has been taken as 2×10^{-2}.

All factors necessary to calculate the flux have now been taken into account, except the laboratory angular dependence of the flux. The factor $e^{-3.0(p\theta)^2}$ in Eq. (1) is not constant over a solid angle of 6.1×10^{-2} sr; in fact, it changes from 1.0 to $\approx 2 \times 10^{-2}$ over this solid angle. Averaging $e^{-3(p\theta)^2}$ over this angular interval yields the value ≈ 0.46.

Putting all these factors into the calculation, one has

$$N = 3.4 \times 10^{-2} \times 6.1 \times 10^{-2} \times 1/3 \times 1/7 \times 3 \times 10^{13} \times 2 \times 10^{-2} \times 8$$

$$\times\, 0.46 \approx 2.1 \times 10^{8}\ \bar{p} \text{ per pulse (at 8 BeV).}$$

Estimating this in the other fashion (i.e., 1% of the appropriate π flux) will not seriously change the numbers involved (in fact, it gives a slightly larger answer).

B. Usefulness of an Experimental Facility at the Booster

This is an energy range for $\bar{p}$ that is readily available at the AGS and CPS now. If one makes an estimate of the intensities that could be available in a separated beam at the AGS after the conversion program is completed (i.e., assuming 10^{13} protons per pulse and using the full beam), one might expect to be able to get intensities $\approx 10^6$ $\bar{p}$/pulse at 8 BeV. The 2×10^8 $\bar{p}$/pulse in the booster could not be extracted easily with anything like 100% efficiency, so the "improvement factor" could be expected to be $\approx$ 10 to 50 in beam intensity.

The assumption is made that important experiments that can be done at the AGS will have, in fact, been done there. So, the question simplifies to the following: will there be, ten years from now, any important experiments involving $\bar{p}$, with $E(\bar{p}) \leq 8$ BeV, that require this last factor of 10 to 50 in the intensity in order for the experiment to be reasonable? Having posed a question to which a certain answer cannot be easily made, one can try to evade the question. Namely a recommendation can be made to try and keep the option of extracting 8-BeV $\bar{p}$ into an experimental area alive without any large expenditure

of money until after the main accelerator construction is completed. Then the question of need may have an obvious answer.

$\bar{p}$ EXPERIMENTS IN SECONDARY BEAM AREAS USING THE EPB*

A. Expected $\bar{p}$ Fluxes

For the moment we will not consider rf separated beams, but will limit discussion to negative beams composed of a mixture of π's, K's, and $\bar{p}$'s. Longo[5] has designed such a beam to operate in the range 50 to 150 BeV with $\Delta p/p = \pm 10\%$ and $\Delta\Omega = 3 \times 10^{-6}$ sr. He assumes the use of gas Cerenkov counters to identify the desired component; this requirement restricts the beam to $I_{max} \approx 10^7$/pulse. Using KMT's $\frac{d^2 N(\bar{p})}{dp\, d\Omega}$ and all of Longo's beam parameters, one could estimate $\bar{p}$ fluxes as $> 10^6$/pulse throughout this range,** but this flux has between 10 to 20 times as many π's present over this energy range (using Trilling's[6] $\frac{d^2N(\pi^-)}{dp\, d\Omega}$ as well). So for these assumed $\frac{d^2N}{dp\, d\Omega}$ and at $E(\bar{p}) < 150$ BeV, this beam has a $\bar{p}$ flux competitive with the acceleration technique.

There are, however, two problems. The first is the assumed $\bar{p}$ flux itself. If one takes the $\bar{p}/\pi$ ratio as 1%, observed at 30 BeV, then the $\bar{p}$ flux falls to between one fifth and one tenth of its former value and becomes much less competitive, particularly at the high energies. In fact, if one takes $\bar{p}/\pi$ as 1% and uses $\frac{d^2N(\pi)}{dp\, d\Omega}$ from Cocconi et al.,[7] one can estimate that instead of 10^6 $\bar{p}$/pulse at 150 BeV, one has more like 10^5 $\bar{p}$/pulse.

The second trouble is the unseparated nature of the beam and the necessity of having very good discrimination against background from the unwanted particles. To summarize, such a beam is competitive in flux for $E(\bar{p}) \leq 150$ BeV, has more background problems, and is not very practical at all for $E(\bar{p})$ in the range greater than 175 BeV. Also π, K, and $\bar{p}$ experiments would compete in scheduling for the same facility, and in the acceleration scheme the scheduling for $\bar{p}$ experiments would be largely decoupled from scheduling of π and K experiments in this beam facility.

B. rf Separated Beams for $\bar{p}$

Lach[8] has done the preliminary design of an rf separated beam with a design momentum of 100 BeV for K mesons. His design is not optimized. Sandweiss's[9] suggestion of the use of circularly polarized rf separators,

---

*In these comparisons I have not tried to match $\Delta p/p$ of the beams with $\Delta p/p$ of the accelerated scheme. Realistic values of $\Delta p/p$ have been taken for each scheme individually. In some experiments the small $\Delta p/p$ favors the acceleration scheme more than is implied in this note.

**This involves some variation of incident proton beam flux as a function of $\bar{p}$ desired momentum, but never involves a flux greater than about 10^{13}/pulse.

instead of the conventional ones, makes such a beam more versatile and leaves, at worst, small energy gaps that cannot be covered for $\bar{p}$ in one beam setup.

To compare Lach's beam with the 2×10^6 $\bar{p}$/pulse from the acceleration scheme, the quantity

$$N(\bar{p}) = \frac{d^2N(\bar{p})}{d\Omega\, dp} \epsilon I t \Delta\Omega \frac{\Delta p}{p} p \qquad (3)$$

has been calculated for different $\bar{p}$ momenta. Here I is the beam intensity used (10^{13}/pulse), t is the target efficiency (1/3), ϵ is the transmission of the beam (0.3), $\Delta\Omega = 4 \times 10^{-6}$ sr, and $\Delta p/p = 2.5 \times 10^{-3}$.

If we wish to compare this example with an assumed 2×10^6 $\bar{p}$/pulse, then we can equate $N(\bar{p}) = 2 \times 10^6$ and solve for the required $\frac{d^2N(\bar{p})}{d\Omega\, dp}$ as a function of the momentum p. This gives

$$\frac{d^2N(\bar{p})}{d\Omega\, dp} \approx 2 \times 10^2 \, (p^{-1}) \, . \qquad (4)$$

For an honest comparison, it should be realized that this rf beam is not optimized. One could improve either ϵ or $\Delta p/p$. So the flux might be as much as 5 times that estimated in Ref. 8, making the rf beam look better than shown here. The results of this comparison are shown in Table I. Here $\left[\frac{d^2N(\bar{p})}{d\Omega\, dp}\right]_{KMT}$ is that found by using KMT's formula[1] and $\left[\frac{d^2N(\bar{p})}{d\Omega\, dp}\right]_{CKP}$ is found by taking 1% of π value $d^2N(\pi)/d\Omega\, dp$ from Cocconi, Koester, and Perkins.[7]

Table I

$\bar{p}$ Momentum (BeV/c)	$\frac{d^2N(\bar{p})}{d\Omega\, dp}$ needed for 2×10^6 $\bar{p}$/pul	$\frac{d^2N(\bar{p})}{d\Omega\, dp_{KMT}}$	$\frac{N(\bar{p})\text{Accel}}{N(\bar{p})RF_{KMT}}$	$\frac{d^2N(\bar{p})}{d\Omega\, dp_{CKP}}$	$\frac{N(\bar{p})\text{Accel}}{N(p)RF_{CKP}}$
50	4	4×10^{-1}	≈ 10	---	---
75	2.7	4.7×10^{-1}	≈ 6	4.2×10^{-2}	≈ 60
100	2	3.4×10^{-1}	≈ 6	8.3×10^{-3}	≈ 60
125	1.6	1.6×10^{-1}	≈ 10	1.6×10^{-3}	≈ 240
150	1.3	5.6×10^{-2}	≈ 25	---	≈ 1000
175	1.1	1.5×10^{-2}	≈ 75	---	---

Table I emphasizes the necessity of keeping as much freedom of choice as possible until $d^2N(\bar{p})/d\Omega\, dp$ estimates can be made with considerably more confidence for proton energies of $\approx$200 BeV. If the most optimistic values in the table are taken and combined with optimization of the rf beam (to yield a factor of 3 to 5) one could easily conclude that the acceleration of $\bar{p}$'s is an unnecessary complication. The pessimistic $\bar{p}$ fluxes from the rf beam, if accepted, would incline one towards very serious work on early implementation of the acceleration scheme.

The real conclusion to be drawn from here is that an intelligent and confident answer on the question of implementing the acceleration scheme for $\bar{p}$ should not be made until beam surveys including $\bar{p}$ production at very small laboratory angles have been completed at the 70-BeV accelerator at Serpukhov.

ACCELERATION OF $\bar{p}$ IN THE MAIN RING

A. $\bar{p}$ Fluxes

Keefe[3] has estimated the $\bar{p}$ flux which can be accelerated as $\approx 2 \times 10^6$ $\bar{p}$/pulse. The only point to emphasize here is that this number is not as uncertain as, for example, the numbers in Table I. There are three reasons for this greater confidence:

1. The scheme uses protons with energy $\approx$ 50 BeV $\leq E(p) \leq$ 75 BeV, so the extrapolation from present data is not so severe.

2. It involves only 8-BeV $\bar{p}$. This is the lower energy end of the spectrum, it is more reliable, and all models tend to agree there.

3. There is an additional freedom, namely, one can adjust the primary proton energy until this 2×10^6 is achieved.

So the intensity estimate in this scheme is probably fairly reliable.

B. Methods of Implementing this Scheme

Any realistic attempt to implement this idea must allow for simultaneous $\bar{p}$ and p acceleration and use. Otherwise it is equivalent to using the full proton beam for $\bar{p}$ production and is an inefficient way to run the accelerator.

All schemes have the common feature of fast extracting one seventh of the protons from the main ring at 50 BeV $\lesssim E(p) \lesssim$ 75 BeV in order to produce the 8-BeV $\bar{p}$'s.

The first scheme envisioned in Ref. 3 is logically described below for one cycle of the entire scheme (p_N is normal proton intensity).

Time (sec)	Main ring use	p Intensity (MR)	$\bar{p}$ int. (MR)	Booster use	Comments
0.0 - 0.33	Filling	7/7 p_N	0	Injecting p to MR	
0.3 - ≈0.5	Accelerate p to 50 BeV	7/7 p_N extract 1/7	0	--	$\bar{p}$ produced at this point
0.5 - ≈0.7	Decelerate p to injection energy	6/7 p_N	0	Storing 8-BeV $\bar{p}$	Flat top of booster
0.7 - ≈0.9	Stabilize and inject $\bar{p}$	6/7 p_N	2×10^6	Injecting $\bar{p}$ to MR	
0.9 - ≈1.7	Accelerate to ≤ 200 BeV	6/7 p_N	2×10^6	--	
1.7 - ≈2.4	Decelerate	0	0	--	
≈ 2.4 -≈2.6	Idle	0	0	--	

An efficiency factor of this (or any) scheme relative to normal proton use can be defined as

$$\epsilon = \frac{\text{normal cycle time}}{\text{cycle time } (\bar{p})} \times \frac{\text{proton intensity (p)}}{\text{normal proton intensity}} . \quad (5)$$

For this scheme $$\epsilon = \frac{2.0}{2.6} \times \frac{6/7\ P_N}{7/7\ P_N} = \frac{2.0}{2.6} \times \frac{6}{7} = 0.66 .$$

This efficiency is not bad, and if flat-topping of the main ring is considered, it gets slightly better. The only difficulty with the scheme is that successive pulses of the main ring magnet are quite different. This could cause some magnet programming problems. In addition, this scheme requires deceleration of the beam through the transition, and it is hard to estimate what the beam loss due to this will be.

Many other magnet pulse arrangements for extracting the protons for $\bar{p}$ production have been considered in this study. The most promising, generally useful arrangement is to take the protons from the leading edge of the main ring pulse, produce $\bar{p}$'s, and store the $\bar{p}$'s in the booster for injection to the main ring on the next magnet cycle. This method is described in the outline below.

Time (sec)	Main ring use	p Intensity (MR)	$\bar{p}$ int. (MR)	Booster use	Comments
-0.2 - 0.0	Idle	0	0	Store $\bar{p}$	End of booster flat top
0.00 - 0.06	Fill $\bar{p}$	0	$0\text{-}2\times10^{6}$	Injecting $\bar{p}$	
0.06 - 0.39	Fill p	0 - 7/7 P_N	2×10^{6}	Injecting p	
0.39 - 0.59	Accelerate to 50 BeV	7/7 P_N extract 1/7	2×10^{6}	Flat top	Make $\bar{p}$ at 8 BeV
0.59 - 1.19	To 200 BeV	6/7 P_N	2×10^{6}	Store $\bar{p}$	
1.19 - 1.89	Decelerate	0	0	Store $\bar{p}$	
1.89 - 2.09	Idle	0	0	Store $\bar{p}$	

For this system $\epsilon = \frac{2.0}{2.1} \times \frac{6}{7} \approx 0.82$.

In addition to a higher ϵ, this is a system in which the main ring cycle is always the same. However, the booster must flat-top for at least 1.5 sec. Discussion with LRL Design Study members has brought out that sufficient cooling and power for this are available in the proposed system. Thought has been given by the electrical engineers to the method of switching from 18 Hz operation of the booster to flat-top, and this does not seem to be an insurmountable technical problem.

Other methods have been considered, such as taking the protons for $\bar{p}$ production off the decelerating phase of the magnet pulse, but they all turned out to be less flexible than the above method.

C. Extraction Techniques

Any machine operation involving fast extraction of either the p or $\bar{p}$ component of the beam, or both, has a straightforward solution. Since the circulating protons are in 6/7 of the MR azimuth and the $\bar{p}$'s are in 1/7 of the MR azimuth, there are on each revolution around the machine the necessary conditions for a pulsed extraction system to remove one component in a fast spill while leaving the other component undisturbed.

This, however, is not the most flexible operation of the accelerator. For that, one would wish to be able to spill slowly both the p and $\bar{p}$ beams. In order to accomplish slow spilling of both beams, a method of separating the equilibrium orbits must be incorporated. Two methods of accomplishing this have been proposed.[10] The first method depends upon the different directions of p and $\bar{p}$ rotation in the accelerator. Both beams are accelerated to the same energy, then two additional rf cavities are energized. These two cavities are spaced an odd number of quarter wavelengths apart so that their force adds for particles going in one direction and cancels for particles going in the other direction. This introduces an energy difference for the two beams and therefore a radial separation of the two orbits. If this ΔE is $\approx 2 \times 10^{-5}$ of the energy, then the separation is $\gtrsim 1$ cm and this appears to be sufficient.

The second method depends upon the change in sign of the charge for p and $\bar{p}$. Introduce into the accelerator a radial or vertical electric field. Depending upon the value of E and the length used, this can be introduced in just one section or in a series of sections $\lambda/2$ apart. Calculations to test the practicability of this assumed the length of the field to be 30 m and solved for the field necessary to yield a 1-cm maximum difference in the orbits. The resulting field was $\approx 10^4$ V/cm, a field that is rather low even for existing techniques. Probably the field should be raised and the length lowered. This field should be turned on slowly in order not to induce large betatron oscillations. The idea of this is not to blow the beam up but to pull the closed orbits for the two beam components apart.

Once the orbits are separated, sequential slow spills of both components become practicable. A flat-top of 100 msec or less would be adequate for the antiprotons because of the low flux. The practicability of simultaneous slow spills depends upon assumed positions of the various extraction elements and detailed orbit calculations which have not been carried out. It should, however, be possible.

D. rf or Accelerated $\bar{p}$ Beams

After these considerations it seems appropriate to recommend that a choice between rf separated $\bar{p}$ beam facilities and the acceleration scheme not be made at the present moment. The choice should be postponed until good beam surveys at Serpukhov are available. This necessarily means that the option of accelerating antiprotons should not be designed out of the machine.

GENERAL NOTES

Some quick estimates of radiation shielding say that if 1/7 of the proton beam is used on an external target at $\approx$ 75 BeV to produce $\bar{p}$'s at 8 BeV in this scheme, the target position in the EBP should be separated radially from the center line of the ring by $\approx$ 10 m if work is to be capable of proceeding at this station while the main ring is running. If one uses the usual 15-mrad line for the EPB, this means about 400 ft from the center of the long straight section from which the p beam is extracted to the target position. The target cave is then about halfway out through the earth shield about the main ring.

If one wished to fill the booster with the maximum $\bar{p}$ intensity, then the 8-BeV $\bar{p}$ beam is not compatible with the normal operation of EPB target stations and it must have its own EPB setup. To achieve the solid angle assumed in that calculation requires the first beam element to be a field lens placed as close as possible to the target position and at 0^{o}. An examination of the proposed general-purpose EPB areas shows that these are not compatible.

Detailed cost estimates are not given here. Rough cost estimates have been done assuming the beam lines shown in Fig. 4. Even these are not given because they depend on assumed beam lines, the complete practicality of which has not been investigated. However, it seems the scheme could be implemented for less than 10 and possibly for less than 5 million dollars. (This ignores the cost of the experimental area.)

The biggest problem in implementing the acceleration technique is probably the shutdown time necessary for building the necessary tunnels and surveying in the magnets, and the accelerator operating time needed for tuning the system to successful operation. All of these delays must compete with other uses of the machine. They are also hard to estimate since they depend to an extent on the capability to schedule construction projects to coincide with normal shutdowns of the machine and to be able to stick to such schedules.

References

1. D. Keefe, G. Mealy, and G. H. Trilling, Antiproton Fluxes from High Energy Proton Collisions, UCRL-16830 Vol. I, April 1966, p. 58.

2. D. Dekkers, J. A. Geibel, R. Mermod, G. Weber, T. R. Willitts, K. Winter, B. Jordan, M. Vivargent, N. M. King, and E. J. N. Wilson, Phys. Rev. 137, B962 (1965).

3. D. Keefe, Acceleration of Anti-Protons at the 200 BeV Machine, UCRL-16830 Vol. II, April 1966, p. 292.

4. Estimate due to Frank Selph, LRL Design Study Group.

5. M. J. Longo, 150 BeV/c Beam for Spark-Chamber Experiments, UCRL-16830 Vol. I, April 1966, p. 137.

6. G. H. Trilling, Pion and Proton Fluxes from High Energy Proton Collisions, UCRL-16830 Vol. I, April 1966, p. 25.

7. G. Cocconi, L. Loester, and D. Perkins, High-Energy Physics Study, UCRL-10022, June 1961.

8. J. Lach, A High Energy RF Separated Beam for the Proposed 200 BeV Accelerator, UCRL-16830 Vol. I, April 1966, p. 190.

9. J. Sandweiss, RF Separated Beam Systems for Use at the 200 BeV Accelerator, elsewhere in this volume.

10. D. Keefe and G. Lambertson, Private Communication, Summer 1966.

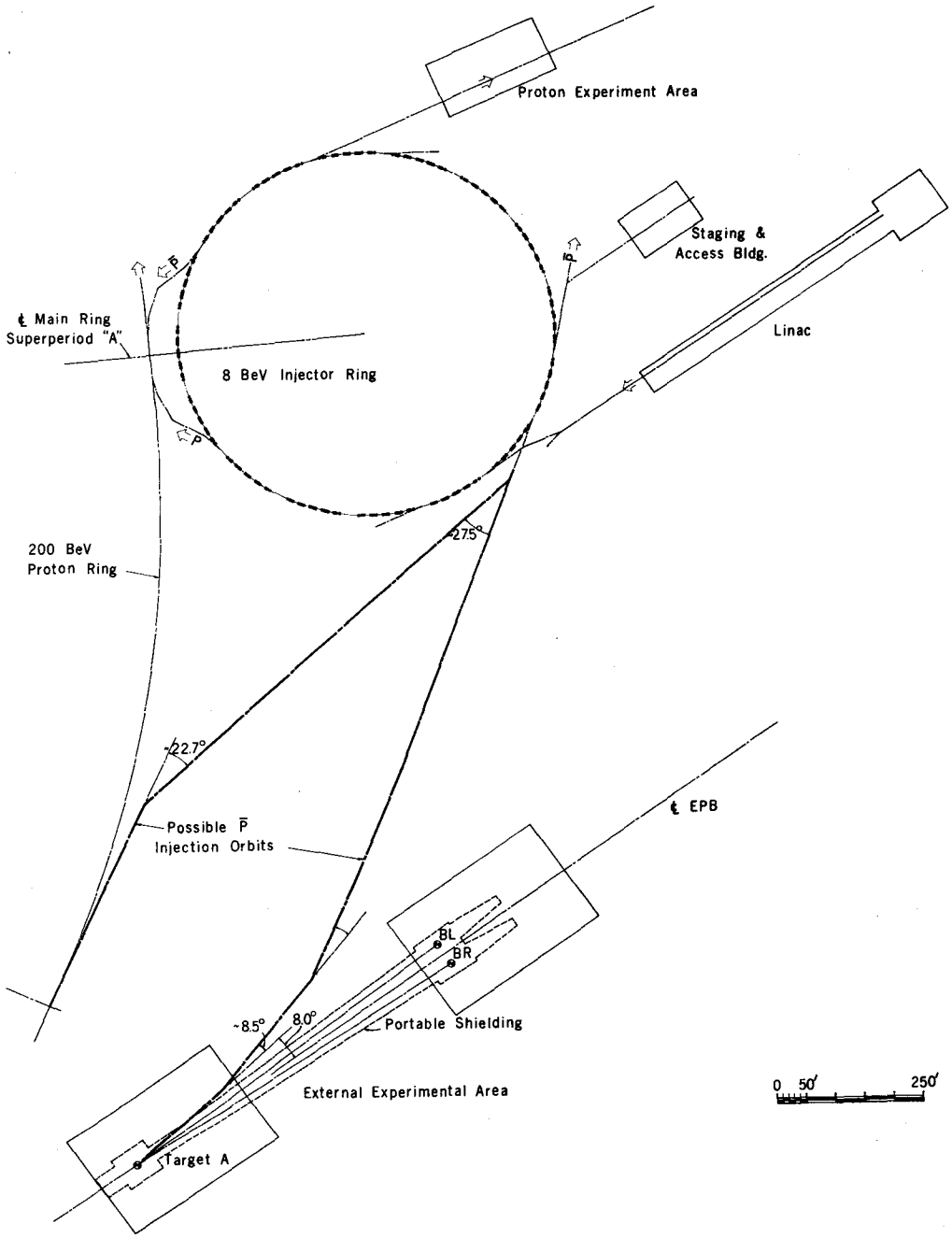

Fig. 4. A plan view of the 8-BeV injector and one EPB area, showing two possible orbits for injecting antiprotons into the injector ring.

C. EXPERIMENTS AND BEAMS

THE NEUTRINO-MUON FACILITY AT THE 200 BEV ACCELERATOR

D. D. Jovanovic

There are many detailed treatises on the neutrino beams[1] at the 200-BeV accelerator. The consensus is that a 1-km-long pion- and kaon-transport channel would be best suited for providing neutrino and muon beams to detectors placed at the end of the channel. Muons were to be deflected into some spark-chamber detector while the neutrino detector envisaged is a large (100-m^3) hydrogen bubble chamber. The main advantages of such a π-K transport channel over the conventional (L = S) arrangement are:

(i) A variable energy and reasonably monoenergetic neutrino beam ($\Delta E/E \approx 20\%$).

(ii) An intense muon beam compatible with the neutrino experiment.

(iii) Less prohibitive shielding requirements for the channel arrangement; e.g., 50-BeV transported momentum vs 200-BeV main beam.

The purpose of this note is to examine in some detail what, if any, are the optimum configurations of the π-K transport system compatible with the muon beam, and to discuss the shielding necessary at the end of the channel. It is this last point that prompted this evaluation. It appears that the previous works did not quite appreciate the full difficulty involved in shielding the neutrino detector from the end of the channel.

The channel as described by Toohig[2] would be 1-km long, consisting of some 20 quadrupoles in a FODO configuration. Sixty-inch-long elements having either a 4- or an 8-inch bore were considered. It was estimated that 10-20% of the muons from pion decay (and a very much smaller fraction of muons from $K_{\mu 2}$ decay) would be captured by the channel.

By using Trilling's or Cocconi's production formulae, one can arrive at a figure of 10^8 - 10^9 π and K (of one sign) being transported by the channel. It is obvious that the "uncaptured" muons from pion decay and particularly muons from K-decay totaling perhaps 10^7/pulse will present shielding difficulties at the neutrino detector. Keefe has pointed out, however, that wide-angle muons from K-decay, i.e., those difficult to capture by the channel, are of considerably smaller momentum than that supported by the channel. These muons may be ranged out by burying the whole length of the 1000-m channel underground. On the other hand, one may envisage a large bending magnet or a magnetized iron shield at the end of the channel, which can deflect unwanted muons away from the bubble chamber. In the opinion of this author, one cannot avoid a shield thickness equivalent to the maximum momentum of muons in the channel.

That is, for a 40-BeV/c pion- and kaon-momentum transport, one cannot avoid a shield thickness of 60-70 ft of steel. No matter how careful a calculation one makes, the $\approx 10^7$ suppression factor necessary to eliminate unwanted muons is very hard to arrive at in any way but by a brute force technique of ranging away all muons.

In the first part of this paper, well-known formulae for a FODO channel are examined in view of the channel optimization, and in the second part some shielding requirements are considered.

DISCUSSION OF THE BEAM

In what follows (see Fig. 1), the channel describes a chain of quadrupoles, each of magnetic length S, and spatial separation L-S with half aperture q. A transmission phase-space boundary for an infinitely long channel is an ellipse which in the middle of the focusing element has the simple form given in Fig. 2.

From thin-lens considerations,[3] we see that the area of the ellipse has the following momentum dependence:

$$A(p) = \frac{\pi q^2}{2L} \frac{2p_o}{p} \left(\frac{p - p_o}{p + p_o} \right)^{1/2} , \qquad (1)$$

where A is the area in cm-radians, p the momentum, p_o the low-momentum cutoff, and q and L are the half-bore and the separation of the quads as represented on Fig. 1. Relation (1) does not contain any dependence on S, the length of iron, but it turns out it is capable of describing channel configurations for very thick lenses; e.g., $S/L \approx 0.5$. In view of the fact that the quadrupole geometric aperture is not a well-defined number (see Fig. 3) an accuracy of 10-20% from the thin-lens calculation suffices. Within this limitation, Eq. (1) describes the transmission very well. The main feature of Eq. (1) is that it depends on the channel geometry only. The momentum-dependent part is a "universal" momentum curve given on Fig. 4, which depends on the momentum cutoff parameter (p_o) only. The maximum in transmission occurs at $p_{max} = 1.62\, p_o$. Thus

$$A_{max} = \frac{\pi q^2}{2L} 0.6 . \qquad (2)$$

From Eq. (2) and the area of the ellipse, one defines the "average channel angle" as

$$\theta_{ch} = 0.3\, q/L , \qquad (3)$$

where θ_{ch} is actually the maximum angle in the mid-focus element whereas θ_d

Fig. 1 (top). Quadrupole configuration of the neutrino beam.

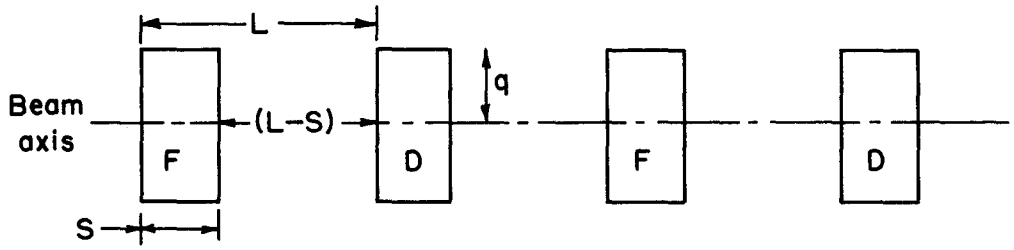

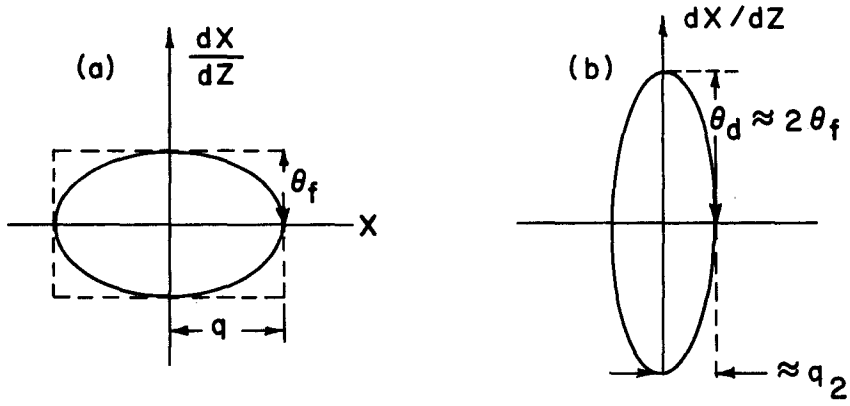

Fig. 2 (middle). Transmitted phase space in the middle of (a) the focusing and (b) the defocusing elements.

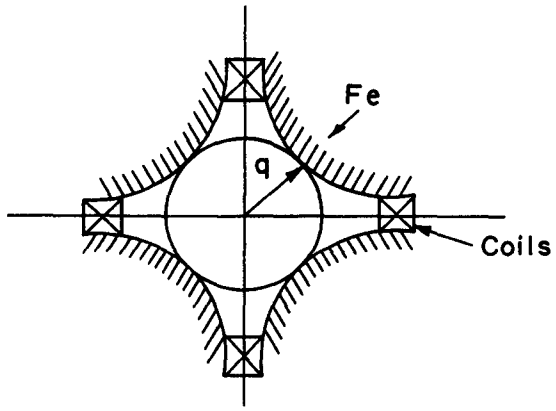

MUB-14151

Fig. 3 (bottom). Quadrupole cross section.

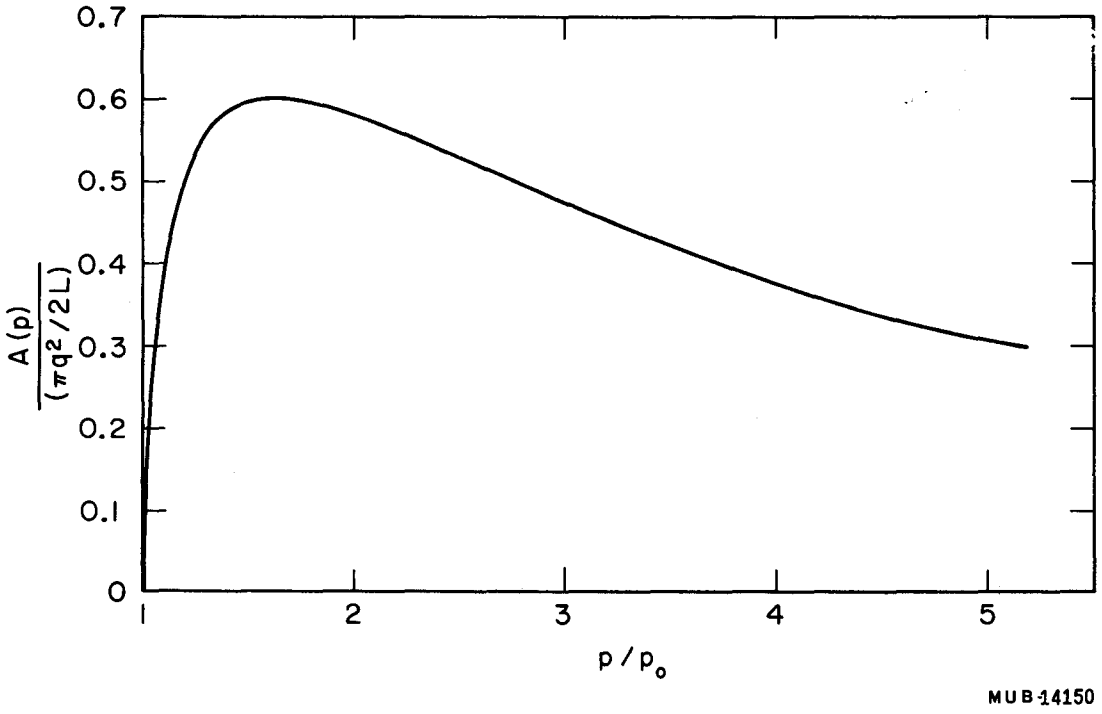

Fig. 4. Momentum-dependent part of channel-transmission function.

for the defocus section is twice as large as θ_{ch}. Both (1) and (3) are solely dependent on channel geometry, i.e., q and L. The expression which relates p_{max} (i.e., the momentum at which the maximum in transmission occurs) and the length of the iron, S, is

$$3.33 \times 10^6 \, p_{max} = GLS/1.21 \ , \qquad (4)$$

where p is in BeV/c, G is the gradient in gauss/cm, and L, S are lengths in centimeters. A more complete relation which was arrived at empirically by the study of actual channels with the aid of an analog computer is

$$3.33 \times 10^6 \, p_{max} = G\,L \left[\frac{S}{0.69 + 0.63\,(S/L)}\right] \ . \qquad (5)$$

Equation (5) seems to describe very well the properties of the existing CERN and Chicago channels for which q/L is in the range $q/L \approx 0.5 - 0.9$.

Table I gives the comparison of the relevant construction parameters for the CERN and ANL channels, together with the p_{max} calculated by Eq. (5).

Table I. Comparison between CERN and ANL muon channels.

CERN	ANL
L = 54 cm	L = 31 cm
S = 30 cm	S = 28 cm
q = 10 cm	q = 10 cm
G = 1000 gauss/cm	G = 655 gauss/cm
24 lenses	32 lenses
P design = 400 MeV/c	P design = 160 MeV/c
Calculated values from (3) and (5):	Calculated values from (3) and (5):
θ_{ch} = 55 mrad	θ_{ch} = 97 mrad
p_{max} = 460 MeV/c	p_{max} = 138 MeV/c
S/L = 0.55	S/L = 0.9
$\frac{\theta_{\pi\mu}}{\theta_{ch}} = \frac{89 \text{ mrad}}{55 \text{ mrad}} = 1.6$	$\frac{\theta_{\pi\mu}}{\theta_{ch}} = \frac{265 \text{ mrad}}{97 \text{ mrad}} = 2.8$

Table II. Channel parameters discussed in text.

20 BeV/c channel	100 BeV/c channel
140 quadrupoles	30 quadrupoles
q = 1 inch	q = 1 inch
S = 60 inches	S = 60 inches
L = 300 inches (25 ft)	L = 1500 inches (125 ft)
G = 10 kG/inch	
$\frac{\theta_{\pi\mu}}{\theta_{ch}} = 2.0$	$\frac{\theta_{\pi\mu}}{\theta_{ch}} = 2.0$

Since the S/L dependence is a rather weak one and does not enter in the channel geometry considerations, Eq. (4) will be used rather than (5) in what follows. Only at the end will S/L be calculated and compared to the thin-lens calculation.

In the design of a neutrino-muon channel, three conditions are to be met:

(i) Injection condition. The phase-space acceptance of the channel should match the phase-space emittance of the source over the wide range of momenta required.

(ii) Pencil-beam condition. The pion (kaon) beam in the channel should be as close to a line source as possible. This means that $\bar{\theta}_{ch} \ll \bar{\theta}_{\nu}$, where $\bar{\theta}_{ch}$ is given by (3) and $\bar{\theta}_{\nu}$ is the mean lab neutrino angle: $\bar{\theta}_{\nu} = 1/\gamma_{\pi}$.

(iii) Muon-capture condition. A good fraction of the μ's from the pion decay are to be captured by the channel.

Condition 3 is not easily stated as an analytic expression, but can be empirically guessed to be:

$$\bar{\theta}_{ch} > \theta_{\mu} \quad \text{where } \theta_{\mu} \approx \frac{0.04}{p_{\pi}} \quad . \tag{6}$$

It can be seen from Table I that (6) is not fulfilled at the existing channels, yet capture efficiency is of the order of 10-30%.

The pencil-beam (2) and muon-capture (3) conditions set the boundary limits on $\bar{\theta}_{ch}$:

$$\theta_\mu < \theta_{ch} < \theta_\nu$$

i.e.,

$$\frac{0.04}{p_\pi} < \bar{\theta}_{ch} < \frac{0.14}{p_\pi} \quad , \tag{7}$$

where p_π is the pion momentum in BeV/c. The injection condition (1) can be arrived at by using the Cocconi production-angle—momentum relation: $\theta_{prod} = 0.5/p_\pi$ and the quoted external beam spot size of 1 mm. This gives:

$$A_{inj} = (0.1 \frac{0.5}{p_{BeV/c}}) \text{ in cm radians} \quad . \tag{8}$$

Setting $A_{inj} = A_{channel}$ (a condition hard to meet in practice over a wide momentum range), one obtains

$$\frac{0.05}{p} = \frac{\pi q^2}{2L} 0.6 \quad . \tag{9}$$

If we also set $\bar{\theta}_{ch} = \theta_\mu$ (good μ capture), then

$$0.3 \frac{q}{L} = \frac{0.04}{p} \quad . \tag{10}$$

Dividing (9) by (10), one obtains a unique solution for q (half-quad aperture)

$$(\frac{0.05}{p}) (\frac{p}{0.04}) = \frac{\pi 0.6}{2} (\frac{1}{0.3}) (\frac{q^2}{L}) (\frac{L}{q})$$

$$q = 2.5/\pi = 8 \text{ mm!!}$$

Such small-bore quadrupoles may be hard to build (5/8-in. bore) and even harder to align; however a superconductor element may eventually be a worthwhile consideration. Using this solution for q, we may proceed to evaluate the L and S parameters of the channel. From (10) it follows that

$$L \text{ (cm)} = 6 \text{ p (BeV/c)} \quad , \tag{11}$$

which is to say that at p = 20 BeV/c the spacing between the quads is 120 cm, and at p = 100 BeV/c the spacing is 600 cm. In turn, this implies 100-1000 such quads in the 1-km channel.

The meaning of this solution is to be understood in the following sense:

(i) Transporting pions and kaons as a pencil beam can be achieved by an almost arbitrary system of quadrupoles. The number and size of quadrupoles in this case is governed mostly by the maximum momentum required of the transport system. Such a channel is indeed the one described by Toohig. In this case, the tuning over all momenta is achieved by varying the quadrupole strength.

(ii) The condition of good muon trapping efficiency, (3), however, requires that the channel accept larger and larger angles as the p_π is decreased. Such a condition is achieved by operating larger and larger numbers of quadrupoles at the maximum gradient for the low-momenta pions in the transport. If a lowest momentum required of the channel is set, the number of quadrupoles is totally determined. At higher momenta, one operates with more and more quads turned off.

(iii) If indeed one wants to achieve a constant and/or maximum muon-capture capability over a wide momentum range--a condition necessitated not by the muon physics requirement, but by the shielding requirements at the bubble-chamber neutrino detector--the above conditions are rather important.

Using the more realistic quadrupole bore of 2 in., q = 1 in., one may by the process outlined above arrive at the channel parameters for 20-100 BeV/c momentum transport system given in Table II. By comparing this channel with present-day low-energy channels, in particular, comparing the $\theta_{\pi_\mu}/\bar{\theta}_{ch}$ ratios, one may expect the μ-capture to be ≈ 20%, being lower when the channel is operated below 20 BeV/c.

SHIELDING CONSIDERATIONS

The μ-capture considerations as seen from the Beam Discussion section suggest the following:

(i) Capturing all muons from π-decay is impractical and/or expensive.

(ii) $K_{\mu 2}$ muons are captured with considerably lower efficiency than π_μ muons since $\theta_{K_\mu} \gg \theta_{\pi_\mu}$.

(iii) The hardest muons to capture are those from low-momentum beams in the channel. However, the shielding at low momenta is also less severe.

From the shielding point of view, what happens to the uncaptured muons is really most relevant. The "lost to the channel" muon may in general (a) miss the next quadrupole aperture, but not miss the iron, and (b) miss the iron completely. Although a possibility exists that the iron of the channel may continue

to transport and retain muons, one in general faces the possibility of a large "halo" of muons in the immediate vicinity of the channel.

For the muons which are captured by the channel, the solution is trivial: One bends the remaining π's and muons away from the bubble chamber by a suitable bending magnet. The cost of such a small-aperture bending magnet (2-in. gap) is not prohibitive. But the "halo" muons represent a beam of very much larger cross section and are very expensive to deal with. Of crucial importance, indeed, is the diameter of such a halo; very detailed calculation may be necessary to get a good estimate of its size. The cost of iron shielding at the end of the channel is in direct relation to the size of this halo. Only a very rough guess is offered here: Assume a 40-BeV/c pion channel. The maximum muon momentum of concern is also 40 BeV/c. For a channel which is buried underground, only the last 100 m will contribute halo muons; the rest of the muons generated upstream will be ranged out. A 10-mrad angle is the guessed cone angle which would contain all "halo" muons. One then has to shield a 4 m^2 area with an iron plug 2 x 2 x 20 meters. This amounts to some 800 tons of steel--a trivial amount. As one would tune to lower momenta, one may get away with the same amount of Fe arranged in a wider but thinner configuration.

Again we stress that a very detailed calculation has to be done to ascertain that multiple scattering leakage and/or skyshine from the channel will not be serious.

Another way of shielding the bubble chamber may be through the use of magnetized iron shields. In such a case, a 10-m-thick magnetized shield would bend 40-BeV/c muons some 6 deg away from the forward direction. Four hundred tons of magnetized shield may cost as little as $400 k. One should note that there are reasons why a magnetic shield may be preferred over the conventional one. For the non-magnetized shield, one source of background in the bubble chamber is the muons produced by the neutrino interactions in the steel. Using only $\sigma_\nu = 10^{-38}$ cm^2 as an asymptotic total neutrino cross section, one finds

$$\frac{\text{no. events in BC}}{\text{no. muons from the shield}} = \frac{1}{25} \frac{\text{(length of hydrogen in BC-meters)}}{E_\nu \text{ (BeV/c)}} .$$

Thus for a 3-m-long bubble chamber, $E_\nu = 20$ BeV/c, and at an event rate of 4/hr one will find every bubble-chamber picture containing a muon. This rate is not prohibitive, but clearly an event-rate factor of 100 higher may be prohibited by the number of μ tracks from the ν interactions in steel. A magnetized shield would greatly suppress this background.

References

1. D. Keefe, Neutrino Beams at High Energies, UCID-10131, Sept. 9, 1964. Vincent Z. Peterson, A "Monochromatic" Neutrino Beam from a High-Intensity 200 GeV Proton Synchrotron, Nov. 30, 1964. (see also 200 BeV Study, UCRL-16830, Vols. I and II.)

2. T. E. Toohig, Parameters of a Muon-Neutrino Facility at the 200 BeV Accelerator, UCID-10180, Feb. 25, 1966.

3. See, for example, A. Citron, M. Morpurgo, and H. Oeveras, The High Intensity Muon Beam with Low Pion Contamination at the CERN Synchro-Cyclotron, CERN 63-35, November 27, 1963.

THE INFLUENCE OF A LINE SOURCE OF NEUTRINOS ON THE CONFIGURATION OF EXPERIMENTAL APPARATUS

T. E. Toohig

One of the primary considerations in building a 200-BeV, high-intensity proton accelerator is the availability of large neutrino fluxes out to energies of the order of 75-100 BeV. The large primary proton flux from the accelerator, coupled with the large secondary particle multiplicities at 200 BeV, make it feasible to obtain neutrino beams with good energy resolution from the decay of momentum-selected π- and K-mesons. This same momentum selection, by determining the sign of the charge of the parent mesons, also determines whether the beam consists of neutrinos or anti-neutrinos. The advantages, characteristics, and method of calculating such a beam have been pointed out by many people in the various studies of the experimental program for physics at a very-high-energy accelerator.[1] The basic idea is to form into a pencil beam a momentum-selected beam of pions and kaons. The parent mesons decay primarily by the two-body modes $\pi \rightarrow \mu + \nu$, $K \rightarrow \mu + \nu$, so that the pencil beam becomes a line source of neutrinos. An obvious and attractive correlary of such a setup is that the muons from the same decays, recaptured by the decay channel, may be used to form a muon beam with intensities of the order of 10^9 muons per 10^{13} primary protons on the target.[1e] Some doubt has been expressed, however, whether this muon beam can be realized in practice.[2] The present paper is concerned only with the neutrino fluxes.

The differential energy distribution of neutrinos from a pencil beam of pions and kaons 1 kilometer in length into a detector of 3-meter radius is shown in Fig. 1 as a function of parent particle momentum. The production distribution of pions and kaons assumed is that due to Cocconi, Koester, and Perkins (CKP).[3] At each momentum it is assumed that the acceptance angle for the channel is equal to the Cocconi angle, $\theta_{CKP} \approx \frac{500}{p}$ mr.

The most noteworthy feature of the distributions in Fig. 1 is the good neutrino energy resolution to be obtained. (It should be borne in mind in what follows that for a given beam momentum the neutrino spikes due to both the pions and the kaons of the same momentum are simultaneously present at the detector.)

The small neutrino fluxes available at present accelerators make it necessary to use an undifferentiated neutrino-antineutrino beam produced by dumping

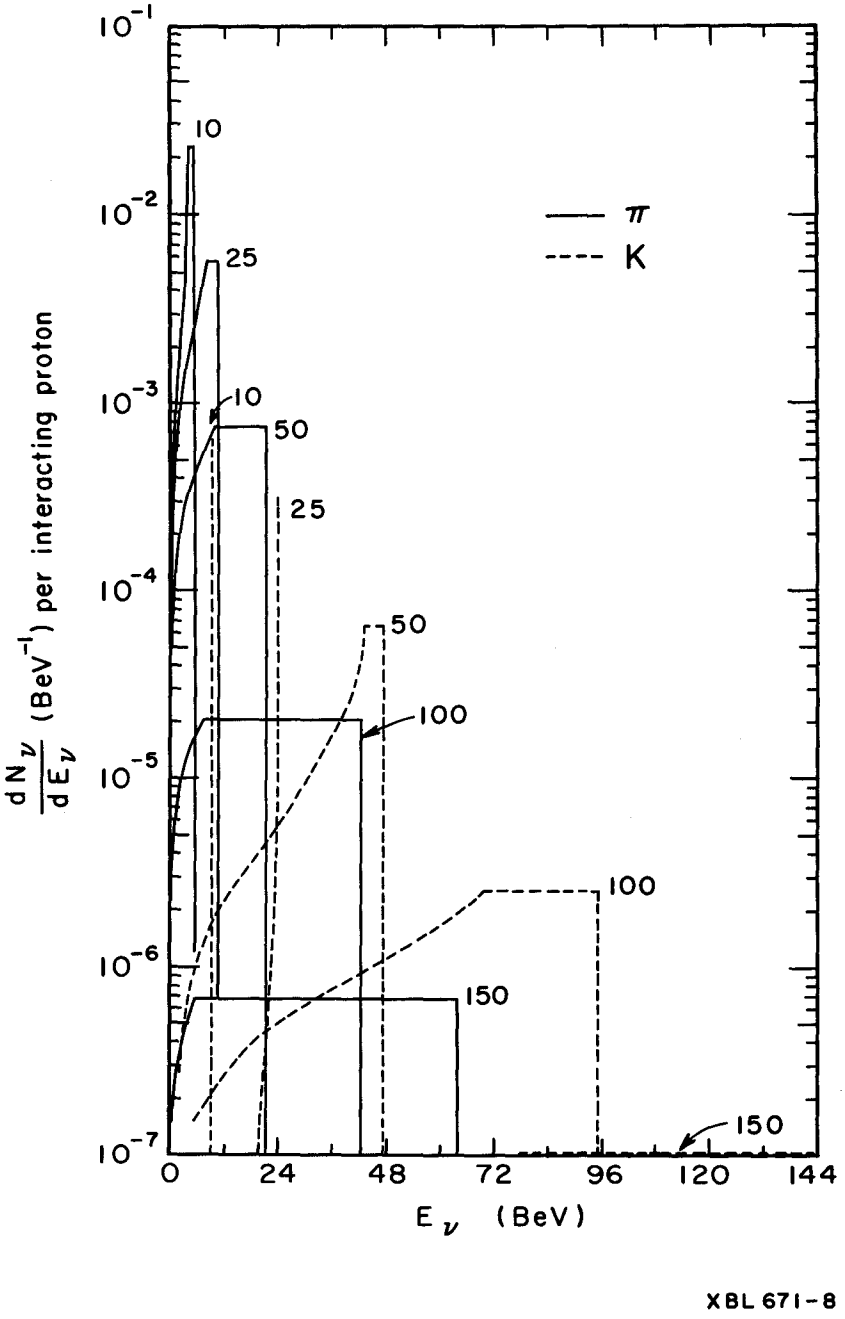

Fig. 1. Neutrino flux from K^+, π^+; 1000-m channel. $(\Delta\bar{p}_{K\pi}/\bar{p}_{K\pi}) = 0.10$. $X_0 = 50$ m. Detector radius is 3 meters. CKP production distribution. $\theta_{capture} = \theta_{CKP} \approx (500/p_{K\pi})$mr.

the primary proton beam onto a target to produce π- and K-mesons. After some decay space, the remaining mesons and all other particles produced in the target are absorbed by a thick iron shield so that only the neutrinos produced in the decay space survive to enter the detector. The optimal condition for such a setup in the absence of focusing devices (horn of plenty, plasma lens) is that the length of shielding be equal to the decay space, L = S (see Ref. 4). The minimum target-to-detector distance is then L + S, on the order of 150 meters for 10-BeV neutrinos arising from $K_{\mu 2}$ decays. One-half the neutrinos from two-body decays are contained in a cone of half-angle $\phi_\nu = \frac{1}{\gamma_{\pi,K}} = \frac{0.494}{10} = 0.49$ mr for 10 BeV/c K's. If this is folded into the production angle and the minimum target-to-detector distance, it is seen that the optimal configuration for experimental apparatus is obtained by maximizing the size of the detector, including the cross-sectional area. For a bubble chamber, in particular, this indicates that a sphere or upright cylinder of large cross section is the optimal configuration from a physics viewpoint, as well as from an engineering viewpoint.

Whatever the engineering considerations may dictate, however, some revision of this conclusion from the physics viewpoint is required once one goes over to a line source of neutrinos. In Fig. 2, the number of neutrinos per interacting proton entering a detector of radius R as a function of $E_{\nu\,max}$ is plotted for various values of R. The flux given is integrated over $0.8\,E_{\nu\,max} \leq E_\nu \leq E_{\nu\,max}$, where $E_{\nu\,max}$ is the maximum neutrino energy available from the decay of a π or K of a given momentum. Here $E_{\nu\,max}$ is the leading edge of a given differential neutrino energy spectrum of Fig. 1. It is obvious from Fig. 2 that there is no great increase in neutrino flux beyond about R = 1 meter for pions and R = 1.5 meters for kaons. This is more evident in Fig. 3, where the data are plotted in terms of elastic neutrino events/day/meter length of hydrogen as a function of the radius of a hydrogen detector. Here the mean free path for a neutrino interaction is taken to be $\lambda_\nu \approx 3\times 10^{13}$ meters, and the number of interacting protons is 3×10^{13}/pulses for 3×10^4 pulses/day. The choice of range of π and K momenta in Fig. 3 is based on the observation from Fig. 2 that, below a neutrino energy of ≈40 BeV, the channel should be tuned for the pion momentum appropriate to that neutrino energy; above ≈40 BeV the appropriate K-momentum should be selected.

If one considers the entire spectrum of neutrinos entering the detector instead of just the high-energy portion $E_\nu \geq 0.8\,E_{\nu\,max}$ of Fig. 3, it is seen from Fig. 4 that the total number of events increases with radius at all energies. The comparison of Figs. 4 and 3 indicates that the effect of increasing the radius of the detector beyond ≈1.5 meters is to increase the number of

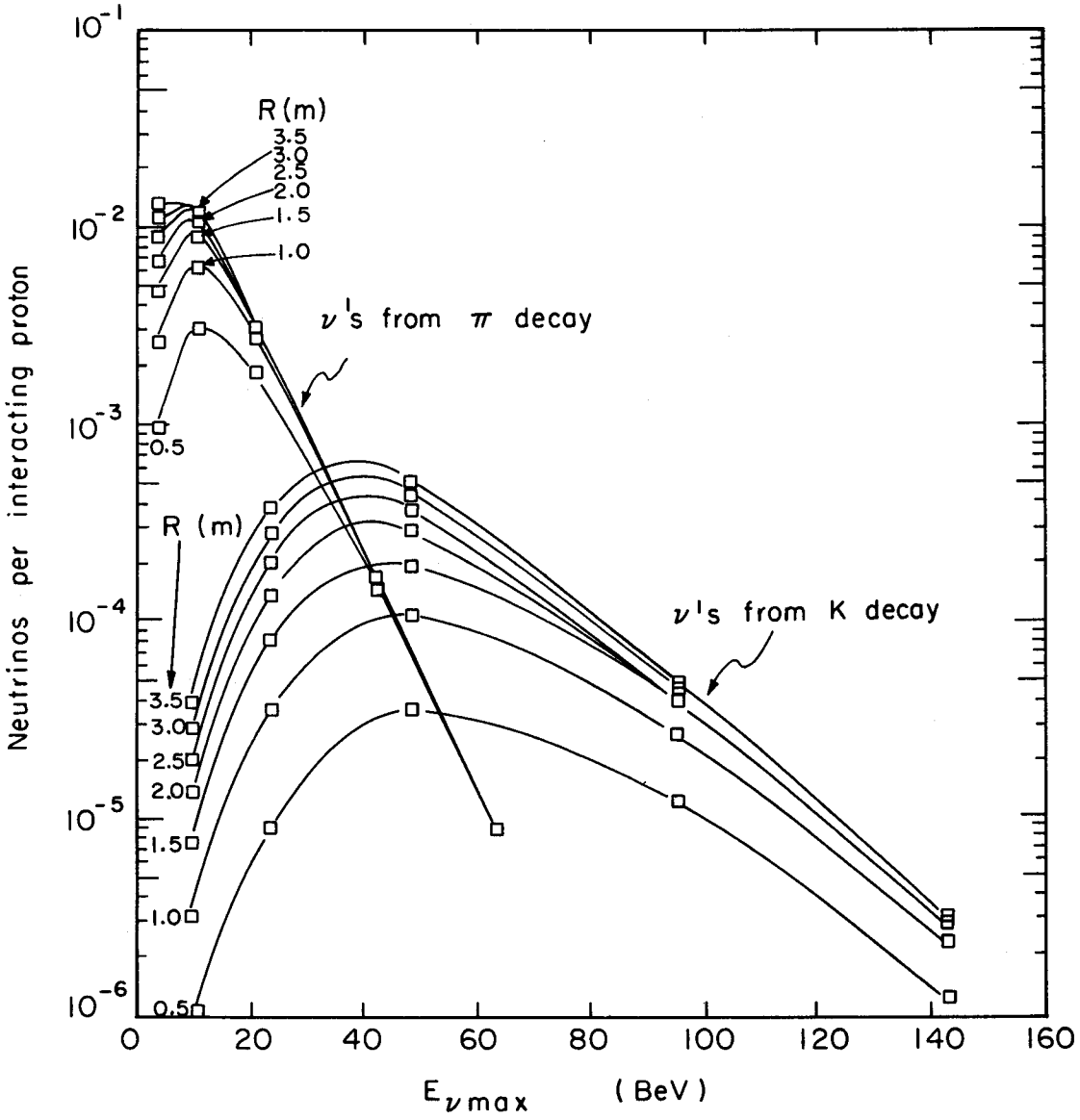

Fig. 2. Integrated neutrino flux; 1000-m channel. X_0 = 50 m.

$$\begin{cases} \phi_{K^+} = 0.1\ \phi_{\pi^+} \\ \dfrac{K \to \mu + \nu}{K \to \text{all}} = 0.63 \end{cases}; \quad \frac{\Delta p}{p} = 0.10; \quad \frac{E_\nu}{E_{\nu\,max}} \geq 0.8.$$

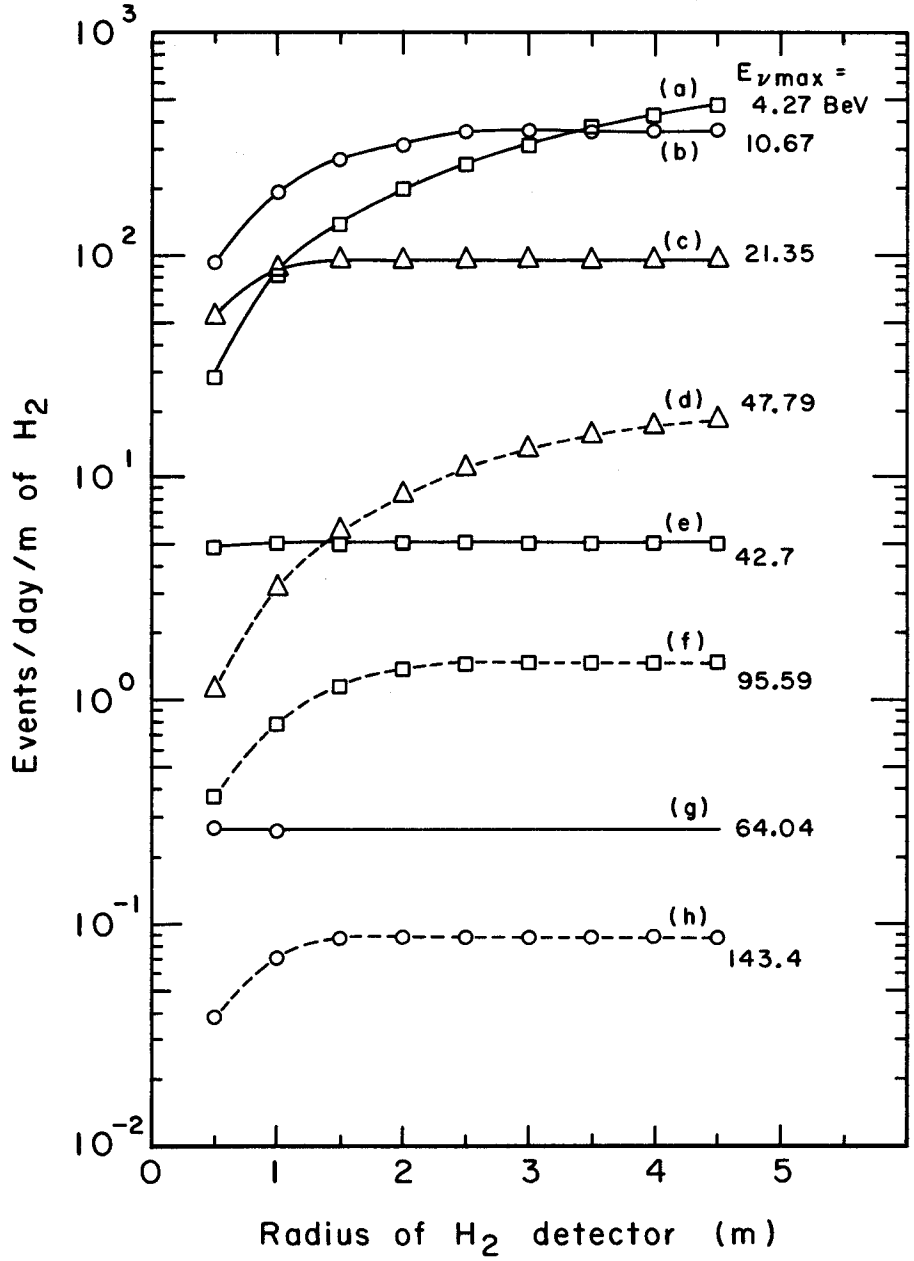

Fig. 3. Neutrino elastic event rate: $E_\nu/E_{\nu\,max} \geq 0.8$; 1000-m channel. ——, neutrinos that originate in the decay of pions; ---, neutrinos that originate in the decay of kaons. (a) p_π = 10 BeV/c; (b) p_π = 25 BeV/c; (c) p_π = 50 BeV/c; (d) p_K = 50 BeV/c; (e) p_π = 100 BeV/c; (f) p_K = 100 BeV/c; (g) p_π = 150 BeV/c; (h) p_K = 150 BeV/c.

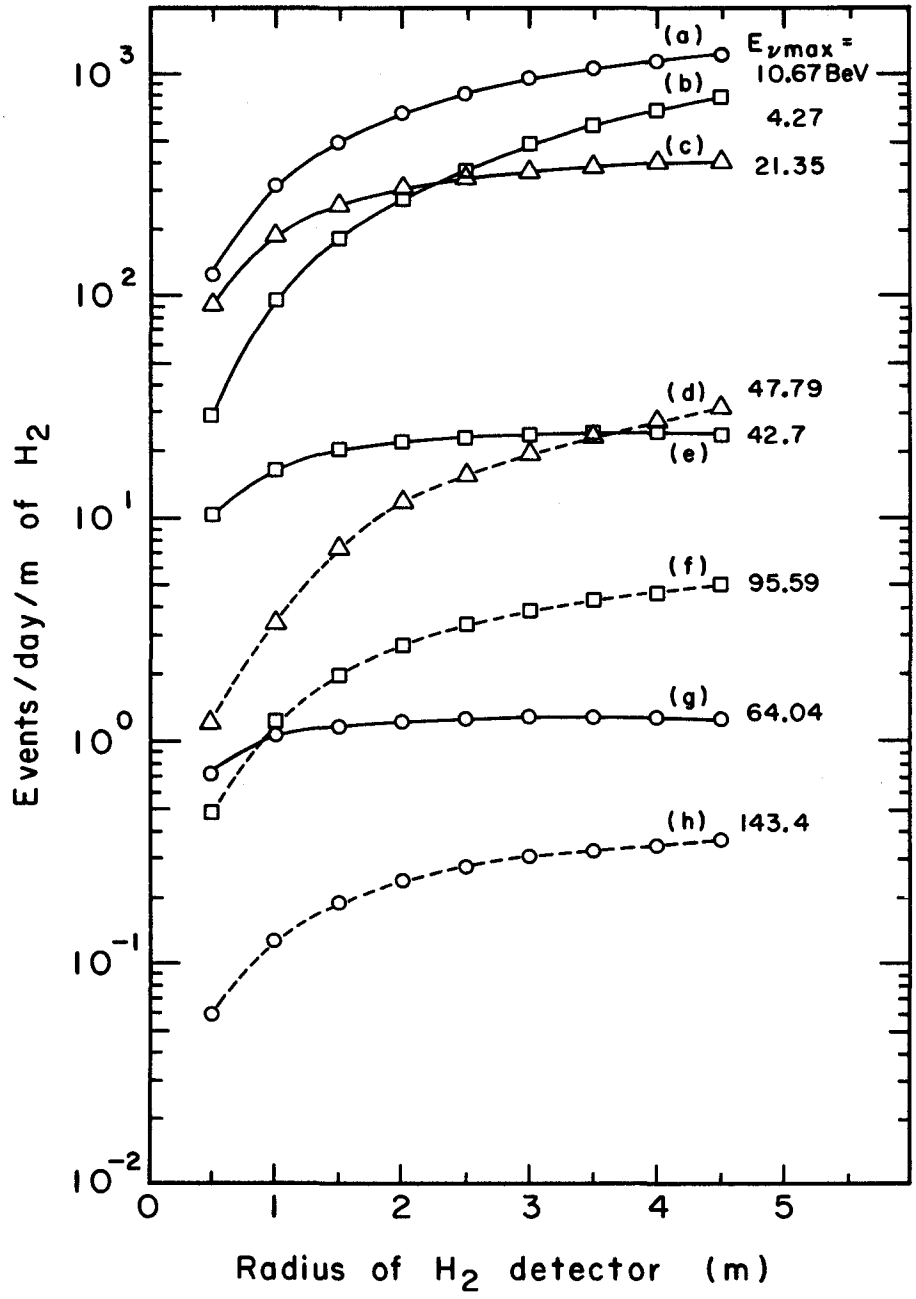

XBL 671-11

Fig. 4. Neutrino elastic event rate: $E_\nu/E_{\nu\,max} \geq 0$; 1000-m channel. ——, neutrinos that originate in the decay of pions; ---, neutrinos that originate in the decay of kaons. (a) p_π = 25 BeV/c; (b) p_π = 10 BeV/c; (c) p_π = 50 BeV/c; (d) p_K = 50 BeV/c; (e) p_π = 100 BeV/c; (f) p_K = 100 BeV/c; (g) p_π = 150 BeV/c; (h) p_K = 150 BeV/c.

events due to the low-energy part of the neutrino energy spectrum from a given parent particle momentum. It is important to notice, for purposes of this note, that in both Fig. 3 and Fig. 4, although the cross-sectional area of the detector increases as R^2, the increase of neutrino flux into the detector is less than quadratic. For a fixed volume of detector, then, the event rate is optimized by distributing the detector material along the beam direction. In other words the optimal configuration of a detector for neutrinos from a line source is not 1:1, a sphere or upright cylinder for a bubble chamber, but something of the order of 2 m in radius and length dictated by the fixed detector volume.

The pencil-beam condition coupled with the decay kinematics of the parent particles imposes certain restrictions on the decay channel. These restrictions and the means of meeting them in practice are discussed by Jovanovic.[2]

References

1. 200 BeV Accelerator: Studies on Experimental Use, 1964-1965, UCRL-16830, Vol. 1, April 1966: D. Keefe, Neutrino Beams at High Energies, p. 311; a. V. Z. Peterson, A "Monochromatic" Neutrino Beam from a High-Intensity 200 BeV Proton Synchrotron, p. 324; b. D. Keefe and V. Z. Peterson, Neutrino Beams from a High-Intensity 200 GeV Proton Synchrotron, p. 364; c. N. C. Dutta, The Effect of the Neutrino Energy Spectrum of Focusing of Parent Mesons in a Long Quadrupole Channel, p. 378; d. C. Matsubara, Beam Transmission as a Function of Momentum for a Limited Aperture Multi-Element Quadrupole Lens Channel, p. 394; e. T. E. Toohig, Parameters of a Muon-Neutrino Facility at the 200 BeV Accelerator, p. 409; f. C. A. Ramm, CERN The 1963 NPA Seminars - The Neutrino Experiment 63-37, p. 111.

2. D. D. Jovanovic, The Neutrino-Muon Facility at the 200 BeV Accelerator, UCRL-16830, Vol. 3 (in preparation).

3. G. Cocconi, L. J. Koester, and D. H. Perkins, Part II, Calculation of Particle Fluxes from Proton Synchrotrons, in The Berkeley High-Energy Physics Study, Summer 1961, UCRL-10022, 1961, p. 167; G. Cocconi, A Target for a 200 BeV Extracted Beam, UCRL-16830, Vol. 3 (in preparation).

4. e.g., N. P. Samios, BNL-7534, Proceedings of the 1963 Summer Study on Storage Rings, Accelerators, and Experimentation at Super-High Energies, June 10 to July 11, 1963.

RF SEPARATED BEAM SYSTEMS FOR USE AT THE 200 BeV ACCELERATOR

Jack Sandweiss

I. GENERAL

Lach[1] has considered the use of rf separated beams at a 200-BeV accelerator and has made a somewhat detailed design of one possible system. During the summer study (August 15 to 31, 1966), the author reviewed Lach's work and identified the several areas for further study given below:

1. The use of circularly polarized microwave deflecting fields may offer a number of advantages. These are discussed in detail in the following section.

2. The required tolerances in magnet stability, both in field and in physical position, as well as the surveying tolerances in positioning the beam magnets, should be carefully studied. In particular, the very high magnification between the target and the first deflector may give rise to some unexpectedly tight tolerances for the front end of the beam. Dipole correcting magnets using beam feedback may be a possible solution.

3. Studies have indicated[2] that significant improvements in the resolution of analysis ambiguities might result from a narrowing of the beam momentum resolution from 0.25 to 0.1%. The bubble-chamber post-analysis section should probably be redesigned for 0.1% momentum resolution.

4. The bubble-chamber end of the beam should be equipped with some sort of counter-triggered fast-turnoff magnet so that a fixed number of particles or perhaps of interactions can be taken per pulse. Because of the large size of the proposed chamber and the complexity of the interactions, a small number of tracks will normally be used. The statistical fluctuation in this number will then be even more serious than it is in present-day experiments.

5. The question of the desirability and feasibility of a "stepping-magnet" system to place subsequent beam particles at equally spaced intervals across the chamber should be investigated.

6. As noted by Lach, a variety of problems are connected with the use of the same beam system for counter spark-chamber experiments and for bubble-chamber experiments.[1] Among these are targeting and beam ejection (slow, fast) techniques, interference between the two experimental areas, and compromises in the basic beam design (see 7 and 8 below).

7. It seems clear to the author that the beam to the large bubble chamber

should be designed to operate at the highest momenta for which adequate flux can be obtained. The reason for this is that it is this beam which "fixes" the location of the large bubble chamber. Beams of $\pi^{\pm}$, p, and $\bar{p}$ can be transported over this length for any momentum of interest. Beams of $K^{\pm}$ down to ≈25 BeV/c can be produced in this system with adequate flux for the bubble chamber. Beams of $K^{\pm}$ with momentum less than 25 BeV/c will have been extensively studied with bubble chambers before the 200-BeV accelerator operates.

8. The situation with counter spark-chamber experiments will be quite different, and the flux of $K^{\pm}$ mesons in the range 10 to 25 BeV/c at the present-day accelerators is almost certainly severely restricted relative to that which will be produced by the 200-BeV accelerator.

It thus seems very likely that a "moderate"-energy, rf separated beam covering the range from ≈15 to ≈40 BeV/c specifically designed for counter spark-chamber experiments would be an important facility for the 200-BeV accelerator.

Because of time limitations, detailed follow-up work on only the first of the above items was possible during the summer study period.

II. USE OF CIRCULARLY POLARIZED MICROWAVE DEFLECTORS

The use of circularly polarized deflecting fields was first considered by Panofsky in his original suggestions for rf separators, and has subsequently been considered by a number of workers in the field. They were rejected for the first generation of rf separators because of the additional complexity required in the microwave system, and because of the $\sqrt{2}$ loss of deflection for fixed total rf power inherent in circular versus linear deflectors.

The advantage of circular polarization stems from the fact that the deflecting field never vanishes but simply points in different directions at different times during an rf period. It is thus possible to operate a two- (or three-) deflector system with zero net deflection of the desired particles. The undesired particle images are spread out into annular rings. The system works in principle so long as the deflection does not also cancel for the unwanted particles. In practice, of course, certain minimum separations must be maintained.

A system containing two circularly polarized deflectors will operate for a given desired particle over bands of momenta whose range depends on the minimum acceptable deflection amplitude of the unwanted particles. This is to be contrasted with the operation of a system containing two linearly polarized deflectors, which functions for two-contaminant rejection only at a few discrete momenta. We have somewhat arbitrarily set the minimum acceptable

contaminant deflection to equal the deflection amplitude of a single deflector. The resulting bands (see, e.g., Figs. 1 and 2) are still not adequate for a general-purpose beam, and one must consider three deflector systems. The simplest mode of utilizing three deflectors is to use only two at any one time. Results of band-pass calculations for two different spacings for best-two-out-of-three systems are shown in Figs. 1 and 2. The spacing in Fig. 2 is the same as that used in the three-deflector (linearly polarized) system designed by Lach. Comparison of the obtainable separation between wanted and unwanted particles for the pass bands (Figs. 1 and 2) with the curves given by Lach show that the best-two-out-of-three circularly polarized system is slightly inferior to the three-deflector linear system.

The natural comparison then is between full-fledged (variable amplitudes, not phases) circular and linear three-deflector systems. The linear system for two-contaminant rejection has a unique solution (except for an arbitrary over-all phase and the absolute power level). The circularly polarized system with three deflectors has two degrees of freedom after cancellation of wanted particle deflection. These degrees must be chosen to give the maximum contaminant deflections. A method for doing this (see Appendix) has been used in a CDC-6600 computer program. Due to limitations of time, only the case for K-mesons as the wanted particle has been studied, and that only over the range 40 to 120 BeV/c. The results are shown in Fig. 3 and compared with the corresponding curve for the linearly polarized system.[1] For the linear system, the relevant curve is the deflection amplitude of the wanted particle when the deflection amplitudes of both contaminants have been cancelled. In both cases, the deflection amplitude for a single deflector is normalized to unity. It can be seen that the circularly polarized system has substantially better band-pass characteristics. In particular, the deep minimum at 50 BeV/c is absent, and the deflection efficiency above 100 BeV/c is substantially better than for the linearly polarized system. However, the energy range of these calculations must be extended, and other beams with pions and antiprotons as desired particles must be studied to complete the comparison.

If the high-energy superiority of the circularly polarized system is confirmed by further calculation, it may be possible to shorten the intercavity spacing in a substantial way.

A final advantage of the circularly polarized system is the use of a small (undeflected image size) central slit rather than a beam stopper, with large areas open above and below to transmit the highly deflected wanted-particle beam. A narrow slit will present less phase space for transmission of the background particles, and it may well be possible to operate with smaller

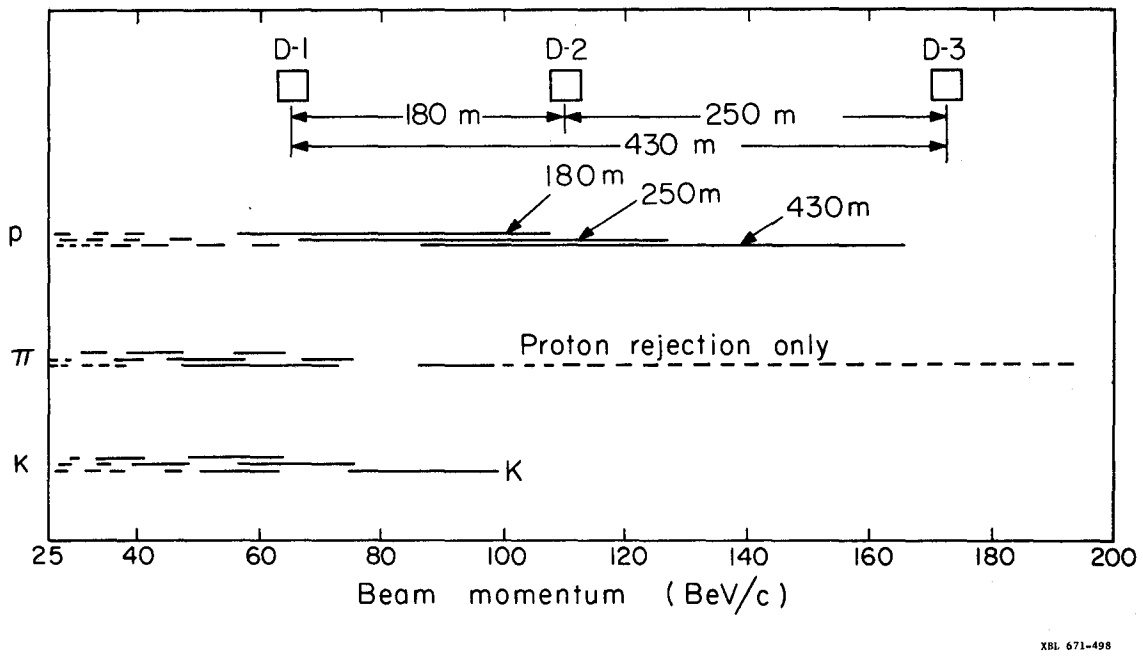

Fig. 1. Momentum pass bands (indicated by the extent of the horizontal lines) for best-two-out-of-three deflector system with circular polarization (cancellation of deflection for wanted particle). Here f = 10 GHz. The pass band corresponds to the region for which the deflection of the least-deflected contaminant is greater than or equal to the deflection imparted by a single deflector. Deflector spacings of 180 and 250 m are shown.

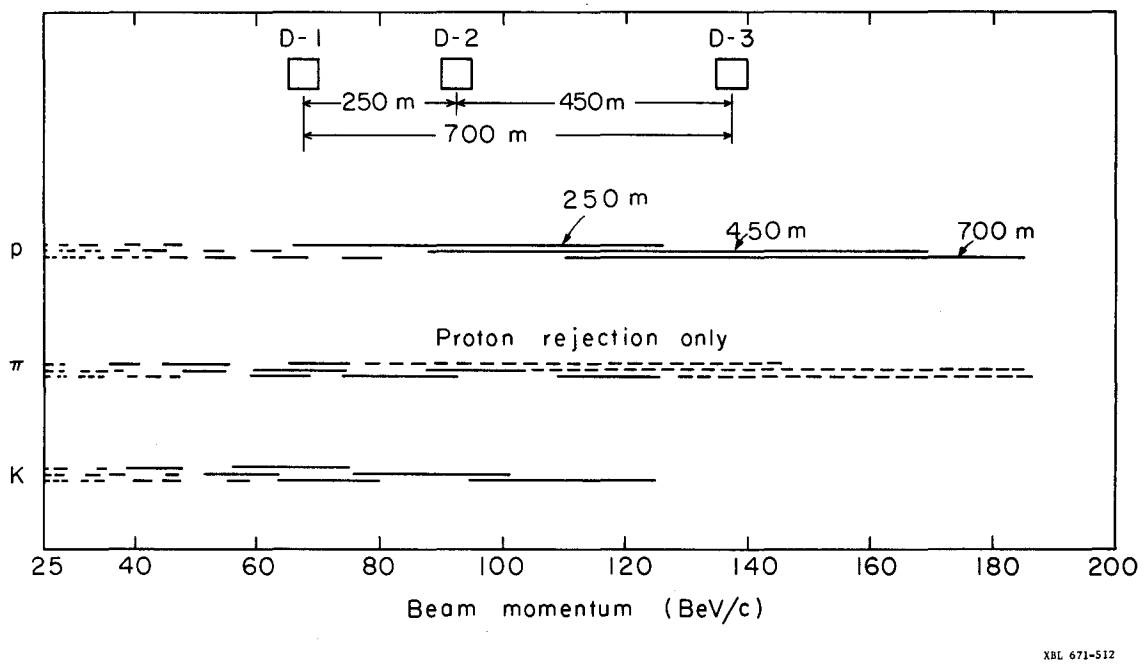

Fig. 2. Same as Fig. 1, except for deflector spacings of 250 and 450 m as shown.

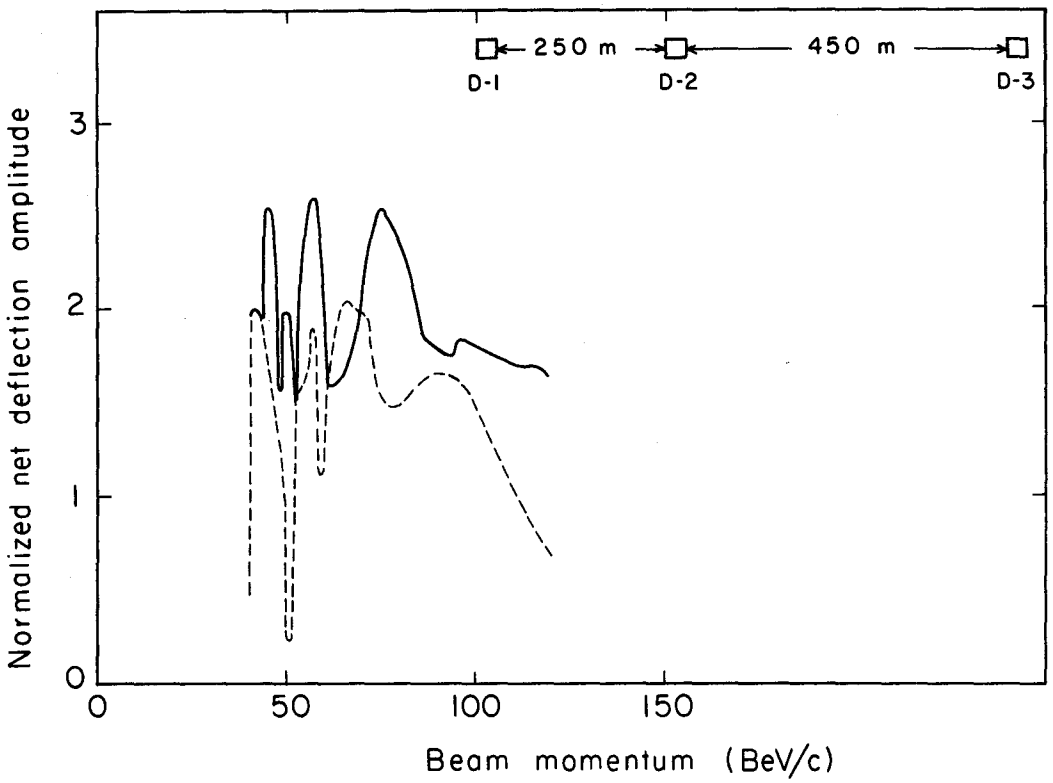

XBL 671-513

Fig. 3. Net deflection of least-deflected contaminant in a three-deflector circularly polarized system as shown (solid line) with zero net deflection for K mesons. As discussed in text, the system has been optimized for maximum deflection of the least-deflected contaminant. For comparison, the deflection amplitude of K mesons for simultaneous cancellation of proton and pion deflections in a "standard" linearly polarized three-deflector system with the same spacing[1] is also shown (dashed line).

separation between wanted and unwanted images than is possible in the linearly polarized system.

Appendix

DEFLECTION CHARACTERISTICS FOR A SYSTEM UTILIZING THREE CIRCULARLY POLARIZED DEFLECTORS

We define the following symbols:

d_i $(i = 1, 2, 3)$ ≡ absolute value of the deflection amplitude for deflector i

$\phi_A(i)$ ≡ phase difference (in radians) between the oscillations of particle A at deflector i and i = 1; A is K-meson, pion, or proton

γ_i ≡ phase in radians of the deflecting field in deflector i. The zero phase is determined by convention to give $\gamma_1 = 0$

D_A ≡ phasor amplitude of the oscillations of the beam of particles A after traversing the three deflectors

$L_{i,i+1}$ ≡ length (in meters) between deflector i and i + 1

P ≡ momentum of the particle beam

f ≡ frequency of the rf deflecting fields

M_A ≡ mass of particle A (A = K, P, π).

The phases $\phi_A(i)$ are determined via

$$\phi_A(i) = \frac{2\pi f L_{i,i+1}}{C} \sqrt{1 + \left(\frac{M_A C}{P}\right)^2}. \qquad (1)$$

The final deflection amplitudes are evidently given by

$$D_A = d_1 \exp\{i[\phi_A(1) + \phi_A(2)]\} + d_2 \exp\{i[\gamma_2 + \phi_A(2)]\} + d_3 e^{i\gamma 3}. \qquad (2)$$

If we wish to operate the system for K-mesons as the desired particle, we set

$$D_K = 0. \qquad (3)$$

We have chosen to determine γ_2 and γ_3 from the (complex) Eq. (3), considering d_i, d_2, and d_3 as given. The over-all scale of deflection depends on the power level, and we arbitrarily for the present discussion set the largest d_i equal to one (1). The problem then is to find the values of d_i which provide the maximum deflection amplitude for the least-deflected contaminant. This was solved for the graph of Fig. 3 by a trial-and-error method, with the aid of the CDC-6600 computer. The procedure is complicated by the fact that one does not know in advance which of the three deflections will be largest,

and hence which one must be set equal to unity. It was necessary at each momentum studied to consider separately all three cases ($d_i = 1$, $d_2 = 1$, $d_3 = 1$).

Inspection of Eqs. (2) and (3) shows that for each set of d_1, d_2, d_3, there are in general two solutions for γ_2, γ_3. For completeness, we give below the various solutions for γ_2, γ_3.

(i) $d_1 = 1$ (solution a)

$$\gamma_2 = \pi + \phi_K(1) - \nu$$

$$\gamma_3 = \phi_K(1) + \phi_K(2) - \nu - \gamma$$

(solution b)

$$\gamma_2 = \pi + \phi_K(1) + \nu$$

$$\gamma_3 = \phi_K(1) + \phi_K(2) + \nu + \gamma,$$

where

$$\nu = \cos^{-1}\left[\frac{1+d_2^2 - d_3^2}{2d_2}\right]; \; 0 \leq \nu \leq \pi$$

and

$$\gamma = \sin^{-1}\left[\frac{\sin\nu}{d_3}\right]; \; 0 \leq \gamma \leq \pi.$$

(ii) $d_2 = 1$ (solution a)

$$\gamma_2 = \phi_K(1) - \pi + \nu$$

$$\gamma_3 = \gamma_2 + \phi_K(2) - \nu - \gamma$$

(solution b)

$$\gamma_2 = \phi_K(1) - \pi - \nu$$

$$\gamma_3 = \gamma_2 + \phi_K(2) + \nu + \gamma,$$

where

$$\nu = \cos^{-1}\left[\frac{1+d_1^2 - d_3^2}{2d_1}\right]; \; 0 \leq \nu \leq \pi$$

$$\gamma = \sin^{-1}\left[\frac{\sin\nu}{d_3}\right];\ 0 \leq \gamma \leq \pi.$$

(iii) $d_3 = 1$ (solution a)

$$\gamma_3 = \phi_K(1) + \phi_K(2) - \pi + \nu$$

$$\gamma_2 = \gamma_3 - \phi_K(2) - \nu - \gamma$$

(solution b)

$$\gamma_3 = \phi_K(1) + \phi_K(2) - \pi - \nu$$

$$\gamma_2 = \gamma_3 - \phi_K(2) + \nu + \gamma,$$

where

$$\nu = \cos^{-1}\left[\frac{1 + d_1^2 - d_2^2}{2d_1}\right];\ 0 \leq \nu \leq \pi$$

$$\gamma = \sin^{-1}\left[\frac{\sin\nu}{d_2}\right];\ 0 \leq \gamma \leq \pi.$$

References

1. J. Lach, A High-Energy rf Separated Beam for the Proposed 200-BeV Accelerator, UCRL-16830, Vol. I (1965), p. 190.

2. R. J. Plano (private communication) and On the Usefulness of Kinematic Fitting at High Energies in a Monster Bubble Chamber (see elsewhere in this volume).

BASIC PROPERTIES OF TURN-OVER MATRICES

E. Regenstreif

INTRODUCTION

Optical systems with transfer matrices of the form

$$M = \begin{Vmatrix} -1 & b \\ 0 & -1 \end{Vmatrix} \tag{1}$$

have been considered by various authors, mainly in connection with imaging and turn-over problems in the interdeflector sections of rf separators.[1,2,3,4,5] However, most of the work seems to have been carried out on a numerical basis and no mention is made of turn-over conditions, to be imposed on the physical parameters of the lenses of which the optical system is made.

An attempt is made here to tackle the problem analytically, in order to formulate turn-over conditions and to consider in detail the situation which arises in the two basic planes of an AG turn-over system.

No use is made of the thin-lens approximation; the thick-lens approach has been applied throughout.

IMAGING AND AFOCALITY CONDITIONS

Consider (Fig. 1) an optical system described by its transfer matrix

$$M = \begin{Vmatrix} a & b \\ c & d \end{Vmatrix} . \tag{2}$$

We assume the matrix to be unimodular, i.e.,

$$ad - bc = 1 . \tag{3}$$

Let x_o, x'_o be the displacement and the slope, respectively, of an incoming ray at a distance p (taken positive toward the left) from the entrance of the system; let similarly x, x' be the displacement and the slope of the outgoing ray at a distance q (taken positive toward the right) from the exit of the system.

The total transfer matrix is then

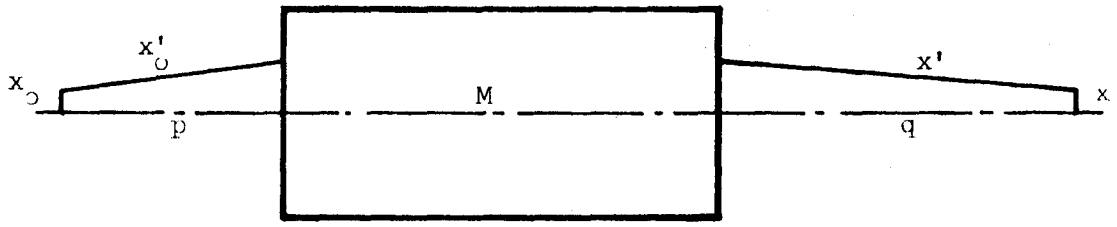

Fig. 1. Illustration of the relevant quantities arising in the transport of a particle through the magnet system M.

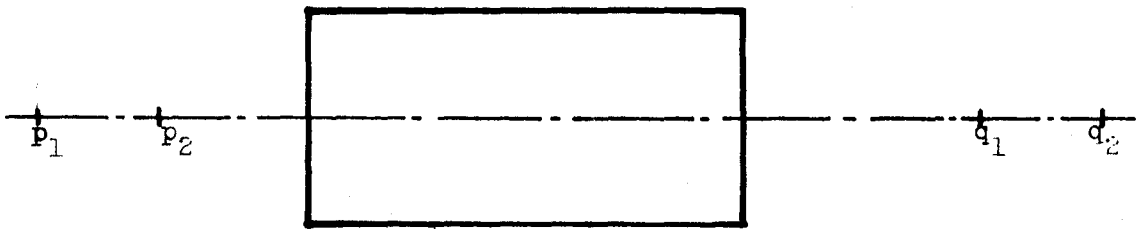

MUB 14130

Fig. 2. Illustration of the quantities arising in Eqs. (45) and (46).

$$T = \begin{Vmatrix} 1 & q \\ 0 & 1 \end{Vmatrix} \times \begin{Vmatrix} a & b \\ c & d \end{Vmatrix} \times \begin{Vmatrix} 1 & p \\ 0 & 1 \end{Vmatrix} . \tag{4}$$

Putting

$$T = \begin{Vmatrix} a_{11} & a_{12} \\ a_{21} & a_{22} \end{Vmatrix} , \tag{5}$$

one has

$$a_{11} = a + cq \tag{6}$$

$$a_{22} = d + cp \tag{7}$$

$$a_{12} = cpq + ap + dq + b \tag{8}$$

$$a_{21} = c , \tag{9}$$

or in other words

$$x = (a + cq)x_o + (cpq + ap + dq + b)x'_o \tag{10}$$

$$x' = cx_o + (d + cp)x'_o . \tag{11}$$

We call the equation

$$cpq + ap + dq + b = 0 \tag{12}$$

the conjugation relation or the imaging condition because, if (12) is satisfied, p and q are the conventional object and image distances.

We call the equation

$$c = 0 \tag{13}$$

the afocality condition because, if (13) is satisfied, the focal distance of the optical system is infinite.

THE TURN-OVER CONDITIONS

A. It is seen from Eq. (10) that for displacement turn-over, i.e.,

$$x = -x_o \text{ with arbitrary } x'_o \ , \tag{14}$$

one must have

$$a + cq = -1 \quad (15a) \qquad\qquad cpq + ap + dq + b = 0 \quad (15b) \ . \tag{15}$$

The second of these equations (15b) is the conjugation relation; the first translates the fact that the magnification is - 1. Equations (15) give

$$p = -\frac{1+d}{c} \tag{16}$$

$$q = -\frac{1+a}{c} \tag{17}$$

with $c \neq 0$; the total turn-over matrix (5) writes in this case

$$T = \begin{Vmatrix} -1 & 0 \\ c & -1 \end{Vmatrix} \ . \tag{18}$$

Any optical system can yield displacement turn-over, provided p and q as given by Eqs. (16) and (17) are positive.

B. It is seen from Eq. (11) that for angular turn-over, i.e.,

$$x' = -x'_o \text{ with arbitrary } x_o \ , \tag{19}$$

one must have

$$c = 0 \qquad\qquad d + cp = -1 \ . \tag{20}$$

The conditions of angular turn-over are therefore

$$a = -1 \tag{21}$$
$$d = -1 \tag{22}$$
$$c = 0 \ . \tag{23}$$

The transfer matrix of the optical system is then

$$M = \begin{Vmatrix} -1 & b \\ 0 & -1 \end{Vmatrix} , \tag{24}$$

and the total transfer matrix is

$$T = \begin{Vmatrix} -1 & b-(p+q) \\ 0 & -1 \end{Vmatrix} . \tag{25}$$

Contrary to displacement turn-over, which is basically independent of the optical system, in the present case the optical system must be chosen so that Eqs. (21) - (23) are satisfied.

C. For complete turn-over, i.e.,

$$\begin{aligned} x &= -x_o \text{ with arbitrary } x'_o \\ x' &= -x'_o \text{ with arbitrary } x_o , \end{aligned} \tag{26}$$

one should have

$$a + cq = -1 \qquad cpq + ap + dq + b = 0 \tag{27}$$

$$c = 0 \qquad d + cp = -1 , \tag{28}$$

and these equations lead to

$$a = -1 \tag{29}$$
$$d = -1 \tag{30}$$
$$c = 0 \tag{31}$$
$$b = p + q . \tag{32}$$

It is seen that the afocality and imaging conditions must both be satisfied; it is also seen that only particular systems can provide (under certain conditions) complete turn-over. Equation (31) may be thought of as giving the image distance under turn-over conditions when the object distance is known.

In the case of complete turn-over, the matrix of the optical system must be of the form

$$M = \begin{Vmatrix} -1 & b \\ 0 & -1 \end{Vmatrix} , \tag{33}$$

whereas the total transfer matrix is the "minus one" matrix

$$T = \begin{Vmatrix} -1 & 0 \\ 0 & -1 \end{Vmatrix} . \tag{34}$$

D. Another way of looking at the problem is to start from the unimodularity of the transfer matrices (2) or (5), and assume a priori that these matrices are symmetric.

The requirement of afocality

$$c = 0 \tag{35}$$

applied to matrix (2) leads then to

$$a = d = +1 \tag{36}$$

or to

$$a = d = -1 \quad . \tag{37}$$

In the first case the matrix

$$M = \begin{Vmatrix} 1 & b \\ 0 & 1 \end{Vmatrix} \tag{38}$$

is that of a drift space of length b, whereas in the second case one is led to

$$M = \begin{Vmatrix} -1 & b \\ 0 & -1 \end{Vmatrix} , \tag{39}$$

which is the angular turn-over matrix of an optical system, according to Eq. (24).

Similarly, the imaging condition

$$a_{12} = 0 \quad , \tag{40}$$

applied to matrix (5), leads either to

$$a_{11} = a_{22} = +1 \tag{41}$$

or to

$$a_{11} = a_{22} = -1 \quad . \tag{42}$$

In the first case the total matrix

$$T = \begin{Vmatrix} 1 & 0 \\ a_{21} & 1 \end{Vmatrix} \tag{43}$$

corresponds to that of a thin lens of converging power a_{21}, whereas in the second case one is led to

$$T = \begin{Vmatrix} -1 & 0 \\ a_{21} & -1 \end{Vmatrix}, \tag{44}$$

which is the total matrix for displacement turn-over, according to Eq. (18).

It should be emphasized that the properties mentioned above hold only in the plane where turn-over is achieved. In an AG system the situation will generally be different in the two basic planes, and it may be difficult or impossible to achieve complete turn-over in both planes.

Because of phase-space considerations, only the case of complete turn-over is important in practice and we shall henceforth limit ourselves to the consideration of complete turn-over possibilities.

LENGTH CONSERVATION UNDER TURN-OVER CONDITIONS

Let us consider two object points characterized by their distances p_1, p_2 from the entrance of an optical system. Let q_1, q_2 be the corresponding image distances (Fig. 2).

The conjugation relation yields in general

$$q_2 - q_1 = \frac{ap_1 + b}{cp_1 + d} - \frac{ap_2 + b}{cp_2 + d} \tag{45}$$

$$q_2 - q_1 = \frac{p_1 - p_2}{(cp_1 + d)(cp_2 + d)} . \tag{46}$$

In the case of turn-over one has $c = 0$, $d = -1$, so that

$$q_2 - q_1 = p_1 - p_2 , \tag{47}$$

both quantities being positive according to our sign convention; the length is therefore conserved.

TURN-OVER WITH A SYMMETRIC TRIPLET

Let

$$M_o = \begin{Vmatrix} A_o & B_o \\ C_o & D_o \end{Vmatrix} \tag{48}$$

be the transfer matrix of the outer quadrupoles of a symmetric triplet, let

$$M_i = \begin{Vmatrix} A_i & B_i \\ C_i & A_i \end{Vmatrix} \tag{49}$$

be the transfer matrix of the inner quadrupole, and let

$$D = \begin{Vmatrix} 1 & \ell \\ 0 & 1 \end{Vmatrix} \tag{50}$$

be the transfer matrix of the drift spaces between the elements; ℓ stands for the distance between the outer and the inner element (or the inter-lens spacing).

If we write M in the form

$$M = M_o D M_i D M_o , \tag{51}$$

we find, with our previous notations,

$$a = d = C_i (A_o + C_o \ell)(B_o + A_o \ell) + A_i C_o (B_o + A_o \ell)$$

$$+ A_i A_o (A_o + C_o \ell) + B_i A_o C_o , \tag{52}$$

$$b = C_i (B_o + A_o \ell)^2 + 2 A_i A_o (B_o + A_o \ell) + B_i A_o^2 , \tag{53}$$

$$c = C_i (A_o + C_o \ell)^2 + 2 A_i C_o (A_o + C_o \ell) + B_i C_o^2 . \tag{54}$$

The condition of afocality ($c = 0$) leads to the solutions

$$\ell = -\frac{1}{C_o} \left[A_o + \frac{C_o}{C_i} (A_i + 1)\right] \tag{55}$$

$$\ell = -\frac{1}{C_o} \left[A_o + \frac{C_o}{C_i} (A_i - 1)\right] . \tag{56}$$

Substituting these solutions in the expressions for a and d (Eq. 52), one finds that only the second value (Eq. 56) leads to a = d = - 1, the first giving a = d = 1, which would correspond to a drift space as seen before.

In the plane where afocality is achieved, the turn-over matrix of the optical system is then

$$M = \begin{Vmatrix} -1 & \frac{1}{C_o}\left(\frac{C_i}{C_o} - 2A_o\right) \\ 0 & -1 \end{Vmatrix} . \qquad (57)$$

For complete turn-over, one should therefore choose the length between the quadrupoles according to Eq. (56), and arrange object and image distances so that

$$p + q = \frac{1}{C_o}\left(\frac{C_i}{C_o} - 2A_o\right) . \qquad (58)$$

Alternatively, Eq. (58) gives the image distance under turn-over conditions if the object distance and the lens elements are known.

USE OF A SYMMETRIC AG TRIPLET

So far we have made no assumption about the outer or the inner elements, except for overall symmetry. For instance, the inner element may be made of a double doublet and the outer elements may also comprise some more complicated structures.

We now consider the case of a symmetric AG triplet. One then has

$$A_o = \cos\theta_o,\ B_o = \frac{1}{k_o}\sin\theta_o,\ C_o = -k_o \sin\theta_o$$

$$A_i = \cosh\theta_i,\ B_i = \frac{1}{k_i}\sinh\theta_i,\ C_i = k_i \sinh\theta_i \qquad (59)$$

in the cdc plane, and

$$A_o = \cosh\theta_o,\ B_o = \frac{1}{k_o}\sinh\theta_o,\ C_o = k_o \sinh\theta_o$$

$$A_i = \cos\theta_i,\ B_i = \frac{1}{k_i}\sin\theta_i,\ C_i = -k_i \sin\theta_i \qquad (60)$$

in the dcd plane.

In these relations we have put

$$k_o^2 = \frac{G_o}{P/Q}, \qquad k_i^2 = \frac{G_i}{P/Q} \qquad (61)$$

$$\theta_o = k_o L_o, \qquad \theta_i = k_i L_i, \qquad (62)$$

G being the gradient, P the particle momentum, Q its charge, and L the length of the quadrupole; i stands for the inner element and o for the outer elements of the triplet.

According to Eqs. (56) and (58), in order to achieve complete turn-over in the cdc plane one must have

$$\ell = \frac{1}{k_o}\cot\theta_o - \frac{1}{k_i}\coth\frac{\theta_i}{2} \qquad (63)$$

$$p + q = \frac{2\cot\theta_o}{k_o}\left(1 + \frac{k_i}{k_o}\frac{\sinh\theta_i}{\sin 2\theta_o}\right), \qquad (64)$$

and in order to achieve complete turn-over in the dcd plane one should have

$$\ell = -\frac{1}{k_o}\coth\theta_o - \frac{1}{k_i}\tan\frac{\theta_i}{2} \qquad (65)$$

$$p + q = -2\frac{\coth\theta_o}{k_o}\left(1 + \frac{k_i}{k_o}\frac{\sin\theta_i}{\sinh 2\theta_o}\right). \qquad (66)$$

Practical values of θ range from zero to $\pi/2$, and ℓ must be positive. We therefore conclude that in the case of a symmetric AG triplet, complete turn-over

is not possible in the dcd plane; in the cdc plane complete turn-over can be achieved provided

$$\frac{k_i}{k_o} > \tan \theta_o \tanh \frac{\theta_i}{2} \; ; \tag{67}$$

ℓ and p + q must then be chosen according to (63) and (64). In the cdc plane the transfer matrix of the triplet is then

$$M_{cdc} = \begin{Vmatrix} -1 & \frac{2 \cot \theta_o}{k_o} \left(1 + \frac{k_i}{k_o} \frac{\sinh \theta_i}{\sin 2\theta_o}\right) \\ 0 & -1 \end{Vmatrix} , \tag{68}$$

whereas the total transfer matrix in this plane is of the form (34).

It is interesting, especially for application to particular cases, to know the matrix elements in the dcd plane of the triplet when turn-over is achieved in the cdc plane. To calculate the elements of

$$M_{dcd} = \begin{Vmatrix} a_{dcd} & b_{dcd} \\ c_{dcd} & d_{dcd} \end{Vmatrix} , \tag{69}$$

it proves convenient to put the expressions given above for a = d, b, and c in the form

$$a = d = A_o C_o C_i \left\{ \left[1/2 \left(\frac{A_o}{C_o} + \frac{B_o}{A_o}\right) + \frac{A_i}{C_i} + \ell\right]^2 - \frac{1}{C_i^2} - \left(\frac{1}{2A_oC_o}\right)^2 \right\} \tag{70}$$

$$b = B_o^2 C_i \left\{ \left[1 + \frac{A_o}{B_o} \left(\frac{A_i}{C_i} + \ell\right)\right]^2 - \left(\frac{A_o}{C_oC_i}\right)^2 \right\} \tag{71}$$

$$c = A_o^2 C_i \left\{ \left[1 + \frac{C_o}{A_o} \left(\frac{A_i}{C_i} + \ell\right)\right]^2 - \left(\frac{C_o}{A_oC_i}\right)^2 \right\} . \tag{72}$$

Taking then into account Eqs. (60) and (63), one finds

$$a_{dcd} =$$

$$d_{dcd} = -\frac{k_i k_o}{2} \sin\theta_i \sinh 2\theta_o \{ [\frac{1}{k_o} (\cot\theta_o + \coth 2\theta_o) - \frac{1}{k_i} (\cot\theta_i + \tanh\frac{\theta_i}{2})]^2$$

$$- \frac{1}{k_i^2 \sin^2 \theta_i} - \frac{1}{k_i^2 \sinh^2 2\theta_o} \} \quad , \tag{73}$$

$$b_{dcd} = -\frac{k_i}{k_o^2} \sin\theta_i \sinh^2 \theta_o \left\{ \left(1 + \coth \theta_o \left[\cot\theta_o - \frac{k_o}{k_i} (\cot \theta_i + \tanh\frac{\theta_i}{2}) \right] \right)^2 \right.$$

$$\left. - (\frac{k_o}{k_i})^2 \left(\frac{\coth \theta_o}{\sin \theta_i} \right)^2 \right\} \tag{74}$$

$$c_{dcd} = -k_i \sin\theta_i \cosh^2 \theta_o \left\{ \left(1 + \tanh \theta_o \left[\cot\theta_o - \frac{k_o}{k_i} (\cot \theta_i + \tanh\frac{\theta_i}{2}) \right] \right)^2 \right.$$

$$\left. - (\frac{k_o}{k_i})^2 \left(\frac{\tanh \theta_o}{\sin \theta_i} \right)^2 \right\} \quad . \tag{75}$$

The knowledge of these quantities makes it possible to study the optical behavior of the triplet in the dcd plane when turn-over is achieved in the cdc plane.

PARTICULAR CASES

(i) Completely Symmetric Triplet

We consider first the case of a completely symmetric triplet which we define by

$$k_i = k_o = k \tag{76}$$

$$L_i = 2L_o = 2L \quad , \tag{77}$$

and therefore

$$\theta_i = 2\theta_o = 2\theta \quad . \tag{78}$$

The turn-over conditions (63) and (64) become now

$$\ell = (1/k)(\cot\theta - \coth\theta) \tag{79}$$

$$p + q = (1/k)\frac{\sin 2\theta + \sinh 2\theta}{\sin^2\theta} \quad , \tag{80}$$

whereas the inequality (67) is written now as

$$\theta < \Theta \quad , \tag{81}$$

being the solution of the equation

$$\tan\theta \tanh\theta = 1 \quad . \tag{82}$$

One finds $\Theta = 53.7$ deg.

The normalized value of ℓ, i.e., $k\ell = \cot\theta - \tanh\theta$, has been plotted in Fig. 3 against θ whereas the object-image relation (80) has been represented in Fig. 4.

For the transfer matrices of the triplet, one finds in the case of consideration

$$M_{cdc} = \begin{Vmatrix} -1 & \dfrac{\sin 2\theta + \sinh 2\theta}{k \sin^2\theta} \\ 0 & -1 \end{Vmatrix} \tag{83}$$

$$M_{dcd} = \begin{Vmatrix} -1 & 0 \\ -k\dfrac{\sin 2\theta + \sinh 2\theta}{\cosh^2\theta} & -1 \end{Vmatrix} \quad . \tag{84}$$

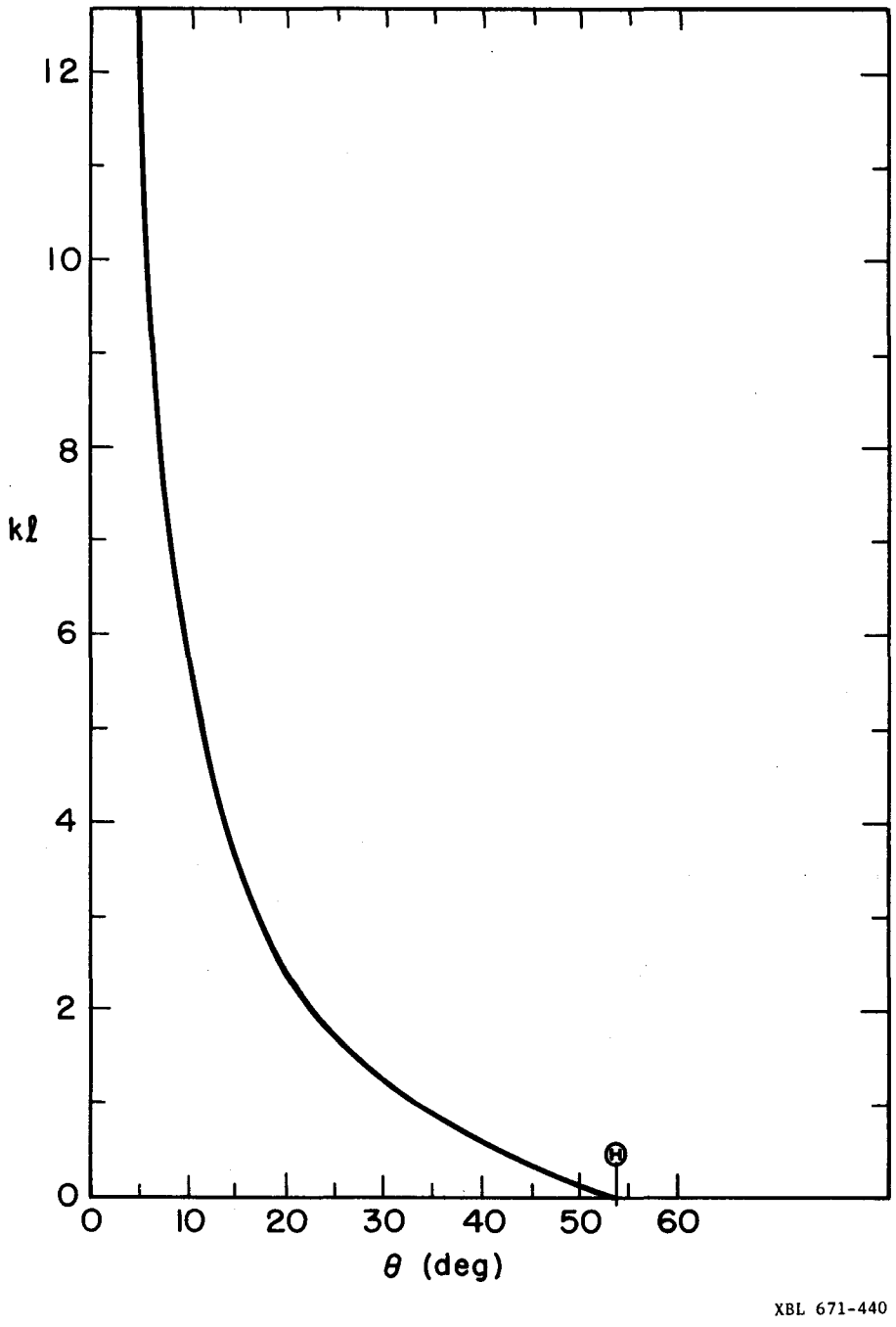

Fig. 3. The function kℓ for the case of the completely symmetric triplet.

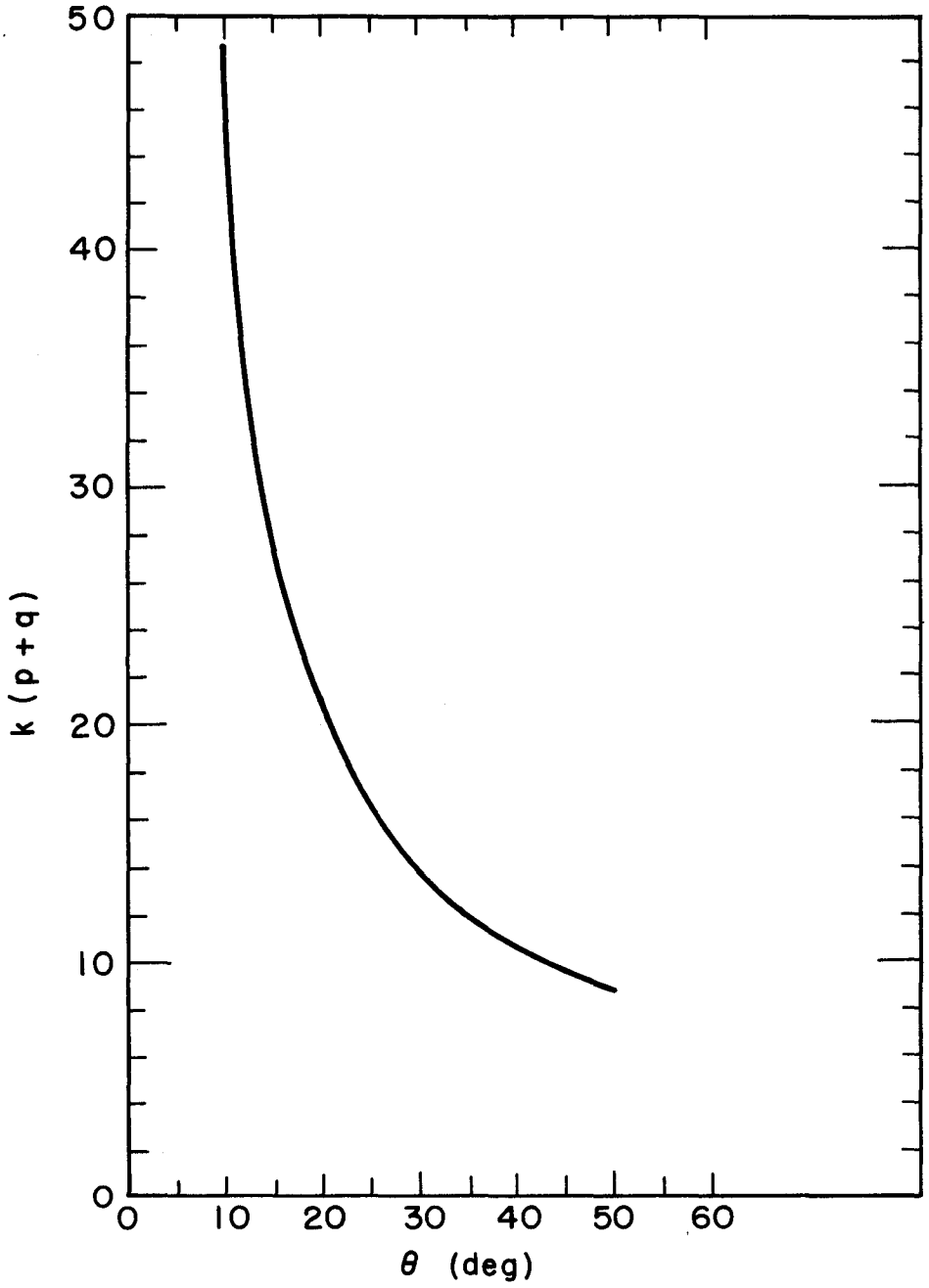

Fig. 4. The relation between object and image distances for the case of the completely symmetric triplet.

Complete turn-over is achieved in the cdc plane; no turn-over takes place in the dcd plane but the transfer matrix has the simple form of a total matrix for displacement turn-over, according to Eq. (18). For p positive, q is negative in the dcd plane, i.e., the image occurs inside the lens. Whereas the focal distance is infinite in the cdc plane, one has for the corresponding quantity in the dcd plane

$$f_{dcd} = \frac{\cosh^2 \theta}{k(\sin 2\theta + \sinh 2\theta)} \quad . \tag{85}$$

The normalized value of this focusing strength, i.e., $k f_{dcd}$, has been plotted in Fig. 5 against θ for $0 < \theta < \Theta$.

(ii) Triplet with Identical Elements

Here we consider the case where

$$k_i = k_o = k \tag{86}$$

$$L_i = L_o = L \quad , \tag{87}$$

and therefore

$$\theta_i = \theta_o = \theta \quad . \tag{88}$$

The turn-over condition is

$$\ell = (1/k)(\cot\theta - \tanh \theta/2) \quad , \tag{89}$$

and one has

$$p + q = (1/k)\frac{\sin 2\theta + \sinh\theta}{\sin^2 \theta} \quad . \tag{90}$$

For ℓ to be positive, one must have $\theta < \Theta$ where Θ is now the solution of

$$\tan \theta \tanh \theta/2 = 1. \tag{91}$$

One finds $\Theta = 63.3$ deg.

The normalized value of ℓ, i.e., $k\ell = \cot \theta - \tanh \theta/2$, has been plotted in Fig. 6 against θ, whereas the object-image relation (90) has been represented in Fig. 7.

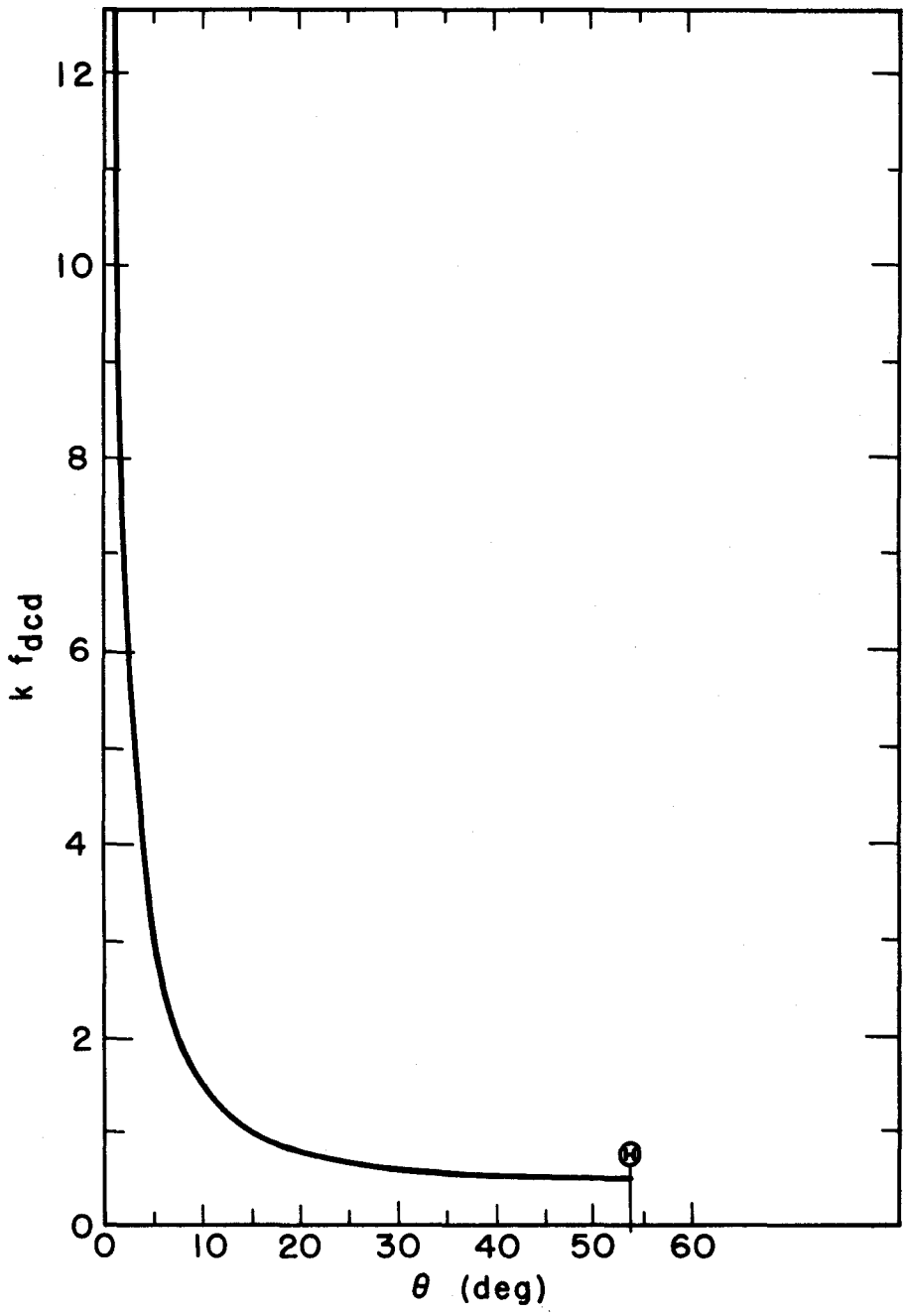

Fig. 5. The normalized focusing strength kf_{dcd} for the case of the completely symmetric triplet.

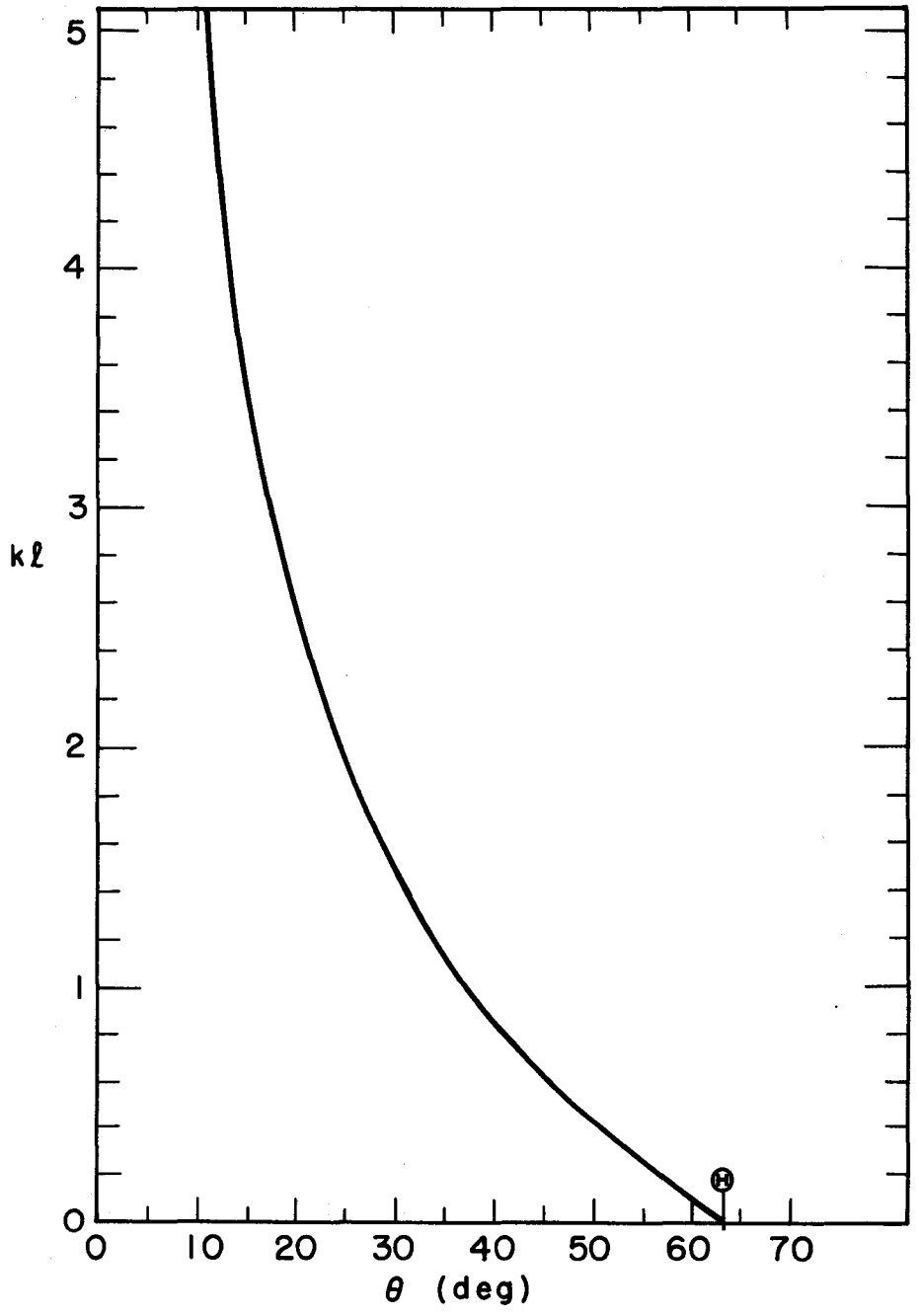

Fig. 6. The function kℓ for the case of the triplet with identical elements.

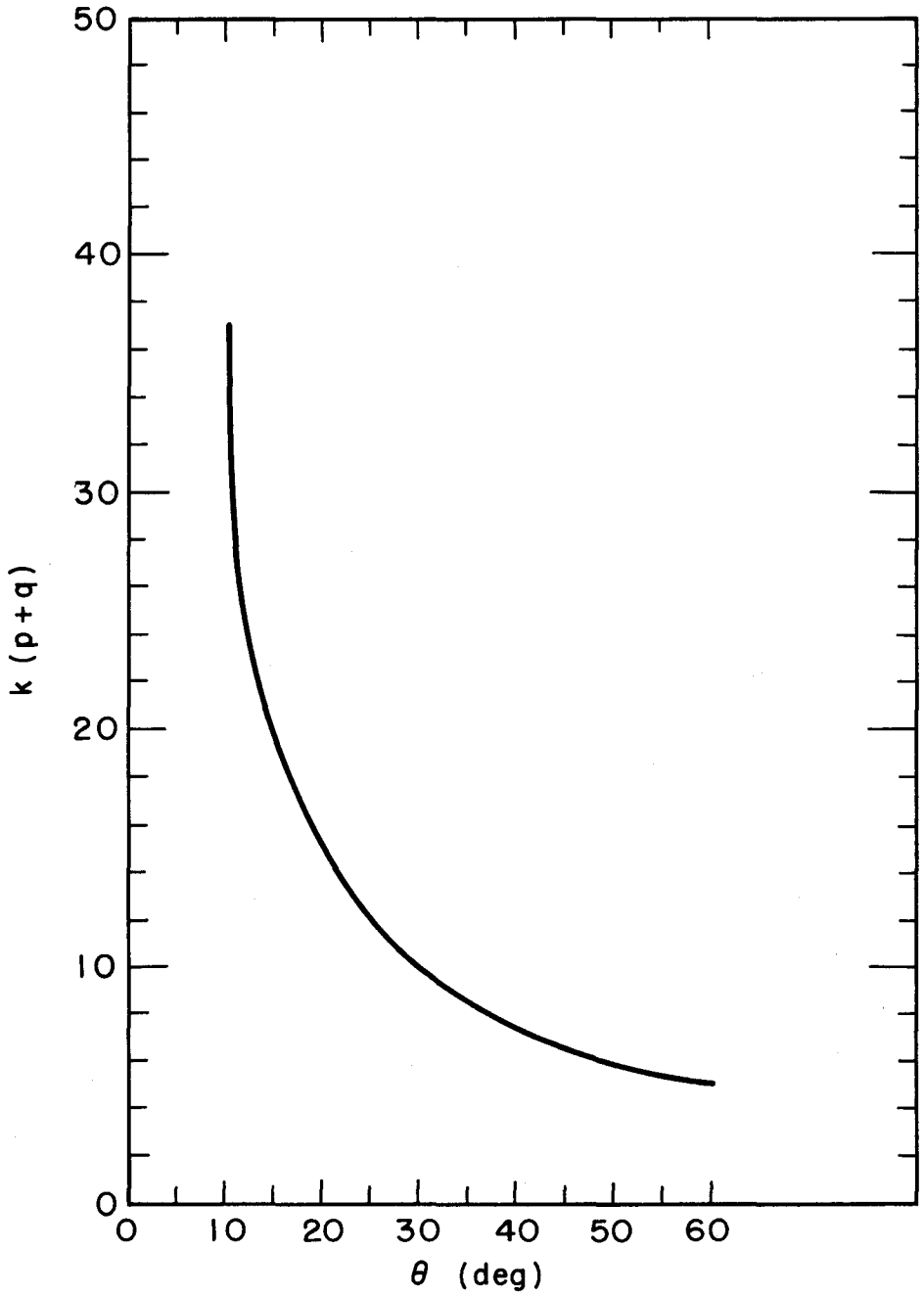

XBL 671-444

Fig. 7. The relation between object and image distances for the case of the triplet with identical elements.

For the transfer matrices one finds here

$$M_{cdc} = \begin{Vmatrix} -1 & \dfrac{\sin 2\theta + \sinh \theta}{k \sin^2 \theta} \\ 0 & -1 \end{Vmatrix} \tag{92}$$

and

$$M_{dcd} = \begin{Vmatrix} \dfrac{1}{2} \dfrac{\sinh 2\theta}{\sin \theta} - \sin\theta \tanh \dfrac{\theta}{2} & \dfrac{1}{k} \dfrac{\cosh^2 \theta - \sin^2 \theta \tanh^2 (\theta/2)}{\sin \theta} \\ k \dfrac{\sinh^2 \theta - \sin^2 \theta}{\sin \theta} & \dfrac{1}{2} \dfrac{\sinh 2\theta}{\sin \theta} - \sin \theta \tanh \dfrac{\theta}{2} \end{Vmatrix} . \tag{93}$$

The matrix (92) describes the complete turn-over in the cdc plane. In the dcd plane the focal distance is given by

$$f_{dcd} = - \frac{\sin \theta}{k(\sinh^2 \theta - \sin^2 \theta)} \quad ; \tag{94}$$

it is always negative. The normalized value of this focusing strength has been plotted in Fig. 8 for $0 < \theta < \Theta$.

(iii) Particular Values of the Ratio k_o/k_i

When turn-over is achieved in the cdc plane, the corresponding transfer matrix (69) in the dcd plane is in general complicated. It is, however, easy to show that if

$$\frac{k_o}{k_i} = \frac{\tanh \theta_o + \cot \theta_o}{\tanh \dfrac{\theta_i}{2} + \cot \dfrac{\theta_i}{2}} \quad , \tag{95}$$

the transfer matrix in dcd plane becomes

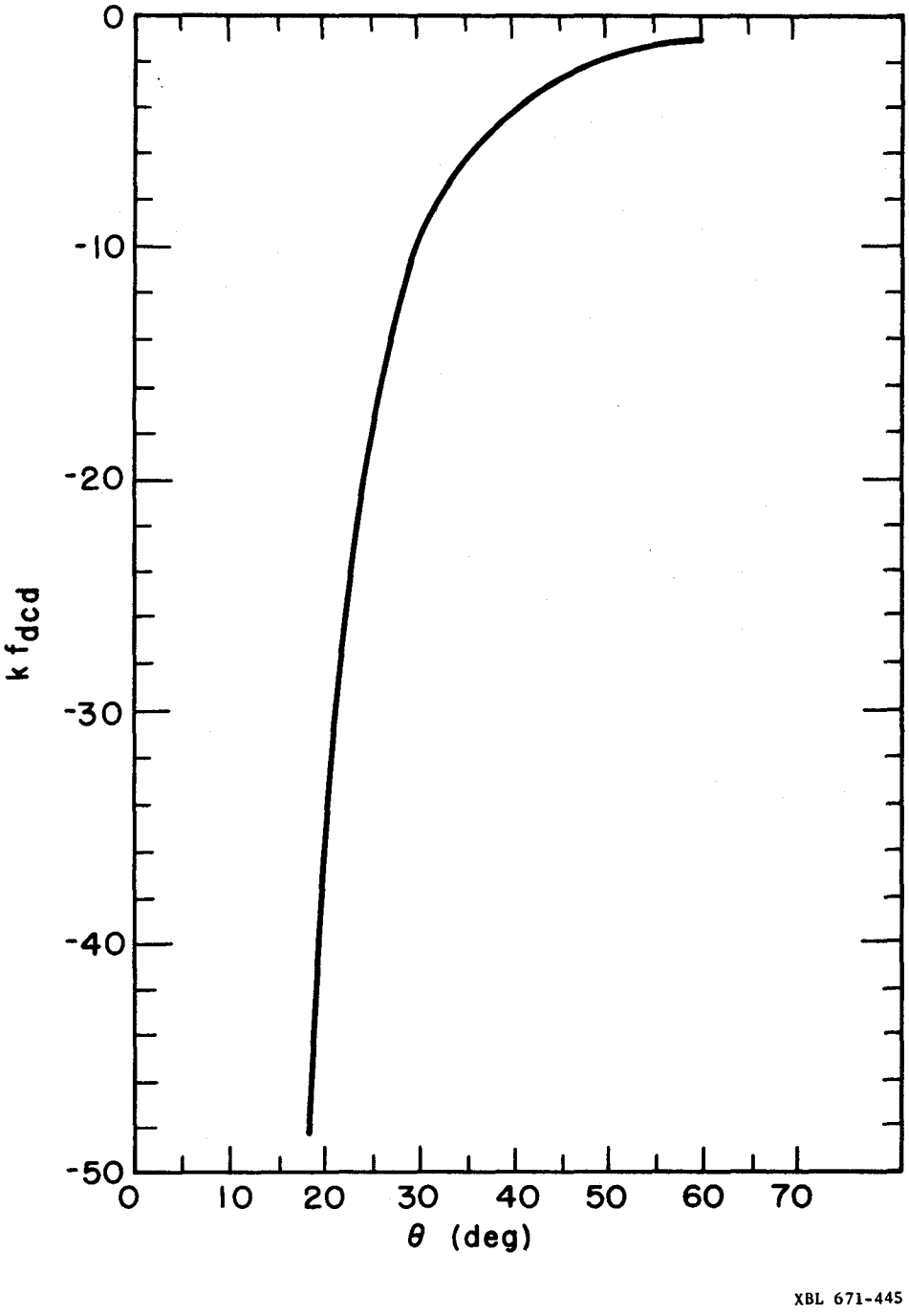

Fig. 8. The normalized focusing strength kf_{dcd} for the case of the triplet with identical elements.

$$M_{dcd} = \begin{Vmatrix} -1 & 0 \\ -\frac{1}{\cosh^2 \theta_o}(k_o \sinh 2\theta_o + k_i \sin\theta_i) & -1 \end{Vmatrix} , \qquad (96)$$

k_o and k_i being related by Eq. (95). This matrix has the form of a total displacement turn-over matrix, according to Eq. (18). By replacing Eq. (95) in the inequality (67), one finds now for the turn-over condition in the cdc plane

$$(\tan \theta_o \tanh \theta_o)\left[\tan(\theta_i/2)\tanh(\theta_i/2)\right] < 1 \quad . \qquad (97)$$

The completely symmetric triplet, considered before, is a particular case of this.

On the other hand, if

$$\frac{k_o}{k_i} = \frac{\cot \frac{\theta_o}{2} + \coth \frac{\theta_o}{2}}{\cot \frac{\theta_i}{2} + \tanh \frac{\theta_i}{2}} \quad , \qquad (98)$$

one finds for the transfer matrix in the dcd plane

$$M_{dcd} = \begin{Vmatrix} 1 & \frac{1}{k_o^2 \sinh^2 \theta_o}(k_o \sinh 2\theta_o - k_i \sin\theta_i) \\ 0 & 1 \end{Vmatrix} , \qquad (99)$$

k_o and k_i being related by Eq. (98). This matrix has the general form of a drift-space matrix. The condition (67) for turn-over in the cdc plane writes now, taking into account Eq. (98),

$$\frac{\tanh \theta_o}{\tan \theta_o} > \tan \theta_i/2 \tanh \theta_i/2 \quad . \qquad (100)$$

(iv) Image Position in the dcd Plane

We have already noted that in the case of a completely symmetric triplet, the image lies inside the lens in the dcd plane when turn-over is achieved in the cdc plane. To show that the same situation arises in the case of a triplet with identical elements, we use the formula giving the image position

$$q = -\frac{ap + b}{cp + d} \quad , \tag{101}$$

which we write here in the form

$$q = -\frac{ac}{(cp + d)^2}\,(p + b/a)\,(p + d/c) \quad . \tag{102}$$

Using now the values of the matrix elements in the dcd plane, as given by Eq. (93), we have

$$a_{dcd}\,c_{dcd} = \frac{[\cosh\theta\,(\sinh^2\theta - \sin^2\theta) + \sin^2\theta](\sinh^2\theta - \sin^2\theta)}{\sin^2\theta\,\sinh\theta} > 0 \tag{103}$$

$$\frac{b_{dcd}}{a_{dcd}} = \frac{\cosh^2\theta\,(\sinh^2\theta - \sin^2\theta) + \sin^2\theta\,(2\cosh\theta - 1)}{k\,\sinh\theta\,[\cosh\theta(\sinh^2\theta - \sin^2\theta) + \sin^2\theta]} > 0 \tag{104}$$

$$\frac{d_{dcd}}{c_{dcd}} = \frac{a_{dcd}}{c_{dcd}} = \frac{\cosh\theta\,(\sinh^2\theta - \sin^2\theta) + \sin^2\theta}{k\,\sinh\theta\,(\sinh^2\theta - \sin^2\theta)} > 0 \quad . \tag{105}$$

For p positive, i.e., a real object, q is negative in the dcd plane; the image lies therefore inside the lens.

CONCLUSIONS

It has been shown that a symmetric triplet can provide a complete turn-over in the cdc plane, and the object-image relations have been plotted out graphically for two practical cases under conditions of turn-over. It has also been shown that in the cases considered, the image lies inside the lens in the dcd plane when turn-over is achieved in the cdc plane.

The case of more complicated quadruplet systems will be considered in a forthcoming paper.

ACKNOWLEDGMENTS

The author is indebted to Dr. H. Foelsche (Brookhaven National Laboratory) and Dr. A. A. Garren (Lawrence Radiation Laboratory) for useful comments and discussions.

References

1. W. Schnell, Discussion of a Radio-Frequency Particle Separator for the CERN Proton Synchrotron, CERN 61-5, 1961.

2. H. Lengeler, CERN/TC/Beam 65-4.

3. J. Sandweiss, RF Separated Beams for the 80" Bubble Chamber, BNL H-13 (Bc), April 1963.

4. H. Foelsche, J. Lach, J. Sandweiss, Optical Design of an RF Separated Beam for the BNL 80-inch Bubble Chamber, BNL HF/JL/JS/MG-1, July 22, 1964.

5. J. Lach, A High Energy RF Separated Beam for the Proposed 200 BeV Accelerator, in 200 BeV Accelerator; Studies on Experimental Use, 1964, 1965, Vol. I, April 1966, p. 190.

SOME THOUGHTS ON THE POSSIBILITY OF MAKING CHARGED HYPERON BEAMS IN THE RANGE 50 TO 100 BeV/c

Victor Cook

TERTIARY 50 BeV/c Ξ^- HYPERON BEAM

The possibility of forming hyperon secondary beams at the 200-BeV accelerator has been considered and the formidable difficulties have been discussed.[1] Longo has described a tertiary Λ^0 beam of usable intensity and purity.[1] The main difficulties result from the short lifetimes of the hyperons and the low yields to be expected in cascaded production processes. Even though the arrangement described here may well be of marginal use, it is perhaps useful to write down some numbers to indicate what one can expect. To be specific, we will consider a 50-BeV/c Ξ^- beam, and an experiment designed to measure Ξ^-p elastic scattering and total cross section.

The beam of Ξ^- would be made in the reaction

$$K^- + p \rightarrow \Xi^- + K^+ + n(\pi^0) \ .$$

A possible scheme for selecting Ξ^- is sketched in Fig. 1. A separated K^- beam of 50-BeV/c momentum strikes a liquid-hydrogen target 25 cm long. The tertiary beam channel is composed of two legs: one to detect and momentum analyze the K^+, and the other to detect and direct the Ξ^- toward an interaction target and final-state detection equipment. Crude momentum measurement on the K^+, done with scintillation counters and a threshold Cerenkov counter* in the Ξ^- leg would provide a trigger for the wire-spark-chamber detection system. Final selection of events would depend upon more accurate measurement of the Ξ^- and K^+ directions, and the K^+ momentum determined with the wire spark chambers, and finally the detection of the Ξ^- decay in the downstream spark chambers.

Some of the useful kinematics for $K^- + p \rightarrow \Xi^- + K$ and $\Xi^- + p \rightarrow \Xi^- + p$ are shown in Figs. 2 and 3. There can be a large background of unwanted triggers, unless the triggering is highly selective. No attempt will be made

*It may be possible to design a differential Cerenkov counter with sufficient resolution ($\Delta\beta/\beta \approx 10^{-4}$ to separate Ξ^- and protons, and $\Delta\beta/\beta \approx 3\times10^{-4}$ to separate Ξ^- and K^-) and angular acceptance ($\approx \pm 2^\circ$), which would certainly help.

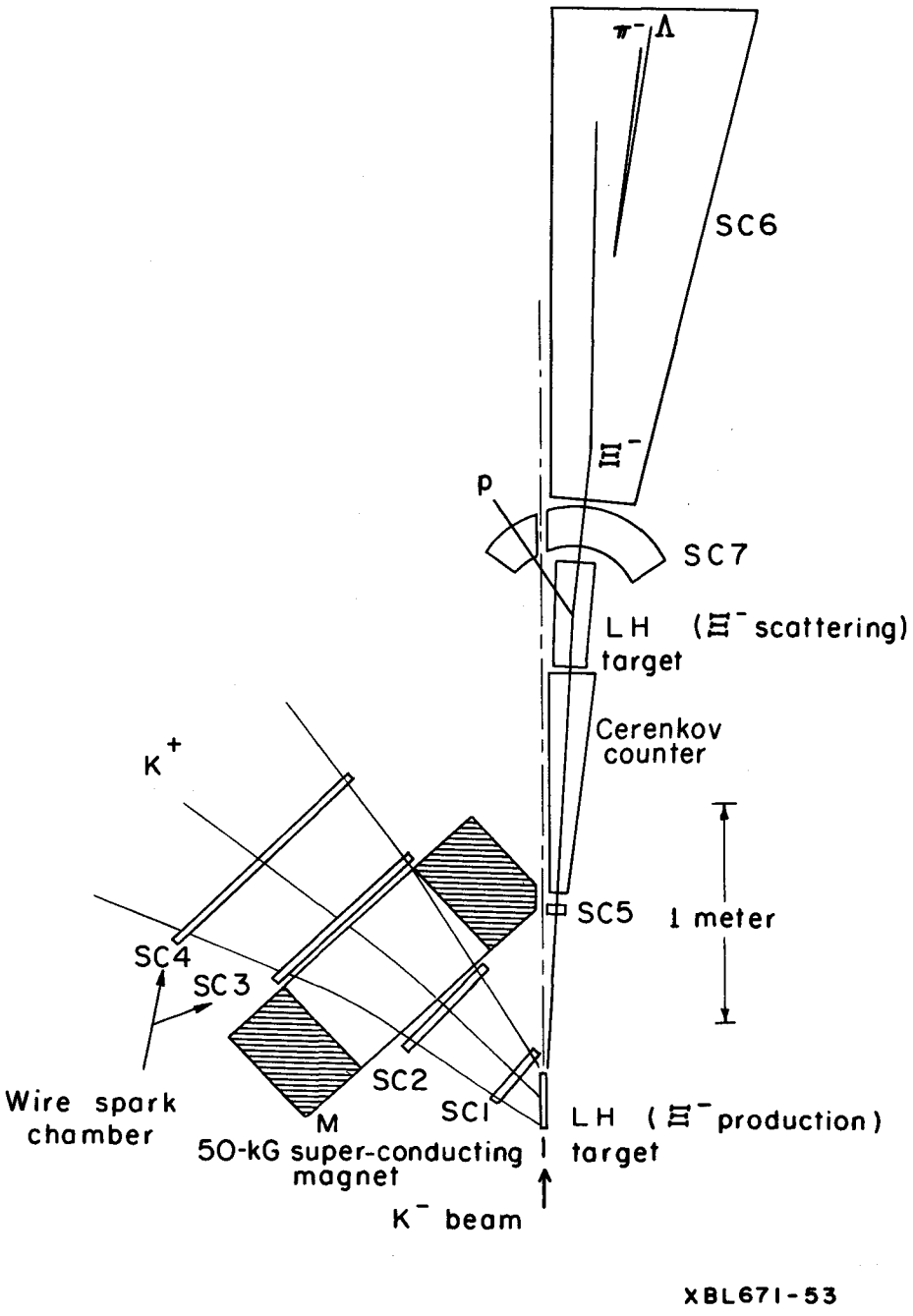

Fig. 1. Possible experimental setup for production and scattering of Ξ^-.

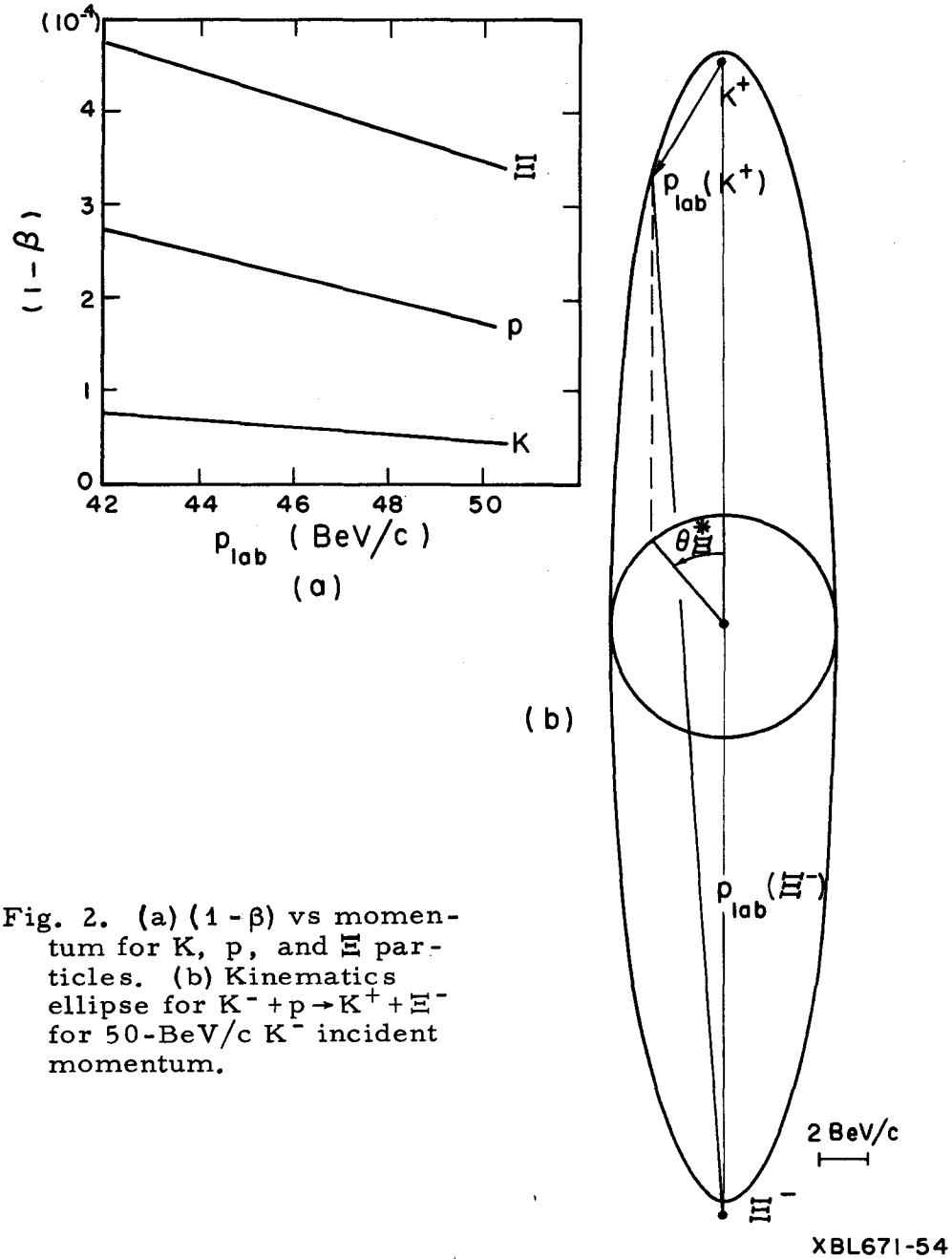

Fig. 2. (a) $(1-\beta)$ vs momentum for K, p, and Ξ particles. (b) Kinematics ellipse for $K^- + p \rightarrow K^+ + \Xi^-$ for 50-BeV/c K^- incident momentum.

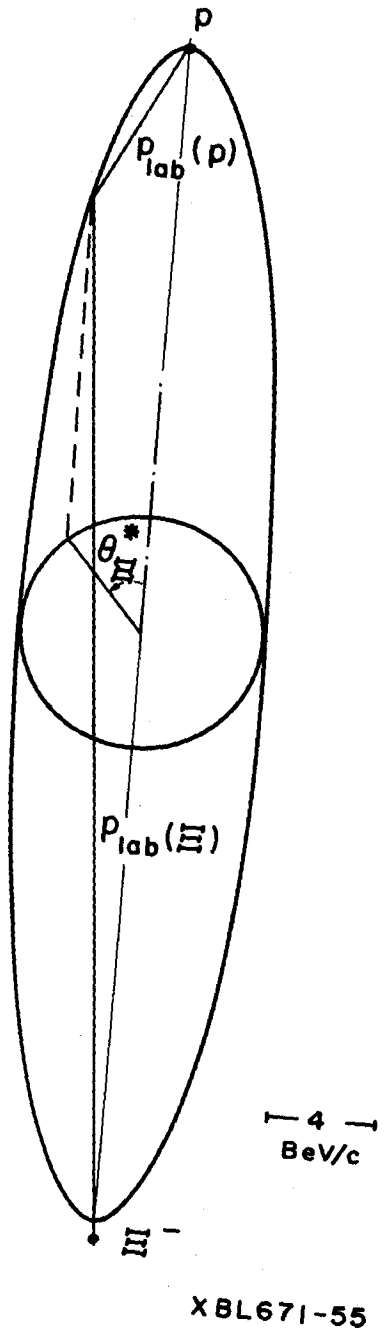

Fig. 3. Kinematic ellipse for $\Xi^- + p \rightarrow \Xi^- + p$ at $p_{lab} = 46$ BeV/c.

here to evaluate the background problems, since there are already serious "rate" problems even if one assumes 100% efficiency in all trigger systems.

The estimated rates given in Table I are meant only to give a rough indication of what one may expect. These rates are not very encouraging, particularly when we attempt to guess at the production cross section for Ξ^- in K^-p interactions.

If this technique is to work at all, the triggering requirements must be made as selective as possible. This means that we can accept only production events involving, at most, several extra pions. According to an analysis of high-energy scattering by Morrison,[2] the production cross section for $K^- + p \rightarrow \Xi^- + K^+$ can be written $\sigma = 5.0\ (p_{lab})^{-3.5}$ mb, where p_{lab} is in BeV/c. At 50 BeV/c, this gives $\sigma(K^- + p \rightarrow \Xi^- + K^+) = 0.006\ \mu b$. Assuming that all partial cross sections involving $\Xi^- K^+$ in the final state are approximately equal, we might expect a total effective cross section of about

$$\sigma [\Xi^- K^+,\ \Xi^- K^+ (n\pi)] \approx 0.04\ \mu b.$$

If this is correct, the expected rates of Table I are reduced by a factor of 25.

Table I. Estimated rates of Ξ^- particles and interactions.

Incident K^- beam	10^7/sec
Ξ^- Produced in 25-cm LH target ($\sigma_{prod} = 1\ \mu b$)	100/sec
Ξ^- Entering scattering target (K^+ detection acceptance included)	0.5/sec
Ξ^- Interaction rate [50-cm target; $\sigma_{tot}(\Xi^- p) = 20$ mb]	0.02/sec
Elastic scatters ($\sigma_{el} = 1$ mb)	0.001/sec

50 TO 100 BeV/c SECONDARY Ξ^- BEAM

Suppose we use only a Cerenkov counter and bending magnets to detect Ξ^- in an unseparated beam. A simple beam setup as shown in Fig. 4 might provide enough flux to make experiments feasible. In this scheme we take advantage of the fact that the Ξ^- is heavier than any of the copious contaminants, so we can use a simple threshold counter of very moderate length.

The bending magnet M_1 spatially separates the external proton beam that passes through the production target and the negative beam in which we are

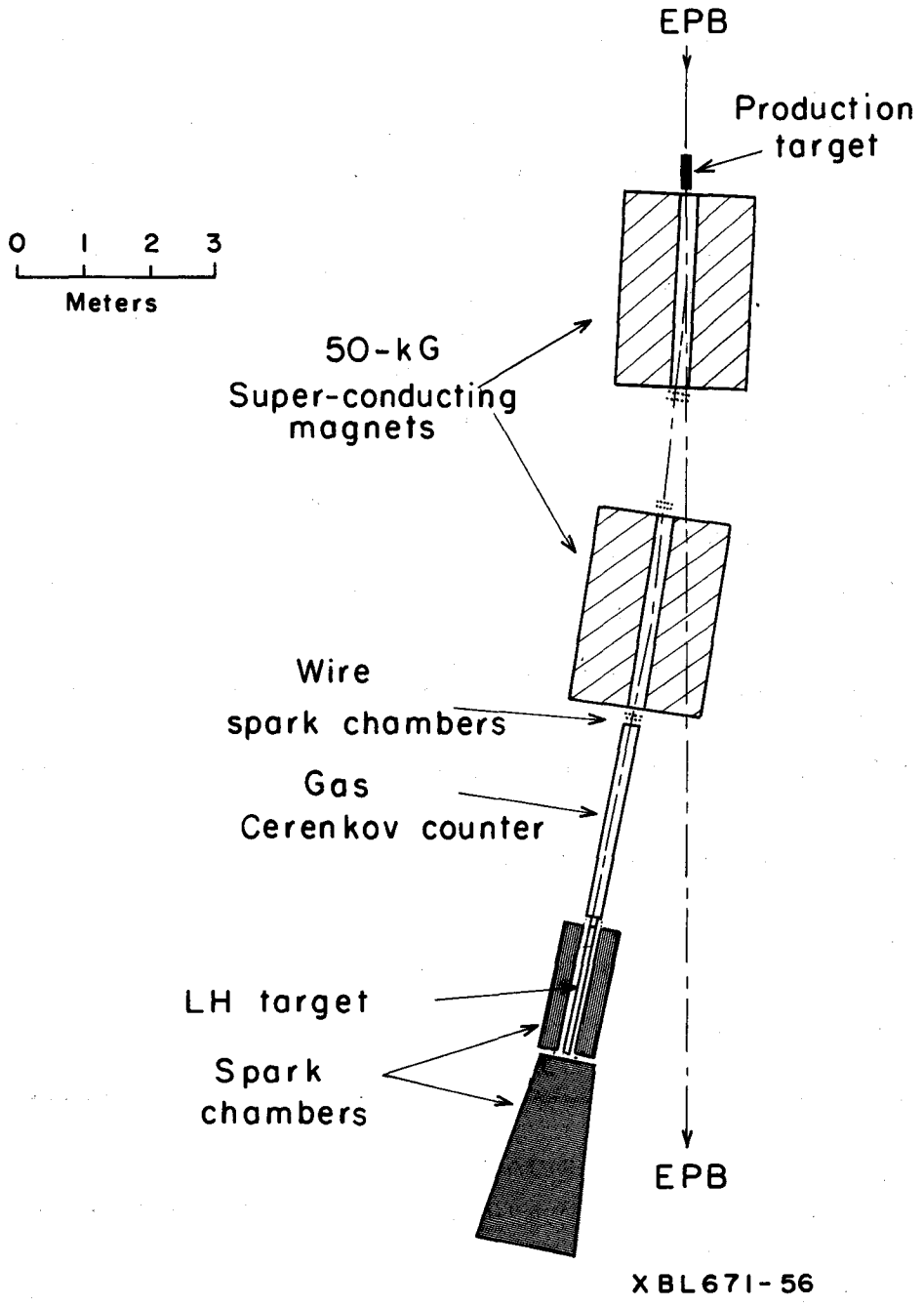

Fig. 4. Schematic layout for 50-BeV/c secondary beam. Bend is 5 deg in each magnet.

interested. Momentum measurement is accomplished with M_2 and the spark chambers and scintillation counters located upstream and downstream of the magnet. The momentum acceptance of the beam channel is quite large (about ± 10%). In fact, that momentum distribution will probably be determined by the production cross section. Cascade selection by the Cerenkov counter can be accomplished only if the momentum bite is limited to a few percent. This can be done with a scintillator, or wire-spark-chamber matrix.

We need not be concerned about δ-ray production since we are using the counter only as an "anti." A gas counter 3 meters long for a 50-BeV/c beam, and 8 meters long for a 100-BeV/c beam, with the gas pressure set at Ξ^- threshold, provides sufficient light to count π^-, K^-, and $\bar{p}$ efficiently enough to ensure a signal-to-noise ratio of more than one. Crude estimates of the performance of such a counter are given in Table II. We might expect that the secondary beam intensity would be limited by acceptable instantaneous rates, since there must be spark chambers in the beam. If 10^7 particles per burst are tolerable, one would have about 5 Ξ^- per pulse [assuming that a tenth of the beam lies within the accepted momentum band (±1%) incident on a scattering target (presumably liquid hydrogen)]. In addition there would be two to three background triggers due to π^-, K^-, and $\bar{p}$ which are not eliminated by the Cerenkov counter. With the total cross section assumed to be 20 mb and the target 2 meters, the event rate would be 0.8/pulse. The accuracy of a cross-section measurement would be limited by the efficiency with which π^-, K^-, and $\bar{p}$ events are eliminated. This efficiency could be improved by increasing the length of the Cerenkov counter, or perhaps by using two counters. Identification of the Ξ^- events in the spark chambers surrounding the scattering target would also improve the rejection of unwanted events, but with some loss in good event rate.

This appears to be a more useful approach than the tertiary beam approach described in the first section; however, the difficulties expected in selecting good events out of a background, which is greater by 5 orders of magnitude, are obvious. A much more careful analysis is necessary before one would seriously propose an experiment involving hyperon-nucleon scattering; however, it does not appear that one can dismiss the possibility out of hand.

Table II. Estimates of Cerenkov-counter efficiency based on presently available techniques and equipment.

Two different beams are considered:

(a) 50-BeV/c beam; 13-meter total beam length; 3-meter Cerenkov counter.

(b) 100-BeV/c beam; 24-meter total beam length; 8-meter Cerenkov counter.

Beam	(a)			(b)		
Particle	π^-	K^-	$\bar{p}$	π^-	K^-	$\bar{p}$
$\Delta\beta = \beta_i - \beta_\Xi$	3.5×10^{-4}	3.0×10^{-4}	1.7×10^{-4}	8.7×10^{-5}	8.6×10^{-5}	4.4×10^{-5}
Total no. of photons[a]	52	45	26	35	34	18
No. of photo-electrons[b]	14	12	7	9.4	9	4.8
(1-Efficiency)[c]	8.3×10^{-7}	6.1×10^{-6}	9×10^{-4}	8×10^{-5}	1.0×10^{-4}	8.3×10^{-3}
[Flux(i)/Flux(Ξ)][d]	1.5×10^{5}	1.5×10^{4}	1.5×10^{3}	4×10^{4}	4×10^{3}	4×10^{2}

[a] If the Cerenkov counter pressure is set to Ξ threshold, the number of photons produced by a particle with velocity $\beta_i (> \beta_\Xi)$ in the S^{11} spectral region is about

$$N \approx 500 \frac{\Delta\beta}{\beta_i} \text{ photons/cm} .$$

[b] Collection efficiency is assumed to be 90%. The quantum efficiency of photomultipliers is assumed to be 30%.

[c] This is calculated with the assumption that all events in which at least one photoelectron is produced are detected.

[d] This is based on crude estimates for the relative intensities at the production target, namely, $\pi^-:K^-:\bar{p}:\Xi^- = 100:10:1:1$.

References

1. M. J. Longo, Experiment with Hyperon Beams at 200 GeV Acceleration, 200 BeV Accelerator: Studies on Experimental Use, 1964-65, UCRL-16830, Vol. I, p. 158.

2. D. R. O. Morrison, On the Variation of Cross-Section with Incident Momentum of Two-Body Reactions at High Energy, CERN Report 66-14, October 6, 1966.

TAGGING OF REAL AND VIRTUAL PHOTONS

R. Wilson and M. Wong

The following report was originally written (September 24, 1965) to compare plans for photo experiments at CEA with a planned muon-scattering experiment at the AGS. This muon-scattering experiment has been proposed and accepted.

It appears that high-intensity muon beams have a very great advantage over gamma and electron beams for studying electromagnetic processes at small momentum transfers. This is of great interest for the 200-BeV proton accelerator, because muon beams of 100 BeV should be easily, although expensively, attainable.

Many experiments become possible. Among the easiest, photoproduction of ρ_o can tell us the ρ-nucleon interaction; π^o and π^+ production tell us details of peripheral interactions. But the list is huge.

A fuller report will be written later and published elsewhere.

INTRODUCTION

Photon beams for experiments in high-energy physics usually are made by bremsstrahlung from electrons on matter. There is then a distribution of photon energies according to the usual Bethe-Heitler formula. For the purpose of this note, the number of photons of energy between k and k + dk can be approximated as

$$N = (t/X_o)\,(dk/k) \qquad (1)$$

up to a maximum energy equal to that of the electron. Here t is the thickness of the target and X_o is the radiation length.

Since it is clearly interesting to measure processes at a definite gamma-ray energy, various procedures have been devised to produce monochromatic or effectively monochromatic beams. Among these is the process of gamma-ray tagging, which is the subject of this note.

After producing bremsstrahlung, the electron has a reduced energy; the scattered energy (apart from a small recoil effect) and that of the gamma ray add to equal the incident energy. Thus by measuring the scattered electron in coincidence with the process under study, the gamma-ray energy is known. This procedure was first used by Weil and McDaniel[1] at Cornell, following the

independent suggestions[1] of Koch and Camac, and most recently by Caldwell et al.[2] at CEA.

It is the purpose of this note to extend their analyses to the processes of inelastic electron and muon scattering by use of the idea of virtual photons.

VIRTUAL PHOTONS

Weizsacker and Williams[3] were the first to show clearly that every charged particle can be considered to be carrying a field of virtual photons. The interaction of these virtual photons with matter will then lead to inelastic scattering. When the energy of the charged particle (E) is large compared with its rest mass (mc^2) and the excitation of the matter, the charged particle will usually be deviated very little from the incident direction. Then both the effective gamma-ray energy and momentum k are given by the difference between incident and scattered energies:

$$k = E_i - E_f \quad . \tag{2}$$

The spectrum and number of virtual gamma rays is approximately the same as that produced by an electron passing through a radiator of thickness

$$\frac{R_{eff}}{X_o} = \frac{2\alpha}{\pi} \ln (E/m) \approx 0.02 \quad . \tag{3}$$

More detailed calculations of this spectrum have been made by Dalitz and Yennie[4] and by Hand and Wilson.[5] For simple calculations, however, Eq. (3) will suffice.

It is worthwhile, at this stage, to remember the important features of such a calculation; an integration must be made over the momentum transferred by the incident charged particle. If the matrix element for the photo process studied varies slowly with momentum transfer, it may be factorized out, and Eq. (3) results. For elementary particle processes, the variation with momentum transfer is of the order of that of the nucleon form factors, which vary negligibly over momentum transfers of the order of an electron mass and not greatly over those of the order of a meson mass. On the other hand, if we calculate bremsstrahlung by the Weizsacker-Williams approach, we find that the relevant matrix element varies fast and we obtain a result which varies as $1/m^2$. We are now prepared to compare the different procedures.

BACKGROUNDS

A gamma-ray tagging experiment with real photons (Case 1) is shown schematically in Fig. 1, and one with the same electrons producing virtual photons (Case 2) in Fig. 2. The muon case (Case 3) is similar to the one shown in Fig. 2.

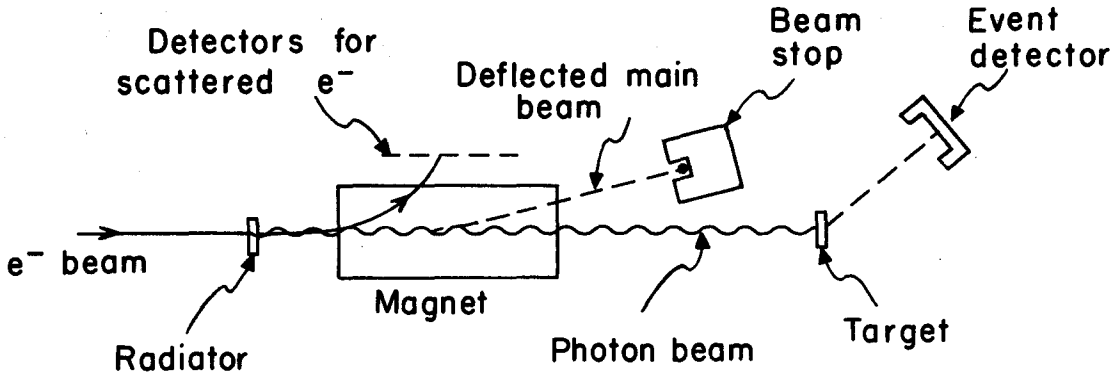

Fig. 1. "Tagging" real photons.

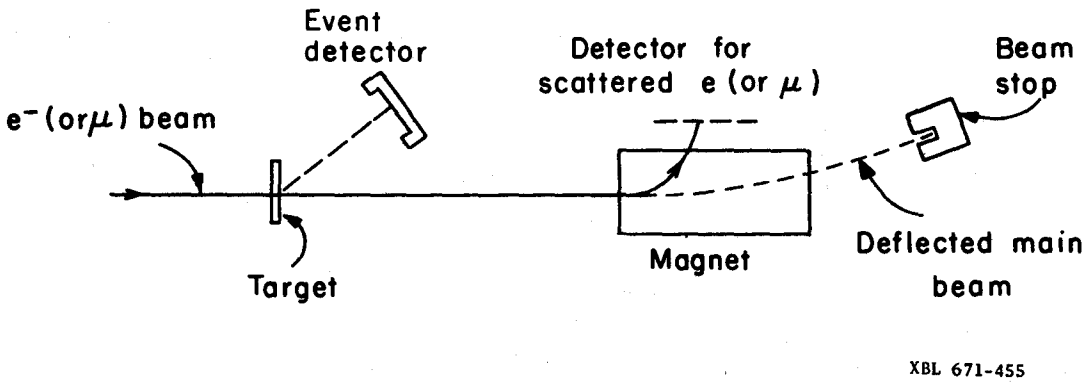

Fig. 2. "Tagging" virtual photons.

Since it will transpire that beam intensity is not a limitation on these experiments, we will consider the background random coincidence rate between the scattered electron counters and the "event" detector as a number of interest, and the event rate of desired events produced by a gamma ray in a small interval, dk, as a number to be kept constant.

We now present in tabular form a comparison between the random rates in the three cases, bearing in mind that the event rate and not the beam intensity is the independent variable. We note also that the principal count rate for scattered electrons accompanies bremsstrahlung with no nuclear process of interest. If we observe scattered muons, the principal rate accompanies nuclear events; bremsstrahlung is about one quarter of this rate. This causes the difference in the rate S (Eq. 6) between Cases 2 and 3.

Table I. Definition of variables.

	Symbol	Units
Beam intensity	N	sec^{-1}
Gamma-ray energy	k	
Radiation length of radiator material	X_o	$g\ cm^{-2}$
Target thickness	t	$g\ cm^{-2}$
Radiator thickness	R	$g\ cm^{-2}$
Number of molecules in a mole	$L=6x10^{23}$	g^{-1}
Atomic weight	A	
Cross section (maybe partial) for event of interest, which can trigger event counter	$\sigma(k)$	cm^2
Solid angle multiplied by efficiency for event of interest	Ω	(fraction of 4)
Count rate in scattered electron detector	S	sec^{-1}
Event rate of desired events	E	sec^{-1}
Total count rate in event detector	T	sec^{-1}
Background coincidence rate	C	sec^{-1}
Effective radiator for virtual photons (Eq. 3)	R_{eff}	$g\ cm^{-2}$
Total resolving time for coincidence (including duty cycle)	τ	sec

Case 1	Case 2	Case 3	
$E = N \frac{R}{X_o} \frac{dk}{k} t \sigma(k) \frac{\Omega L}{A}$	$N \frac{R_{eff}}{X_o} \frac{dk}{k} t \sigma(k) \frac{\Omega L}{A}$	$N \frac{R_{eff}}{X_o} \frac{dk}{k} t \sigma(k) \frac{\Omega L}{A}$ (Same as Case 2)	(4)
$T = N \frac{R}{X_o} t \frac{\Omega L}{A} \int_o^{k\,max} \frac{\sigma(k)dk}{k}$	$N \frac{R_{eff}}{X_o} t \frac{\Omega L}{A} \int_o^{k\,max} \frac{\sigma(k)dk}{k}$	$N \frac{R_{eff}}{X_o} t \frac{\Omega L}{A} \int_o^{k\,max} \frac{\sigma(k)dk}{k}$ (Same as Case 2)	(5)
$S = N \frac{R}{X_o} \frac{dk}{k}$	$N \frac{t}{X_o} \frac{dk}{k}$	$N \frac{t}{X_o} \frac{dk}{k} 4 \left(\frac{M_e}{M_\mu}\right)^2$	(6)
$C = T S \tau$			(7)
$= \tau N^2 \frac{R^2}{X_o} t \frac{\Omega L}{A} \frac{dk}{k} \frac{\sigma(k)dk}{k}$			(8)
$= \frac{E^2 \tau \left[\int_o^{k\,max} \frac{\sigma(k)dk}{k}\right]}{t\Omega (L/A)(dk/k)[\sigma(k)]^2}$	$\frac{E^2 \tau \left[\int_o^{k\,max} \frac{\sigma(k)dk}{k}\right]}{R_{eff} (L/A)(dk/k)[\sigma(k)]^2}$	$4\left(\frac{M_e}{M_\mu}\right)^2 \frac{E^2 \tau \left[\int_o^{k\,max} \frac{\sigma(k)dk}{k}\right]}{R_{eff}\, \Omega\, (L/A)(dk/k)[\sigma(k)]^2}$	(9)

We now note that these Eqs. (9) are identical in the two cases (1 and 2) if $R_{eff} = t$. If $t < R_{eff}$, tagging of virtual photons is preferable. For a liquid-hydrogen target, this corresponds to a target 20 cm long. With targets longer than this, tagging of real photons is preferable if only electron beams are available. Tagging of virtual photons with muon beams is always preferable.

We note that the count rate in the detector for scattered electrons (S) is given mainly by the probability for emitting gamma rays (except for Case 3) and not by a reaction of interest.

The random coincidence rate, then, represents the number of times two scattered electrons appear in the time interval for detection, and we cannot therefore identify the gamma-ray energy unambiguously. If we have detectors for the whole range of scattered electron energies, these confusing events can be identified at once by noting that two particles exist and, hence, can be ignored; otherwise, the usual delayed count must be made and the events subtracted from the undelayed, with the usual statistical problem.

We note, in passing, a feature about Eqs. (8) which has prevented frequent use of tagged photons. If either the solid angle Ω or the cross section σ is small, C becomes large. Until recently,[2] only small solid-angle detectors could be used. The advent of large solid-angle detectors (spark chambers) makes the technique of great utility.

ILLUSTRATIVE NUMBERS

Consider, for example, the measurement of a partial cross section for strange-particle production by 1-6 BeV photons in intervals dk/k of 0.05 over this range; $\sigma(k)$ is about 5 μb. We use a target of liquid hydrogen 20 cm long ($= 1.4\ g/cm^2$) which is about equal to R_{eff} ($R_{eff}/X_o \approx 0.023$). Here $\tau = 10^{-6}$ seconds (10^{-8} seconds with a duty cycle 1 in 100). We assume that the event counter detects no events with gamma-ray energies less than 1 BeV [$\sigma(k) = 0$ for $k < 1$ BeV]. Then for Cases 1 and 2 we obtain:

$$C = 70\ E^2/sec \quad .$$

So if E is one event in 10 minutes, $C/E = 1/6$, which is a tolerable random rate.

The requisite beam intensity, N, can be found from Eq. (4) and is 3.4×10^6 electrons per second (Case 2), and the same for Case 1 if the radiator thickness is the same as the target thickness in radiation lengths ($R/X_o = t/X_o$).

For muons, we find for one event in 10 minutes, $C/E = 10^{-5}$ which is negligible. The requisite muon rate is twice as big (7×10^6/sec) due to the change in R_{eff}.

Electron accelerators produce beams of about 10^{12} per second, so our earlier assumption that electron-beam intensities do not set the upper limit is confirmed. Muon beams have intensities of the order of 10^6/sec, so this is not now true for muons. We could increase the count rate for muons by using a

longer target or larger beam. Clearly, we could use muon beams up to 10^{11}/ sec and event rates in our example of 40 per second, without bad random rates. We could not, however, use a more intense electron beam. The comparison between muons and electrons is more favorable to muons if an accelerator (for example SLAC) with a poorer duty cycle than 10^{-2} is considered. For a duty cycle of 2×10^{-4}, τ becomes 5×10^{-5} sec and for T = 1/10 min C/E = 8 for Cases 1 and 2—an impossible situation. For muons, however, C/E remains tolerable at 5×10^{-4}.

As a second illustrative example, we consider a measurement of the total gamma-proton cross section, excluding pair production and other purely electrodynamic processes. The cross section is about 100 μb from 1 to 6 BeV. This measurement could also involve taking spark-chamber pictures of each event.

We can identify the event by either of two methods. First, we can count any charged particle produced at a large angle, such that low-momentum-transfer pair production is excluded. Second, we can use an anticoincidence method. The event detector, a total-energy gamma-ray shower counter in the forward direction, can detect either gamma rays or electron-positron pairs produced in the absorber. The event is then identified by the presence of a scattered electron and the absence of a gamma-ray or electron-positron pair.

Again consider a hydrogen target 20-cm long, and tag photons in intervals dk/k of 0.05 from 2 BeV to 6 BeV. We assume $\sigma(k)$=100 μb from 400 MeV to 6 BeV. Then for an event rate of 1/sec for each channel, we find that

$$\frac{\text{chance coincidence rate}}{\text{event rate}} = 6.5\% \qquad \text{Case 1}$$

$$\frac{\text{chance coincidence rate}}{\text{event rate}} = 6.4\% \qquad \text{Case 2}$$

$$\frac{\text{chance coincidence rate}}{\text{event rate}} = 1.3 \times 10^{-3}\% \qquad \text{Case 3}$$

The beam intensitites required are about 10^7/sec in all cases.

Note that in the example chosen here, the target is longer than R_{eff} and Case 1 offers a more favorable choice than Case 2. There may, however, be problems about the spread of gamma-ray energies due to the shower production.

It is worth noting that for a duty cycle of 2×10^{-4} (SLAC), this experiment could be operated with a count rate of 1/10 sec and a chance-to-event rate of 30%. An experiment of this type has in fact been proposed (Group D - SLAC). At SLAC, however, the use of a muon beam would be particularly advantageous.

ELECTRON TAGGING WITH LOW-MOMENTUM-TRANSFER CUTOFF

For completeness we note an alternative procedure to make tagging of virtual photons attractive. Muons are attractive because low-momentum-transfer events (which predominate in bremsstrahlung) are automatically

suppressed and do not appear in the scattered electron counting rate, S. Hand[6] has suggested a method of accomplishing the same result using electrons. He proposes blocking from the scattered electron detector those electrons scattered at very small angles $\theta \lesssim m/E$, and allowing only those with $\theta \gtrsim 5\ m/E$ to reach the detector. This achieves artificially, but messily, the same suppression of low-momentum-transfer events as achieved by the use of muons. However, beams of electrons are more easily available and more intense than beams of muons, so that this method has considerable merit.

INELASTIC ELECTRON SCATTERING AT LARGE-MOMENTUM TRANSFERS

The procedure discussed above integrates over all scattered electron directions. We may wish not to do this, and if we do not we obtain an inelastic-electron-scattering experiment. Now the question of minimizing the background amounts to minimizing the radiative correction. This depends on the factor log (q^2/m^2), which varies only slowly between electrons and muons since q^2 is now kept constant. The advantage of muons rests solidly in limiting the number of gamma rays and electrons produced in other directions than that seen by the detector and, hence, indirectly influencing the background.

RADIATIVE CORRECTIONS IN TAGGING

There remains a possibility that two gamma rays are produced in the radiation process, or, for the virtual process, a real gamma ray emitted in addition to the nuclear process. Either of these occurrences would result in an incorrect identification of the gamma-ray energy from Eq. (1). The probability of a double radiation process, relative to a single radiation process, is

$$\frac{2\alpha}{\pi} \ln (E/m) \quad .$$

If the radiator thickness is increased, these radiative processes which occur for zero target thickness will be made worse by degradation of the incident electron beam. By using the same ideas of virtual photon theory which formed the main argument of this note, we can see that the probability of two-photon emission will be double the probability for zero radiator thickness, when the thickness or radiator R equals the value given by $R/X_o = 2\alpha/\pi \ln (E/m)$, and will increase in proportion to R.

For Case 2 (virtual photon tagging) we must not increase the target thickness much more than this amount either, or there will be real bremsstrahlung in addition to the nuclear process. For Case 3, virtual photon tagging with muons, the problem is almost nonexistent because of the low probability that the muon will radiate.

ACKNOWLEDGMENTS

This report is written to make clear to the authors and collaborators some of the points at issue; the understanding of them derives from many discussions over the last three years with Professors L. N. Hand and Walker and Mr. T. M. Knasel. The authors are, therefore, not sure whether any statement

is original; however, we believe they have not before been clearly written.

References

1. J. W. Weil and B. D. McDaniel, Phys. Rev. 92, 391 (1953).

2. D. O. Caldwell, J. P. Dowd, K. Heinloth, and M. D. Rousseau, Rev. Sci. Instr. 36, 283 (1965). Previous uses of photon tagging are listed here.

3. E. J. Williams, Kgl. Dansk. Videnskab. Selskab 13, No. 4 (1935).

4. R. H. Dalitz and D. R. Yennie, Phys. Rev. 105, 1598 (1957).

5. L. N. Hand and Richard Wilson, Inelastic Electron-Proton, Positron-Proton, and Muon-Proton Scattering, in 1963 Summer Study Report, SLAC 25, vol. II, pp. 1-30.

6. L. N. Hand, Electroproduction at SLAC, in 1963 Summer Study Report, SLAC 25, vol. II, pp. 31-68.

SOME ELECTRON-PHYSICS STUDIES WITH THE 200 BeV ACCELERATOR

W. Selove

In this note, I describe rough estimates of flux intensities for some electron and photon beams of simple design, and comment on the usefulness of these beams for some experiments to test Quantum Electrodynamics (QED).

1. Electron-flux intensity for a simple beam. We consider as an example of a possible beam of interest one with a few percent momentum resolution at 100 BeV/c. We estimate here the energy spectrum for an electron beam at 0 deg, produced by converting the γ-ray flux coming from the decay of π^0 mesons produced in a target in the primary proton beam. A crude representation is given in Fig. 1.

One finds that for such an electron beam, the γ and π^0 energies which principally contribute to the final intensity lie in bands slightly higher than the final electron energy--about 0 to 20 BeV higher, for a 100-BeV electron beam. For these conditions, the angles between the directions of the π^0 and the resulting γ, and between the γ and the resulting e, are very small compared with the angular breadth of the initial π^0 production, and therefore we can make a very simple estimate of the final electron intensity without the necessity for complicated angular integrations.

We hence write, for 0-deg production:

$$\frac{d^2N_\gamma(p_\gamma)}{dp_\gamma\, d\Omega} = \int_{p_\gamma}^{\infty} \frac{2}{p_{\pi^0}} \frac{d^2N_{\pi^0}}{dp_{\pi^0}\, d\Omega}\, dp_{\pi^0}, \tag{1}$$

and a similar expression for the next conversion, $\gamma \to e$. In (1), the factor 2 corresponds to the fact that there are two gamma rays from each π^0; the $2/p_{\pi^0}$ gives the differential spectrum of γ's from a π^0 of momentum p_{π^0}.

Taking $d^2N/dp_{\pi^0}\, d\Omega$ from Ref. 1 (p. 44) and approximating it in the region p_{π^0} just above 100 BeV/c by

$$\left.\begin{aligned} \frac{d^2N_{\pi^0}}{dp_{\pi^0} d\Omega} &\approx N_0 \exp(-ap_{\pi^0}) \\ \text{with } a &\approx 1/(20\ \text{BeV/c}), \end{aligned}\right\} \tag{2}$$

we find that

$$\left(\frac{d^2N_\gamma}{dp_\gamma\, d\Omega}\right)_{E_\gamma = 100\ \mathrm{BeV/c}} \approx \frac{2 \cdot 20}{115} \frac{d^2N_{\pi^0}}{dp_{\pi^0}\, d\Omega}. \qquad (3)$$

In (3) the 20 represents 1/a, and the 115 represents the effective value of the $1/p_{\pi^0}$ factor in (1) integrated with the approximation (2). Thus

$$\frac{d^2N_\gamma}{dp_\gamma\, d\Omega} \approx \frac{1}{3} \frac{d^2N_{\pi^0}}{dp_{\pi^0}\, d\Omega} \text{ at 100 BeV/c.} \qquad (4)$$

Similarly, if we convert these γ's using a converter of t radiation lengths (the optimum value of t for a high-energy electron beam would be about 1), we get in a thin-converter approximation

$$\frac{d^2N_e}{dp_e\, d\Omega} \approx \frac{t}{6} \frac{d^2N_\gamma}{dp_\gamma\, d\Omega} \text{ at 100 BeV/c.} \qquad (5)$$

Thus finally,

$$\frac{d^2N_e}{dp_e\, d\Omega} \approx \frac{t}{20} \frac{d^2N_{\pi^0}}{dp_{\pi^0}\, d\Omega} \text{ at 100 BeV/c.} \qquad (6)$$

That is, using a radiator of about 1 radiation length, one will obtain at 100 BeV/c an electron flux about 5% of the π^0 flux.

Using calculated beam intensities for charged particle beams (Ref. 1, p. 291), and estimating the π^0 flux from the primary target as being at least as large as the π^- flux, we conclude that in a beam made as discussed above, the intensity of e^+ or e^- in a few-percent momentum band at 100 BeV/c would be about one-twentieth of the π^- intensity, or about a few times 10^6 electrons/sec. (This is for a solid angle of about $4 \cdot 10^{-6}$ sr; several times as much intensity could be obtained by using a greater solid angle.)

2. Electron flux intensity for a somewhat purified beam. The beam of Fig. 1 would contain many more hadrons than electrons. The relative number of hadrons can be cut down in two simple ways. (a) Use a sweeping magnet

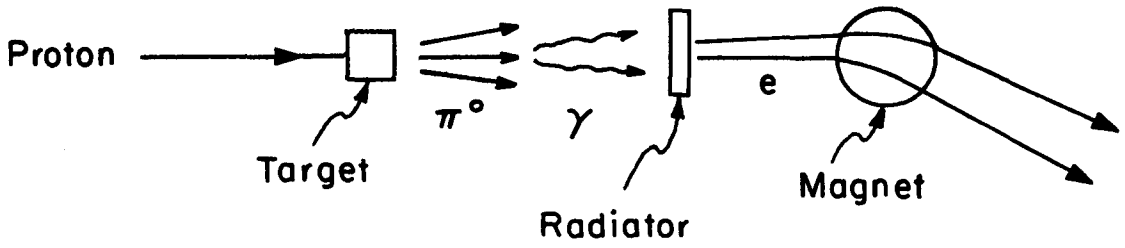

XBL671-344

Fig. 1. Illustration of the type of beam discussed in the text.

between the target and the radiator (Fig. 1). (b) In the final momentum-analyzed electron beam, insert a beam purifier, an attenuator which attenuates hadrons more than electrons. The only such attenuator I have thought of is one made of deuterium. (Tritium would be even better, but the improvement may not be worth the safety hazard; these hydrogen isotopes must be used in the form of liquid--or perhaps high-pressure gas -- for an attenuator of this kind.)

With these refinements, one can estimate that an electron beam can be obtained of purity corresponding to about one electron to one hadron, and of intensity perhaps 1/2 to 1×10^6 electrons/sec in a momentum band of a few percent at 100 BeV/c. The source at the radiator would be 1 to 2 inches in diameter, depending on how close one could put the radiator to the target and still sweep charged particles away between the two.

At 50 BeV/c, a flux several times as great (in a few percent momentum band) could be obtained.

3. Photon flux intensities. From Eqs. (4) and (6) above, the continuous photon spectrum will have an intensity approximately 10 times the electron intensity. Thus within a cone of about 1 mr from the primary proton beam direction, the photon intensity at 100 BeV/c will be about 10^7 photons/sec per BeV/c.

This photon flux will be accompanied by a neutron flux about 10 times as strong, at 100 BeV/c.

A more pure photon beam, free of neutrons, can be produced by using a magnetically deflected electron beam to make photons. In this case, however, the flux will be no more than about 10^4 photons/sec per BeV/c, at 100 BeV/c.

Finally, monochromatic photon beams can be made by positron annihilation, and tagged photon beams by bremsstrahlung. For these types of beams, the intensities will be lower still.

4. Some QED experiments with these beams. I remark here on a few experiments for which the above beams might be used.

(a) Positron annihilation. With a positron intensity of 10^6/sec, at 100 BeV/c, and a reasonable hydrogen target (1 to 10% of a radiation length), there would be 10 to 100 annihilations per second. With a reasonable detection geometry, this would permit measuring the angular distribution for annihilation in reasonably narrow bins [$\Delta(\cos\theta) = 0.2$], with an actual counting rate in the weakest bin of several tens of events per hour.

Positron annihilation at 100 BeV/c is equivalent to a colliding $e^+ - e^-$ interaction with two 220-MeV/c beams. Colliding-beam positron-electron experiments will soon be carried out with much higher energies. However, it may well be worthwhile to measure the annihilation directly, so as to get a

direct measurement of the absolute cross section.

(b) Wide-angle pair production (WAPP) and wide-angle bremsstrahlung (WABR). The more intense of the photon beams described above will probably permit a measurement of WAPP at 100 BeV/c. It is not possible to give a detailed calculation of counting rate without a detailed experimental design, but a crude estimate can be obtained by making a comparison with figures from existing experiments. The flux given here, $\approx 10^7$/(sec-BeV/c), is about 10^{-3} of the flux used by Asbury et al.[2] As a function of electron 4-momentum-squared, u, and of beam momentum, p, the effective cross section that can be obtained can be expected to vary at a rate, depending on the experimental geometry, between p/u and 1/p; thus going from 4 or 5 BeV/c (Ref. 2) to 100 BeV/c might increase the cross section at fixed u by about 20. It seems likely that the photon intensity will be sufficient to permit WAPP, with useful statistical accuracy (≈10%), for values of |u| appreciably larger than those so far tested.

The electron intensity would be somewhat lower, and so WABR experiments at correspondingly large values of |u| might be marginal. It would nevertheless be important to try to do WABR as WAPP--the latter tests for large space-like values of |u|, and the former tests also for large time-like values. No WABR experiment has yet been carried out successfully (although one is being attempted at Frascati).

References

1. 200-BeV Accelerator: Studies on Experimental Use: 1964-1965, Vol. I, UCRL-16830, April 1966, pp. 44 and 291.

2. J. G. Asbury, W. K. Bertram, U. Becker, P. Joos, M. Rohde, A. J. S. Smith, S. Friedlander, C. Jordan, and C. C. Ting, Phys. Rev. Letters 18, 65 (1967).

PHOTON AND ELECTRON BEAMS AT THE 200 BEV PROTON ACCELERATOR

C. A. Heusch

INTRODUCTION

In these notes we have collected a number of considerations that bear on the possibility of using the 200-BeV proton accelerator as a source of photon and electron beams. We are primarily concerned with the questions of whether the setting up of such beams can be expected to be feasible, and have reasonable intensities and spectral characteristics.

As to the motivation for the actual building of an electron-photon facility, should it prove practically realizable, a subsequent note[1] reviews some of the questions presently of interest in photon physics that may or may not be solved by the 20-BeV SLAC (and its probable 40-BeV extension). Any such study in futurism can be only lightly conjectured. Only the crudest extrapolations make target yield estimates at 200-BeV possible; and what problems physicists will be facing 8 or 10 years from now is obviously a wide-open question. Still, certain features appear discernible now, beyond years of operation of SLAC and the various electron storage-ring projects.

We will, therefore, focus our interest on beams with energies greater than 40 BeV. Certain experiments at lower energies will be of interest because of the excellent duty-cycle characteristics of this machine ($\approx$20% compared with 10^{-4} at the SLAC); it will be seen that there is a large number of lower-energy photons available for such contingencies, although we will not present any details of this aspect.

Above 40 BeV, however low the intensities, this will be the only machine source of photons and electrons; and although the yield will be seen to compare unfavorably with our present electron accelerators, it should be remembered from the start that the use of large-solid-angle detection devices can, in the presence of a long beam dump, recover some of the loss.

GENERALITIES ABOUT BEAMS

It will be seen that the electron and photon yields from pp or p-nucleus interactions result mainly from secondary mechanisms, and that conversion and reconversion, $e \rightarrow \gamma \rightarrow e \rightarrow \ldots$, are the prime means of beam purification. Let us

therefore have a look at some facts about changes in intensity and spectral characteristics with which we have to live.

The primary yield of γ's and e's in a pp collision is relatively small; production of π^0 and subsequent decay dominate. For a monochromatic π^0 source, the decay photon spectrum is (see Fig. 1):

$\underline{\pi^0 \rightarrow \gamma\gamma}$

$$N_\gamma(k)dk \approx \frac{dk}{E_{\pi^0}} = \text{const. } dk \qquad (1)$$

$$\text{with the condition } \int N_\gamma(k)dk = 2N_{\pi^0},$$

where N_γ is the number of photons per unit energy interval and k is the photon energy. To the lowest-order approximation, the conversion of a photon looks the same (Fig. 2), viz,

$\underline{\gamma \rightarrow e^+e^-}$

$$N_{e\pm}(E_\pm)\, dE_\pm \approx \frac{1}{k}\, dE_\pm, \qquad (2)$$

with the normalization

$$\int N_{e^+}\, dE_+ = \int N_{e^-}\, dE_- = N_\gamma.$$

The bremsstrahlung process has, to lowest order, the well-known logarithmic shape (Fig. 3):

$\underline{e \rightarrow e'\gamma}$

$$N_\gamma(k)\, dk \approx \frac{dk}{k}. \qquad (3a)$$

Note that both changes in spectral composition as represented by Eqs. (2) and (3) deplete the high-energy end of the spectrum, the bremsstrahlung process much more strongly than pair production.

As a realistic example, consider a spectral region of the primary photon yield which can be approximated, over an interval, by a linear energy dependence Take

$$N_\gamma\, dk \approx (a - bk)\, dk. \qquad (3b)$$

If these photons pass through a converter and give rise to pair production, the emergent electrons will have a spectrum [according to Eq. (2)] given by

$$N_\pm\, dE_\pm \quad [a \ln(k_{max}/E_\pm) - b(k_{max} - E_\pm)]\, dE_\pm. \qquad (3c)$$

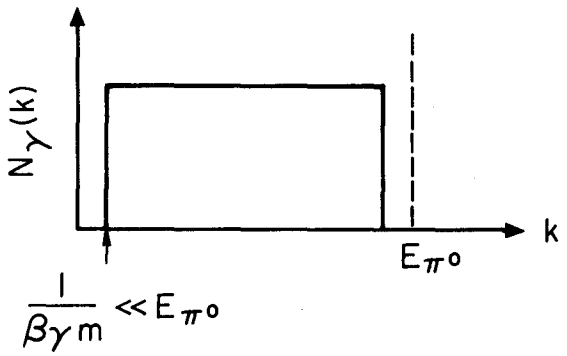

Fig. 1. Photon spectrum for $\pi^0 \rightarrow \gamma + \gamma$.

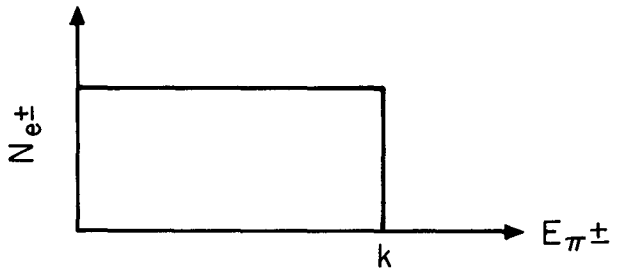

Fig. 2. Electron spectrum from pair production.

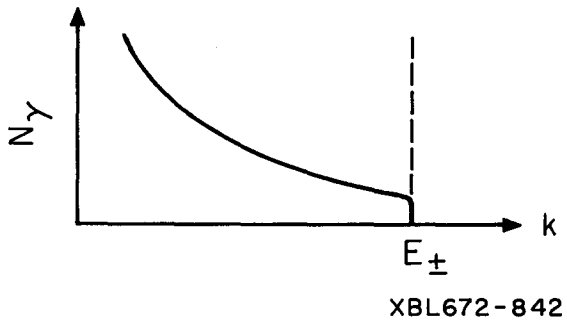

Fig. 3. Photon spectrum from bremsstrahlung.

If we use $a = 10$ and $b = 0.07$ we can crudely approximate the γ flux at about 0° for energies greater than 100 BeV. If we are then interested in the photon flux between 100 and 110 BeV, the intensity loss we suffer by going from photons to electrons is (for a radiator thickness of 1 radiation length) measured by the fact that 23 photons will give rise to 4 electrons, or a reduction in flux to about 17%. This is an important fact we have to keep in mind.

By choosing convenient converter and radiator materials as well as advantageous kinematical regions, we will nevertheless be able to enrich primary beams, both photons and electrons, by means of these processes.

TARGET YIELDS

In the absence of any substantiated yield calculations for 200-BeV proton-nucleon collisions, we base our yield estimates for electrons and photons on Trilling's flux parametrization;[2] very recent independent estimates of Hagedorn and Ranft[3] appear to be in rough quantitative agreement with these estimates. For further reference, we show, in Figs. 4(a) and 4(b), the normalized π and proton yields as given by Trilling[2] for an incoming proton momentum of 200 BeV/c.

Note that the proton yield is peaked at high energies, whereas the pion yield slopes off quasi-exponentially towards the upper energy limit and becomes very small there.

For further reference, we will make the following simplifying assumptions: The neutron yield has the same spectral distribution as the protons, with a multiplicity smaller, but of the same order. Neutral π mesons are emitted with a yield $(N_{\pi^+} + N_{\pi^-})/2$ (positive and negative pion yields are different because of the isobar production mechanism considered by Trilling[2]); K mesons have spectral distributions like the pions, with a yield of about one-tenth that of the pions. Antiproton yields have been estimated by Keefe et al.[4] They are approximately one-tenth of the π yields at corresponding energies and angles. All other target products will be disregarded. Given the crudeness of our knowledge of π and nucleon yields, these assumptions do not appear restrictive.

In calculating the photon and electron yields, we make the further assumptions that (a) all photons originate in $\pi^0 \rightarrow 2\gamma$ decay, and (b) the decay photons will be emitted in the forward direction of the π^0. This latter assumption leads to an error in angular distribution which is characterized by the decay angle containing half of all the photons, viz,

$$\frac{\theta_{\gamma\gamma}}{2} = \arcsin\frac{m}{E} = \begin{cases} 1.17 \text{ mrad for } E_{\pi^0} = 120 \\ 2.33 \text{ mrad for } E_{\pi^0} = 60 \end{cases} \text{(BeV)}.$$

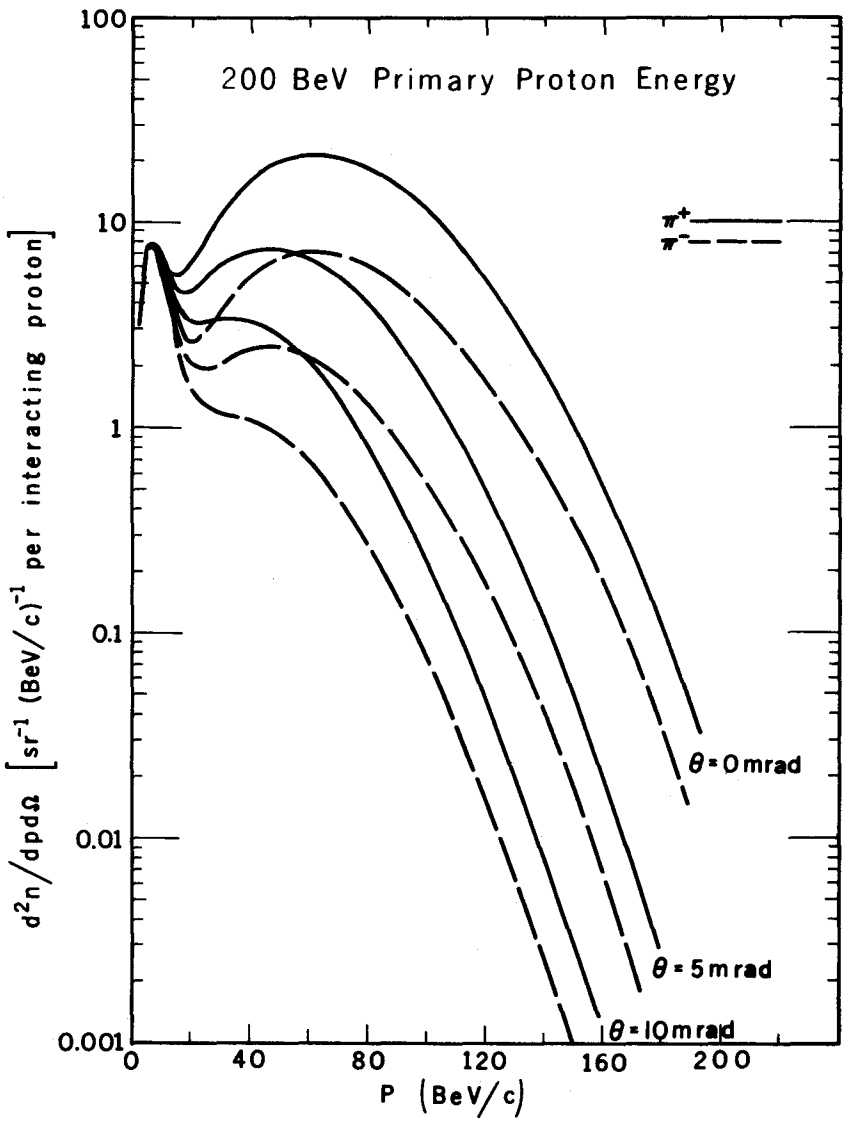

Secondary Pion Momentum Spectrum
per Unit Solid Angle

MUB-6401

Fig. 4. Estimates, according to Trilling, of yields from 200-BeV proton collisions for (a) secondary pions and (b) (opposite page) protons (see UCRL-16830, Vol. 1). (a) Secondary pion momentum spectrum per unit solid angle.

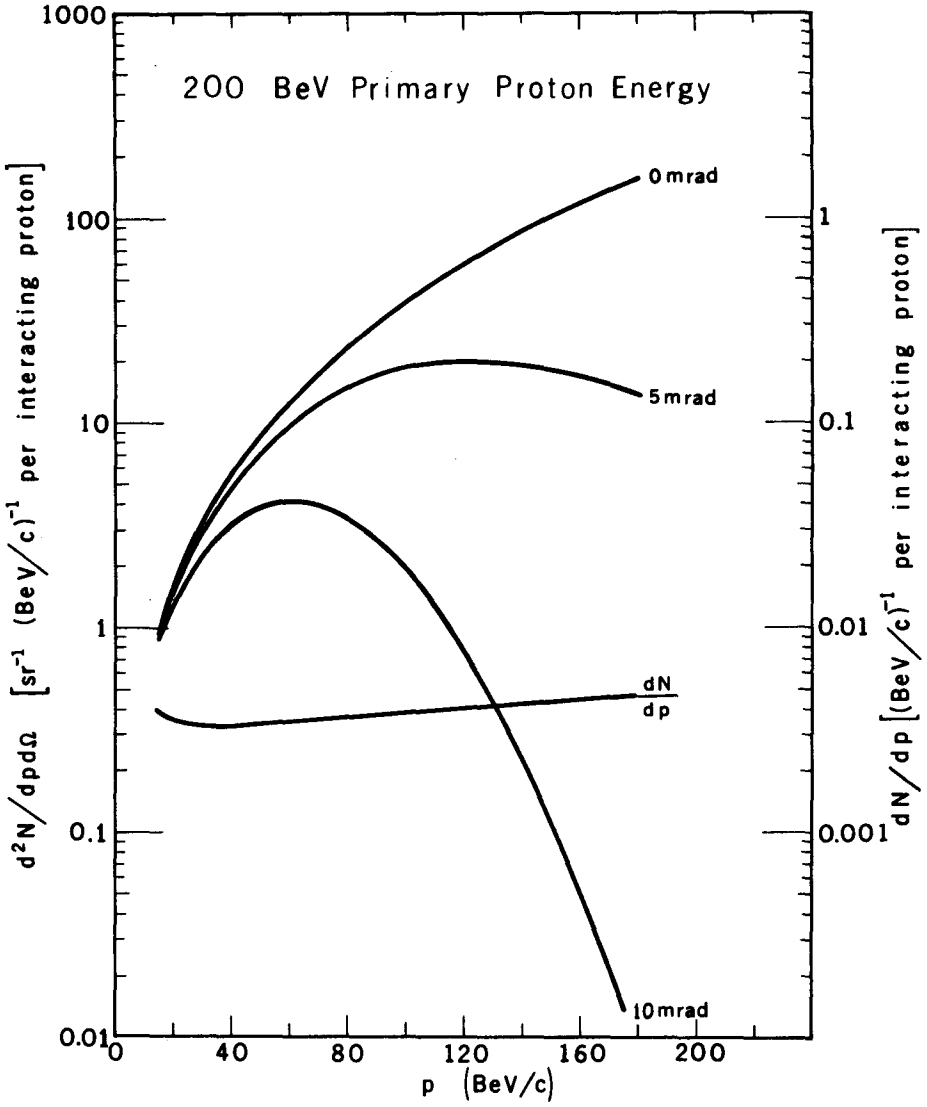

Secondary Proton Momentum Spectrum

MUB-6403

Fig. 4(b). Secondary proton momentum spectrum.

It is seen that the effect will be small since any physical aperture will be of this order and will therefore average over a comparable angular bin. (c) We neglect π^0 reabsorption in the nucleus, and (d) we do not consider γ conversion in the target (see below).

With these assumptions, we obtain for the photon yield per interacting proton

$$\frac{d^2N}{dk\,d\Omega} = 2\left[\frac{a}{A^2}\, e^{-Ap}(Ap+1) - \frac{d}{2f}\, e^{-fp(p+2h)} + \frac{dh}{\sqrt{f}}\, e^{fh^2}\,\frac{\sqrt{\pi}}{2}\,\mathrm{erf}\,\{\sqrt{f}(p+h)\}\right]_{p=k}^{p=p_B}, \quad (4a)$$

where the angular dependence is given by

$$A = b + c\theta^2$$
$$h = \frac{g\theta}{2f}, \quad (4b)$$

and the numerical factors are

$$a = 1.65$$
$$b = 0.34$$
$$c = 36.8$$
$$d = 1.04\times10^{-2}$$
$$f = 2.6\times10^{-4}$$
$$g = 3.9$$

Here p is the momentum of the decaying π^0's and p_B the incident proton momentum.

The structure is obviously that of Trilling's π yield formulas, with the first term dominating at low p momentum, and the second and third stemming from the decay of high-energy pions (the third term is zero at $\theta = 0$ mrad). Figures 5 and 6 show the part of the spectrum which is of interest to us; Fig. 5 gives the energy dependence and shows the expected depletion of the high-energy end, with a strong enhancement at lower energies (very large amounts of 10 through 50-BeV photons will be available). The strong peaking in the forward direction is seen in Fig. 6. Note that a comparison with Fig. 4(a) shows a reduction of γ yield vs π yield at 0 deg of order 3 at 120 BeV; 10 at 180 BeV; and 1 at 60 BeV.

If instead of photons, we want to extract electrons from the primary target, we take as the only sources (a) Dalitz decays of π^0's (this spectrum follows directly from the one shown in Figs. 5 and 6); and (b) π^0 decay photons which convert within the target. A look at Table I shows that for maximum photon yield we will choose a material with λ/X_0 small (e.g., liquid hydrogen). For maximization of electron yield, we take λ/X_0 large (e.g., Al). This makes photons originating in the target traverse a mean of $0.25\,X_0$ ($\approx$20% conversion)

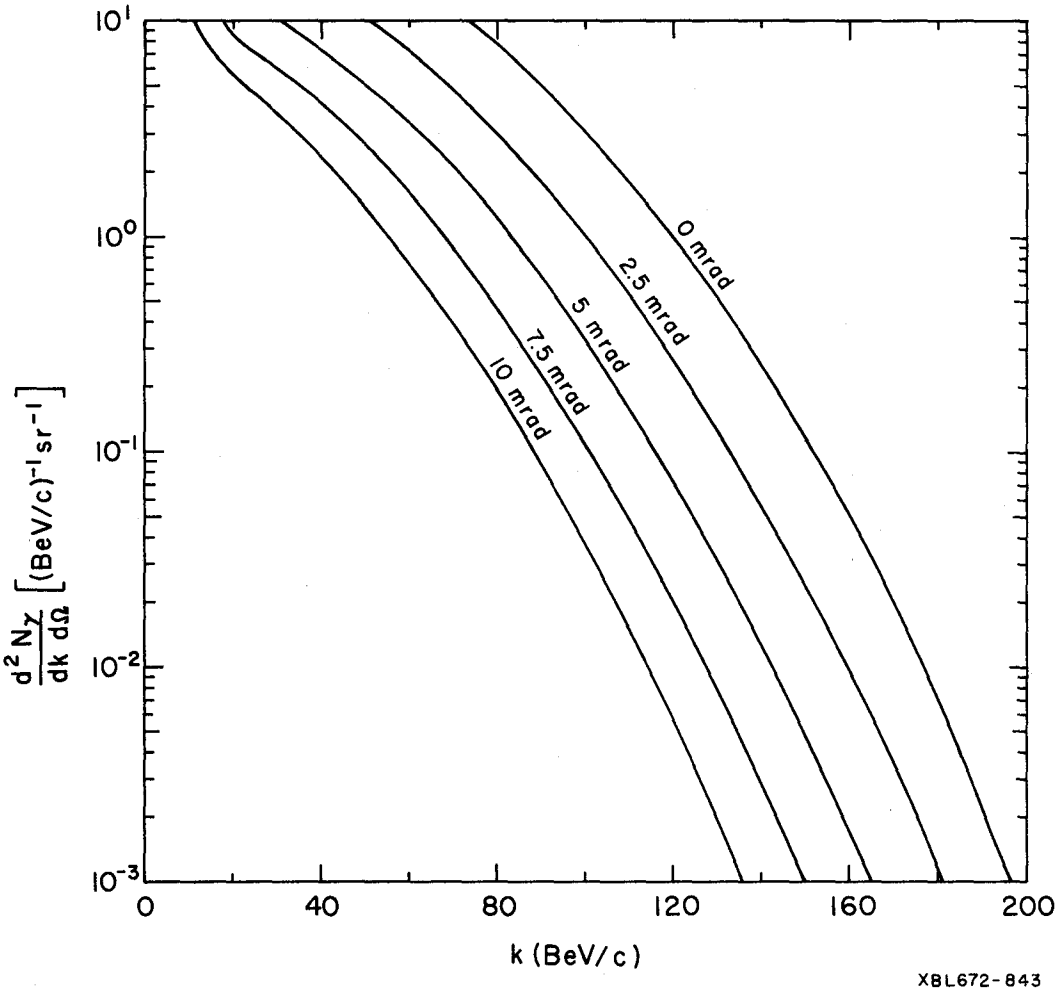

Fig. 5. Estimate of photon yield, per interacting proton, from 200-BeV pp collisions. See Eq. (4a).

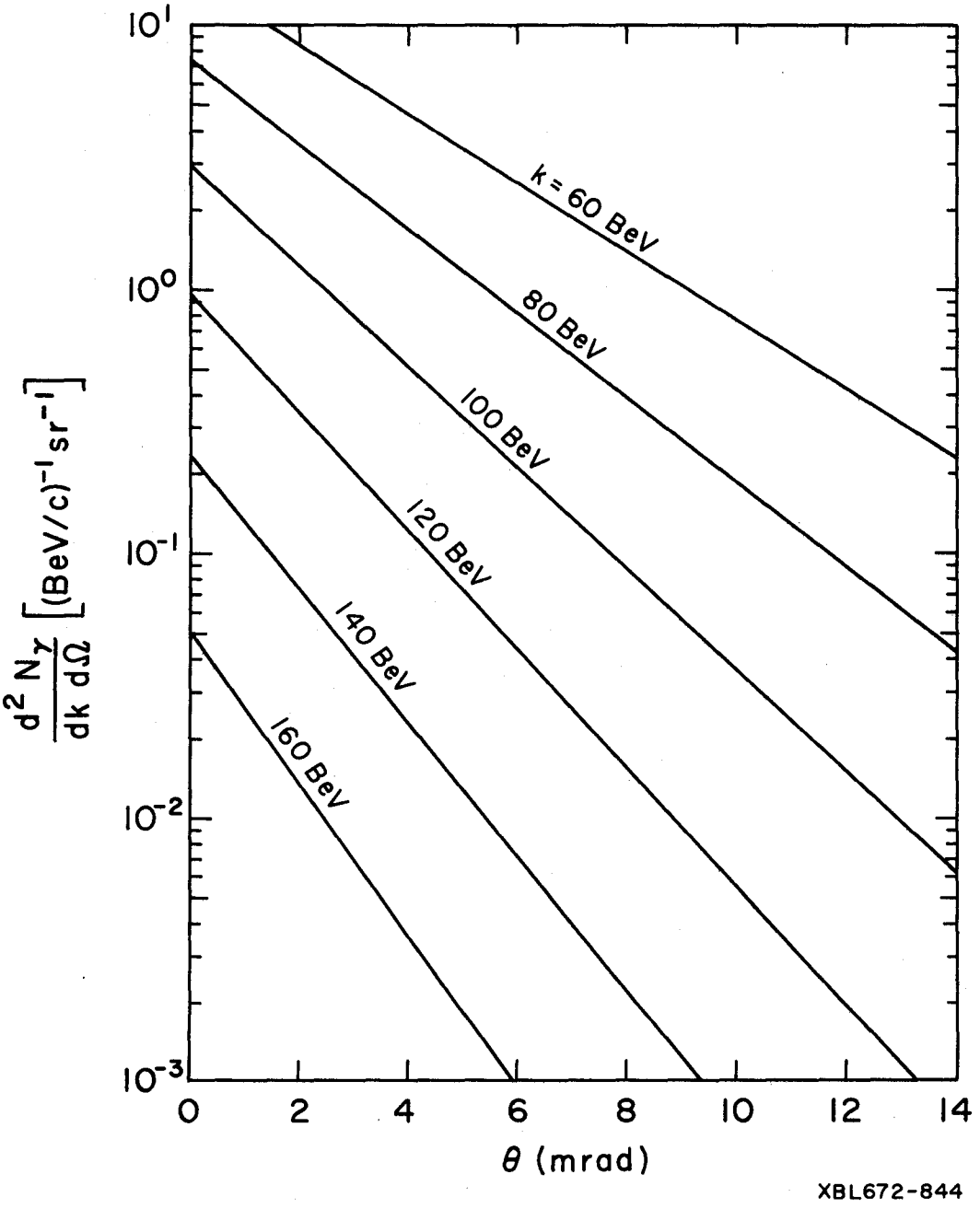

Fig. 6. Angular dependence of photon yield from 200-BeV pp collisions. See Eq. (4a).

in the first case, $2.5\,X_0$ (≈80% conversion) in the second. In the second case, the electron component stemming from γ conversion in the target has a depleted upper spectral region according to Eqs. (3a, b). Although total γ and $e^{\pm}$ yields are comparable from these two schemes, the primary electron beam will be suitable for lower energy experimentation mainly.

Table I. Geometric mfp and radiation length for various target materials.

Target material	λ(cm)	X_0(cm)	λ/X_0
H_2 (liq.)	470	820	≈ 0.5
Be	37.7	34.7	≈ 1
C	33.1	18.5	≈ 2
Al	36.9	8.9	≈ 5
Cu	14.8	1.3	≈ 10
Pb	17.4	0.58	≈ 30

Primary targeting facilities should be such that for a firm, fixed beam setup of the neutral beam, the minimum angle can be varied from 0 to ≈ 15 mrad. This can be achieved by a sequence of magnets upstream from the target, which will be able to sweep the external proton beam into the target at angles varying from ≈ 0 to 1 deg (see Fig. 7). Since the entire yield of interest to neutral beam users is contained within a cone of ≈20-mrad opening angle, this will make beam setups vastly simpler. In the following, we will assume that this angular range is accessible.

SECONDARY BEAMS

When the emission angle is assumed to vary from 0 to 15 mrad without movement of the physical beam aperture, the two principal secondary beams will be the photon and electron beams illustrated diagrammatically in Figs. 8(a) and 8(b). If not specifically desired, it is not advisable to set up an e^+ beam for reasons of beam contamination (see below). It is seen that only minor adjustments have to be used in order to switch from the photon to the electron beam.

Photon Beam

Consider a setup with a typical quadrupole angular aperture of ±1.5 mrad. (Quadrupoles of this aperture will be available, and bending magnets will have larger acceptance angles.) Then, as an example, consider a liquid-hydrogen target of thickness $t = \lambda$. Suppose we are interested in photons in the interval

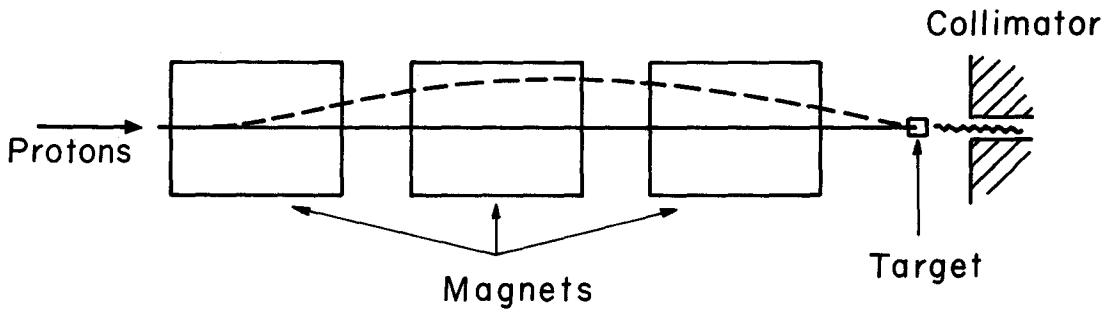

Fig. 7. A way of varying the production angle observed by a fixed neutral beam collimator hole.

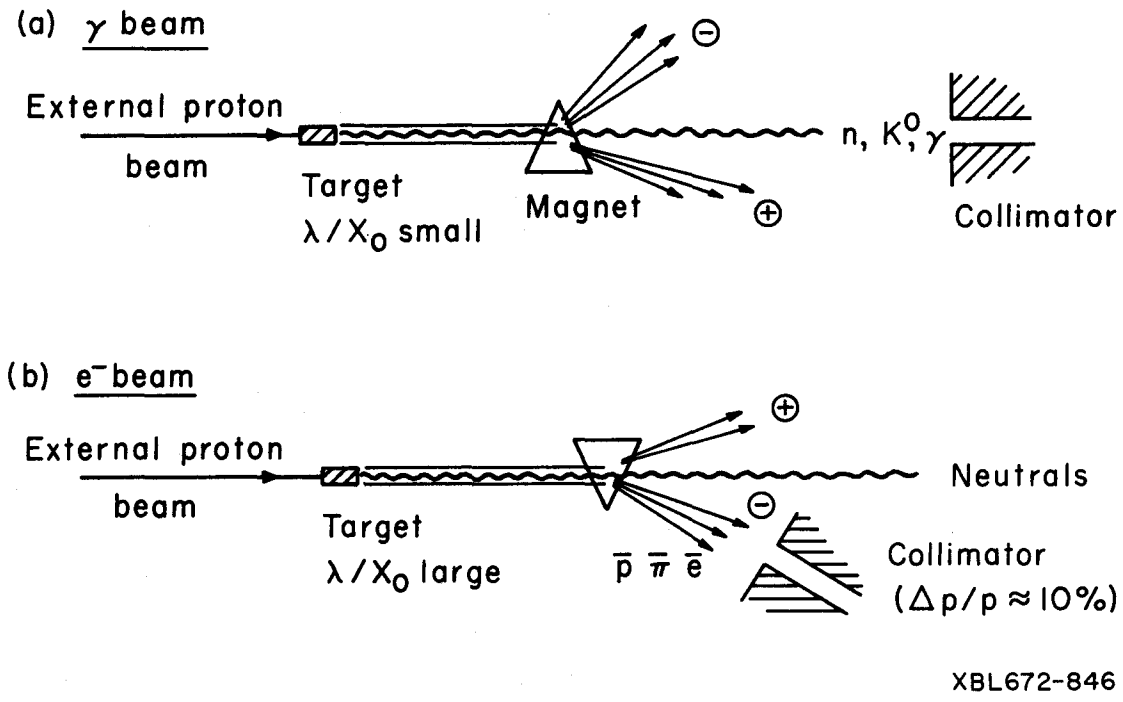

Fig. 8. Schematic representation of realization of (a) photon beam and (b) electron beam.

$100 \leq k \leq 110$ BeV. At 0 mrad $\leq \theta \leq 1.5$ mrad, Fig. 6 shows an average yield of approximately 1.5 $sr^{-1}(BeV/c)^{-1}$. Thus the flux accepted into the assumed angular aperture is about $1.5\times10^{-5}\times10\times3\times10^{13}\approx5\times10^{9}$ per beam spill. At 10 BeV it will be 20 times as great.

A glance at Fig. 4(b) shows that this appreciable beam is contaminated strongly by neutrons: The total ratio of neutrons to photons of energy >100 BeV is of order 2000. The beam is therefore not suited for most experimental use. A conversion, with subsequent momentum analysis, yields (see Fig. 9) a negatively charged beam with 5×10^{8} e^-, 2×10^{9} π^-, and about 10^{8} $\bar{p}$ in a momentum band $100 \leq p \leq 110$ BeV/c. Reconversion to photons finally, in conjunction with electron detection devices and shower counters to tag photon energies, plus a differential Cerenkov counter upstream from the radiator, leaves us with a respectable γ beam of $\geq5\times10^{7}$ photons per pulse (dependent on the electron momentum bite accepted by the tagging bank) in the region between 80 and 110 BeV. For large solid-angle detectors, this leads to a sizable event rate in many reactions of interest. Main contaminants will be about 10^{7} neutrons (from $\bar{p}p$ annihilation in the radiator). We have assumed that we are able to shield against scattered primary neutrons.

Similarly, one can estimate beam intensities at various angles; at larger angle, the integrated neutron flux going through the first radiator is much smaller [cf. Fig. 4(b)], making $\approx$ 10 mrad a preferable beam angle for a purer beam, if intensity is not a major problem.

At 50 through 60 BeV, beams of as much as approximately 10^{10} photons per spill seem feasible.

Electron and Positron Beams

In a like fashion, we have estimated the intensity of primary electron beams and their secondaries. With a copper or aluminum target of 1 nmfp thickness, about 80% of all photons will be converted into electrons. With a rough depreciation factor of $\approx$10 for the upper spectral region (and with the loss of electrons in the target disregarded), the beam will contain, per secondary electron, around 100 BeV, 20 π^-'s, 2p^-'s, and 2 K^-'s. Assuming the charge-exchange cross section $\pi^-p\rightarrow\pi^0n$ to be negligibly small at these energies, we see that the photon yield from this beam will be contaminated, upon further conversion in a ($1X_0$, 1/30 λ) radiator, by about 10 to 20 neutrons and antineutrons per tagged γ ray, a ratio which at low general intensities should not pose any problems.

The overall intensity of the primary electron beam is of order 10 below the γ beams in the upper spectral part, of order 2 below at about 60 BeV. Conversion and reconversion to a clean electron beam leads to small intensities (of order $< 10^{6}$/pulse).

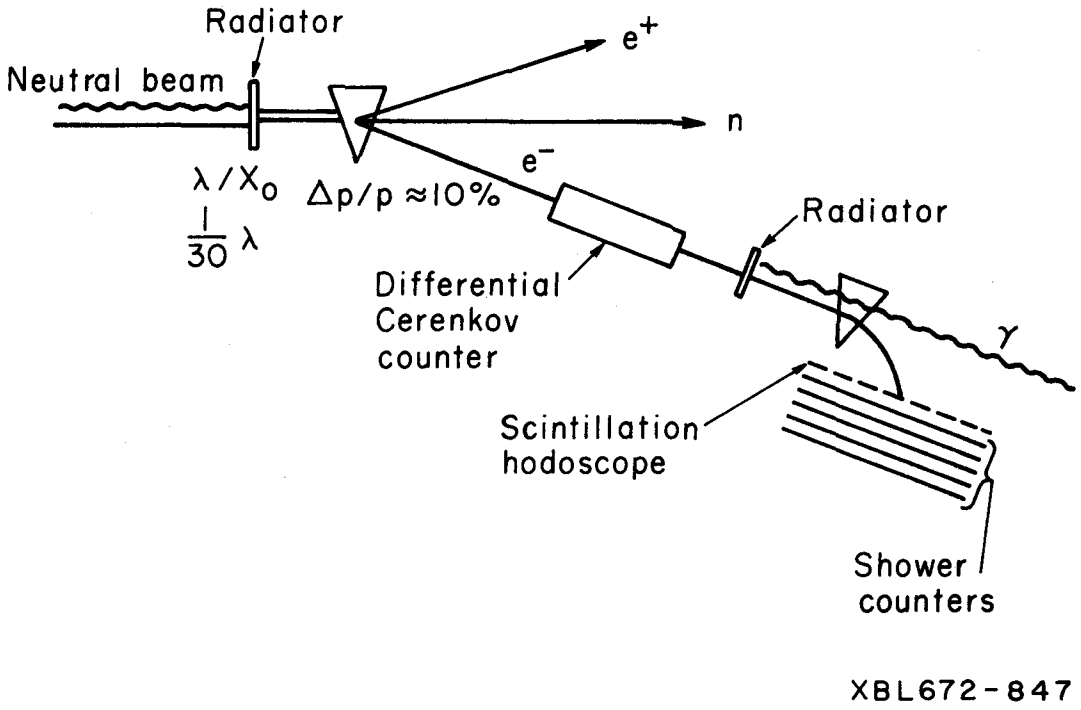

Fig. 9. Tagged photon beam with two conversion stages used.

In the absence of large neutron fluxes, multi-BeV electrons or photons in the final state (or in the tagging bank) are readily identifiable, with small contamination, by various kinds of shower counters with good energy resolution.[5] It is suggested that every momentum-defining bank of bremsstrahlung-degraded electrons, in a γ-tagging setup, be followed by a bank of large shower Cerenkov counters (cf. Fig. 10). Moreover, DISC Cerenkov counters will be able to distinguish π^- and μ^- from electrons as high as $\approx$30 BeV/c and antiprotons from electrons as high as 200 BeV/c, and should be used upstream from the radiator. A photon-tagging trigger is then defined by DISC $\times$ scintillator $\times$ shower counters $\times$ $\overline{\text{veto}}$.

DAUGHTER BEAMS: MONOCHROMATIC AND POLARIZED PHOTON BEAMS

A look at Fig. 5 makes it clear that the spectral composition of the primary photon yield, and hence of any subsequent γ beams, is hard to define, and certainly hard to measure. Photon-initiated reactions will be severely handicapped by this lack of kinematical input. The classical method of endpoint subtraction often used at electron machines is a mild headache even with the relatively well-known Bethe-Heitler spectrum (demanding, among other things, precise knowledge of the spectral shape, and large counting rates for good statistics). It is out of the question here.

We wish to briefly review the methods presently known and used of fixing the energy or polarization of the incoming photon, indicating their operability under our beam conditions.

Collimation of Bremsstrahlung Cone

The bremsstrahlung cone generated by the passage of an electron through a thin target is known to contain regions of well-defined plane polarization, although, upon integration over the solid angle, no net polarization results. Mozley and co-workers[6] have successfully collimated regions of net polarization of about 20% in connection with photoproduction experiments at the Stanford Mark III linac. Obviously, most of the bremsstrahlung intensity is lost, and in addition, very thin radiators must be used in order to prevent the multiple scattering from smearing out the effect.

In the context of the low intensities discussed here, this scheme need not be further considered.

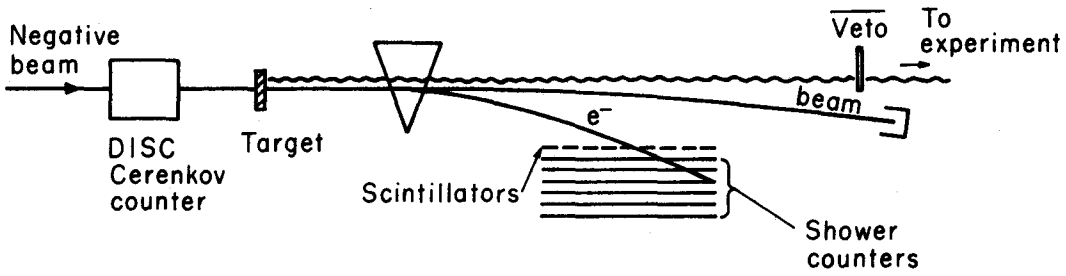

Fig. 10. Detail of tagged γ-ray experiment.

Coherent Bremsstrahlung from Crystals

Instead of an amorphous substance, a single crystal can be chosen as a radiator for bremsstrahlung production. By thus destroying the symmetry of the cone and introducing a reference plane, we end up with a net polarization upon overall integration. It can be shown that the momentum transfer to the nucleus can only be of the following order:

Longitudinal momentum transfer:

$$\text{sharp lower limit:} \quad q_{min} = \delta \approx \frac{m^2 k}{2E_1 E_2}$$

$$\text{diffuse upper limit:} \quad q_{max} \approx 2\delta \left(\text{for } \theta = \frac{m}{E_1}\right)$$

Transverse momentum transfer:

$$q_{max} \approx 2\, m \frac{k}{E_1} \approx 1 \,,$$

where k is the momentum of the incoming photon, and E_1 and E_2 are the electron energies before and after the scatter. This defines a disk-shaped region in momentum space containing all the end points of possible momentum transfer vectors [cf Fig. 11(a)]. In the crystal's momentum space, the inverse lattice, this disk may or may not contain inverse lattice points, where the Bragg condition is met, viz, $\vec{p}_2 - \vec{p}_1 = h$ where $|h| = 2\pi/a$ = inverse lattice constant.

Incidence under a small characteristic angle with regard to one of the principal axes will then bring about a sudden stepwise contribution to the intensity [cf Fig. 11 (b, c)]. From integration over the disk (amorphous case), this becomes a summation over inverse lattice points. It leads to spectral peaks such as those measured at DESY for 6-BeV/c incident momentum and shown in Fig. 12(a).[7] Proper choice of lattice point, angle of incidence, and radiator crystal (here diamond) lead to large enhancement over the Bethe-Heitler-type bremsstrahlung spectrum. The peak is also seen to be highly polarized [Fig. 12(b)].

This method presents serious problems: Diamond crystals of thickness $\gtrsim 0.02\ X_0$ are not presently obtainable; thus only about 2% of the electrons can undergo a bremsstrahlung process. Also, extreme care must be taken to ensure precise angular alignment ($\approx 10^{-5}$ rad); and there is always a continuous background present which can be evaluated only through very tedious subtraction methods. Last and not least, the presence of large neutron fluxes will in a short time damage the single crystal seriously.

Compton Scattering of Laser Photons

This method, proposed by Milburn[8] and by Arutyunian et al.[8] in 1963, utilizes the small phase space taken up by the light output of a high-power laser to scat-

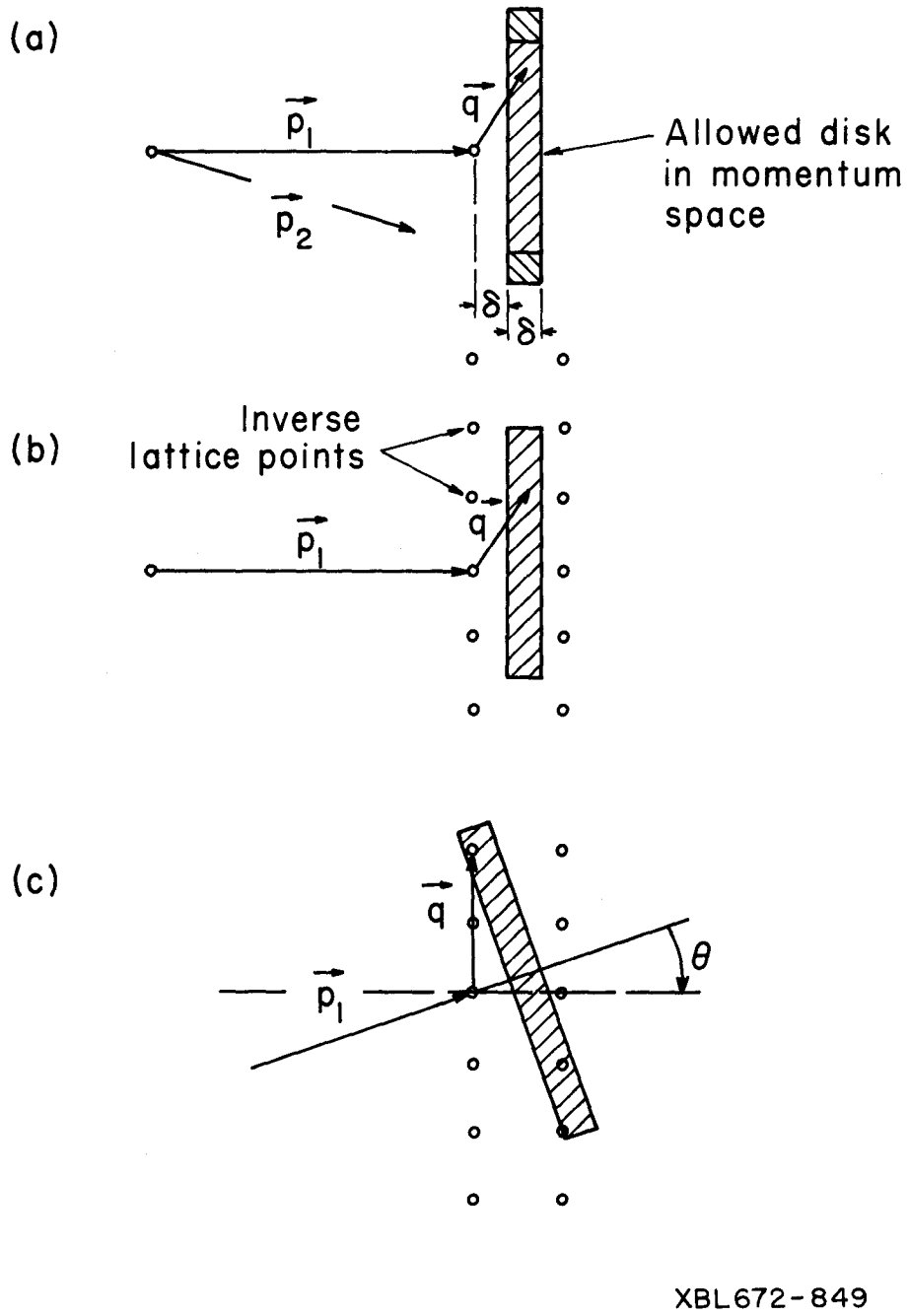

Fig. 11. Illustration of how coherent bremsstrahlung can occur from crystals.

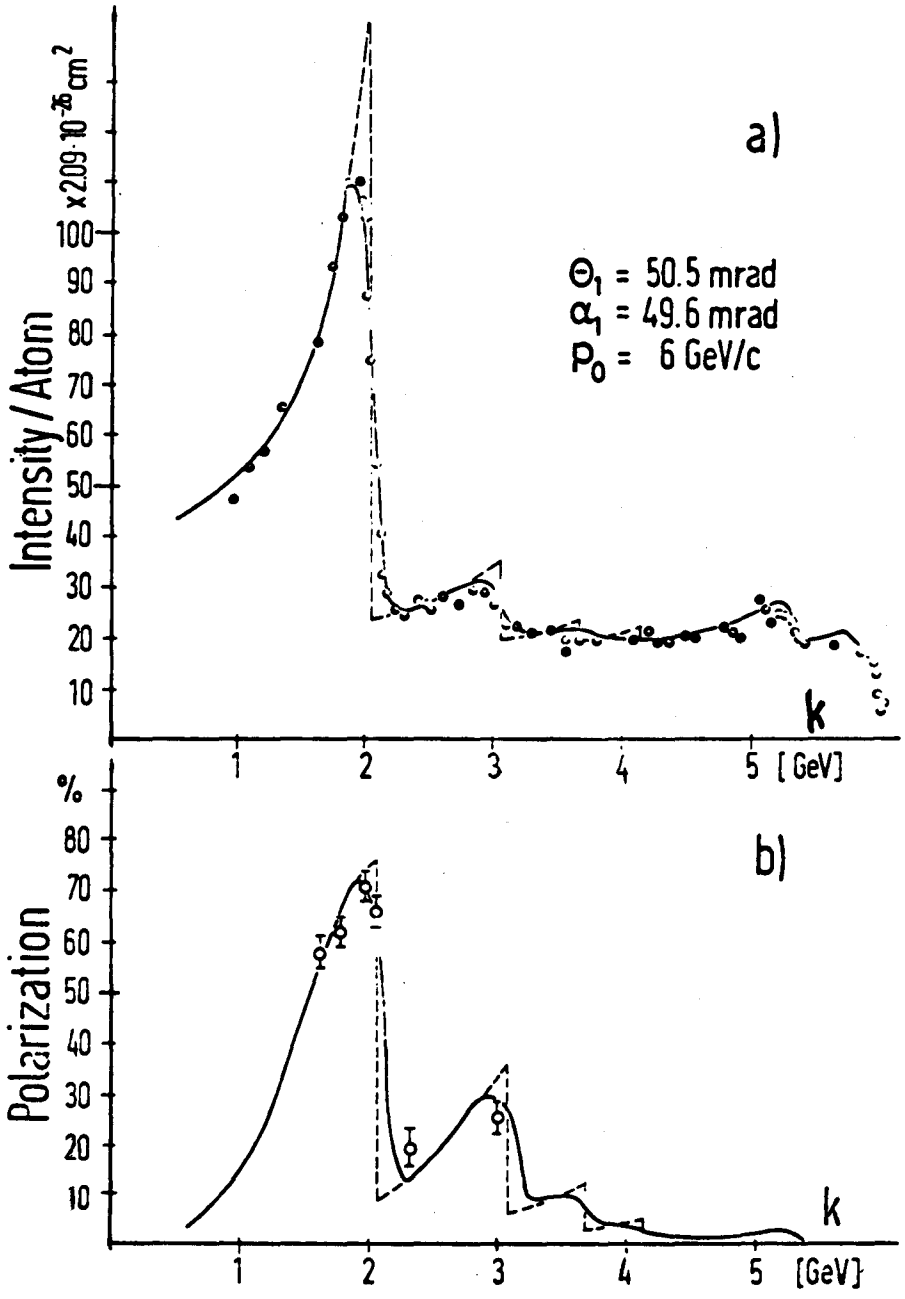

XBL 671-530

Fig. 12. Results of measurements of coherent bremsstrahlung from a crystal found at DESY (Ref. 7). (a) Intensity; (b) polarization.

ter the photons off a well-collimated electron beam. At 180-deg scattering angle, doubly Doppler-shifted photons have been observed at the Cambridge Electron Accelerator. The spectrum is essentially flat up to its maximum value, but with increasing primary energy it will peak more strongly toward the upper end. The advantages lie in the unique relationship between photon energy and emission angle (see Fig. 13: with proper collimation, the uppermost spectral components can be singled out); and in the fact that the Compton-scattered photons largely retain their original polarization. That makes the production of plane as well as circularly polarized high-energy photon beams feasible. Table II gives a few parameters on obtainable energies and polarization, as quoted by Milburn.[8] The

Table II. Maximum photon momentum and polarization for γ rays produced by Compton scattering of a laser beam with an electron beam.

E_e (BeV)	k_{max} (BeV/c)	p_{max}
1	0.028	1.00
5	0.63	0.99
10	2.2	0.97
20	2.3	0.91
40	22.0	0.77
60	36.0	0.67

photon intensities obtainable are, for a parallel electron beam, $I \propto I_e I_\gamma \sigma / r_\gamma \theta_\gamma$, where σ is the Compton-scattering cross section, $r_\gamma \theta_\gamma$ is the phase space factor of the laser photons, and I_γ their intensity. Obviously, a high-power laser with good duty cycle (possibly free-running for the 20% duty cycle of this machine) is necessary to take advantage of the electron beams feasible here. Also, both electron and laser photon beam phase space have to be kept at a minimum, and matched, to maximize the yield. With presently available ruby-laser power levels, possible photon yields are small even with the large electron currents of the SLAC.[8] However, the laser power level can be strongly multiplied by the use of CO_2 lasers (presently by a factor of $\approx$20). These developments have to be awaited.

The main backgrounds are due to bremsstrahlung processes in air or residual gas, so that a good vacuum in the interaction region is mandatory. One complication is the extremely sharp collimation necessary to select the uppermost spectral part (of order 1 mm at 1000 ft distance) which poses strict alignment problems, and stringent requirements on the electron beam size.

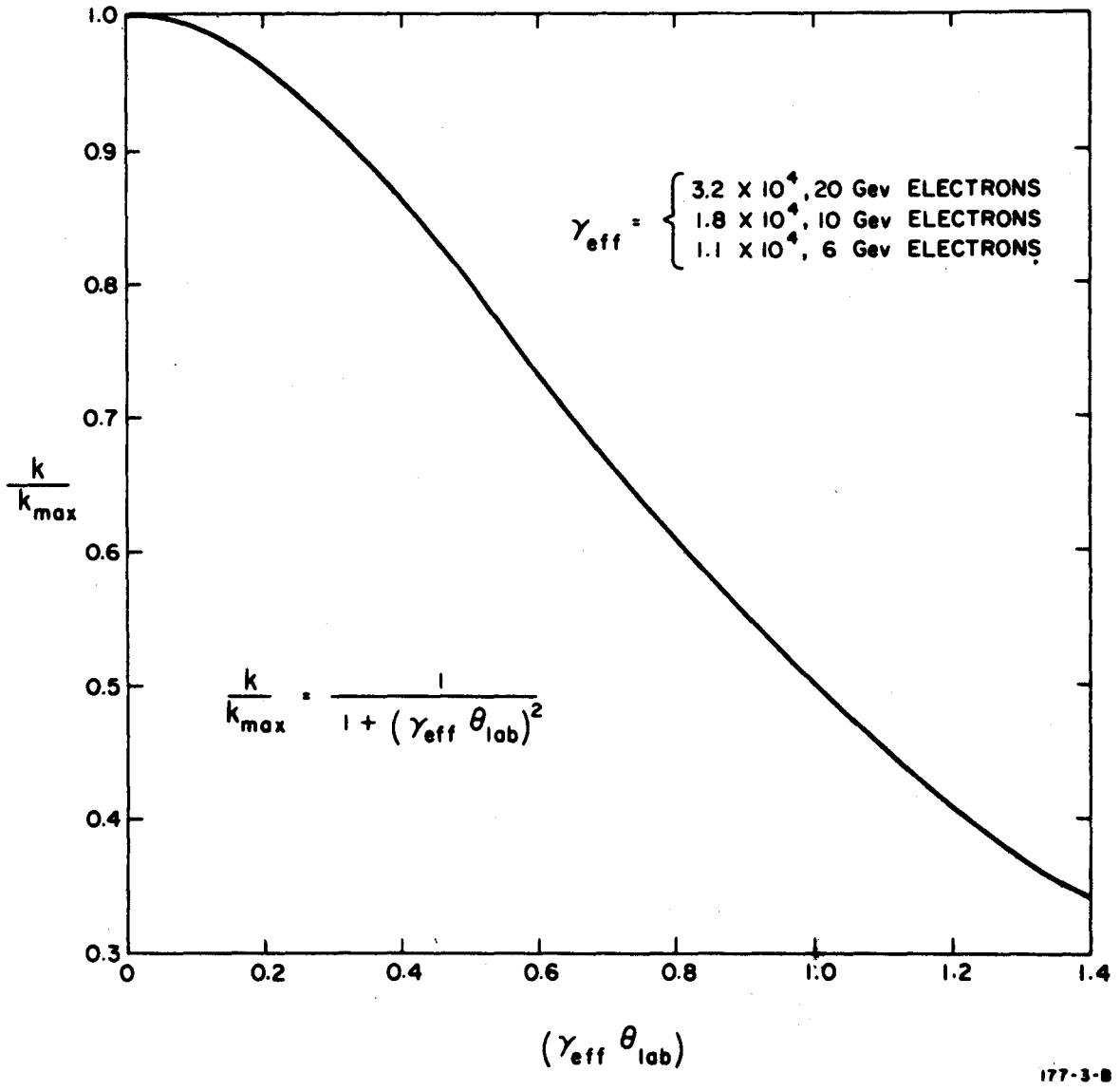

XBL 671-531

Fig. 13. Output photon energy vs laboratory system angle.

Positron Annihilation

An elegant method of photon beam monochromatization is currently being explored at SLAC.[9] If a well-collimated positron beam of energy E_+ were to hit a target consisting of electrons at rest, the resulting annihilation radiation would be monochromatic in a sharply defined cone around the incident momentum. In hydrogen targets, there are backgrounds due to bremsstrahlung production off the protons and off the target electrons; however, the characteristic angles for the bremsstrahlung process are much smaller ($\approx\gamma^{-1}$) than those for the annihilation radiation ($\approx\gamma^{-1/2}$), so that only a small part of the bremsstrahlung intensity extends into a cone we may choose. If we keep the thickness of the hydrogen target small (to reduce the effects of multiple scattering), a typical photon yield at any small angle will look like Fig. 14(a): A line spectrum of large intensity, due to e^+e^- annihilation, sits on top of a background composed of two bremsstrahlung spectra; the electron bremsstrahlung contribution extends up to the annihilation peak, and the proton part continues to higher energies.

The annihilation photon flux is approximately given by[9]

$$I = I_+ \times 0.024 \ \frac{E_+}{k_1} \ (1 + \frac{k_1^2}{k_2^2}) \ (\frac{dk}{k})^3,$$

where k_1, k_2 are the energies of the two annihilation quanta. (The angular uncertainty due to multiple scattering has to be matched by the secondary collimator which determines the final dk/k.) Suppose we are willing to accept a final dk/k of 5%; then at $\Delta E_+/E_+ = 1\%$, and $I_+ \approx 10^6$, $k_1 = k_2 = E_+/2$, a photon flux of ≈ 10 per pulse can be expected. At lower energies (see Fig. 5), where positron beams may be appreciably more copious, this method may become marginally interesting. However, both the fact that positron beams have worse background problems than electron beams (see above), and the necessities of a thin annihilator and of precise beam definition and collimation, present obstacles that will be hard to overcome in the context studied here.

As an illustration, we show in Fig. 14(b) the yields expected at SLAC from a primary positron beam of 10^{10} per burst, with a $\Delta E_+/E_+$ of 1%, and dk/k = 1%.

Tagged Photon Beams

If all of the above-mentioned methods for the fixation of the energy and polarization parameters of photons are either unfeasible or very marginal, our interest will focus on the determination of photon energies through tagging. Without going into details of the procedure, we mention the various possibilities.

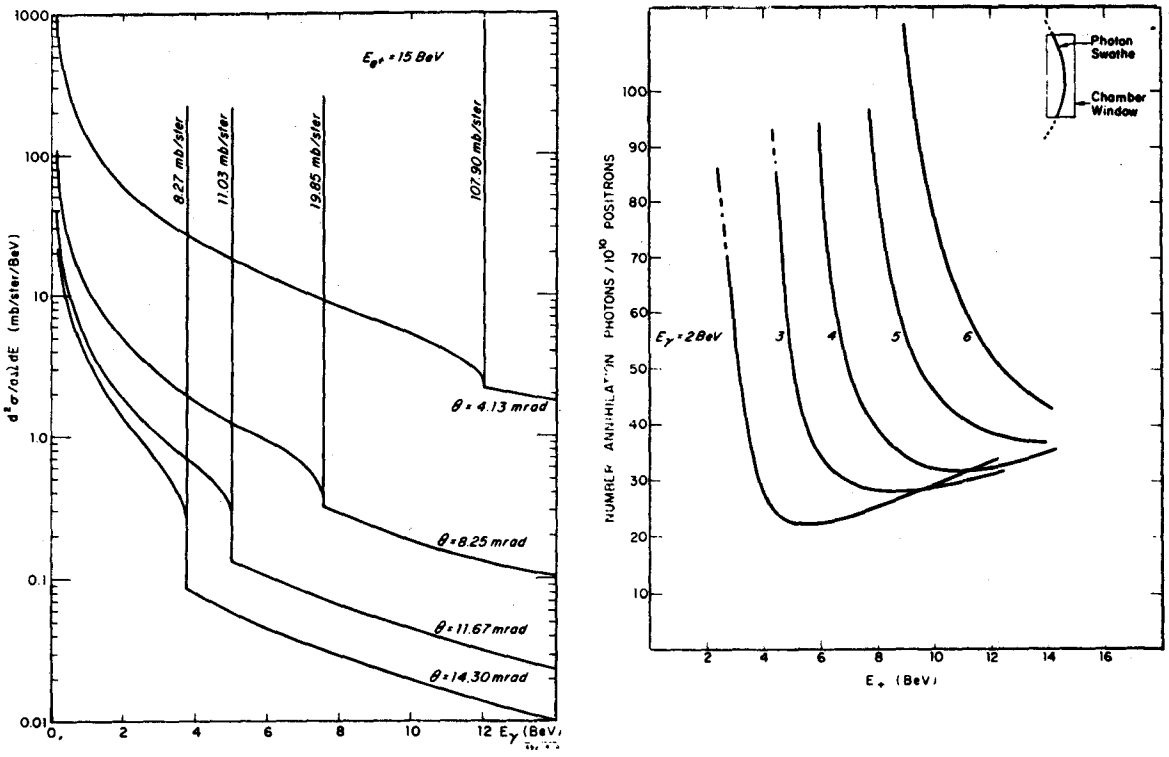

XBL 671-532

Fig. 14. Number of photons per 10^{10} e^+; I 1% energy resolution, expected in the chamber window acceptance and attenuation in 10-rad length of hardner included.

TAGGING OF REAL PHOTONS. The procedure, as illustrated in Fig. 10, has been well established in many places: A monochromatic electron beam hits a radiator; the resulting bremsstrahlung quanta go forward, and the decelerated electrons are momentum-analyzed in a bending magnet and a subsequent counter hodoscope. Such a beam may contain a large bite of photon energies, if desirable. A typical arrangement accepts the upper 20% of the spectrum and divides it into 20 channels of $\Delta p/p \approx 1\%$.

The efficiency of the method is limited by double bremsstrahlung corrections (i.e., the emission of two or more quanta in the bremsstrahlung process; this seems to be a small effect, since most second and further photons are of too small an energy to severely falsify energy determination of the energetic photons[10]); and by the occurrence of two subsequent bremsstrahlung processes (the probability for which is given by the target thickness in terms of radiation lengths). This latter limits the radiator thickness, and therefore the conversion efficiency, to a few percent for most applications.

On the whole, this method is readily available and easily adapted to differing requirements. The deflected electron is easy to identify in shower counters, and intensities as well as duty cycle in our application favor this method more highly than in its application at existing accelerators.

TAGGING OF VIRTUAL PHOTONS. The applicability of large-solid-angle detection devices around a 20% duty-cycle machine makes the detection of inelastically scattered electrons and muons in coincidence with other final-state particles possible. Therefore, the tagging of virtual photons is possible as well as that of real photons.

It is well known that, in a Weizsäcker-Williams picture, one can describe inelastic electron or muon scattering in terms of the interaction of charged particles with a field of virtual photons.[11] For high incident particle momenta and not-too-large dependence on momentum transfer of the reaction matrix element to be studied, the number and spectrum of the virtual photons is approximately like that of real photons generated in a radiator of thickness $0.02\ X_0$ for incident electrons; and approximately one-fifth that for incident muons.

Wilson and Wong,[12] who compared signal-to-background noise for real and virtual photon tagging, suggest that, for low-duty-cycle machines, the tagging of virtual photons by inelastic muon scattering may be preferable to real photon tagging, at small momentum transfers. However, within the context of the electron beams studied here, the relatively low intensities and the good duty-cycle characteristics make it preferable to use the more efficient and more direct method of tagging real photons.

It should, however, be kept in mind that, as a by-product of the planned μ-neutrino facility, fairly large muon beams will be available,[13] so that μ-scattering experiments will certainly be able to implement the projects to be studied by a possible electron-photon facility.

SUMMARY

In the context of primary proton fluxes of $\approx 10^{13}$/pulse at 200 BeV/c, we have discussed the possibility of setting up a facility for the study of electron-and-photon-initiated processes.

Within the framework of the model adapted for the calculation of secondary particle yields, it seems relatively easy to build photon beams of interesting intensities as high as ≈120 BeV, and considerably more intense beams in the energy region between 20 and 60 BeV. Although there is a heavy contamination of the primary photon beams by neutrons (and K's), these can be well purified by means of conversion and reconversion at the cost of considerable intensity losses. Similarly, electron beams can be set up and enriched, although the spectral shape is less advantageous. Small intensities resulting from beam purification can be tolerated for many purposes, by means of the use of large solid-angle detectors. In many respects, the good duty-cycle characteristic of the 200-BeV proton synchrotron will make it a photon source comparable to , or superior to, the projected 40-BeV extension of the SLAC. No unusual apparatus is needed for the physical setting up of such an electron-photon facility. It can coexist in an extracted proton beam with other charged beams, although it may demand special target materials.

Various devices for the production of monochromatic and polarized beams were reviewed. Most schemes appear, as of now, marginal or submarginal due to intensity and beam definition problems. However, the tagging of real (as well as virtual) photons is easy to build into the system, and appears to be very useful in these beams.

References

1. C. A. Heusch, Some Problems in Multi-BeV Photon Physics (following paper).
2. G. Trilling, Pion and Proton Fluxes from High Energy Proton Collisions, UCID-10148, May 1966.
3. R. Hagedorn and J. Ranft, Statistical Thermodynamics of Strong Interactions at High Energies, CERN Th-715 (1966).
4. D. Keefe, G. Mealy, and G. Trilling, Antiproton Fluxes from High Energy Proton Collisions, UCID-10149, May 1966.

5. C. A. Heusch and C. Y. Prescott, CTSL-41 (1964); IEEE NS-12 (1965) 213; P. D. Luckey, Proceedings of the International Symposium on Electron and Photon Interactions at High Energies, Hamburg, Germany, 1965. p. 397.
6. R. E. Taylor and R. F. Mozley, Phys. Rev. 117, 835 (1960); R. C. Smith and R. F. Mozley, Phys. Rev. 130, 2429 (1963).
7. G. Barbiellini, G. Bologna, G. Diambrini, and G. P. Murtas, Phys. Rev. Letters 8, 112 (1962); Phys. Rev. Letters 8, 454 (1962); L. Criegle, G. Lutz, H. D. Schultz, N. Timm, and W. Zimmermann, Phys. Rev. Letters 16, 1031 (1966).
8. R. H. Milburn, Phys. Rev. Letters 10, 75 (1963); SLAC Report 41 (1965); F. R. Arutyunian and V. A. Tumanian, Phys. Letters 4, 176 (1963); F. R. Arutyunian, I. I. Goldman, and V. A. Tumanian, JETP 45, 312 (1963).
9. G. Chadwick, Annihilation and Bremsstrahlung Intensities in the Monochromatic Beam, SLAC TN-66-13 (Mar. 1966).
10. L. Hand (SLAC, Stanford, California), private communication.
11. L. Hand and R. Wilson, Inelastic Electron-Proton, Positron-Proton, and Muon-Proton Scattering, SLAC-25 (Part II) (1963).
12. R. Wilson and M. Wong, Tagging of Real and Virtual Photons, this volume.
13. Timothy E. Toohig, Parameters of a Muon-Neutrino Facility at the 200 BeV Accelerator, UCID-10180, Feb. 1966.

SOME PROBLEMS IN MULTI-BeV PHOTON PHYSICS

C. A. Heusch

INTRODUCTION

These notes contain a few ideas about the physics of photon- or electron-initiated interactions in the energy region of many BeV. They are being written at a time at which the 20-BeV electron linac at Stanford, California, and the 2×1.5 BeV e^+e^- storage ring Adone at Frascati are coming into their own. Other machines are being built, but only in the storage ring field are somewhat higher energies projected.

The physics problems which are being tackled by these new facilities are numerous and exciting. Some of the questions mentioned in these notes may be answered by experiments done there; at this time it is obviously impossible to say at which energy various asymptotic conditions will be met, viz, where phenomena postulated for the high-energy limit will start to prevail.

The projected 200-BeV proton synchrotron has been shown to be a fairly good source for photon and electron beams with energies as great as at least ≈ 120 BeV (Ref. 1). In addition to being the only machine source for photon beams of energies greater than 20 BeV, its duty-cycle characteristics make possible many investigations not likely to be performed at other machines.

To what extent the curiosity of physicists will have been diverted into new directions by new experimental evidence and theoretical speculations is obviously unpredictable as of this date. A few problems stand out as likely candidates for our interest 8 to 10 years from now. The topics mentioned are chosen according to personal prejudice, and without any attempt at completeness.

STRONG-INTERACTION PHYSICS

Much of the motivation for building the 200-BeV proton accelerator comes from the desire to study strong vertices initiated by protons or pions. This motivation can be largely translated into interest in the corresponding reactions initiated by photons, both real and virtual. Conservation of spin angular momentum, isospin, and U spin lend additional interest to this initial state for strong processes.

Peripheral Processes

At large s-channel energies and small momentum transfers, Drell[2] predicted large meson-production cross sections due to one-particle exchange mechanisms. These predictions, based largely on the fact that, e.g., an almost real π is being exchanged in a large-impact-parameter collision (cf. Fig. 1), have been largely borne out experimentally. However, the relationship between this mechanism when applied to vector meson photoproduction (Fig. 2) and the diffraction mechanism (Fig. 3) is not clear at this point; an OPE model will always exhibit a dip at 0 deg because of the exchange of quantum numbers with the target nucleon, whereas the diffraction mechanism is characterized by the well-known maximum at 0 deg. Recent bubble-chamber data from DESY[3] indicate that for E_γ between 2 and 6 BeV, the diffraction mechanism dominates ρ production up to about 6 BeV, whereas the ω is primarily produced through OPE (which decreases with increasing incident energy), plus some diffraction admixture.

Measurements at Stanford will show whether energies > 30 BeV will be needed to check the relative merits of the diffraction and OPE mechanisms.

In addition, as Drell[2] pointed out, charged single-pion photoproduction at 0 deg is a good tool to test the non-peripheral features (like isobar intermediate states) of the interaction, since conservation of spin angular momentum suppresses the forward cross section through the necessary spin flip of the target nucleon.

Since all pseudo-elastic models for vector meson photoproduction [diffraction, multiperipheral model (Fig. 4)] give a 0-deg amplitude increasing linearly with E_γ, it will be possible, at high energies, to test various suggested[4] explanations of the puzzling experimental fact that ϕ photoproduction is strongly suppressed with respect to ρ and ω. With the help of symmetry arguments one can show that the OPE model can be made to account for the suppression of ϕ production, but completely fails to explain the large ρ/ω production ratio; whereas the diffraction mechanism, theoretically attractive because it can proceed via the exchange of systems with no quantum numbers, predicts the right ρ/ω ratio, but overestimates the observed ϕ rate by a factor of about 10. Replacing the simple diffraction mechanism by a pion ladder (multiperipheral model of Amati, Fubini, and Stanghellini,[5] proposed as a model for vector meson photoproduction by Berman and Drell[6]), Harari[4] showed that the low ϕ production rate can be accounted for, but not the correct ρ/ω production ratio. Precise data on ($V^0 = \rho, \omega, \phi$) photoproduction at high energies will obviously be very important for the solution of this puzzle.

Fig. 1

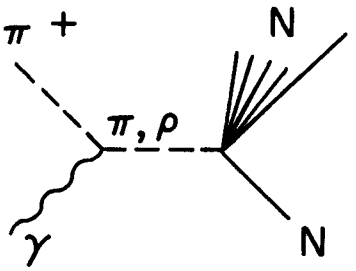

Fig. 2

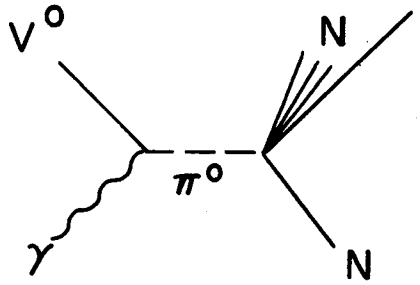

Fig. 3

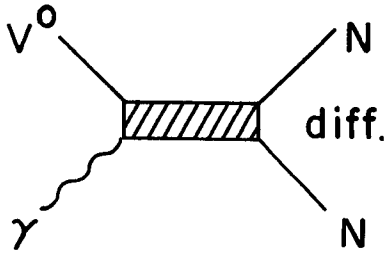

Fig. 4

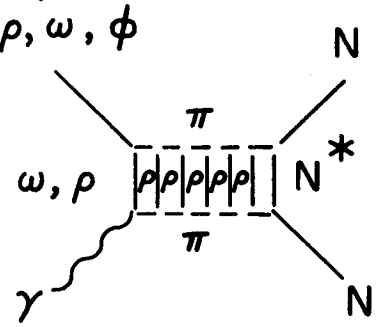

Fig. 5

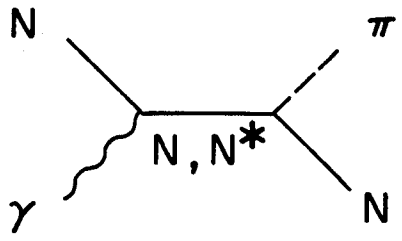

Fig. 6

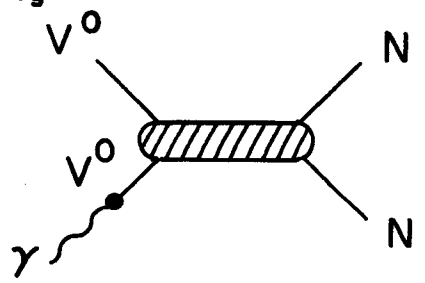

Figs. 1-6. Diagrams of processes discussed in the text.

XBL673-982

Regge-Pole Analysis

Parametrization of high-energy scattering data in terms of Regge poles has recently been very successful for a number of reactions. For some trajectories involved in t-channel exchange in high-energy photoproduction (the π and ρ trajectories in $\gamma p \to n\pi^+$, and the ρ and ω trajectories in $\gamma p \to p\pi^0$, etc.), a similar parametrization has been attempted.[7] If one trajectory dominates the production in some kinematical region, the cross section can be written as[8]

$$\frac{d\sigma}{dt} \propto s^{2\alpha(t)-2}.$$

It would be particularly interesting to see evidence for various baryon (N^*) exchanges in backward meson production (Fig. 5).

The only trajectories which can couple to the γV^0 vertex in neutral vector meson photoproduction are[4] the P, P', and the R ($I = 1$, $C = +1$, $G = 1$). Since the R can be shown to contribute negligibly, experiments at high energies should bear out the predictions of P, P' exchange, viz, (a) deviations from a linear s-dependence of the forward amplitude for the process $\gamma p \to pV^0$ should vary like $\sim\sqrt{s}$; (b) only an SU(3) singlet or the $I = 0$ member of an octet can be exchanged in the t-channel. This last prediction, of course, ties in with the diffraction picture.

The Photon in Symmetry Schemes

Starting from the Gell-Mann—Nishijima formula

$$Q = \frac{1}{2} Y + I_3, \tag{1}$$

and given that both Y and I_3 can be identified with generators of SU(3), the electromagnetic current j_μ due to

$$Q = \int j_0 \cdot d^3x \tag{2}$$

is generally postulated to transform like the member of an octet

$$j_\mu \sim (\lambda_3 + \frac{1}{\sqrt{3}} \lambda_8)_\mu \in \underset{\sim}{8}. \tag{3}$$

This is an essentially untested assumption. Nauenberg[9] pointed out that (1) may be written as

$$Q = \frac{1}{2} Y + I_3 + D, \tag{1'}$$

where D is a quantum number which happens to be zero for all known particles. It might, e.g., add a part to the current which transforms like a singlet.

Another possibility is that Eq. (2) should be replaced by

$$Q = \int j_0 \, d^3x + \underbrace{\int \cdots d^3x}_{=0} \, . \qquad (2')$$

where the current in the first integral transforms like an octet, and the second contains a current which happens to integrate out to zero, but may belong to $\underset{\sim}{1}$, $\underset{\sim\sim}{27}$, $\cdots$. Although, at present, our best guess is that the photon can be represented as

$$|\gamma\rangle = |\rho\rangle + \frac{1}{\sqrt{3}} |\phi_0\rangle \, , \qquad (4)$$

which means $j_\mu \in \underset{\sim}{8}$, this assumption has to be tested. One possible test is the comparison of the leptonic decay rates of vector mesons, which for the octet assignment (and spin = 0) should be

$$\rho \to \ell^+\ell^-/\omega \to \ell^+\ell^-/\phi \to \ell^+\ell^- = 9:1:2.$$

This relation has not yet been borne out experimentally. Another test would be the comparison of the direct γV^0 couplings in the diagrams of Fig. 6. A number of predictions have been made by Harari[4] for strange-particle production; great care must be taken in these comparisons to account for kinematical and phase-space effects.

Statistical Calculations

Drell and collaborators[10] have suggested using the octet assignment for the photon for tests of the role played by the statistical model in high-energy interactions. The idea is this: We confine ourselves to central collisions in which s and t are large with respect to the masses of the particles involved in the reaction, viz,

$$s, t \gg m^2;$$

we then average the cross sections observed over energy and momentum transfer intervals which are large with respect to the mass splitting within the multiplets. Then, the final-state channels should show up with the weight assigned to them by the appropriate Clebsch-Gordan coefficients only. A number of specific comparisons are suggested in Ref. 10.

It is presently unclear whether, for a definitive test of the validity of statistical model assumptions in high-energy processes, the form developed in Ref. 10 is sufficient, where only the s channel is taken into account. Possibly an extension of the method to include the t and u channels in the considerations may become necessary. At any rate, valuable information may be gathered at high s, t along these lines.

Measurement of $\sigma_{tot}(\gamma p)$

One obvious experiment which will be of interest in various contexts is the measurement of the total strong-interaction cross section of photon-proton scattering. It has been suggested, for example, that the electromagnetic current may not lead to an asymptotically constant value for the total cross section, $\sigma_{tot}(\gamma p)$, in contrast to the generally postulated behavior for $\sigma_{tot}(\pi p)$, $\sigma_{tot}(pp)$, etc. Since electromagnetic processes (pair production, Compton scattering) are very strongly peaked forward, a large-solid-angle detector could be triggered by larger angle particle counters, vetoed by small-angle shower counters (see Fig. 7). Alternatively, the measurement could be done with a bubble chamber, using the e^+e^- pairs for a flux normalization.

Of similar interest is the measurement, through the diagrams in Fig. 6, of $\sigma_{tot}(V^0 p)$. Various estimates have been put forward by Drell and Trefil,[11] Ross and Stodolsky,[12] and Joos.[13] Experimental results are of obvious interest in view of the various symmetry schemes. For example, SU(6) predicts not only

$$\sigma_{tot}(\rho N) = \sigma_{tot}(\omega N) = \sigma_{tot}(\phi N),$$

but also

$$\sigma_{tot}(\rho N) = \sigma_{tot}(\pi N)$$

which is not presently borne out by the evaluation of References 11 and 12.

TESTS OF QUANTUM ELECTRODYNAMICS

It is not clear that the existence of fairly intense photon and electron beams at energies >50 BeV will be able to contribute to our knowledge of the validity of Q.E.D. at small distances. The construction of 3-BeV storage rings for e^+e^- guarantees higher center-of-mass energies than can be provided by the 200-BeV accelerator. Results should be awaited from the very precise new (g-2) experiment at CERN, from the 1.5-BeV e^+e^- clashing beams of Adone, and from the expected 3-BeV storage rings at CEA. It should be kept in mind, however, that at the 200-BeV accelerator, the counting rates may be adequate for experiments such as wide-angle bremsstrahlung or wide-angle e and μ pair production, which cannot be performed at the storage rings.

Fig. 7

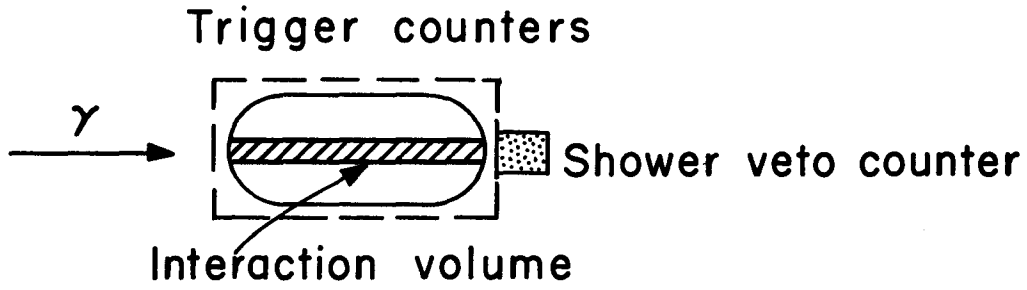

Fig. 7. σ_{tot} measurement for γp.

Fig. 8

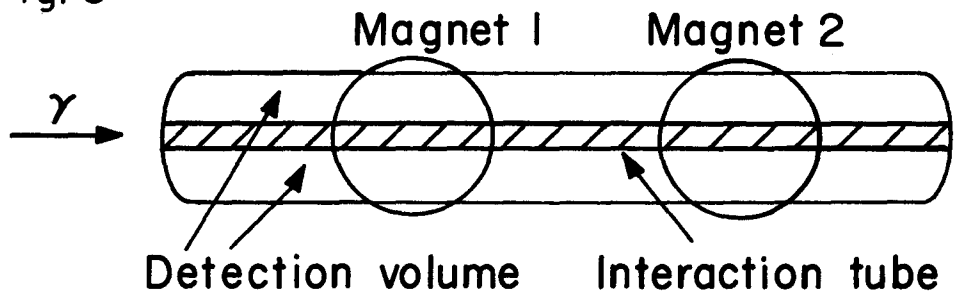

Fig. 8. Possible streamer chamber arrangement. Counters are triggered according to specific reaction.

XBL673-983

WEAK INTERACTIONS

Photon and electron beams are of considerable possible value for the study of weak interactions. The electromagnetic current is useful for investigations of vector current behavior on the grounds of the conserved vector current (CVC) hypothesis. It is assumed that the vector part of the weak current (both the strangeness-conserving and the strangeness-changing currents) belongs to the same octet to which the electromagnetic current [Eq. (3)] belongs.

The weak-interaction Lagrangian can be simply expressed in terms of vector and axial vector currents, F_i and F_i^5. Gell-Mann's[14] postulate that the fourth components of these vector and axial vector currents satisfy the local equal-time commutation relations

$$\begin{aligned} [F_{i4}, F_{j4}] &= [F_{i4}^5, F_{j4}^5] = if_{ijk} F_{k4} \\ [F_{i4}, F_{j4}^5] &= [F_{i4}^5, F_{j4}] = if_{ijk} F_{k4}^5 \end{aligned} \tag{5}$$

can, as Adler[15] pointed out, be tested in high-energy neutrino-induced νN, $\tilde{\nu}$N reactions which, at large E_ν, become independent of the four-momentum transfer q^2. For the vector part alone, Bjorken,[16] after performing an isospin rotation, derived the inequality

$$\frac{d\sigma_{tot}(ep)}{dq^2} + \frac{d\sigma_{tot}(en)}{dq^2} > \frac{e^4}{q^4} . \tag{6}$$

A similar equation can be written down for μp scattering. Experiments based on Adler's and Bjorken's sum rules are the only real tests of local equal-time commutation relations. All other tests go through the assumption that PCAC (partially conserved axial current) constitutes a link to the π or K fields, or through some specific dynamical assumptions. The inequality (6) makes it possible to test the current commutators (5) by means of electron and muon beams at nominally infinite momentum. Adler and Gilman,[17] however, have shown that these relations, which are at the very basis of our present understanding of weak interactions, can be tested at energies as low as 5 to 10 BeV for the case $q^2 = 0$. For $q^2 > 0$, however, the incident energies needed for the test of local commutation relations increase rapidly. In this domain, we see a field for inquiries of very fundamental importance for the 200-BeV machine's electron (and μ) beams.

Moreover, it is obvious that, in principle, electron beams can be used as a probe for many weak-interaction phenomena. At high energy and large

momentum transfer, the relative rate for the weak channel

$$ep \rightarrow \nu n$$

can be shown to be not hopelessly submerged by the prevalent electromagnetic scattering process

$$ep \rightarrow ep.$$

Counting rates may still be forbiddingly low. Hopefully experiments at Stanford will indicate whether experiments of the type $ep \rightarrow \nu B$ can be used to test weak-interaction selection rules.

A REMARK ON DETECTION EQUIPMENT

In a concluding remark, we want to stress the general feasibility of experiments on the above-mentioned phenomena. Fluxes are not prohibitively low if properly used in conjunction with large-solid-angle detection devices. Both bubble chambers and spark- or shower-chamber systems can be used; the latter, taking advantage of the long beam spill of the 200-BeV accelerator, can be triggered so that even very small cross sections may lead to acceptable counting rates. Specifically, a detection system like the one shown in Fig. 8 could be used to detect large-momentum-transfer processes. It is an expansion of a system presently in initial operation at SLAC (Mozley and collaborators), viz, a large streamer chamber surrounding a reaction tube, encased in a large magnet. Pulsing the chamber at 600-800 kV does not become more difficult with size.[18] It would therefore seem possible to make the following changes: lengthen the chamber from 2 to 10-20 m; possibly, fill the reaction tube with liquid hydrogen instead of gas, for smaller cross-section studies; replace the magnet—which would become prohibitively large—with one or two short magnets as indicated (good enough for adequate momentum resolution over a wide range). The problem is then largely one of taking adequate pictures of very long tracks.

The Mozley group at SLAC is presently planning to have a photon beam of no more than 10^5 to 10^6 sec^{-1} impinge on their interaction tube; this would lead to good events about once per minute. Such beam intensities are entirely feasible at multi-BeV photon energies.[1]

It should also be kept in mind that parasitical running of an electron-photon facility is possible, so that other experiments can be performed with the same primary target in the extracted proton beam of the 200-BeV synchrotron.

ACKNOWLEDGMENTS

It is a pleasure to thank S. D. Drell and H. Harari for very informative conversations.

References

1. C. A. Heusch, Photon and Electron Beams at the 200 BeV Proton Accelerator, this volume.

2. S. D. Drell, Proc. Int. Symp. on Electron and Photon Interactions at High Energies (Hamburg 1965), Vol. I, p. 71.

3. German Bubble Chamber Collaboration, DESY 66-32 (November 1966).

4. H. Harari, Phenomenological Analysis of the Photoproduction of Neutral Vector Mesons and Strange Particles, SLAC-PUB-239 (Phys. Rev., to be published).

5. D. Amati, S. Fubini, and A. Stanghellini, Nuovo Cimento 26, 896, (1962).

6. S. M. Berman and S. D. Drell, Phys. Rev. 133, B791, (1964).

7. See, e.g., L. S. Osborne, Proc. Int. Symp. on Electron and Photon Interactions at High Energies (Hamburg 1965), Vol. I, p. 91. M. Braunschweig et al., University of Bonn preprint, 1966: D. Caldwell et al., U.C. Santa Barbara preprint, 1966.

8. G. Zweig, Nuovo Cimento 32, 689, (1964).

9. M. Nauenberg, Phys. Rev. 135, B1047, (1964).

10. S. D. Drell, D. R. Speiser, and J. Weyers, Preludes in Theoretical Physics (J. Wiley and Sons, New York, 1966), p. 294.

11. S. D. Drell and J. Trefil, Phys. Rev. Letters 16, 552 (1966).

12. M. Ross and L. Stodolsky, Phys. Rev. 149, 1172 (1966).

13. H. Joos, Phys. Rev. Letters 24B, 103 (1967).

14. M. Gell-Mann, Physics 1, 63 (1964).

15. S. L. Adler, Phys. Rev. 143, B1144 (1966).

16. J. D. Bjorken, Phys. Rev. Letters 16, 408 (1966).

17. S. L. Adler and F. J. Gilman, CALT-68-69 (Phys. Rev., to be published).

18. A. Odian (1966) private communication.

A NOTE ON PARTICLE IDENTIFICATION IN HIGH-ENERGY HIGH-INTENSITY BEAMS

A. Roberts

For counter and spark-chamber beams, we require detectors capable of unambiguously selecting one kind of particle, even when such particles constitute only a small fraction of the incident beam. Partial solutions to this problem have been proposed;[1,2] it is the purpose of this note to point out that the new version of DISC[3] appears to offer a nearly complete answer to the problem, for well-collimated beams.

The new DISC (Differential, Isochronous, Self-Collimating) is a gas-filled focusing Cerenkov counter. Its properties are as follows:[4,5]

Length	2 m
Cerenkov angle	2.5 deg
Resolution, $\Delta\beta/\beta$	3.10^{-6}
Absolute velocity accuracy	10^{-6}
Angular acceptance	1.2 mrad
Beam diameter	(about 10 cm)
Rejection ratio	$\geq 10^5$
Maximum counting rate	$\approx 10^8$ sec^{-1}.

DISC achieves its high resolution because chromatic dispersion in the gas Cerenkov radiator has been removed to first order by a doublet axicon lens achromatized at 3500Å (a considerable achievement in optical design). DISC has been used at CERN in two test runs.[3,4] It readily separates pions and muons at 11.3 BeV/c, and it has essentially no background between peaks, which recommends it for the selection of the less abundant beam components. The emittance exceeds that proposed for high-momentum secondary particle beams.[2]

Table I shows the quantity $1-\beta$ for some beam particles at a few momenta.

Table I. Values of $1-\beta$.

Particle momentum (BeV/c)	μ	π	K	p
50	2.2×10^{-6}	3.8×10^{-6}	49×10^{-6}	176×10^{-6}
100	0.55	0.96	12.	44.
150	0.25	0.43	5.5	20.
200	0.14	0.24	3.0	11.

From Table I, the present resolution is adequate for K-p distinction at all energies, and for K-π distinction at all energies except possibly the very highest, where some slight improvement in resolution is needed. For the lighter particle, the resolution is insufficient.

Even higher resolution (to $\Delta\beta/\beta = 10^{-7}$) is possible, according to the authors,[5] by decreasing the Cerenkov angle and increasing the length in inverse ratio to $\Delta\beta/\beta$. This would allow direct separation even of the light particles. However, other limitations may supervene; and the present resolution suffices for most experiments, as we will now argue.

SEPARATION OF π, μ, e

Up to about 50 BeV/c, electrons are distinguishable from the unresolved π-μ peak; π-μ separation should be good up to about 30 BeV/c. However, in practice the separation of these particles may not pose a serious problem, since other procedures are available. The intensity of the combined eμ contamination in a pion beam is usually well under 10%. In many experiments the presence of the leptons is of no consequence other than as a correction to the observed beam intensity. When necessary, electrons can be effectively removed from the beam by a lead radiator before the last momentum-selecting magnet, without seriously degrading the pion beam quality. If the total beam intensity is not too high, the lead radiator may take the form of a lead-scintillator sandwich anticoincidence counter, which produces large pulses from electrons only.

Muons can be electronically selected or removed by taking advantage of their long range, and by using an anticoincidence counter after a thick (1-2 m) Fe absorber following the experimental equipment. Muon intensities are usually low enough to allow anticoincidence counter use in beams up to at least 10^8 sec^{-1} total intensity. The arrangement of Fig. 1 would remove most e and μ contamination from the beam. To select muons, only the Fe filter is needed (no DISC is required).

It remains only to devise a method for selecting high-energy electrons. It may be possible to develop a reliable detection system based on the relativistic rise of ionization, since the γ of electrons is over 100 times greater than that of any other particle in the beam. Even if such a detector is not available, the fact that electron experiments are usually significantly different from hadron experiments can be used. Thus, if the electrons are used to produce bremsstrahlung, the pion contamination will not be significant. Improvements in DISC may also solve this problem.

COMPARISON OF DISC AND THRESHOLD COUNTERS

The use of threshold Cerenkov counters to select electrons is possible; however, there is a relation worth pointing out, between the resolution of DISC counter and the minimum length of a threshold counter whose discrimination is just equal to that of the DISC. We now show that the length of threshold counter required to give 50 photons for a particle of velocity c, if the threshold is set at $\beta = 1 - \Delta\beta$, is given by $L = 0.05/\Delta\beta$ cm.

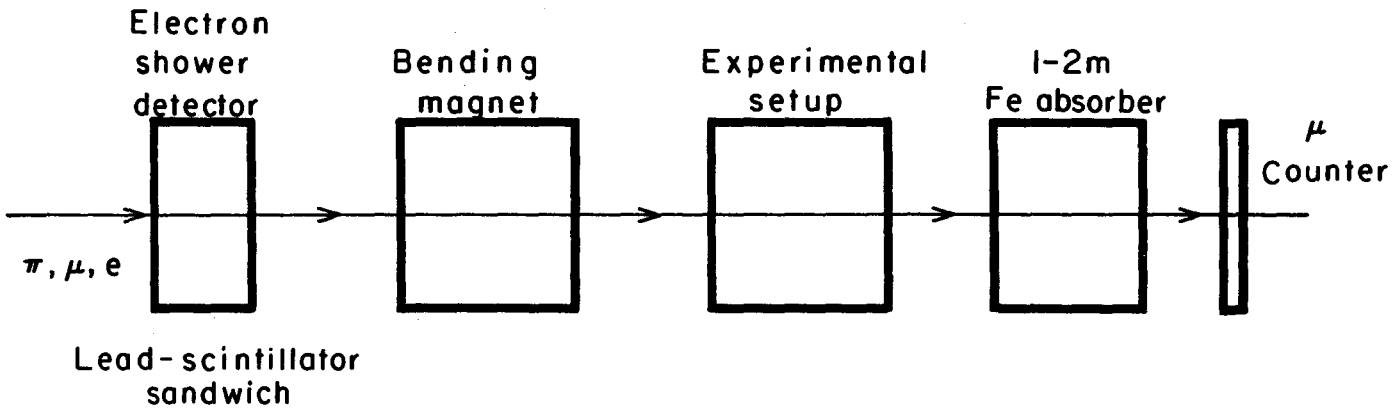

Fig. 1. Purification of pion beam. (The bending magnet is the last momentum-selecting element of the beam.)

The following relations[1] hold for Cerenkov counters, for $\beta \approx 1$. Let $\cos\theta = 1-\Delta c$, $\beta = 1-\Delta\beta$, $n = 1+\Delta n$. Then since $\cos\theta = 1/n\beta$, $\Delta n = \Delta c+\Delta\beta$, where $\Delta\beta = 1/2\gamma^2$, and $\Delta c = \theta^2/2$. For an ideal gas, $\Delta n = \eta p$, where η is a constant and p is the pressure in atmospheres.

The Cerenkov threshold is defined by $\Delta c = 0$, or

$$\Delta\beta_{thr} = \Delta n = \eta p = 1/2\gamma^2_{thr}.$$

The light output useful for an S-11 photocathode depends only on the cone angle θ, and is $dN/dL = 500 \sin^2\theta$ photons/cm. In a threshold counter whose threshold is defined by γ_{thr}, a particle of velocity c will have a cone angle θ given by $\eta p = \theta^2/2$, so that $dn/dL = 500 \sin^2\theta = 1000 \eta p = 1000 \Delta\beta$. To obtain 50 photons the required path length L is

$$L = 50/1000 \Delta\beta = 0.05/\Delta\beta \text{ cm.}$$

For $\Delta\beta = 3.10^{-6}$, L = 167 m.

Consequently to improve upon the DISC at its current performance level requires a threshold counter at least 167 m long. With the possible exception of electrons, DISC seems well-suited to all other necessary particle selection, without requiring very long beams. Its major disadvantages are cost and complexity; but these are not by any means disqualifying.

RANGE OF ALLOWABLE BEAM INTENSITIES

Since secondary beams may well exceed 10^9 particles sec^{-1}, we ask if the selected particles can be used with so high a background rate. If the $\bar{p}$ and K^- abundances are of the order of 1%, and the DISC is usable to rates of 10^8 sec^{-1}, particle selection will be feasible for total beam rates up to 10^{10} sec^{-1}. For lower abundances, e.g., in positive beams where there are many protons, still higher fluxes should be tolerable. If the experimental setup cannot tolerate such high fluxes of unwanted particles, then either the beam must be reduced or particle separators must be used; these will of necessity be limited to at most a few beams.

It must be noted that techniques are currently available[6,8] for desensitizing small areas of large spark chambers, so that well-focused beams of high intensity can be transmitted without interfering with normal chamber operation. In one case[8] an average current of 8.10^9 protons/sec, with a peak rate of over 2.10^{11} sec^{-1}, was transmitted without decreasing the spark-chamber efficiency. The limit to this technique is reached when there is an appreciable probability of an unwanted particle obscuring the desired event, by interacting in the apparatus during the sensitive time of the spark-chamber system. This limit would in many cases exceed 10^9 particles/sec.

Meunier et al.[5] have proposed a particle-separation scheme in which the DISC is used to generate a trigger for a pulsed electrostatic separator. The separation is a function of p only, so that the same geometry may be used for any particle by turning the DISC to select it. The separated beam is then pure

as well as monochromatic. The method unfortunately suffers from the disadvantage that since the particles are highly relativistic, the trigger can catch up to the DISC-selected particle only if the latter can be stored for a time equal to the delay in the triggering electronics. Such storage requires deflection by a magnet through a large angle—enough to allow the arc-chord difference to make up the $\approx$ 100 nsec delay. So large a magnet is readily contemplated only if a large storage ring will be available for other purposes.

References

1. D. Keefe, Separation of Particle Beams at High Energies, in The Berkeley High Energy Physics Study, Lawrence Radiation Laboratory Report UCRL-10022, June 15, 1961, p. 137.

2. M. Longo, 150 GeV/c Beam for Spark-Chamber Experiments, Lawrence Radiation Laboratory Report UCID-10124, August 21, 1964, p. 137.

3. P. Duteil, L. Gilly, R. Meunier, J. P. Stroot, and M. Spighel, Rev. Sci. Instr. 35, 1523 (1964).

4. G. Cocconi, Secondary Particle Production from p-p Collision with the 19.4 GeV/c External Proton Beam at CERN, Lawrence Radiation Laboratory Report AS/Experimental/04, July 26, 1966.

5. R. Meunier, M. Spighel, J. P. Stroot, and P. Duteil, CERN 65-27, 1965.

6. S. Bernstein et al., Proc. IEEE Prof. Group in Nuclear Science, (Purdue Conf. on Instrumentation, 1965), NS-12, 120 (1965).

7. R. A. Schluter et al., Nucl. Instr. Methods, 41, 309 (1966).

8. T. M. Knasel, J. K. Walker, and M. Wong, Rev. Sci. Instr. 36, 270 (1965).

TRANSITION RADIATION DETECTORS FOR ULTRAHIGH ENERGIES

C. M. York

I. INTRODUCTION

Ginsburg and Frank[1] calculated the properties of "transition radiation" from a charged particle when it crosses the surface between one dielectric and another as indicated in Fig. 1. Note that the charge induces an image charge in the dielectric as it approaches the surface. As the charge nears the surface, the separation between the charge and its image decreases until they coincide at the point of impact. The charge and its image comprise a dipole, whose strength increases until it suddenly disappears at the instant of contact. This varying dipole gives rise to a time-dependent perturbation of the electromagnetic field of the particle, causing it to radiate quanta. The quanta are the "transition radiation" to be discussed below.

Ter-Mikaelyan[2] and Garibyan[3] have considered the possibility of producing this transition radiation for a periodic structure of dielectric slabs, arranged as indicated in Fig. 2. The dielectric susceptibility of the material of the slabs is ϵ_1, whereas that of the vacuum is ϵ_2. (We take $\epsilon_1 > \epsilon_2$.) The thickness of the slab is ℓ_1, and the distance of separation is ℓ_2. The periodic structure has a cell length, $\ell = \ell_1 + \ell_2$, and the ratio of these lengths is $a = \ell_2/\ell_1$. It is assumed that the energy of the emitted photon, $E_j = h\nu$, is much smaller than that of the charged particle, i.e.,

$$h\nu \ll E_1 \text{ and } E_2. \tag{I-1}$$

Here E_1 is the particle energy as it enters the stack of dielectric slabs, and E_2 is its energy as it leaves. Conservation of energy gives

$$h\nu \approx E_1 - E_2 = \delta E, \tag{I-2}$$

where we have neglected any energy transfer to the array of dielectric slabs. Conservation of momentum along the z-axis gives

$$\vec{v} \cdot \frac{(\vec{p}_2 - \vec{p}_1)}{v} - \frac{h\nu\sqrt{\epsilon}}{c} \cos\theta = \frac{2\pi h}{\ell} r. \tag{I-3}$$

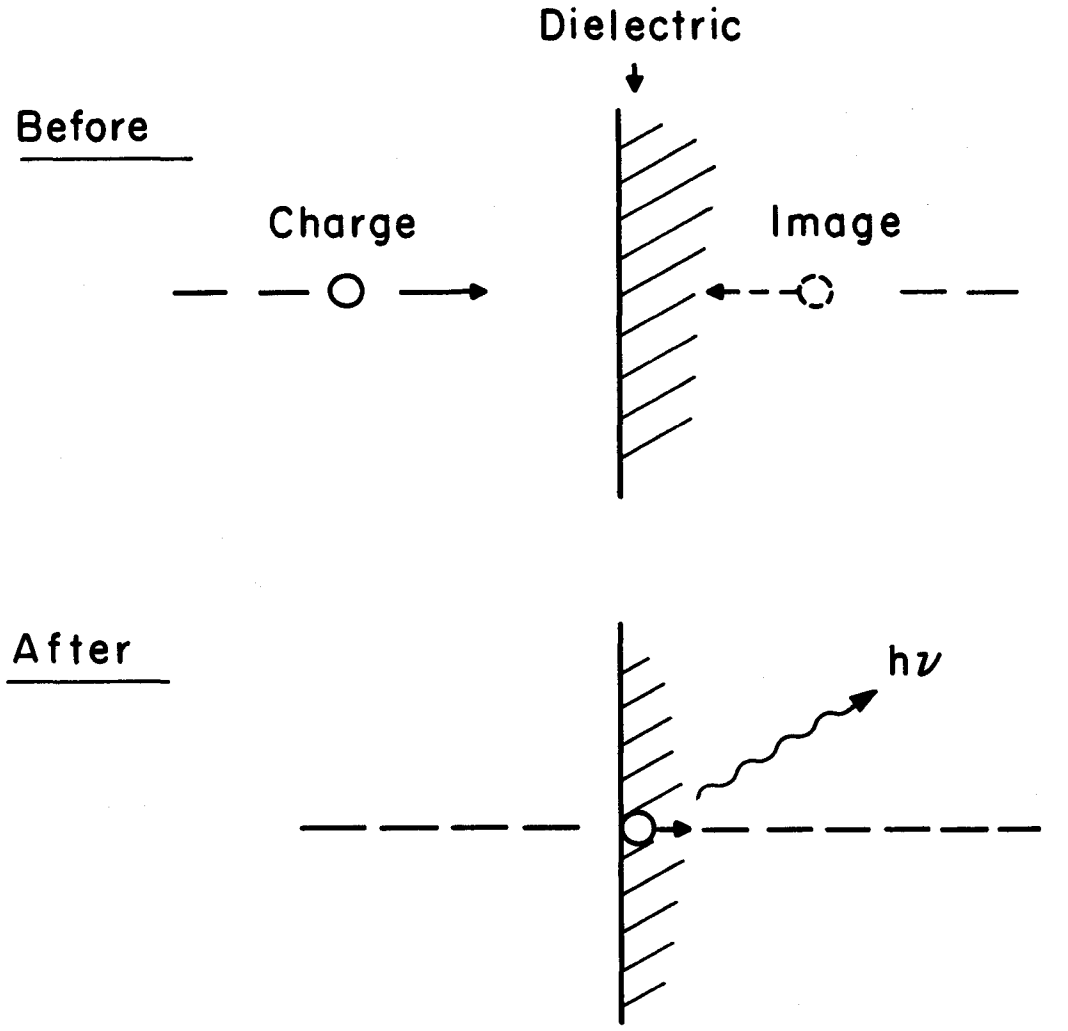

XBL 671-446

Fig. 1. "Transition radiation" from a charged particle.

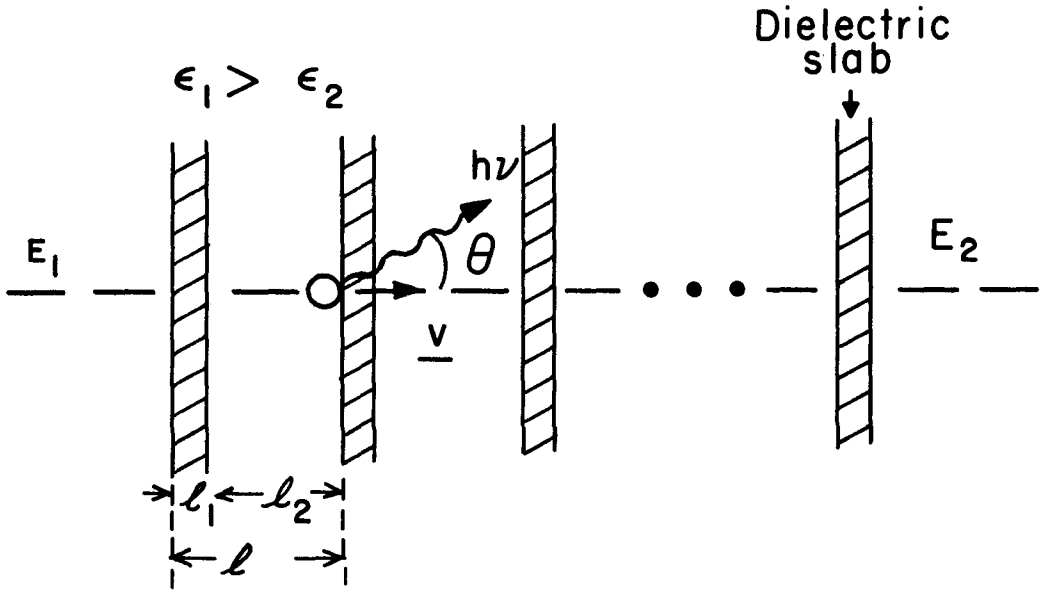

XBL 671-447

Fig. 2. "Resonance radiation" from a charged particle.

Here v and p are the particle velocity and momentum, θ is the angle of emission of the quantum, and r = 0, ±1, ±2, ··· is an integer which can be thought of as the "order" of the emitted radiation. The term on the right is just the momentum transferred to the dielectric, $\delta\vec{p}$, when the photon is emitted, and is a kind of semi-classical quantization condition for emission of the radiation. The $\sqrt{\epsilon}$ is seen to be just the relative index of refraction of the dielectric and the vacuum.

For very high momenta

$$\vec{v} \cdot \delta\vec{p} \simeq \delta E = h\nu.$$

If this is substituted into Eq. (I-3) and a slight rearrangement is made, then we can write

$$1 - \frac{v\sqrt{\epsilon}}{c} \cos\theta = 2\pi \frac{v}{\ell} \cdot \frac{1}{\nu} \cdot r. \qquad \text{(I-4)}$$

The right-hand side now clearly shows that the period of the radiation, $1/\nu$, gives "resonances" when it becomes an integral multiple of the time required for the particle to traverse a cell length, ℓ/v. It is this fact that has led to the emitted radiation, $h\nu$, being called "resonance radiation." An acoustical analogy is the sound emitted by a stick dragged along a picket fence.

II. PROPERTIES OF THE RESONANCE RADIATION

Some Special Cases of Eq. (I-4)

1. Let $\ell \to \infty$; then Eq. (I-4) becomes

$$1 - \frac{v\sqrt{\epsilon}}{c} \cos\theta = 0.$$

This is just the classical expression for the emission of Cerenkov radiation in an infinite medium of index of refraction, $\sqrt{\epsilon}$, when $\epsilon > 1$. If $\epsilon < 1$, then $\cos\theta > 1$ can occur and in this case no radiation is emitted.

2. Another way in which the right-hand side of Eq. (I-4) can go to zero is to set r = 0. This can be interpreted to mean that when the Cerenkov condition obtains (at r = 0), there will be no resonance radiation.

3. Finally consider the possibility that

$$v/c \to 0.$$

Then Eq. (I-4) gives

$$\nu = 2\pi \frac{n}{\ell} r,$$

and the frequency of the radiation is emitted in resonance with the periodicity of the structure, ℓ/v (just as in the acoustical analog).

The Frequency of the Emitted Radiation

Consider next the limits in the frequency of the emitted radiation. To obtain these we consider only those values of $|\cos\theta| \leq 1$. Furthermore, to make the algebra tractable we consider only frequencies of the emitted radiation which are large compared to the characteristic atomic frequencies of the dielectric medium, i.e.,

$$\nu \gg \nu_{\text{atomic}}.$$

The dielectric susceptibility can then be written

$$\epsilon = 1 - \frac{4\pi Ne^2}{m_e \nu^2}, \tag{II-1}$$

where N is the density of electrons in the material. If we solve Eq. (I-4) for $\cos\theta$ and apply the condition $|\cos\theta| < 1$, we can write

$$1 + \frac{v\sqrt{\epsilon}}{c} \geq \frac{2\pi}{\nu} \frac{v}{\ell} r \geq 1 - \frac{v\sqrt{\epsilon}}{c} \quad . \tag{II-2}$$

From this condition a number of the fundamental properties of the radiation can be deduced.

1. The maximum frequency can be obtained from the right-hand equality. The constants

$$a = \frac{2\pi c r}{\ell} \quad \text{and} \quad b = \frac{2\pi e^2}{m_e} N \tag{II-3}$$

can be introduced. If $\gamma = (\sqrt{1 - \beta^2})^{-1} \gg 1$ and $\beta \approx 1$, you can show that

$$\nu_{max} = \frac{4\pi c r}{\ell} \gamma^2. \tag{II-4}$$

2. To obtain the minimum value of ν, use the left-hand inequality of Eq. (II-2). It can be transformed into

$$\nu_{min} = \frac{2b}{a} [1 + \sqrt{1 - 4(1 - v/c)b/a^2}]^{-1}.$$

Again as $\beta \to 1$,

$$\nu_{min} = \frac{b}{a} = \frac{Ne^2 \ell}{m_e c r} . \qquad \text{(II-5)}$$

3. Consider these limits. For given r and ℓ, the maximum frequency of the emitted quanta is limited by the total energy, or γ, of the radiating particle. This is consistent with the conservation of energy and is a condition similar to that which enters the theory of Williams and Weizsacker[4] in their treatment of radiation from a moving charge. The lower limit is seen to depend upon the order of the radiation, r, as well as the geometric arrangement of the dielectric slabs, given by ℓ, and the density of electrons in the slabs, N.

4. The limits upon the radiated frequency have assumed that E_1, and hence γ, is much greater than that of the emitted quanta. But suppose that we construct a detector of this type with given N and ℓ, and restrict ourselves to the selection of first-order radiation with r = 1, only. (That it is possible to do this in practice will be shown below). If now ν_{min} is fixed, we must require that ν_{max} be greater than or equal to ν_{min} in order to detect any radiation at all. Thus at $\nu_{min} = \nu_{max}$, we have a condition set upon the minimum γ which can be detected. The expression becomes

$$\gamma_{r,t} = \left(\frac{E}{mc^2}\right)_{r,t} \geq \frac{\ell}{2cr}\sqrt{\frac{Ne^2}{\pi m_e}} . \qquad \text{(II-6)}$$

Such a detector will then act as a threshold-γ-detection device in the same way that a threshold velocity selector can be made using the Cerenkov radiation.

The number of photons emitted by the particle as it traverses a slab of the material is given by

$$dN = \frac{4p^2(1+a)^2}{137\pi \ell_1} \frac{[1 - A\nu' - \frac{1}{\nu'}]}{(1 - \frac{p}{\nu'})^2(1 + \frac{pa}{\nu'})^2} \times \sin^2\left[\frac{a}{a+1}\pi - \frac{\pi}{\nu'}\left[\frac{ap}{1+a}\right]\right]\frac{d\nu'}{\nu'^3} . \qquad \text{(II-7)}$$

Here $p = \dfrac{N_1 - N_2}{N_1 + aN_2}$,

$A = \dfrac{1}{4r^2}\left(\dfrac{\gamma r,t}{\gamma}\right)$,

and $\nu' = \nu/\nu_{r,\,min}$.

This is a somewhat more generalized formula than those used above, and N_1 corresponds to the electron density in the dielectric, ϵ_1, whereas N_2 is the corresponding density in the space between slabs. Although our elementary derivation above considered this space to be a vacuum, this was a needless restriction. Later Eqs. (II-5) and (II-6) will be given in this more general form. The $\gamma_{r,\,t}$ appearing in A is just the threshold value of γ obtained from Eq. (II-6). Similarly $\nu_{r,\,min}$ is the value of ν obtained from Eq. (II-5) for a given value of r.

The spectrum of photon frequencies obtained from this last expression can be plotted for various orders, r, when the parameters of the apparatus have been chosen. Figure 3 shows the intensity of photons $f(\nu')$ of frequency ν' plotted for the various orders, r = 1, 2, 3, etc. Here $a = 1$; $\gamma = 2.2\,\gamma_{1,\,t}$; r = 1, 2, 3, $\cdots$; and the dielectric is paper in air.

Finally, from the fundamental Eq. (I-4) we can estimate the values of θ, the angle of emission of the quanta at various frequencies, ν. For $\cos\theta \simeq 1$, we can show that at $\nu \approx \nu_{min}$ and with $\beta \simeq 1$, that

$$\theta \approx \frac{r}{\ell_1}\left(\frac{\pi m_e c^2}{N_1 e^2}\right)^{1/2} = \frac{r}{\ell}\left(\frac{\pi}{N_1 r_e}\right)^{1/2}, \qquad \text{(II-8)}$$

where r_e is the classical radius of the electron.

III. THE DESIGN OF A RESONANCE RADIATION DETECTOR

In the following we shall assume that a threshold detector for γ is desired. That is, a momentum-analyzed beam containing a mixture of particles with various rest masses will be given. Then all particles with given γ or greater will be detected either for coincidence or veto purposes. Thus $\gamma_{r,\,t}$ will be given. The formulae which then must be used in a sequential order are summarized in Table I. The formula for $\gamma_{1,\,t}$ requires that we choose the materials of the dielectric slabs and their separating gaps to fix N_1 and N_2. Low-Z materials should be used to minimize those background effects caused by delta rays. Estimates of these effects will be given below. The separation ratio a can be any value greater than zero, and in the examples below, a = 1 or 50 will be used. The first equation then can be used to determine the thickness of the slabs, ℓ_1.

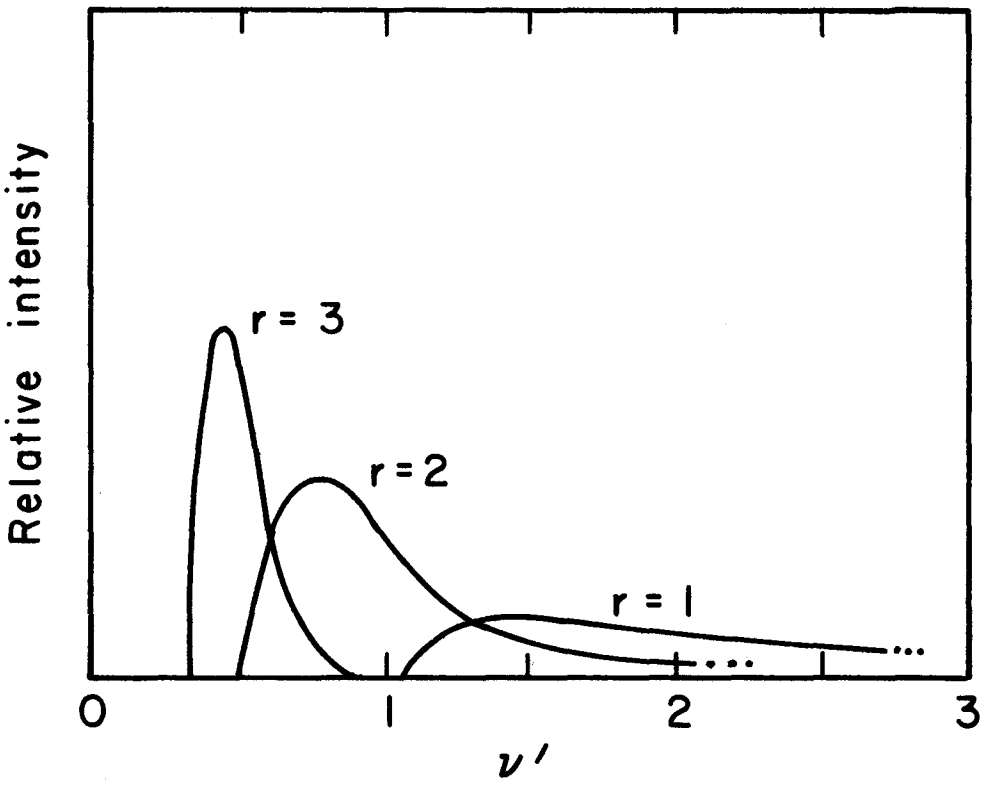

XBL 671-448

Fig. 3. Differential frequency spectrum of resonance radiation ($\alpha = 1$).

Table I. Formulae related to the design of a resonance radiation detector.

$$\gamma_{1,t} = \left(\frac{E}{mc^2}\right)_{r=1,\ \nu=\nu_{min}} = \ell_1 \left[\frac{r_e}{\pi}(1+a)(N_1+aN_2)\right]^{1/2} \qquad (1)$$

$$\nu_{min} = \ell_1 r_e c (N_1 + aN_2) \ [sec^{-1}] \qquad (2)$$

$$dN = \frac{4p^2(1+a)^2}{137\pi\ \ell_1}\ \frac{d\nu'}{\nu'^3}\ \frac{\left[1 - A\nu' - \frac{1}{\nu'}\right]}{(1-\frac{p}{\nu'})^2(1+\frac{pa}{\nu'})^2}$$

$$\times \sin^2\left[\frac{a}{a+1}\pi - \frac{\pi}{\nu'}\left[\frac{ap}{1+a}\right]\right] \qquad (3)$$

$$n_k = dN\, e^{-\mu\ell_1}\left[1 + e^{-\mu\ell_1} + e^{-2\mu\ell_1} + \cdots + e^{-(k-1)\mu\ell_1}\right] \qquad (4)$$

$$\theta_{max} \simeq \frac{r}{\ell_1}\left(\frac{\pi}{N_1 r_e}\right)^{1/2} \qquad (5)$$

With a, N_1, N_2, and ℓ_1 now fixed, the magnitude of $\nu_{1,min}$ is determined from the second equation in the table. In the detectors to be considered here, let us detect only first-order radiation, i.e., set r = 1, and screen out all of the higher orders with an optical filter of some suitable material which transmits only frequencies greater than $\nu_{1,min}$.

These parameters can then be used in the third equation to determine the number of photons generated per traversal of a charged particle through a dielectric slab. This number, dN, will be used to calculate the total number of photons emerging from the stack of dielectric slabs. If n_k is the number of photons emerging from a stack of k slabs, then $n_1 = dN\, e^{-\mu\ell_1}$ emerge from the first slab, where μ is the absorption coefficient of the dielectric for photons in the frequency range $1 < \nu' < 2$. For two slabs we have

$$n_2 = dN\, e^{-\mu\ell_1} + dN\, e^{-\mu 2\ell_1} \text{ etc.}$$

Finally,

$$n_k = dN\, e^{-\mu\ell_1}(1 + e^{-\mu\ell_1} + \cdots + e^{-\mu(k-1)\ell_1}). \qquad (III-1)$$

This equation is the fourth given in Table I and provides an estimate of the total number of photons to be detected.

Although we have carefully avoided the question of actually detecting this resonance radiation, it will be useful to know the angle at which the photons are emitted. Hence the fifth equation provides the means for determining this angle.

Applications of the Equations

Before proceeding to some numerical examples, a number of useful tables of constants will be provided. Table II(a), taken directly from the work of Alikhanyan et al.,[5] gives the constants needed for numerical evaluation of the first three equations in Table I. Here the authors have assumed that $a = 1$, and that the materials are to be mounted in air or vacuum. Notice that two light metals are included and should behave just like the dielectrics in the frequency range $\nu \gg \nu_{atomic}$. Table II(b) has been provided to give an indication of the atomic constants, such as the position of the K-edge and mass absorption coefficients of the materials used in Table II(a). It is worth commenting that for these materials, the mass absorption coefficient, μ, decreases slowly with decreasing wave length below 0.1 Å.

Table II. Table of constants used in evaluating the equations of Table I.[a]

(a)

Material	$N_1(\times 10^{-23}\ cm^{-1})$	$E_\gamma = h\nu_{1,min}$ (MeV)[b]	$\frac{E}{mc^2}_{1,t} \cdot \frac{10^{-5}}{\ell_1}$[c]
Paper	(2-3)	$(1.1\text{-}1.7)\,\ell_1$	1.6-2.4
Polyethylene	2.8	$1.53\,\ell_1$	2.21
Be	4.9	$2.72\,\ell_1$	2.95
Al	7.8	$4.33\,\ell_1$	3.72

a. Data from Ref. 5

b. $h\nu_{1,min} = 5.55\times 10^{-24} N_1 \ell_1$

c. for $a = 1$

(b)

Material	λ_k [Å]	E_γ [eV]	$\mu(@\lambda = 1.0\ Å)\ [cm^{-1}]$	$\mu(@\lambda = 0.1\ Å)$
Be	110.68	112	0.55	≈0.13
C	43.65	284	1.36	0.142
Al	7.95	1559	14.12	0.156

The equations of Table I have been used to calculate a typical set of values for polyethylene radiators. These results have been collected into Table III for convenience. In addition to the parameters set forth in the table, the following values were used: $\Delta\omega' = 2$; $\omega' = 1.5$; $\gamma = 1.1\,\gamma_{1,t}$; and $k = 10$. The choice of frequencies was based on the spectral distribution shown in Fig. 3 for $r = 1$. The small number of radiators, $k = 10$, was dictated by the mass absorption coefficient of carbon for the radiation emitted. The table immediately suggests some problems of design. First, for $\gamma = 40$ the thickness of polyethylene, 1.8×10^{-4} cm = 0.00007 inches, suggests a rather severe mechanical and procurement problem for such thin sheets. Because the threshold energy for particle detection varies directly as ℓ_1, this mechanical limit on thickness may set a corresponding limit on the threshold energy. The upper limit on the angular divergence of the emitted radiation restricts the means used to detect the resonance radiation.

Table III. Design parameters for a resonance radiation detector with polyethylene radiators.

γ	a	ℓ_1 [cm]	$E_{\gamma min}$ [eV]	λmin [Å]	dN	n_{10}	θ_{max} [mr]
40	1	1.8×10^{-4}	286	43.6[a]	290	600	13
100	1	11.4×10^{-4}	715	17.3	116	160	2.1
400	1	18×10^{-4}	2860	4.3	29	132	1.3
1000	1	114×10^{-4}	7150	1.7	12	22	0.2

a. Note that for carbon, $\lambda_k = 43.6$ Å, so Eq. (II-1) is no longer valid.

The Alikhanyan Detector

In order to fix upon a clear conception of the type of detector under discussion, consider that tested by Alikhanyan et al.[5, 6, 7] Figure 4 shows the experimental arrangement which he used to detect resonance radiation produced by cosmic-ray muons of very high energy. These muons had a horizontal trajectory to utilize the atmosphere as an absorber and the larger flux of very-high-energy muons in the spectrum at large zenith angles. The resonance radiation was generated in a stack of 300 paper sheets ($Z \approx 6$), $\ell_1 = 2\times10^{-2}$ cm, glued to wooden frames to give a separation of $\ell_2 = 1$ cm. The incident muon and its accompanying resonance radiation emerged from the stack of paper and traversed, in order: a xenon-filled chamber, $10\times10\times40$ cm^3, filled to 5-cm Hg pressure above atmospheric; and a threefold Geiger counter coincidence

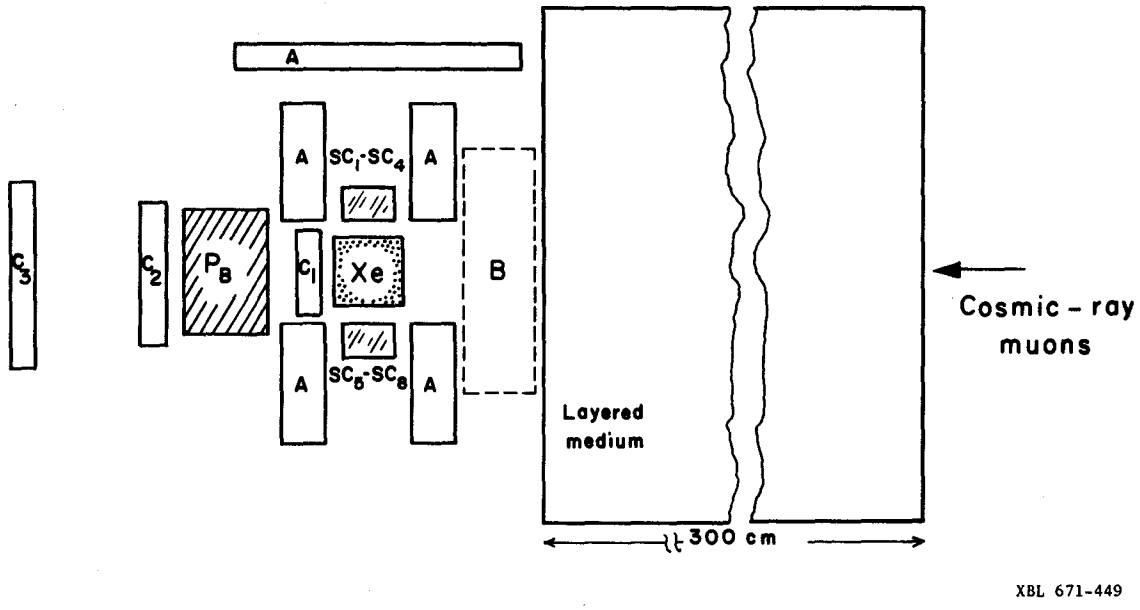

Fig. 4. Alikhanyan's apparatus for the detection of resonance radiation. For explanation of symbols, see text.

telescope, $C_1C_2C_3$, containing 16 cm of lead. The threshold energy for detection is $(E_{1,t}/mc^2) = 2.57\times10^4$ and $E_{\gamma min} = 36.0$ keV. Cosmic-ray air showers were vetoed by the anti-coincidence counters, A, shown in the figure.

The resonance radiation is detected in an ingenious way. Photons in the energy range, $E_\gamma > 36$ keV, are absorbed with high probability in the xenon gas. (The K-edge of xenon is at 35 keV.) The xenon then re-emits its characteristic K x-ray which is detected in the NaI crystal counters, $(SC_1\text{-}SC_4)$ $(SC_5\text{-}SC_8)$, above and below the xenon chamber. By setting the discriminators on the NaI counters to detect only these K x-rays and by requiring that one be detected in each of the two crystals in coincidence with the passage of a muon, background effects are greatly reduced. The discriminator levels were set with the aid of a Ce^{144} gamma-ray source. The efficiency of transferring resonance quanta into the detected xenon x-rays is estimated to be 34%.

After running the apparatus for 7526 hours, 100 events were detected. Control measurements were periodically performed by placing a plexiglass absorber, B, of thickness 11.5 g/cm^2, between the stack of papers and the xenon chamber as shown in the figure. Only three events in 1800 hours were recorded in this configuration. This corresponds to a background of about 13%.

Other Suggested Detection Schemes

In addition to the method involving the xenon detector described above, several other methods have been considered.[5] A xenon-filled proportional counter could be inserted in place of the xenon chamber shown in the figure. It would then be necessary to distinguish between the ionization produced by the passage of the muon through the gas and the ionization produced by the resonance radiation. Similarly, if the scintillation properties of xenon at high pressure were used to detect the ionization due to the resonance radiation, the background caused by the muon passage would have to be distinguished. Neither of these possibilities is as effective as that used in the above experiment, which has been called the "characteristic radiation" method of detection.

Another scheme for separating the resonance quanta from the charged particle has been called the "Compton Scattering" method. If the energy of the emitted resonance quanta is such that the photo effect is small compared with the Compton effect in the layered medium, then these quanta will no longer emerge from that medium with the angular divergence given in Eq. (II-8). Instead they will Compton scatter and emerge at much larger angles, and be considerably degraded in energy. To compute the fraction of photons escaping would require a detailed Monte-Carlo-type calculation which has not been done.

Background Effects

A primary source of soft x-rays of energy equivalent to those emitted in the resonance radiation is the bremsstrahlung produced by δ rays which are created by the primary charged particle passing through the layered medium. The number of these bremsstrahlung γ rays is given by an expression of the form[5]:

$$N_{\delta\gamma} = \iint_{\epsilon\, E_\gamma} R(\epsilon)\, N_\delta(E_o, \epsilon)\, d\epsilon \cdot N_\gamma(\epsilon, E_\gamma)\, dE_\gamma. \qquad \text{(III-2)}$$

Here $N_{\delta\gamma}$ is the number of photons produced per g/cm^2 of the layered medium, and E_o is the energy of the incident particle which produces N_δ delta rays with energy between ϵ and $\epsilon + d\epsilon$. These δ rays have a range $R(\epsilon)$ in the layered material, and they produce N_γ photons with energy between E_γ and $E_\gamma + dE_\gamma$. The limits on the integrals are such that $E_o > \epsilon$ at all times. The expression for N_δ is

$$N_\delta(E_o, \epsilon)\, d\epsilon = 2\pi \frac{N}{A} Z\, r_e^2\, m_e c^2 \cdot \frac{1}{\beta^2} \cdot \frac{d\epsilon}{\epsilon^2},$$

where β is the velocity of the incident particle. The number of photons is

$$N_\gamma(\epsilon, E_\gamma)\, dE_\gamma = \frac{4}{137} \frac{N}{A} Z^2\, r_e^2\, \ell n(183\, Z^{-1/3}) \left\{ \frac{m_e c^2 + \epsilon}{\epsilon} \right\} \frac{dE_\gamma}{E_\gamma}.$$

There are no satisfactory analytic expressions for $R(\epsilon)$, but useful empirical formulas can be found.[8] Table IV has been taken from the work of Alikhanyan et al.[5] to give some insight into the magnitude of this effect. In his version of such a detector, cf. Fig. 4, the calculated contribution is very small, but it is not clear that his measurements have eliminated all contributions of this sort. The plexiglass absorber would cut out both resonance radiation photons and these δ-ray photons.

A second form of background which is especially relevant in the Alikhanyan device arises from K levels in the xenon being exited directly by the passage of the incident particle. The number of such photons is

$$n = \frac{N}{A} \int_{E_k}^{E_o} \sigma_k(E_\gamma) \cdot N(E_\gamma)\, dE_\gamma,$$

where $\sigma_k(E_\gamma)$ is the cross section for the photoelectric effect in the K-shell

Table IV. Bremsstrahlung produced by δ rays in various materials.[a]

	$N_{\delta\gamma} \times 10^2$ (photons/g/cm^2)$^{-1}$		
E_γ (MeV)	Be	CH_2	Al
0.01	3.00	1.66	15.5
0.05	2.24	1.20	11.3
0.10	1.54	0.83	7.7
0.20	1.31	0.71	6.6
0.40	1.06	0.57	5.3
0.70	0.90	0.48	4.5
1.00	0.70	0.42	3.9
2.00	0.60	0.31	1.5

a. Data from Ref. 5.

of xenon, and

$$N(E_\gamma)\, dE_\gamma = \frac{2}{137\pi}\, \ell n\,(E_o/E_\gamma)\, \frac{dE_\gamma}{E_\gamma}$$

is the number of virtual photons in the field of the incident particle.[4] In the case of the detector described above, this contribution is small, and in any event is accounted for in the background subtraction.

These two detailed estimates of background are given to indicate the type of problems that can arise and are not in any way meant to exhaust the possible troubles that such detectors have.

IV. COMMENTS AND CAUTIONS

The primary purpose of the above discussion has been to set forth the material in the literature in a concise and straightforward fashion. In reading the various articles, one will be struck by the circular, or spiral, arguments of Ter-Mikaelyan and the multitude of misprints in the printed equations. For example, in Ref. 5, Eq. (II-7) omits a rather crucial superscript which squares the term, $(1 + a)$. Every effort has been made to present the correct formulae here.

The information about Alikhanyan's experimental verification of the resonance radiation must be considered as interesting, but hardly convincing. Although the ideas for detecting the x-rays are ingenious, much more work

remains to be done before detectors of this sort can be used operationally. As reported by Inman and Muray (cf. Ref. 1), the experimental detection of transition radiation is well established and may provide a more reliable means of particle detection.

References

1. V. L. Ginsburg and I. M. Frank (cf. Nobel Lecture by I. M. Frank), Usp. Fiz. Nauk 18, no. 3 (1943)(English trans.) 1943; 17, no. 1; cf. also JETP (USSR) 16, 15 (1948). F. W. Inman and J. J. Muray, IEEE Trans. Nucl. Sci., NS-13, 373 (1966).

2. M. L. Ter-Mikaelyan, JETP 25, 296 (1953). (Russia) Izv. Akad. Nauk SSSR, Ser. Fiz. 19, 657 (1955); Doklady Akad. Nauk SSSR 134, 318 (1960); (English trans.) JETP 39, 1693 (1960); Nucl. Phys. 24, 43 (1961). With A. D. Gazazyan, JETP (trans.) 12, 1183 (1961).

3. G. M. Garibyan, JETP 37, 527 (1959); (English trans.) JETP 10, 372 (1960).

4. cf. W. Heitler, Quantum Theory of Radiation, 2nd Ed., Oxford Univ. Press, London, 1947, p. 263.

5. A. I. Alikhanyan, F. R. Arutyunyan, K. A. Ispiryan, and M. L. Ter-Mikaelyan, JETP 44, 1122 (1963); (English trans.) JETP 14, 1421 (1962).

6. A. I. Alikhanyan, Loeb Lectures at Harvard University (unpublished) February 1965.

7. L. C. L. Yuan, Recent Developments in High-Energy Counters, in Proceedings of the Purdue Conference on Instrumentation for High-Energy Physics, May 1965, IEEE Trans. Nucl. Sci., NS-12, No. 4, p. 206 (August 1965).

8. K. Siegbahn, Beta and Gamma-Ray Spectroscopy, North-Holland Pub. Co., 1955.

A SCHEME FOR SEPARATED PARTICLE BEAMS, USING FAST-PULSING MAGNETS

J. A. Kadyk

Recently, considerable progress has been made in the development of fast-pulsing magnets.[1] Although the field strength of these magnets is small, it is sufficient to allow switching between adjacent beam channels, when used together with septum magnets, providing the emittance of the beam is sufficiently small. Rise times of 50 nsec have been achieved, and 10-15 nsec rise times are expected to be achievable.

In addition, there has been an impressive degree of success in the development of devices which can be used to identify particles in the very-high-energy region, i.e., > 20 BeV (Refs. 2, 3, and 4). Although these devices have not been fully proven, they promise to afford identification, perhaps into the region 100-200 BeV.

With these parallel developments in technique becoming realities, it becomes interesting to consider a new method of beam separation at very high energies; this method is, perhaps, subject to less stringent energy-scaling laws than either electrostatic or rf separated beams (or at least different scaling laws).

METHOD

The scheme of particle separation can be explained in terms of Fig. 1. Since all secondary particles are traveling at essentially the velocity of light, it is necessary to provide a means of having the magnet-triggering signal arrive anead of the identified particle by a sufficiently long (and known) time interval that the magnet will be pulsed on just before the particle arrives. Sufficient bending in the particle's path, as shown above, can accomplish this. For purposes of orientation, it is expected that $\theta_1 \approx \theta_2 \approx$ 10-20 deg, and that L = 1000 to 3000 feet.

The difference in transit time between the particle and trigger signal (laser beam) is necessary for: (a) amplification of particle-identification pulse, (b) laser triggering, and (c) pulsed-magnet triggering and rise time. This time difference, Δ, can be easily calculated from the above geometry as follows:

$$\Delta = (D_1 + d + D_2) - L = (D_1 + d + D_2) - (D_1 \cos\theta_1 + d + D_2 \cos\theta_2)$$

$$\Delta = D_1 (1 - \cos\theta_1) + D_2(1 - \cos\theta_2).$$

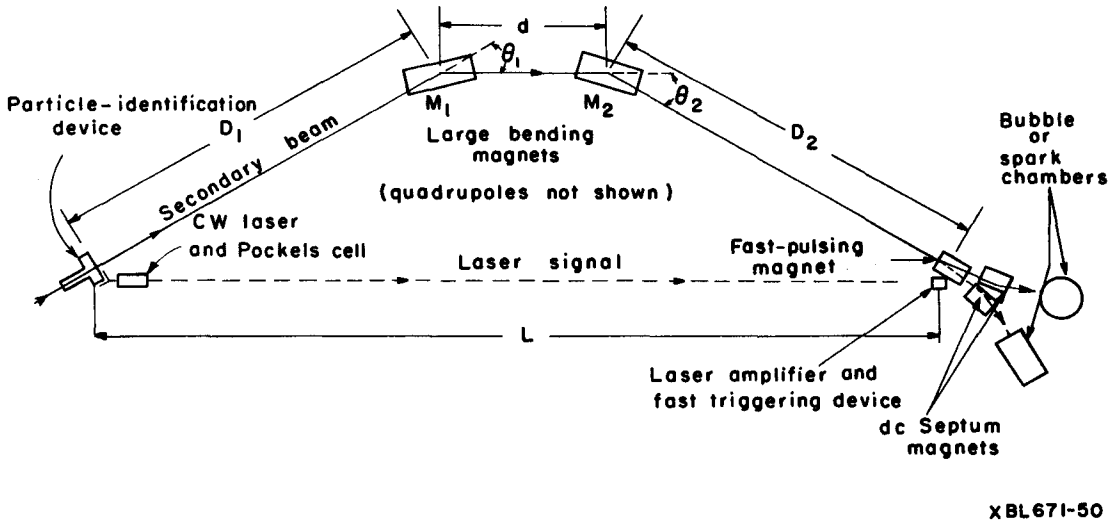

Fig. 1. Illustration of technique for separating particles with fast-pulsing magnets.

The symbols are explained in Fig. 1.

Since θ_1 and θ_2 are small, if we put $\theta_1 = \theta_2 = \theta/2$, and $D_1 = D_2 \approx L/2$, we get

$$\Delta \approx D_1 \frac{\theta_1^2}{2} + D_2 \frac{\theta_2^2}{2} \approx \frac{L}{2} \frac{\theta^2}{4} = \frac{L\theta^2}{8}.$$

Since light travels very nearly 1 ft in 1 nsec, we have

$$\Delta(\text{nsec}) = \frac{L\ (\text{feet})}{8}\ \theta^2\ (\text{rad}^2).$$

Figure 2 shows a graph of delay times as a function of θ (total bending angle) for various beam lengths. Also shown is the total length of assumed 50-kG superconducting magnets M_1 and M_2 at 20, 50, and 100 BeV (L_M is the total length of all magnets).

As an example, suppose that the irreducible delays mentioned above total 40 nsec, and it is desired to separate 50-BeV particles. Then for a 1000-ft beam, one needs a total bend of 32.5 deg, and M_1 and M_2 would each be about 31 feet long; alternatively, a series of bending magnets 62 feet long must be used. If the beam is 2000 feet long (which is only 1.7 $K^{\pm}$ decay lengths), however, only a 23-deg bend and 44 feet of magnets are needed.[5]

INSTRUMENTAL TIME DELAYS

The intrinsic difficulty in making such a scheme succeed seems to be in reducing the time delays mentioned above. These will be discussed in turn.

Amplification of Particle Pulse

As an example of one means of particle identification, we might choose the disc counter, discussed by Cocconi.[2] The Cerenkov light from this counter could be allowed to strike a photomultiplier with short transit time. Existing photomultipliers (e.g., RCA 1P21) can be made to give approximately 1-volt signals with 20-25 nsec delays. However, special devices under development promise to give delays at least as short as 10 nsec. An example would be the transmission photomultiplier sketched here (Fig. 3). The voltage between foils or electrodes is typically several kilovolts, leading to very short delays.

Laser Triggering

In order to get very fast response from a laser, it should probably consist of one laser operating in a CW mode, which can be used to discharge an energized laser at the deflection magnet. The two lasers are separated by a

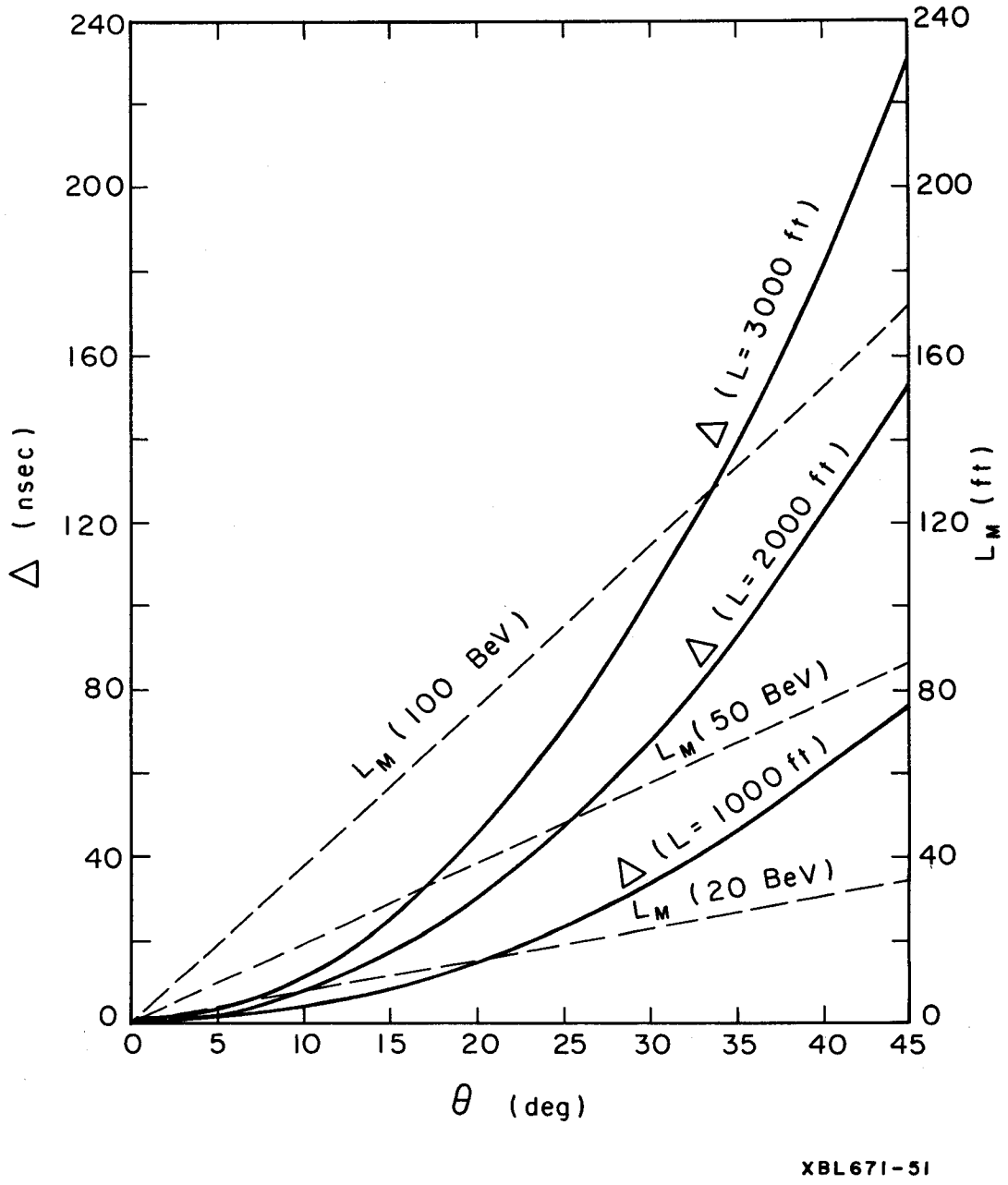

Fig. 2. Difference in transit time, Δ, between arrival of the particle and trigger signal vs total bending angle (θ). Values for total magnet lengths (M_1 plus M_2) in feet are the same as the transit-time difference values.

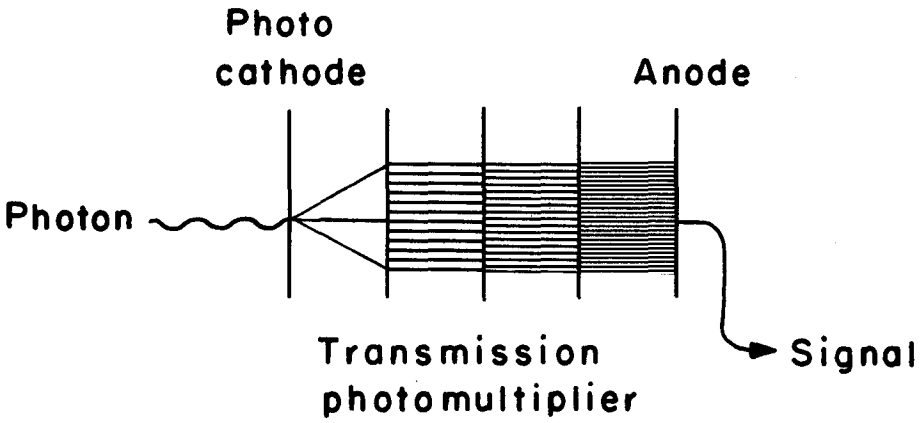

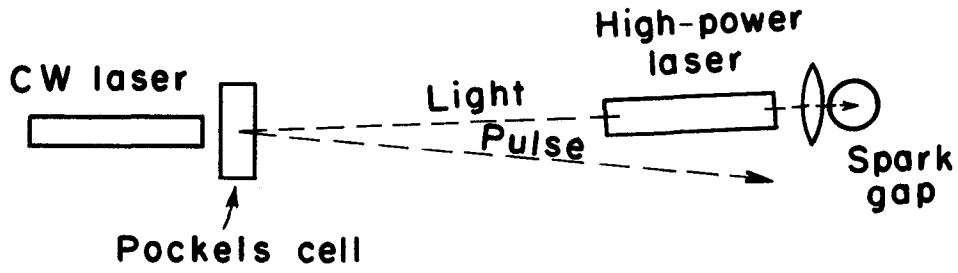

XBL671-52

Fig. 3 (above). Schematic of transmission photomultiplier.

Fig. 4 (below). Diagram of use of Pockels cell and lasers to produce fast pulsing.

Pockels cell, which has an intrinsic response much shorter than a nanosecond. Effectively, the turn-on time is limited only by the buildup of voltage on the Pockels cell, which probably can be done in a few nanoseconds. A scheme suggested by Kerns is illustrated in Fig. 4. Using the deviation of the extraordinary ray which traverses the Pockels cell, the CW light beam can be swept onto an excited laser located at the triggering gap. This has the advantage of being essentially an on-off device, whereas a Pockels cell used with the ordinary ray has some light leakage. Also, for multiple triggering, i.e., for several beam particles, different gaps might be triggered in succession by sweeping the CW beam past them. Flash tubes to energize the lasers will fire just before the anticipated beam bursts to the bubble chamber, and the flash will last sufficiently long that several laser pulses are possible, corresponding to several particles directed into the chamber.

Pulsed-Magnet Triggering

The laser signal can be focused on the electrode of a spark gap in order to quickly switch power to the fast-pulsing magnet. It is expected that the breakdown of the spark gap will occur in less than 5 nsec. The anticipated rise time of the magnet is about 10-15 nsec, so that the total delay from light signal until full magnetic field is present might be approximately 20 nsec. The duration of the pulsed field can be made as short as necessary, by connecting a shorted transmission line to the magnet input (i.e., 10-20 nsec). In principle, repetition of pulses could occur after this very short delay by triggering a number of different gaps in succession.

The sum of these several delays may well be expected to be at least as short as 40-50 nsec. As can be seen from Fig. 1, this would permit operation with a reasonable magnet length.

ACCIDENTAL RATES

In order that the separated beam be relatively pure, the accidental rate must be determined. Let us assume a ratio (B) of background to wanted particles at the target, and a spill time of 1 msec for the beam burst (this is probably about right for the next generation of large bubble chambers, but if it is too long, the results should be scaled appropriately). Then, typically, for separated $K^{\pm}$ beams, the background ratio will have increased to $B \exp[L/(\gamma\beta c\tau_K)]$ at the pulsed magnet. If the pulse length is 20 nsec, then the purity of the beam can be deduced as follows: Let

N = number of wanted particles extracted.

Then, the total number of particles in 1 msec is

$$BN \exp[L/(\gamma\beta c\tau_K)].$$

Hence, the contamination fraction is

$$\frac{20\times 10^{-9}\ \text{sec}}{10^{-3}\ \text{sec}}\ BN \exp[L/(\gamma\beta c\tau_K)] = 2\times 10^{-5}\ BN.$$

For B = 10, $\exp[L/(\gamma\beta c\tau_K)] = 10$, and N = 5, the contamination is ≈10%, providing the beam spill has no rf structure. Here N = 5 should be at least enough beam particles, and N = 1 or 2 may be more reasonable, giving proportionately higher purity. Of course, if it is technically feasible to pulse the magnet many times, a long spill can give approximately 1000 wanted particles to a counter or spark chamber on each accelerator cycle.[6]

EMITTANCE

A small enough emittance must exist for the secondary beam to permit separation. Indications are that targets as narrow as 0.13 mm may be used. From the known constancy of transverse momentum of the secondary particles, we expect most of the beam to be contained within about a 2-mrad cone, and thus arrive at an emittance of 0.26-mm-rad. This appears to be small enough for use of the fast-pulsed separator magnet.

SCALING LAW

The difficulty in going to higher momentum with this system is associated with the increase in bending power needed, measured by L_M. Since $\Delta = 1/8(L\theta^2)$ = constant (determined by shortest achievable delay times), we have:

$$\theta = \sqrt{\frac{8\Delta}{L}} = \frac{(50\ \text{kG})\ L_M}{(B\rho)} \propto \frac{L_M}{P},$$

$$L_M \propto P\sqrt{\frac{8\Delta}{L}},$$

where P = beam momentum. Now, if L is assumed fixed, then $L_M \propto P$. However, if L is assumed $\propto P$, then $L_M \propto \sqrt{P}$.

This scaling law is to be compared with those of electrostatic and rf separators (L_S = total separator length needed).

Electrostatic separators: $L_S \propto p^3$ (or p^2, if emittance assumed $\propto 1/p$)

rf Separators: $L_S \propto p^2$, for fixed frequency.

W(power) $\propto p^2a^2$ (= constant, if $a \propto 1/p$),

where a = angular deflection in rf separator.

Most of the quoted numbers and many of the ideas contained herein are the result of conversations with Glen Lambertson, Ed Hartwig, Joe Murray, Dick Mack, Fred Kirsten, and Quentin Kerns, none of whom should be held responsible for mistakes or unjustified claims made in this paper.

References

1. E. Hartwig (private communication); see also 200 BeV Accelerator Design Study, June 1965, UCRL-16000, Vol. I, p. IX-70.

2. J. V. Allaby, G. Bellettini, G. Cocconi, A. N. Diddens, S. Gjesdal, G. Mattiae, E. J. Sacharidis, A. Silverman, A. M. Wetherell, J. P. Garron, L. Hugon, R. Meunier, M. Spighel, J. P. Stroot and P. Duteil, The First Experiment Using the CERN Slow Extracted Proton Beam: Particle Production in 19.4 GeV/c Proton-Proton Interactions, CERN NP/Int. 66-2, June 1966; and P. Duteil, L. Gilly, R. Meunier, J. P. Stroot, and M. Spighel, Rev. Sci. Instr. 35, 1523 (1964).

3. J. J. Murray, Recent Progress in the Development of a Microwave Gated Photomultiplier - The DCFEM, 1966 SLAC Instrumentation Conference.

4. M. L. Ter-Mikaelyan, 1966 SLAC Instrumentation Conference and Soviet Phys. Doklady 5, 1015 (1961); A. I. Alikhanyan et al., Soviet Phys. JETP (English Translation) 17, 756 (1963).

5. Although this may seem like a lot of magnet length, it should be pointed out that the magnet apertures can probably be made quite small, so that total field volume is not a big departure from present beams. Note that the present rf beam (beam 4) at BNL for the 80-inch chamber contains 72 ft of conventional bending magnets with much larger apertures than are anticipated for the present scheme.

6. A standard way to improve the purity of the beam beyond the values discussed here is to simply veto all identifications when more than one particle occurs within the gate length of the pulsed magnet. Appropriate anti-coincidence counters and conventional techniques may be used to accomplish this.

D. EQUIPMENT

PRELIMINARY CONSIDERATIONS ON THE CHARACTERISTICS OF A LARGE SPARK-CHAMBER DETECTING SYSTEM FOR COMPLEX HIGH-ENERGY EVENTS

A. Roberts

The recent report of the bubble-chamber study group on the problems facing bubble-chamber analysis of high-energy events has prompted me (and others) to look more closely at the alternative use of spark chambers and associated electronic equipment for the analysis of high-energy interactions, to see whether their use can overcome any of the difficulties associated with bubble chambers. We will not discuss neutrino interactions, since I have not considered them. It will not be the purpose of this note to solve any problems, but only to point out directions in which solutions may be sought.

To begin with, we list demonstrated properties of spark-chamber detectors at lower energies:

1. Momentum accuracy as great or greater than the bubble chamber (less scattering, no turbulence, and so on);
2. Ability to trigger on events specified by counter logic;
3. Very high total data-gathering rate;
4. Flexibility in experimental arrangements, e.g., complete separation of gamma-ray detection from momentum measurement, and use of many counter techniques such as time-of-flight, and others;
5. A wide choice of data-gathering and data-analysis procedures;
6. Advanced operational automatic-data-analysis systems.

As a basis for the design of a detecting system, the following characteristics of high-energy events, produced by particles of, say, 50 BeV/c or more, are relevant:

1. The multiplicity of charged particles is high, averaging 6 or more.
2. The multiplicity of neutral pions averages about 3; zero neutral-pion events are relatively rare.
3. There are so many channels that the average cross section for any individual channel is very small—of the order of a microbarn. Selective triggering is of the utmost importance if reasonable results are to be obtained on any channel without first amassing millions of pictures.
4. The average inelasticity of high-energy events, deduced from cosmic-ray data, is about 0.5. This is the fraction of the original energy retained by

the primary particle after the collision. Therefore, there is at least one very fast forward particle (which may not be the original one, for reasons such as exchange of charge, and strangeness).

5. Most particles have transverse momenta of 400 MeV/c or less. This implies that a forward cone of half-angle 50 mrad will contain nearly all particles of 8 BeV/c and over.

6. Very slow (< 1 BeV/c) particles are frequently present. This means that sideways and backward angles must be observed if all particles are to be seen. Long narrow detectors are not desirable for this purpose.

In addition, we note several facts pertaining to data analysis:

1. The identification of charged particles increases in difficulty with increasing momentum. The best technique available at present involves the gas Cerenkov detector, which measures particle velocity.

2. The only Cerenkov detector capable of measuring simultaneously the direction and velocity of several particles over a considerable angular range is the Cerenkov ring-image detector.

3. Without the detection of gamma rays, event analysis will be limited to a very few channels. It is therefore important to detect the existence, and to measure the direction and at least the approximate energy of all gamma rays produced. For gamma-ray detection and kinematics, we have a choice of two methods: either the heavy-plate spark-chamber shower detector, or momentum analysis of electron pairs from a thin radiator. The latter can be reconciled with the requirement for high detection efficiency only at great expense (many plates, large volume of magnetic field).

4. The detection of heavy neutrals, like neutrons, is highly desirable; but failure here will not block nearly as many channels as the escape of neutral pions. Some high-energy neutral kaons or baryons (Λ, Ξ^0) may escape detection, but this will in general lower channel detection efficiency rather than destroy it.

5. Event identification will require very accurate momentum determination; just how accurate must be the subject of a later Monte Carlo investigation. The accuracy must be sufficient to identify any missing particles. The primary momentum must be very well known.

From these considerations we can proceed to sketch the characteristics of a possible high-energy spark-chamber system:

1. Momentum analysis to at least 1% accuracy up to 3 BeV/c, and to 30 MeV/c at energies above 3 BeV/c. (The figures are subject to modification after Monte Carlo analysis.) This implies that the greatest length of magnet is needed to cover the forward cone of fast particles, and therefore the magnet need not occupy an excessive volume; perhaps 2 by 1 by 3 meters is big enough.

2. The region in which momentum and velocity are measured must be surrounded by a shell of heavy-plate gamma-detecting chambers, with 98% or better efficiency for gamma rays of 50 MeV or higher. Existing data on gamma-ray showers in spark chambers indicate that ± 1 deg precision in direction, and 10-20% in energy are attainable. This requirement runs into difficulties with items such as magnet yokes and coils. The brute-force solution is to put this array of gamma-ray chambers inside the magnet, covering the entire 4π solid angle at the target.

3. For the forward cone of fast particles (greater than 5 BeV/c), one should try to use Cerenkov ring detectors, since the cone is sufficiently limited to allow radiators of 1-2 meters without excessively large optics. For successful use, however, the radiator must be free of magnetic field. Consequently the topology of the system demands a field-free forward cone, followed by a magnetic field, a magnetic field for analyzing particles emitted outside the cone, and the whole enclosed by heavy-plate spark chambers so that no gamma ray escapes unseen. The volume of magnetic field needed is large, though not in comparison with the 100 cubic meters proposed for the bubble chamber.

The usefulness of the Cerenkov ring detector may be established by looking at a few sample calculations of its properties. Figure 1 shows a sketch of such a detector.

Table I illustrates some numerical values; one might want to use two or more ring detectors in succession to cover a wide range of γ.

Since for a given momentum the γ of protons, kaons, and pions are about as 1:2:7, the above examples indicate that proton identification and kaon identification are possible in a given range of γ. In addition, the spark chambers before and after the ring detector show which track is being identified, and by locating the center of the Cerenkov ring, improve the velocity accuracy.

Figure 2 gives a sketch of a first approximation to a system of this sort.

A magnetic field covering an area about 4×7 meters has a central field-free region to accommodate the Cerenkov detectors. The central region cannot be shielded with iron without destroying outgoing charged particles, so the field cancellation will have to be done with bucking coils. The depth of the field in the Z direction will be about 1.5 meters; the entire boundary of the $1.5 \times 4 \times 7$ m volume will be covered by gamma-detecting spark chambers, probably with electronic (non-visual) readout.

Figure 3 is a sketch of how the desired field configuration might be achieved.

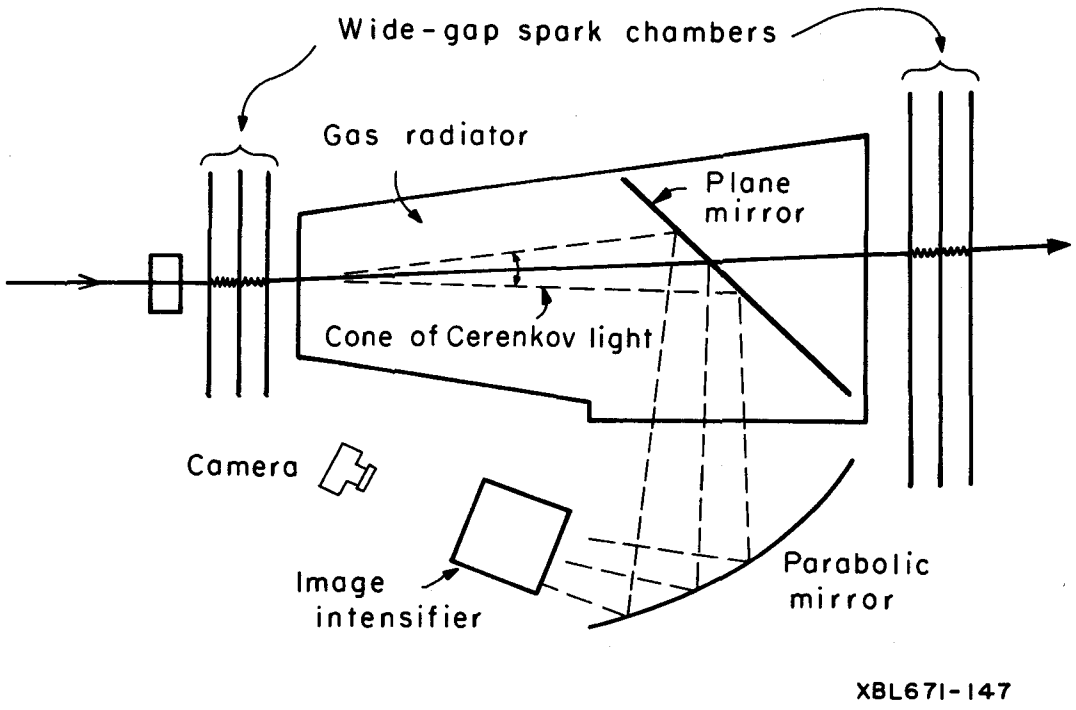

Fig. 1. Cerenkov ring-image detector, with trajectory-defining spark chambers before and after.

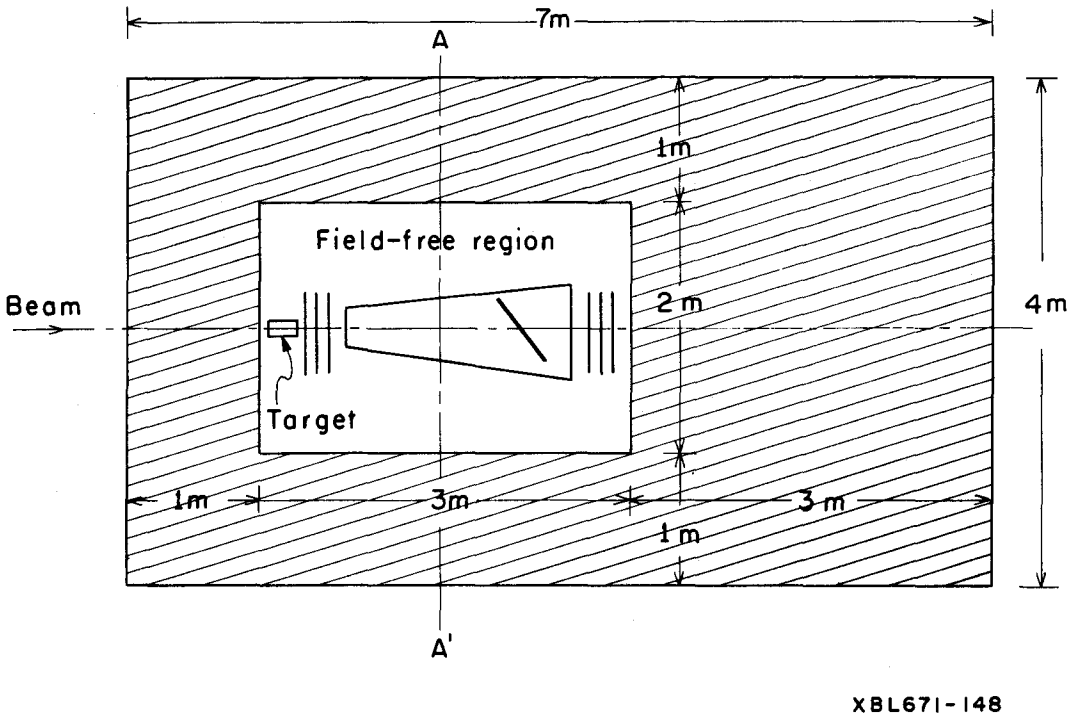

Fig. 2. Schematic diagram illustrating the proposed way of using the Cerenkov ring detector in combination with a magnetic field. Shading indicates magnetic field.

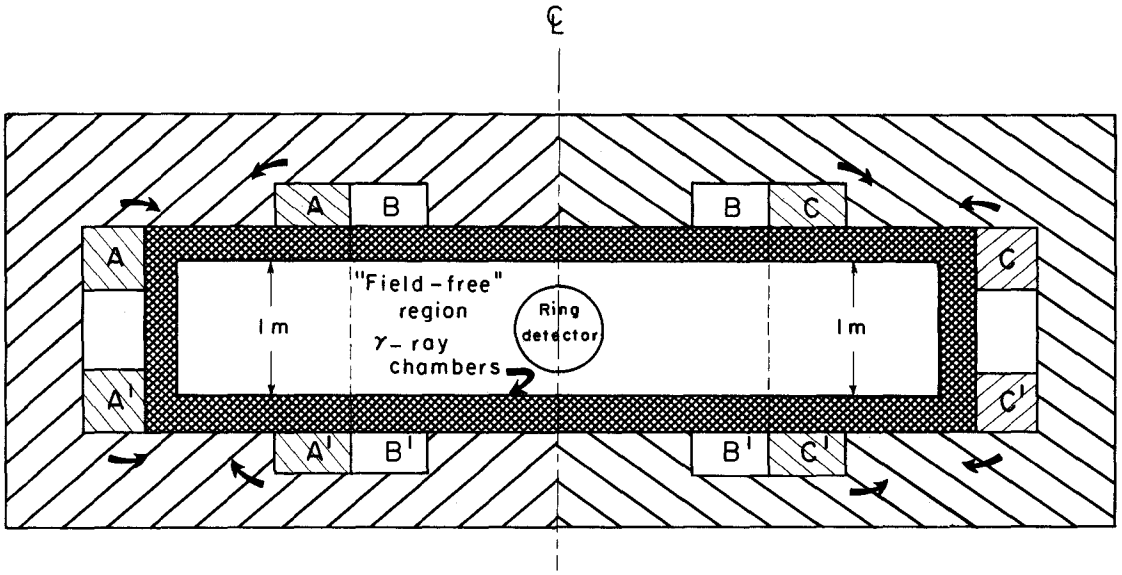

XBL671-149

Fig. 3. Elevation of section A-A', Fig. 2, showing coils A-A', C-C', and bucking coils B-B' used to obtain a field-free region. Yoke may not be needed over field-free region.

Table I. Numerical values.

Case I. Radiator 0.5-m long. Index n = 1.005. Mirror covers cone of half-angle 150 mrad. Mirror diameter 30 cm, aperture f/1.66, focal length 50 cm. Threshold ($\gamma = E/mc^2$) = 10.

γ	Cone angle (mrad)	No. of quanta	Radius of image (cm)
15	0.075	180	3.75
30	0.095	225	4.75
∞	0.10	250	5.0

Case II. Radiator 1.50-m long. Index n = 1.002. Mirror covers cone of half-angle 110 mrad. Mirror diameter 45 cm, aperture f/1.1. Focal length 50 cm. Threshold γ = 16.

20	0.038	120	3.8
40	0.058	220	5.9
∞	0.063	300	6.3

CONSIDERATIONS ON THE USE OF HYDROGEN-NEON MIXTURES IN THE LARGE HYDROGEN CHAMBER

George E. Kalmus

In this paper I will be dealing with one possible mode of operating the large hydrogen chamber, that is, by filling it with mixtures of hydrogen and neon.[1] The purpose of doing this is to detect and measure γ rays (usually from the decay of π^0 mesons) by conversion to $e^{\pm}$ pairs in the liquid. There are other ways in which γ rays can be detected, which may be preferable in certain experiments but which I will not deal with here.

There is a general feeling among physicists that as the incident-particle energy increases, the importance of catching all the secondary particles including the neutrals also increases. When more than one neutral is missing, clearly the event cannot be constrained. At 50 BeV the pion multiplicity is ≈ 6, so that on the average there are two π^0 per event.

In this paper I assume that it is possible to operate a bubble chamber with all mixtures of hydrogen and neon.[1] The numbers calculated for Table I and Figs. 1 through 5 are based in general on the fact that the chamber is ≈ 8 m long (along beam direction) and has a diameter of ≈ 4 m. I also assume in all the calculations that the chamber is in a field of 40 kG.

The purpose of tables and graphs is to enable one to optimize the conditions for any particular experiment.

In Table I are listed some of the physical parameters of interest that change with the concentration of the neon-hydrogen mixture.

A comment should be made about the uncertainty in the momentum of a measured track due to small-angle nuclear scatterings; this is discussed by Gluckstern[2] and applies only to strong-interacting particles. At energies greater than 10 BeV/c, the cross sections for small-angle scatters are less than one-half the geometric cross sections; therefore their frequency of occurrence is less than one for every two interactions lengths. By measuring the momentum of the track in sections and comparing these momenta with each other, one may obtain an idea of where the scatters occur. The error due to the nuclear scattering term varies as θ^2_{min}, where θ_{min} is the minimum scattering angle that can be detected. Now θ_{min} decreases with energy, because although small angles cannot be directly seen, the recoil proton in a reaction in hydrogen is a signature for a scatter.

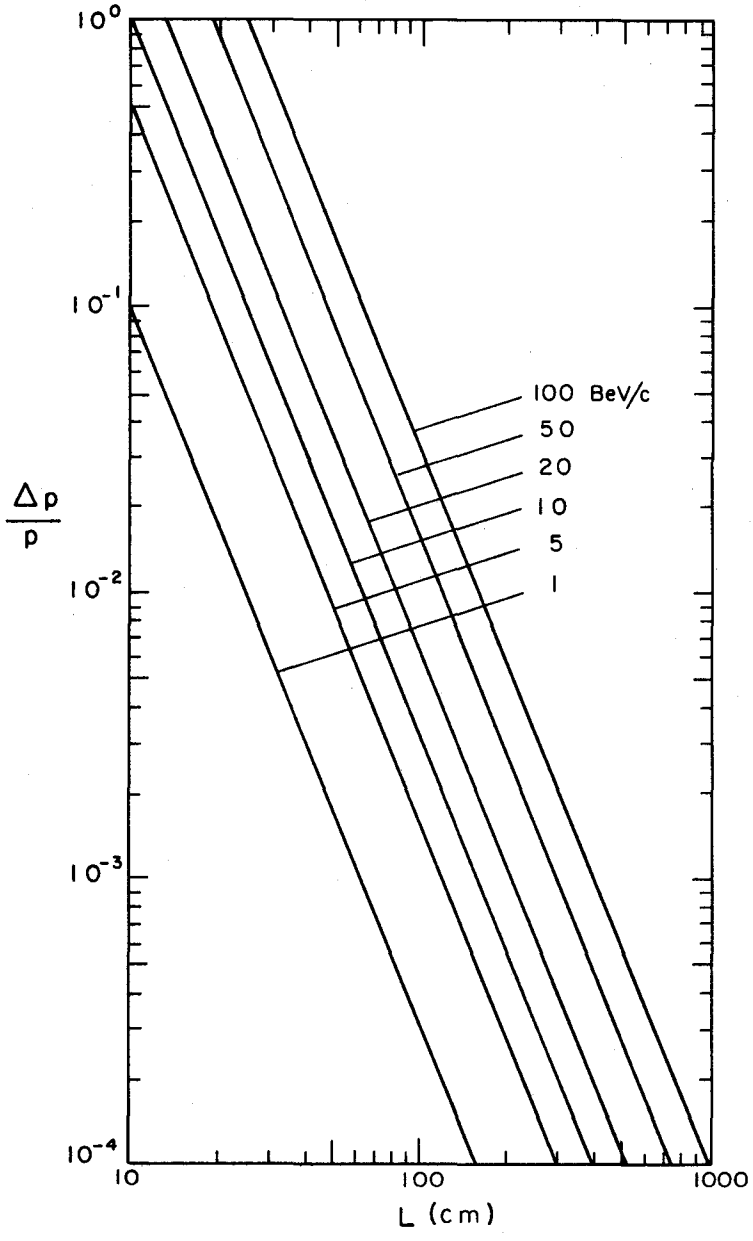

Fig. 1. Error in measuring the momentum of various momenta tracks as a function of length due to the setting error only. Tracks have been assumed to be flat, i.e., perpendicular to the magnetic field and parallel to the film plane. The formula used to plot these curves was derived from Gluckstern's paper[2] and is based on the assumption that the measurement was made with a flying spot device, and that the error on the master point is 100 μ in space.

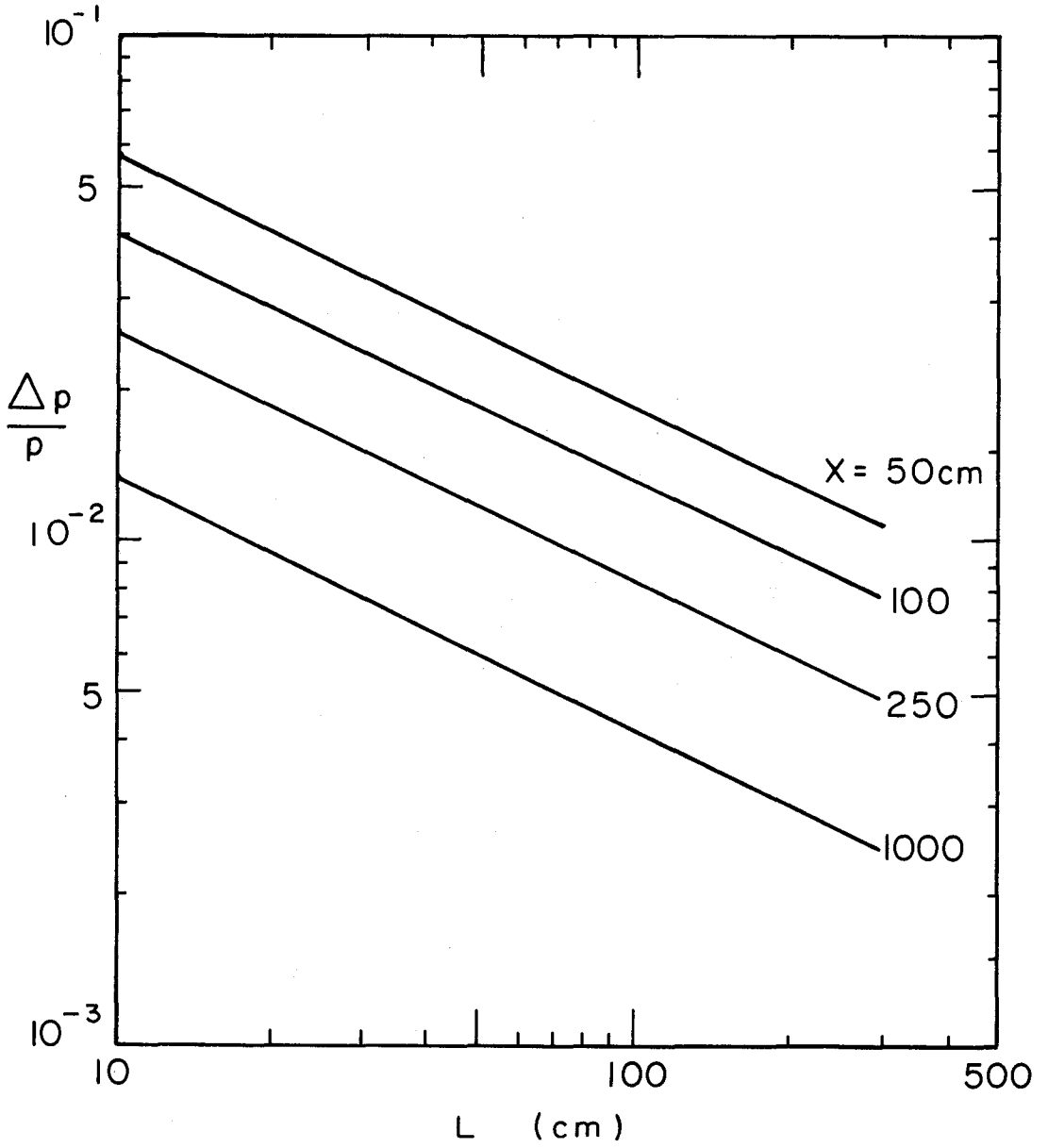

Fig. 2. Momentum error due only to multiple scattering in measuring a 20-BeV/c track in hydrogen (X_0 = 1000 cm) and in liquids of X_0 = 250, 100, and 50 cm. The formula used for hydrogen is given by Gluckstern[2] and applies to electrons with momenta greater than 10 BeV/c. (The error in momentum measurement when considering a 1-BeV/c electron is ≈ 15% less than for a 20-BeV/c electron, but for a 100-BeV/c electron, $\Delta p/p$ is ≈ 8% greater than for a 20-BeV/c one.) The multiple-scattering error for strongly interacting particles is within a few percent of that for electrons. The curves for other liquids were obtained by scaling the hydrogen curve by $\sqrt{X_0(H_2)/X_0(\text{liquid})}$.

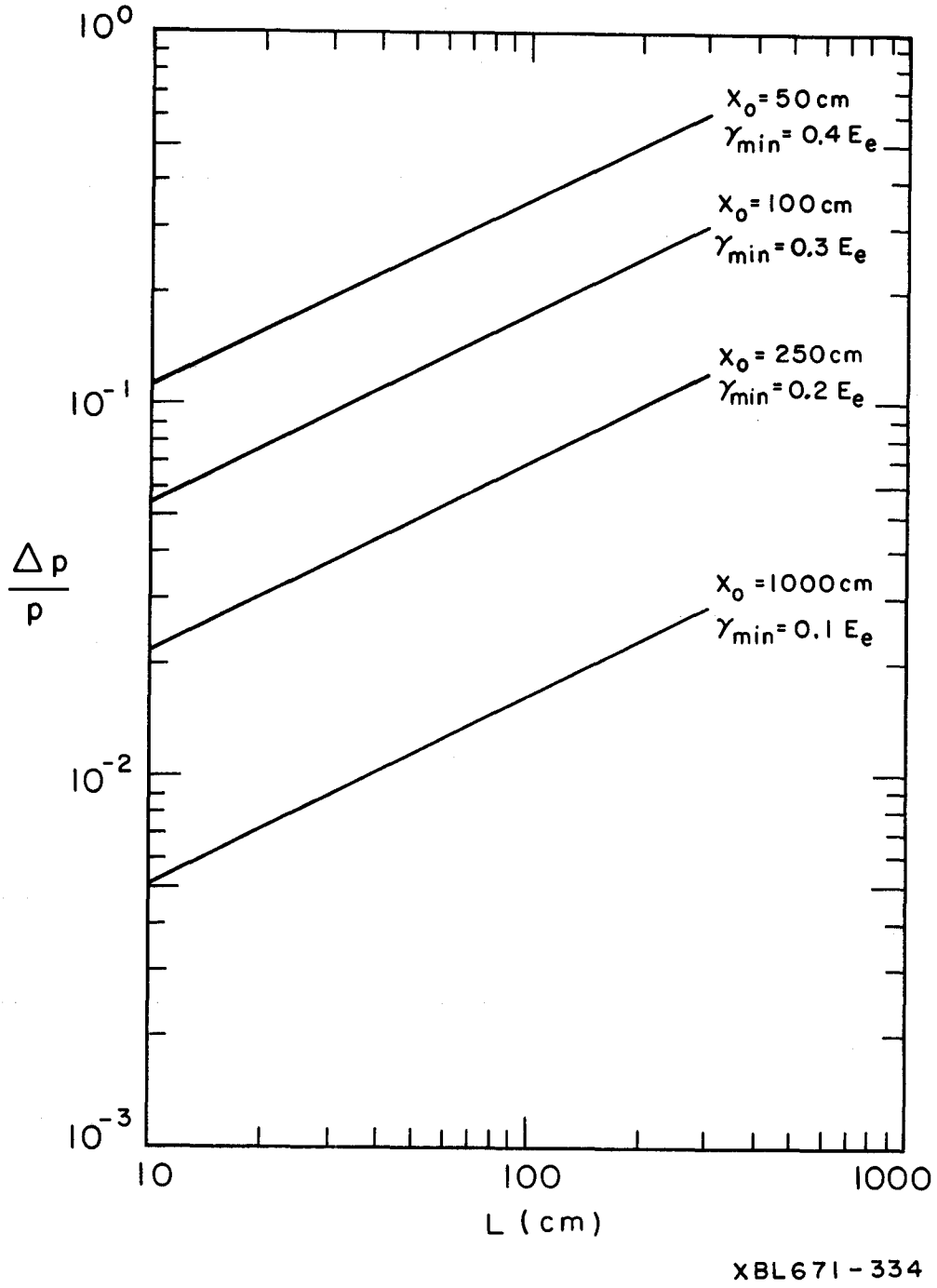

Fig. 3. Momentum error due to bremsstrahlung loss for electrons as a function of track length for liquids of the same radiation length as Fig. 2. In the calculation, the method of Behr and Mittner was used to measure the electrons.[3] This method depends on one's being able to detect large single radiation losses by some means. I have chosen the minimum single radiation which can be detected (γ_{min}) as shown in the graph for each radiation length. These have been chosen somewhat conservatively; however, they are probably not too far wrong. Note that the error due to bremsstrahlung loss is not Gaussian and that the method used is only approximate.

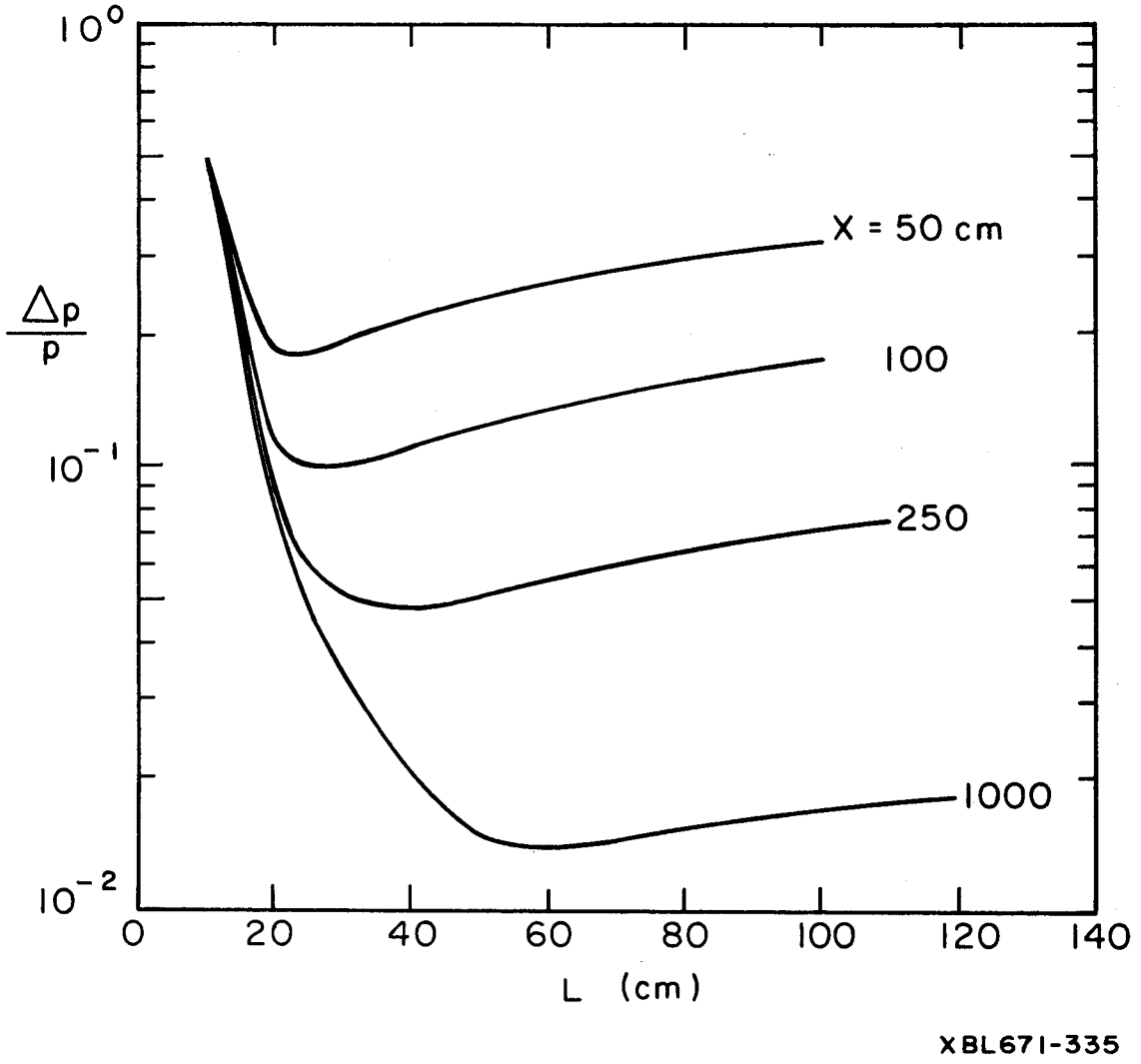

Fig. 4. Total error in the momentum, with no correlation assumed for a 5-BeV/c electron. It can be seen from Figs. 4 and 5 that there is an optimum length for measuring an electron track. Also, it can be seen that this optimum length is not very long compared with the dimensions of the proposed "monster" chamber. Fisher's papers give optimum lengths for measuring angles in hydrogen, and also show calculations and optimizations of other parameters for pure hydrogen.[4,5]

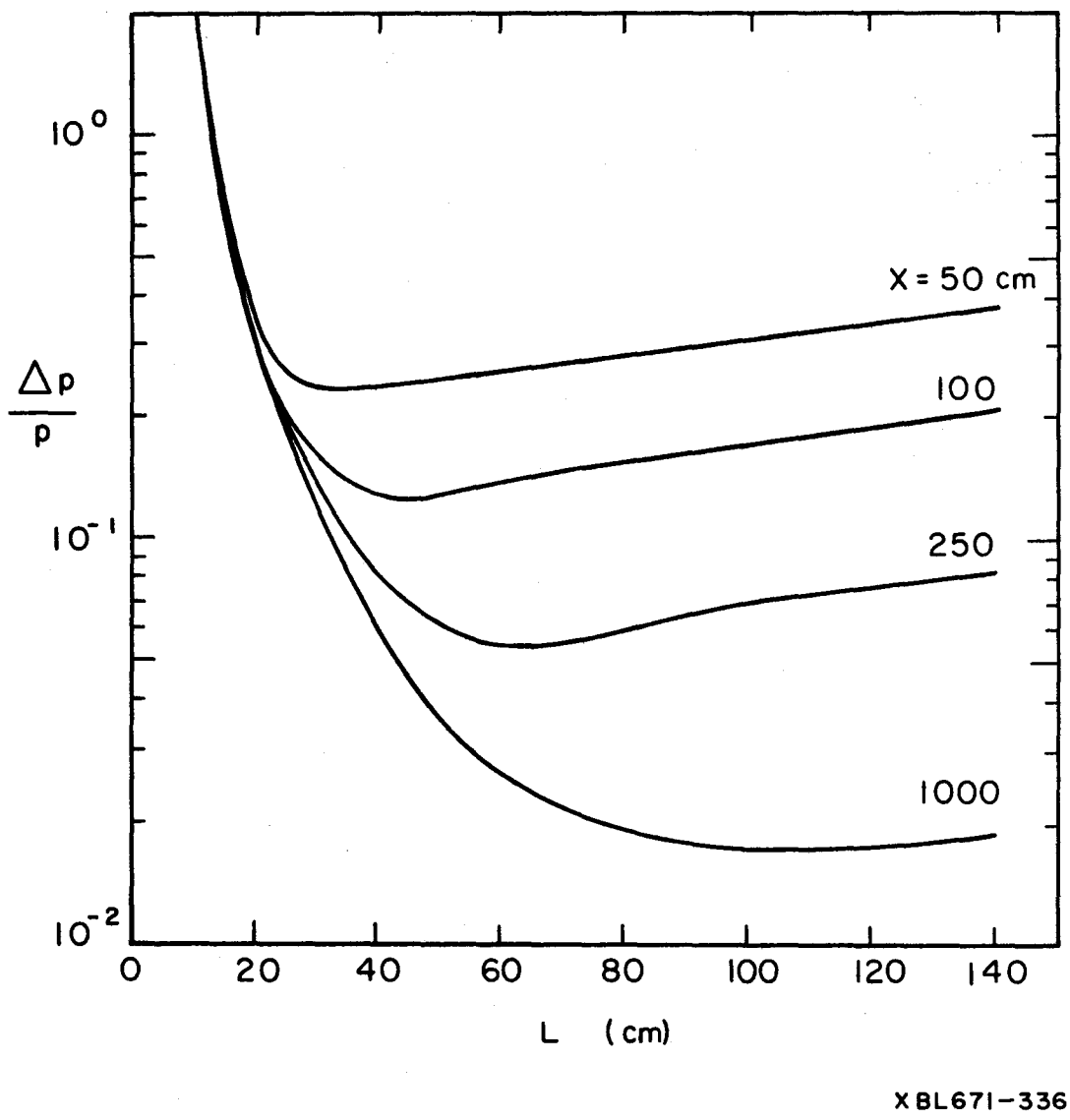

Fig. 5. Same as Fig. 4, but for 20-BeV/c electron.

Table I. Properties of hydrogen-neon mixtures.

1	2	3	4	5	6	7	8	9	10	11	12
H_2 vol. (%)	ρ (g/cc)	Int. length (cm)	Int. in H_2 (%)	X_o (cm)	Conv. length (cm)	200 cm $P_{1\gamma}$	200 cm $P_{4\gamma}$	300 cm $P_{1\gamma}$	300 cm $P_{4\gamma}$	400 cm $P_{1\gamma}$	400 cm $P_{4\gamma}$
100	0.0585	470	100	995	1280	0.15	5×10^{-4}	0.20	1.6×10^{-3}	0.27	5×10^{-3}
95	0.103	397	80	384	495	0.32	1×10^{-2}	0.46	0.045	0.56	0.098
90	0.148	337	65	238	306	0.48	0.053	0.62	0.15	0.73	0.28
85	0.182	296	54	172	220	0.60	0.13	0.74	0.30	0.84	0.50
80	0.237	263	45	134	172	0.69	0.23	0.82	0.45	0.90	0.66
75	0.281	237	38	111	142	0.76	0.33	0.88	0.60	0.94	0.78
70	0.326	215	32	94	121	0.81	0.43	0.92	0.72	0.96	0.85
50	0.504	158	17	59	76	0.92	0.72	0.98	0.92	0.995	0.98
25	0.727	119	6	40	51	0.98	0.92	0.998	0.99	1.0	1.0
0	0.95	95	0	30	39	0.99	0.98	1.0	1.0	1.0	1.0

Column
1 - Percentage of H_2 by volume in mixture
2 - Density of mixture (g/cm^3)
3 - Nuclear interaction length (cm)
4 - Percentage of interactions on free protons
5[a] - Radiation length [cm(X_o)]
6 - Conversion length (at ∞ energy) = 9/7 X_o (cm)
7 - Probability of converting 1 γ (∞ energy) (200 cm)
8 - Probability of converting 4 γ's (∞ energy) (200 cm)
9 - Probability of converting 1 γ (∞ energy) (300 cm)
10 - Probability of converting 4 γ's (∞ energy) (300 cm)
11 - Probability of converting 1 γ (∞ energy) (400 cm)
12 - Probability of converting 4 γ's (∞ energy) (400 cm)

a. Calculated from $X_o = \frac{137\, m^2\, c^4 [1 + 0.12\, Z^2/(82)^2]}{4\, e^4\, NZ\, (Z + \xi)\, \ln(183\, Z^{-1/3})}$, where $\xi = 1.39$ for H_2 and 1.30 for Ne.

Assuming that a 100-MeV/c proton can be detected in hydrogen (≈3 mm), then at 50 BeV/c the momentum error due to this term is $\approx 10^{-3}$ for a track 200-cm long; this is smaller than the multiple scattering error. When the interaction does not occur in pure hydrogen, and the incoming particle reacts with a nucleon in the neon, the signature no longer holds. However, for mixtures of hydrogen and neon in which the fraction of interactions in hydrogen is $\gtrsim 1/2$, the mean free path for an interaction in neon is $\gtrsim 4$ times the interaction length of the mixture.

In conclusion, I have tried to present only some of the parameters which are important in designing an experiment in hydrogen-neon mixtures. The parameters also give a good indication on how large such a chamber has to be in order to detect and measure secondaries to a certain accuracy, especially γ rays from π^0's. One final point should be made; I have throughout assumed a magnetic field of 40 kG. An increase in this field would be of great benefit to increased accuracy.

References

1. A. Prodell, Rev. Sci. Instr. 36, 1174 (1965).
2. R. L. Gluckstern, Nucl. Instr. Methods 24, 381 (1963).
3. L. Behr and P. Mittner, Nucl. Instr. Methods 20, 446 (1963).
4. C. M. Fisher, The High Field Bubble Chamber Project, Rutherford High Energy Laboratory, Physics Group Note HFBCP/5, July 1966, Appendix I, Eq. (11).
5. C. M. Fisher, First Thoughts About Bubble Chamber for 300 GeV Machine, Rutherford High Energy Laboratory Report, HFBCP/P/7, August 1966.

SOME DESIGN CONSIDERATIONS FOR A LARGE HYDROGEN BUBBLE CHAMBER

J. B. Shafer

The following is a resumé of information gathered during the seven-week Study Program and presented briefly at the seminar of August 25. The writer is indebted to Bill Fowler, Bob Watt, Paul Hernandez, Bob Meuser, and Clyde Taylor (Livermore) for much of the material discussed here. A series of deliberations with other members of the Bubble-Chamber Subgroup of the Study Program (G. Kalmus, T. Toohig, J. Kadyk, R. Ely, and R. Plano) have been helpful.

INTRODUCTION

The chief topic under investigation by the writer was the "aspect ratio" desirable for a monster bubble chamber, a volume of approximately 100 m^3 being assumed. Heretofore, an aspect ratio (length-to-width ratio) of 1 to 1 has been considered optimum for large chambers; the justification has been that broad incident neutrino beams and isotropically emitted gamma secondaries are better studied with a wide chamber than with a narrow, long one. The usual design has been that of an upright, circular cylinder;[1] examples are the 12-ft (diameter) chamber of Argonne National Laboratory, the 14-ft chamber of BNL,[2] and the 3.5-m chamber of CERN. (The only exception is the comparatively small chamber of Saclay, which is 1.6 m in diameter by 4 m long.)

Engineering considerations, though not clearly spelled out in reports, have evidently played a dominant role in existing bubble chamber designs. Because of the comparative simplicity in the construction of a cylindrical chamber body and of a circular (superconducting) magnet, the upright-cylinder design has dominated recent developments. The physics grounds for such a design do not seem particularly solid (see below). Further, with the advent of unusually shaped superconducting magnets of appreciable size (the Avco magnet discussed below and the Taylor-designed magnet for the Alvarez balloon project), it appeared to several Study Program physicists that the question of the geometry of a monster chamber should be re-examined in the light of recent physics and engineering developments.

PHYSICS CONSIDERATIONS

Neutrino Interactions

Previous calculations by Stevenson and Chinowsky[3] on the use of neutrino beams, which will be produced with fairly high intensity by the 200-BeV accelerator, have dealt only with the energy range $1 \leq E \leq 10$ BeV. However, Toohig's studies[4] indicate:

1. Neutrino fluxes, perhaps to 100 BeV, will be usable;
2. Neutrinos incident on a chamber will be contained in a narrower cone than might have been expected.

Figure 1 presents a plot of Toohig's, with some additions. His results are the values of total neutrino flux, n_ν (in units of interactions per unit length), incident on a circular area of the indicated radius R; curves of n_ν vs R for several pion momenta are represented by the solid lines. Note that the flux is still useful for energies greater than 20 BeV; and that for such energies, a radius of 2 m is the maximum required for nearly total acceptance.

For a fixed chamber volume, it is very clear from Fig. 1 that the aspect ratio should be greater than 1 for maximization of the total number of interactions. The dashed lines added to Toohig's curves represent the total number of interactions per day for 10-BeV and 40-BeV neutrinos for the indicated radius, with the volume always equal to 100 m^3. (The chamber is assumed to be a horizontal cylinder.)

From Fig. 1, it can be concluded that a ratio of length (L) to diameter (D) of 3 to 1 (an aspect ratio of 3 to 1) is preferable to a ratio of 1 to 1. Other considerations (transverse momentum in production and decay processes, or simply the curvature of a medium-energy beam of charged particles) probably make the choice of a radius less than 1.7 m undesirable.

We conclude that a diameter of 3.5 m and a length of 10 m is a good choice for neutrino physics.

Strong Interactions

One particular interaction for which the writer has studied the kinematics at high energy is

$$K^- + p \rightarrow K^+ + \Xi^-.$$

As incident energies approach 100 BeV, kinematic behavior becomes almost completely independent of the comparatively negligible masses of incident or product particles; therefore, the momenta and angles in the c.m. system and in the laboratory system hold for any two-body reaction, such as

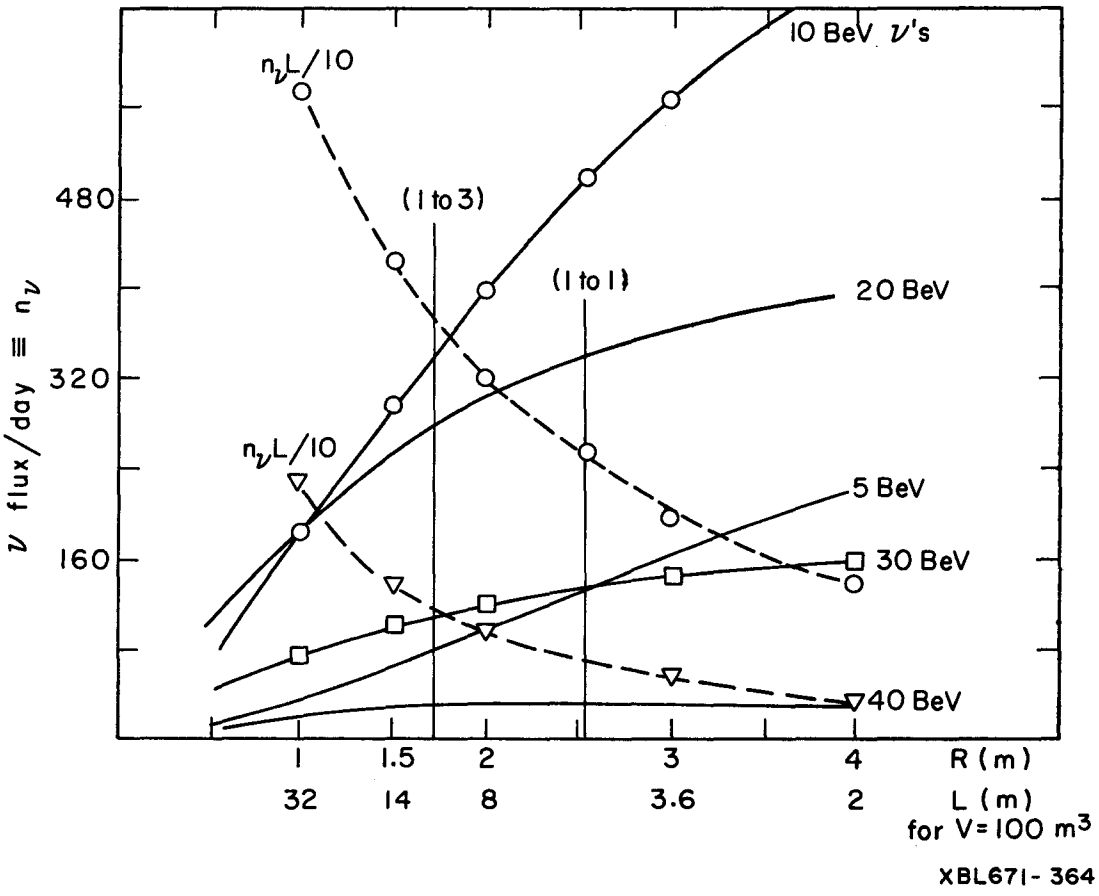

Fig. 1. Neutrino interactions per day in liquid H_2 vs the radius of a cylindrically shaped H_2 chamber. The solid lines show the interactions per day per meter for a given radius and the dotted lines show the interactions per day for a fixed volume of 100 m^3. $\pi \rightarrow \nu$ in a 1000-m beam. The ordinate is interactions per meter per day.

$$\begin{matrix}\pi^- \\ K^-\end{matrix} + p \rightarrow \begin{matrix}N^{***} \\ Y^{***}\end{matrix} + \begin{matrix}\pi \\ K,\end{matrix}$$

where N^{***} and Y^{***} represent some resonance a little higher in mass than those already discovered. The reaction producing the Ξ (or some Ξ^{***}) has two interesting features which may cause it to put definite requirements on chamber design:

1. The Ξ (or Ξ^{***}'s) go preferentially forward in the c.m. frame, and hence go forward with high momentum in the laboratory system frame. (The simplest diagram is that involving exchange of a Λ.)

2. The Ξ undergoes a several-step decay, which must be completely observed for sure identification of the particle.

Figure 2 shows the momentum and angle dependence of Ξ production from threshold to 1.7 BeV/c; the forward peak is likely to become sharper with increasing energy.

Figure 3 presents the kinematics (Blaton diagram) for the reaction $K^- + p \rightarrow K^+ + \Xi^-$ at 10 BeV/c incident K momentum. Even if the c.m. angle θ_{Ξ^*} equals 45 deg, the momentum of the Ξ in the lab system is very high and the direction is very close to the incident direction: p_{Ξ}(lab) = 9.3 BeV/c and θ_{Ξ}(lab) = 8.5 deg.

Figure 4 presents the Blaton diagram for an incident momentum of 100 BeV/c. With a c.m. angle as large as 45 deg, p_{Ξ}(lab) = 82 BeV/c, and θ_{Ξ}(lab) = 3.5 deg.

It is of interest to note the mean decay length of the Ξ and its daughter, the Λ. A 100-BeV/c Ξ lives on the average for 12 ft in the laboratory frame; a 100-BeV/c Λ (not unreasonable, as the Λ from a Ξ tends to take most of the laboratory momentum of the Ξ) lives on the average for a distance of 23 ft. On the basis of the strong-interaction discussion here, it seems reasonable to have a fairly long chamber, with L about 10 m or 30 ft.

Target Thickness

"Target" thickness is a special consideration. It is considered desirable by some physicists to have the chamber length approximately equal to a mean interaction distance for strong interactions. This distance is 16 ft for the geometric cross section in hydrogen of 60 mb; it is 33 ft for the fairly common high-energy cross section of 30 mb.

CONSTRUCTION OF CHAMBER BODY AND MAGNET

Briefly, two methods have seemed most promising for the expansion system of a large chamber.

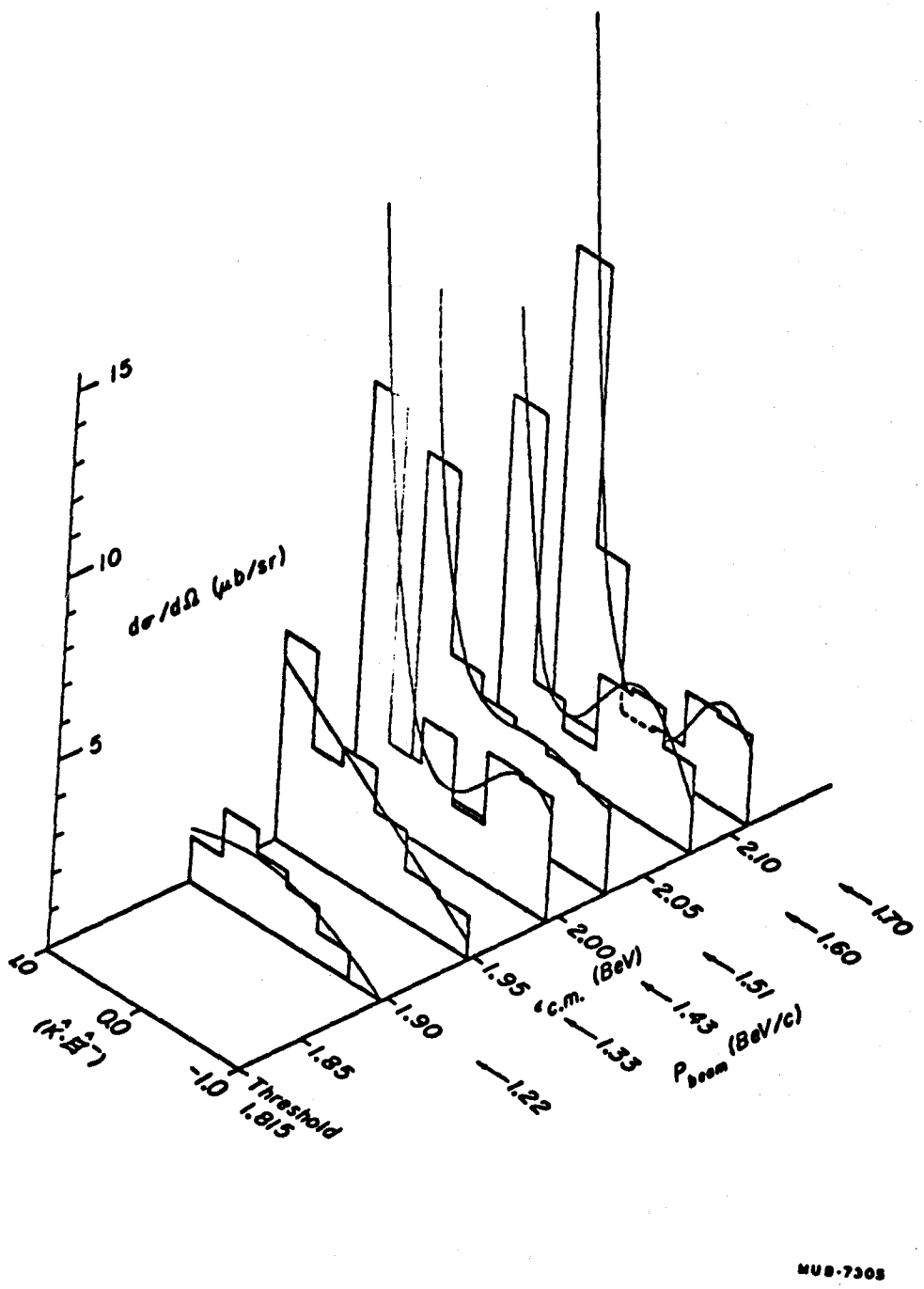

Fig. 2. The differential cross section, $d\sigma/d\Omega$ (μb/sr) for $K^- p \rightarrow \Xi^- K^+$ vs c.m. energy. From J. Peter Berge, Philippe Eberhard, J. Richard Hubbard, Deane W. Merrill, J. Button-Shafer, Frank T. Solmitz, and M. Lynn Stevenson, Some Properties of Ξ^- and Ξ^0 Hyperons Produced in $K^- p$ Interactions between 1.05 and 1.7 BeV/c, Phys. Rev. 147, 945 (1966).

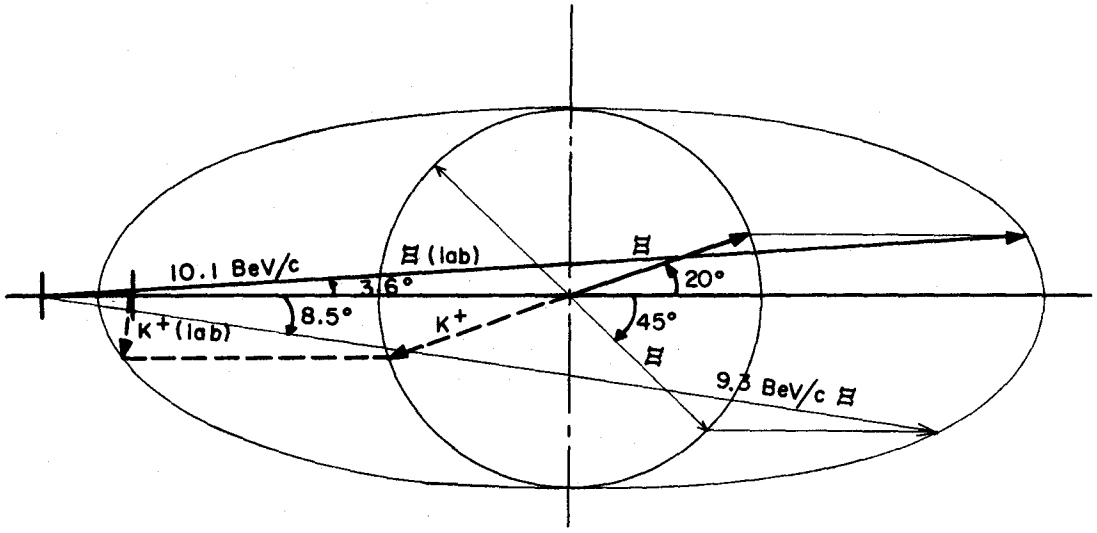

XBL671-365

Fig. 3. Blaton diagram for the reaction $K^- + p \rightarrow K^+ + \Xi^-$ at 10-BeV/c incident K^- momentum. $p^* = 2.00$ BeV/c, $\overline{\gamma} = 2.46$, $\overline{\eta} = 2.25$; ℓ_{Ξ} at 10 BeV/c = 1.2 ft, and ℓ_{Λ} at 10 BeV/c = 2.3 ft.

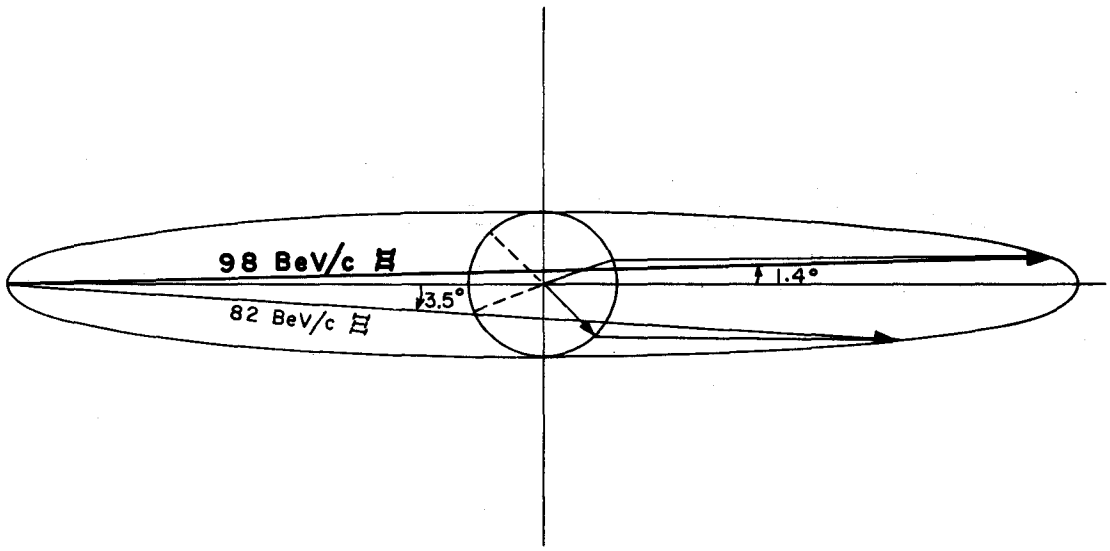

XBL671-366

Fig. 4. Blaton diagram for the reaction $K^- + p \rightarrow K^+ + \Xi^-$ at 100-BeV/c incident K^- momentum. $p^* = 6.78$ BeV/c, $\overline{\gamma} = 7.35$, $\overline{\eta} = 7.30$; ℓ_{Ξ} at 100 BeV/c = 12 ft, and ℓ_{Λ} at 100 BeV/c = 23 ft.

1. An Ω bellows permitting either the top or the bottom of the chamber to be raised or lowered. (This was demonstrated to perform very well in the 25-inch bubble chamber at LRL and, according to Hernandez and Watt at LRL, can readily be extended to monster chambers.)

2. A flexible baffle which may be moved to compress or expand the volume within the chamber. (BNL has designed a Fiberglas baffle for future use in the 14-ft chamber and will check out a half-scale baffle in their 7-ft "test facility.") Both the bellows and the baffle systems are operated by piston (resonant) in the big chambers now designed. A third scheme, a system of laminated metal (s. s.) diaphragms, was planned initially for the 12-ft Argonne chamber, but was dropped in favor of the already proved Ω bellows.

Figure 5 shows the construction of the ANL (Argonne) large chamber,[5] with the large bellows at the bottom (in a circular configuration). It will easily provide the required expansion of 0.5 to 1.0% of the total volume. The sides of the chamber are joined to the bottom pole tip; the space below the bellows and chamber bottom is evacuated. Eddy currents in the movable metal bottom may cause a heating problem, so that cooling by squirting liquid H_2 onto the bottom may be necessary. The superconducting (SC) magnet coils (circular) are outside the vacuum jacket.

Figure 6 shows the latest design of the BNL bubble chamber.[6] The Fiberglas baffle of varying thickness is visible at the bottom; the thickness at the center is 3 to 4 in., and the total excursion during the expansion-compression cycle is of comparable magnitude. Fiberglas was chosen to prevent eddy currents; a large-dished Fiberglas structure was successfully fabricated for a NASA project, but it is not known with certainty whether such a Fiberglas baffle will perform well at liquid-hydrogen temperatures. The piston is also of Fiberglas in this design. Scotchlite is mounted on the baffle and on the side walls. Here the circular SC magnet coils are inside the vacuum jacket. The piston is resonant (as was that in the ANL design), with an estimated period of about 70 msec. The total volume of the BNL chamber is to be 65 m^3, and the useful volume about 46 m^3.

A possible design for a 100-m^3 monster bubble chamber, such as is desired for the 200-BeV accelerator, is shown in Fig. 7. The body is a horizontal circular cylinder, perhaps 4 m in diameter and 10 m in maximum length. The coils are elongated, with straight sides and circular ends; they are in flat pancakes, except that they might be flared open at the ends (see below). One possibility for expansion, that of several baffles along the bottom actuated by one piston per baffle, has been put aside in favor of the more predictable Ω bellows. (No problems are foreseen in fabrication or use of a bellows of the required size.[7]) Two pistons might suffice to actuate the bellows assembly; three would certainly do so.

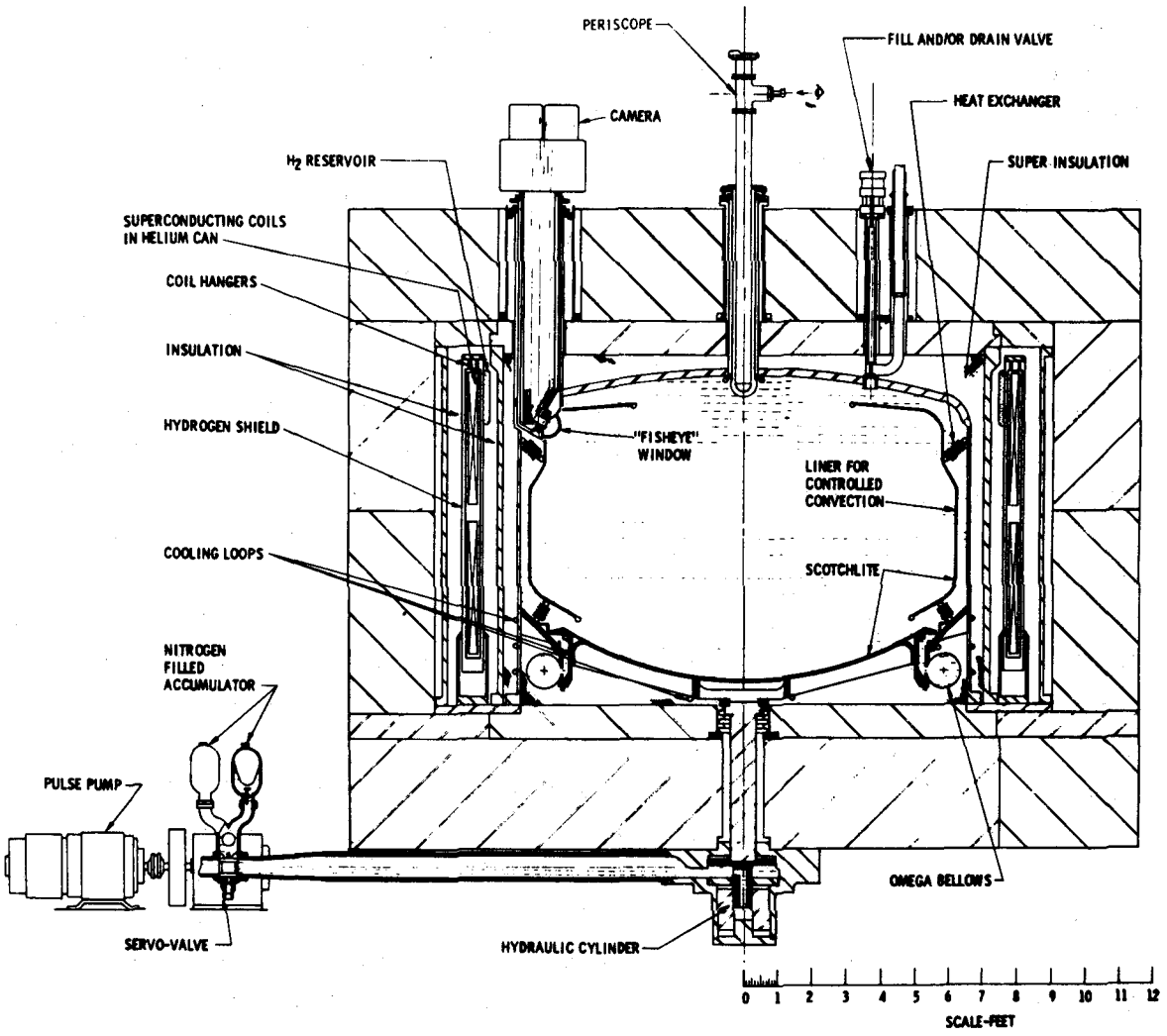

Fig. 5. Layout of the proposed Argonne 12-ft hydrogen bubble chamber (from Ref. 5).

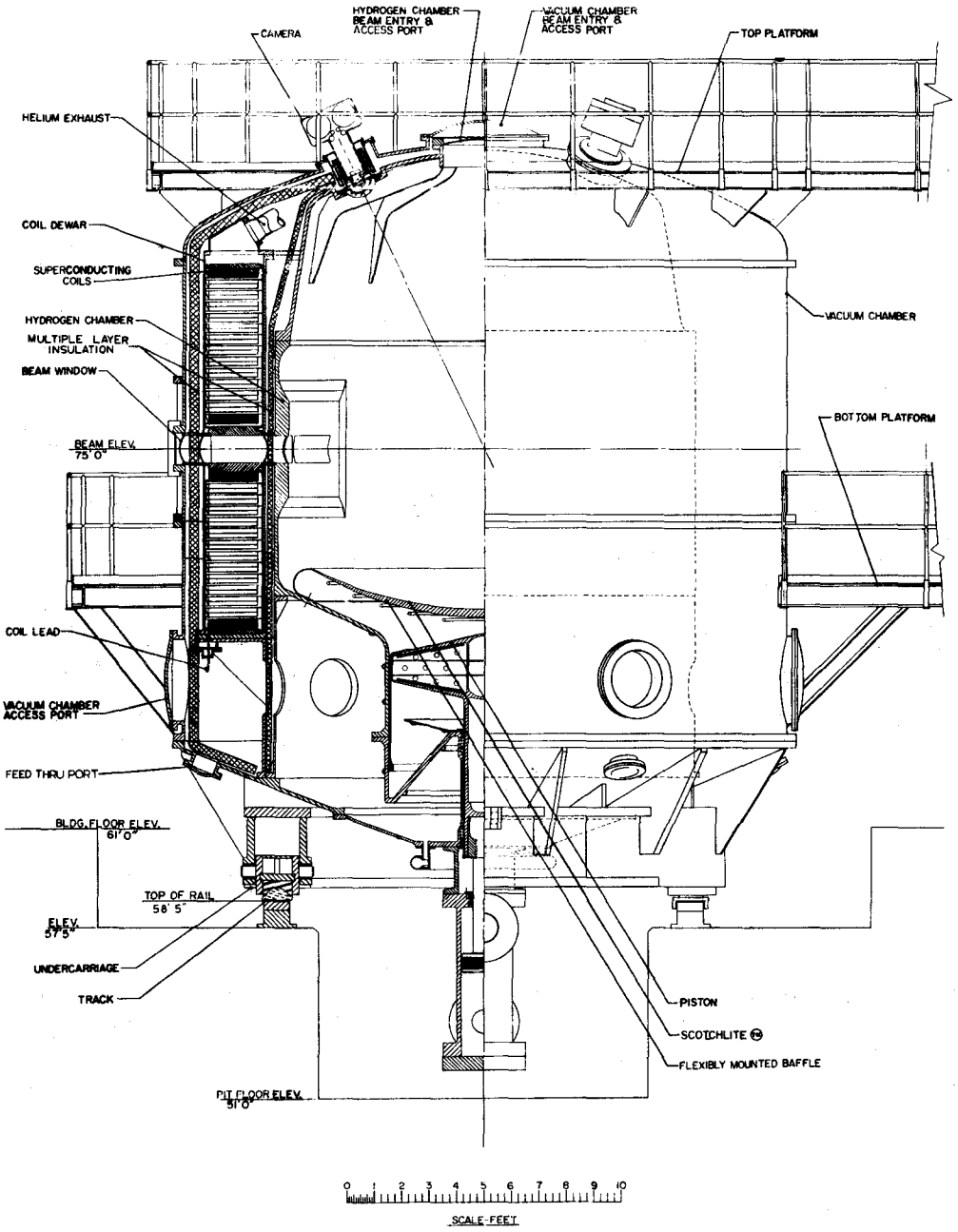

XBL 671-535

Fig. 6. Layout of the proposed Brookhaven 14-ft hydrogen bubble chamber (from Ref. 6).

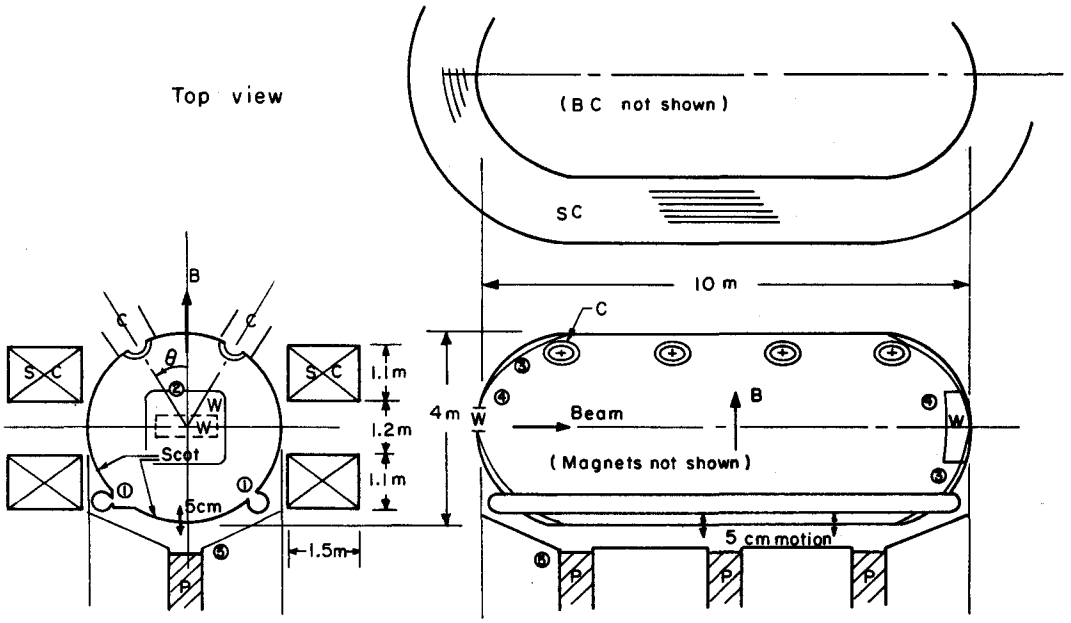

XBL671-367

Fig. 7. Rough schematic of proposed 100 m^3 chamber for the 200 BeV accelerator. Symbols used are: C camera; Scot Scotchlite; SC superconducting magnet; P piston; W thin window; B magnetic field.

Expansion from one end of the chamber has not really been ruled out, except that the desire to bring secondaries out a rear "window" might make it unattractive. A time of 10 msec would be required to make a 10-m-long chamber sensitive. It is possible that the expansion-pressure curve might be "flat-bottomed"--perhaps by having two pistons slightly out of phase.[7]

An advantage of the horizontal cylinder for the monster chamber is apparent in the optics; as the longest distance through which a camera must photograph in the transverse plane (perpendicular to the incident beam) is 4 m, one can--with many pairs of cameras--reduce the visibility or turbulence problems which might arise with the 6-m-diam spherical chamber (whose longest dimension is 6 m even after truncation). It has not been established how severe the optical turbulence problems will be for large chambers, but turbulence may become an important factor.

Several magnet designs have been considered. The first possibility to be examined for a long chamber was the type (SC) called a "saddle coil" by C. Taylor of Lawrence Radiation Laboratory, Livermore; this structure, designed by Taylor for the Alvarez high-altitude experiment and also developed by Avco, amounts to elliptical windings collapsed onto each half of a cylinder. The field, which is transverse to the axis of the cylinder, can be made uniform to within 15 or 20%. There is a major difficulty for bubble chamber use, however; radial stresses vary considerably as the windings flatten out, assume a circular shape, and also close up the gap between the two halves. Both Taylor and Avco engineers enclose their magnets with the equivalent of many circular I-beams--two concentric cylinders with many webs between them spaced along the length of the cylinder. The bending moment tending to break open the cylinder scales like $B^2 \times (\text{diameter})^2$, and (from a quick estimate by Taylor) would require two 1-in.-thick cylinders spaced about 2 ft apart for a 30-kG field in a 3.5 by 10 m chamber. With such constraining structures as this, it appears that access for pistons and for cameras would pose severe problems.[8]

A preferable scheme would be flat coils in a "race-track" geometry. The chief restraining forces necessary would be those to keep top and bottom coils separated and those to keep the sides from pushing out. It should be possible to provide such forces and still give access to the chamber.

The use of a circular coil (with some wasted field volume) for the long chamber has by no means been ruled out; engineering would be simpler and considerably less expensive.

A rather simple IBM-7044 program was written to calculate the field and the stresses on windings for the race-track geometry. (It includes no iron,

and could be readily modified for other geometries. Length and diameter as well as winding spacing are variable input data.) The assumption was made that the sort of stabilized NbTi ribbon (a sandwich of $\lesssim$ 1 mil of SC with 50 mils of Cu on either side, the whole about 2 in. wide) developed by Atomics International for BNL might be used. The spacings described by Prodell in the Laverick report[8] were adopted and calculations were made with a coil containing 100 turns per pancake by 20 pancakes per coil by 2 coils (see dimensions of Fig. 7). If one wished to produce a 20-kG (40-kG) field at the center of the chamber, with about 50 kG (100 kG) near the ends, 30×10^6 amp-turns (60×10^6 amp-turns) would be required for the configuration studied. Probably more windings than the 4000 turns mentioned would be necessary to achieve these fields in practice, with the sort of SC current densities now possible; the 4000 turns should probably be multiplied by 1.5 (or 3) for the fields mentioned.

Figures 8 and 9 show the results of field calculations. (The overall dimensions of the coils were as given by Fig. 7, but computer time was shortened by taking every tenth winding horizontally, with each carrying 10 times the usual or stated current.) The figures show that the field increases by a factor of about 2.5 from the center to the ends of coils. It is remarkably uniform in the lateral and vertical directions; the transverse or nonvertical components are negligible except in the region close to the coil ends. Note that the race-track coils for the 72-inch bubble chamber also produce a field which increases somewhat at the chamber ends.

An interesting possibility for modification of the high-field regions would be to separate the two coils severely at the chamber ends and thus reduce B_z while introducing axial field components (and stray flux) which might be useful in certain experiments on interaction products (with external spark chamber and counter detectors).

Some magnet-design figures (compared with or extrapolated from BNL estimates) are as follows: BNL now expects, for their 14-ft chamber, to obtain 10 000 amp/conductor (with a 4-in. wide NbTi ribbon) and requires 18×10^6 amp-turns to produce 30 kG throughout the cylindrical volume. (This is to be compared with the 30×10^6 amp-turns stated above as the mmf necessary to produce 20 kG at the center with an average of 30^+ kG throughout for the 100 m^3 chamber. A slightly impractical 7500 amp per 2-in. wide ribbon is required by the above coil dimensions.) BNL estimates the 14-ft chamber coil to cost about \$1 700 000 (without spacers); the coil described above for a 100 m^3 chamber would cost perhaps \$8 000 000.

BNL's estimated stored energy is 125 MJ; the above-described coil has, with an average B^2 of perhaps $(33\ kG)^2$, a stored energy of

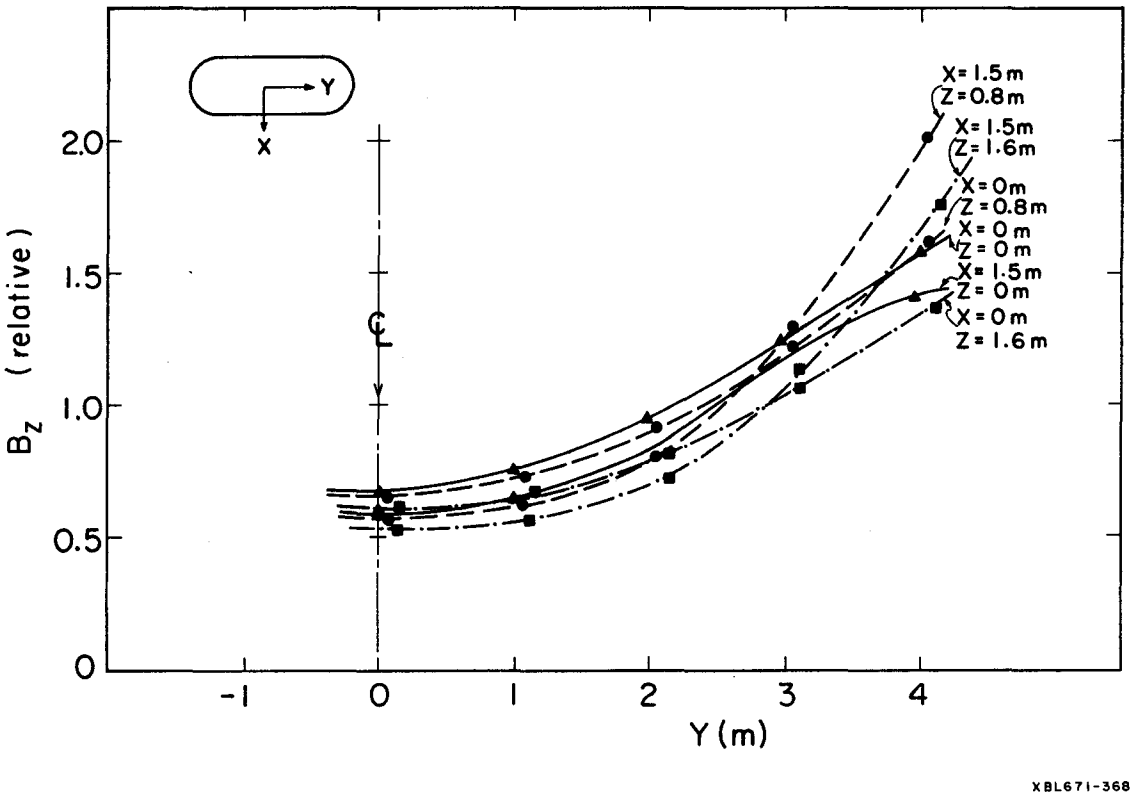

Fig. 8. B_z vs Y for X = 0 and 1.5 m and for Z = 0.0, 0.8, and 1.6 m for the race-track configuration proposed for the magnet for the 100 m^3 hydrogen chamber. B_z (kG) is ordinate x (NI) x 10^{-6}.

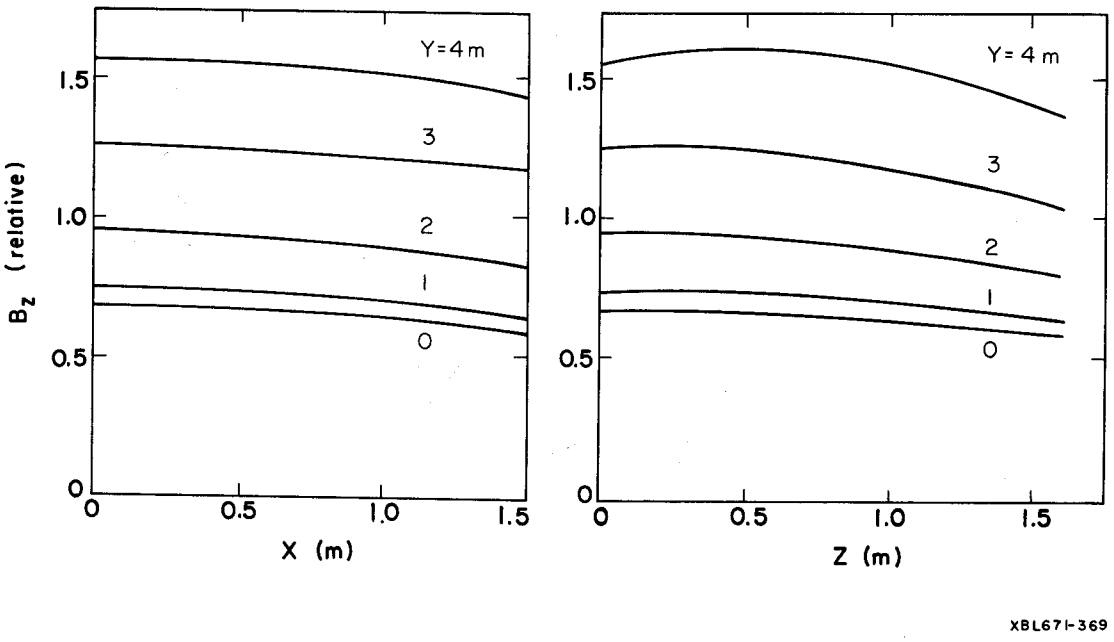

Fig. 9. B_z vs X and B_z vs Z at Y = 0, 1, 2, 3, and 4 for the race-track configuration proposed for the magnet for the 100 m^3 hydrogen chamber. B_z(kG) is ordinate x (NI) x 10^{-6}.

$$125\ \text{MJ} \times (33\ \text{kG}/30\ \text{kG})^2 \times (35\ \text{m}^2/24\ \text{m}^2) \times (4\ \text{m}/4\ \text{m}) \approx 220\ \text{MJ}.$$

BNL's compressive load is estimated at 30 000 tons; scaling gives (roughly) for our large coil a load of

$$30\,000 \times (33/30)^2 \times (35/24) \approx 50\,000\ \text{tons}.$$

Figure 10 presents some program-calculated numbers which give a crude idea of the stress variation (force per unit length on the individual winding) for the race-track coil. Note that there is a net attractive force between upper and lower coils, but that it is greater at the curved ends than along the straight sides. Further, the total force appears to be roughly only one-half the load estimated above.

CONCLUSION

A bubble chamber with an aspect ratio of 3 to 1 favoring the beam direction has many advantages over a chamber more nearly equal in all dimensions, in experiments involving both neutrino interactions and strong interactions. Although the cost per cubic meter might be greater for the former chamber, none of the engineering problems appear to be unsurmountable. More detailed engineering and cost comparisons are certainly necessary; in view of the possible advantages to the physics program, these should be made before any final decision is made on the configuration of the large chamber.

Footnotes and References

1. Of course, an upright cylindrical chamber is ideal only if all interactions occur near the center; products go out isotropically, and decaying particles are at rest in the laboratory system.
2. BNL's proposed chamber has a total volume of about 65 m^3 and a useful volume of 46 m^3.
3. W. Chinowsky, Monster Bubble Chamber Document, in UCRL-16830, Vol. 2, p. 53 (1966); and M. L. Stevenson, Bubble Chamber Physics at the 200 GeV Accelerator, in UCRL-16830, Vol. 2, p. 85 (1966).
4. T. E. Toohig, The Influence of a Line Source of Neutrinos on the Configuration of Experimental Apparatus, this volume.
5. E. G. Pewitt, Innovations in Bubble Chamber Devices, IEEE Trans. Nucl. Sci. 12, 149, August 1965.
6. 14-Foot Cryogenic Bubble Chamber Project, BNL 9695, Dec. 1965.
7. R. Watt and P. Hernandez (Lawrence Radiation Laboratory), private communication.
8. For interesting material on the Taylor coil and others, see the report, Meeting on the Design of Large Superconducting Bubble Chamber Magnets,

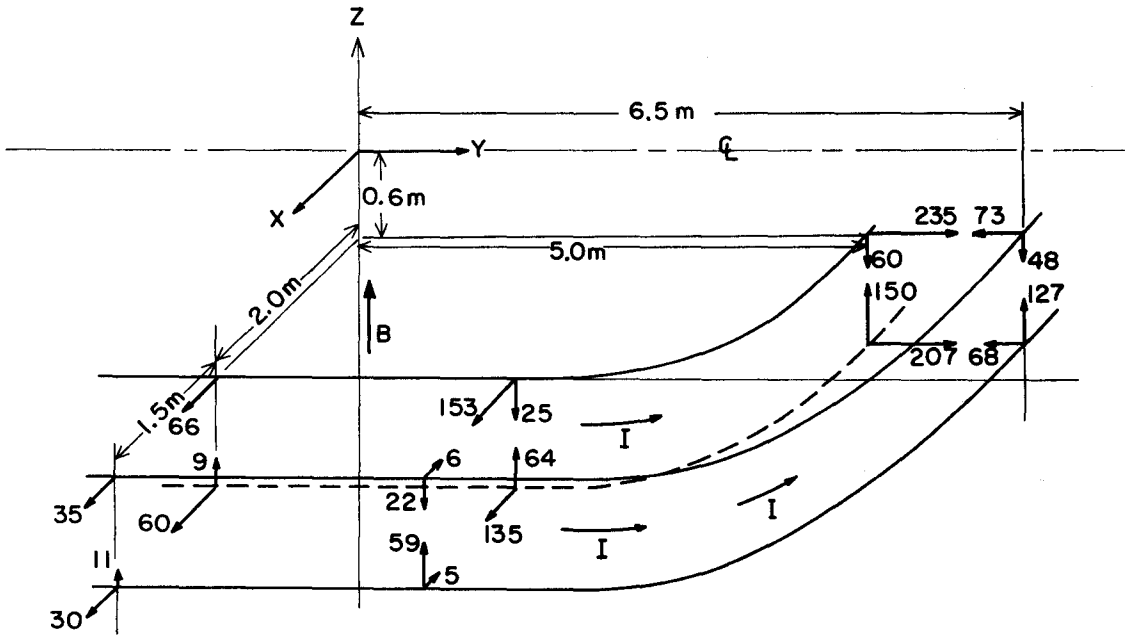

XBL671-370

Fig. 10. Calculated stresses on the coils of a magnet with a race-track configuration and a size suitable for the 100 m^3 hydrogen chamber. B ≈ 20 kG at X = Y = Z = 0; B ≈ 50 kG at X = Z = 0, Y = 4 m; I = 7500 A, N = 4000 turns total. Each number gives force/$\Delta\ell$ in lb/in. for a single winding (components are shown). Other quadrants of bottom and top coils are similar.

edited by Laverick on the Argonne Conference, ANL-7192 (March 25, 1966). See also R. B. Meuser, The Potential of Superconducting Magnets for Use in the Experimental Areas: Preliminary report, this volume.

ON THE USEFULNESS OF KINEMATIC FITTING AT HIGH ENERGIES IN A MONSTER BUBBLE CHAMBER

R. J. Plano

INTRODUCTION

An attempt has been made to gain some quantitative insight into the applicability of standard kinematic-fitting techniques, using a giant bubble chamber at incident momenta of 150 BeV/c. Events of the type $\pi^+ + p \rightarrow N^{*++} + \rho^0$, $N^{*++} \rightarrow \pi^+ + p$, $\rho^0 \rightarrow \pi^+ + \pi^-$, were generated with standard Monte Carlo techniques, and then fitted with the assumptions of various mass combinations. A detailed description of this general-purpose Monte Carlo program, called MOCK, is available.[1]

Systematic errors due to such factors as turbulence in the liquid, and imperfect knowledge of the optical constants and magnetic field, were ignored throughout, although they may well be the major source of errors.

Trilling,[2] as well as others,[3,4] has considered this problem, but without making detailed simulations.

ERROR EQUATIONS

All error estimates are based on three-point measurements of the tracks. These are derived in numerous places[5,6] and are reproduced in Table I for easy reference. Units are radians, BeV/c, meters, and webers/m^2 (10^4 gauss), so $p = (0.3\ HR)/\cos\lambda$. The general forms are given and then evaluated for $a = 0.0001$ m (100 microns), $b = 0.00036$ m, $X_0 = 10$ m, and $H = 2\times10^4$ gauss.

Note that although δp decreases monotonically as ℓ increases, the angular errors have a minimum (when the multiple-scattering error is twice the measurement error). In order to determine the optimum length, ℓ_{opt}, for the measurement of ϕ, let

$$\delta\phi = \left\{ \frac{A^2}{\ell^2} + B^2\,\ell \right\}^{1/2} .$$

Then $\ell_{opt} = 1.26\,(\frac{A}{B})^{2/3}$ and $\delta\phi_{min} = 1.38\,(AB^2)^{1/3}$.

By substitution from Table I, we find

$$\ell_{opt} = 105\,(a\sqrt{X_0}\,p\beta)^{2/3} = 0.5\,(p\beta)^{2/3} .$$

$$\delta\phi_{min} = \frac{0.085}{\cos\lambda}\left(\frac{a}{X_0 p^2\beta^2}\right)^{1/3} = \frac{0.0018}{\cos\lambda}\,(p\beta)^{-2/3} .$$

Table I. Formulae for measuring and multiple-scattering errors.

	General		With specified values of parameters	
Error	Measuring error	Multiple-scattering error	Measuring error	Multiple-scattering error
δp	$\frac{32.6\ a}{H \cos\lambda} \left(\frac{p}{\ell}\right)^2$	$\frac{0.0572\ p}{H\sqrt{X_0}\ \beta\sqrt{\ell}\ \cos\lambda}$	$\frac{1.6\times10^{-3}}{\cos\lambda} \left(\frac{p}{\ell}\right)^2$	$\frac{8\times10^{-3}\ p}{\beta\sqrt{\ell}\ \cos\lambda}$
$\delta\phi$	$\frac{5.1\ a}{\ell \cos\lambda}$	$\frac{0.0069}{p\beta \cos\lambda} \sqrt{\frac{\ell}{X_0}}$	$\frac{5\times10^{-4}}{\ell \cos\lambda}$	$\frac{2\times10^{-3}\sqrt{\ell}}{p\ \beta \cos\lambda}$
$\delta\lambda$	$\frac{1.41\ b}{\ell}$	$\frac{0.0086}{p\beta} \sqrt{\frac{\ell}{X_0}}$	$\frac{5\times10^{-4}}{\ell}$	$2.5\times10^{-3}\ \frac{\sqrt{\ell}}{p\beta}$

H - Magnetic field (assumed parallel to Z axis) (20 000 gauss)
a - Measurement error in XY plane in chamber (100 microns)
b - Measurement error in Z coordinate in chamber (360 microns)
X_0 - Radiation length (10 meters)
β - Velocity of particle (v/c)
δp - Error in momentum p
$\delta\lambda$ - Error in dip angle λ (angle between track and XY plane)
$\delta\phi$ - Error in azimuth angle ϕ
ℓ - Length of track
R - Radius of curvature of track

It is also of interest to find the ratio of measurement error to multiple-scattering error. This is given by

$$\frac{\delta p_{meas}}{\delta p_{ms}} = 0.2\ \frac{p\beta}{\ell^{3/2}} \quad \text{and} \quad \frac{\delta\phi_{meas}}{\delta\phi_{ms}} = 0.25\ \frac{p\beta}{\ell^{3/2}}\ .$$

From these results, we construct Table II.

From this table it can be seen that most secondary tracks will be measured with an accuracy not too far from optimum in a chamber large enough to allow 5 to 10 m for each track. Longer lengths will not improve the situation greatly, as the mean free path for a strong interaction (which would probably produce neutral secondaries) is about 10 m.

Although these error equations are fairly rough approximations, they are useful for gaining insight and give usefully accurate results. Measuring many points along each track would of course decrease the errors, but this advantage would be offset by the contribution to multiple scattering by small-angle strong-

interaction elastic scattering and, of course, by systematic errors and distortions. A more detailed set of error equations is now being developed.

Table II. Table of errors for tracks of different momenta.

$p\beta$ (BeV/c)	8	64	125	216
ℓ_{opt}(m)	2	8	12	18
$\delta\phi_{min}$ (mrad)	0.45	0.11	0.07	0.05
ℓ (in meters) for $\frac{\delta p_{meas}}{\delta p_{ms}} = 1$	1.3	5.2	8	12
δp (ℓ = 4m)(BeV/c)	0.33	0.49	1.7	4.7
$\delta\phi$ (ℓ = 4m)(mrad)	0.51	0.14	0.13	0.13

GENERATION OF EVENTS

The N^* and ρ^0 masses are randomly selected from a Breit-Wigner distribution. The production angle is then randomly selected on the basis of a one-pion exchange model, and the N^* and ρ^0 are allowed to decay isotropically in their c.m. systems.

The length of the incident track is randomly selected from a flat distribution between 1 and 4 m. The other track lengths are determined by the resulting coordinates of the production vertex and the individual direction and momenta of the tracks, unless a Monte Carlo procedure indicates that the particles interacted before leaving the chamber, but with at least one m of track length. The interaction mean free path was taken to be 10 m. Errors are then generated for each track and the "measured quantities" moved from their exact values by an amount given by a Gaussian random variable times the error. The square of the missing mass, $(MM)^2$, and its error, $\delta(MM)^2$, are calculated, for all permutations of the masses consistent with conservation of charge, baryon number, and strangeness, assuming the mass of each particle is known as well as for permutation of the masses. The apparent mass of each track is also calculated on the basis of the "measurements" on the other tracks.

The event is then fitted as a four-constraint event by means of standard mathematical techniques.[7] It may be of interest to note that the least-mean-squares fit did not converge properly on either a 36-bit or a 60-bit computer using single precision. Both word sizes were more than adequate when double precision was utilized for the vectors and matrices used in the fit.

The question as to whether all numbers generated by the program are, to some extent, random is an important question. The number of checks made make it highly unlikely that the results are wrong to any great extent. In

addition, the following checks gave additional assurance:

1. Events were generated in which the "measurement" errors were set to zero. These fitted the input quantities with zero chi squared and exactly conserved energy and momentum.

2. The calculated errors in the measured quantities agreed with hand calculations.

3. The chi-squared distribution for the correct mass assignment followed (at least very roughly) a chi-squared distribution. This somewhat unrealistic simulation of real life was doubtless due to the neglect of systematic errors.

4. Finally, the errors and chi-squared discrimination showed a reasonable dependence on the measurement accuracy, radiation length, and magnetic field.

DISCUSSION OF RESULTS

Perhaps the most surprising result is that considerable discrimination is indeed possible at this energy. This is greatly aided by the fact that the proton is normally quite slow ($p \approx 1.5$ BeV/c), but the conclusions remain unchanged for p as high as at least 10 BeV/c. Mass assignments which misidentify the proton have chi squares normally greater than 100 and often much greater than 1 000, when 4 is expected. On the other hand, it is impossible to discriminate against the possibility that the two fast pions from the ρ^0 ($p \approx 10$-140 BeV/c) are really kaons, even for measurement errors as small as 50 microns.

It seems feasible to detect missing neutrals, as momentum conservation is typically good to ≈ 400/MeV/c along the beam and ≈ 40 MeV/c transverse to the beam. This is buttressed by the fact that the error in the missing-mass squared (if no particle is actually missing and the charged tracks are correctly identified) is typically 0.1 to 0.5 m_π^2. If a pion is actually missing and at high momentum, the error in its MM^2 is $\approx m^2_{proton} = 50\ m_\pi^2$, but such π^0's can be detected by the large nonconservation of momentum.

A problem arises because if the charge tracks are misidentified and the resulting chi squared is very large, the error in the missing-mass squared jumps to 5 to 100 times m_π^2 ($\approx m_p^2$). This does not appear to be serious, as the large chi squared will signal trouble.

If a fast pion interacts in less than 3 m, or if the measurement error is increased to 200 microns, the error in the missing-mass squared increases to ≈ 2 to 5 times m_π^2. This increase indicates that a chamber much smaller than 8 m or a measurement accuracy much larger than 100 microns would very strongly decrease the usefulness of the chamber for strong-interaction physics.

Table III gives a very rough summary of the results for a few sets of initial conditions based on about 5 events in each case. The hypotheses in Table IV refer to the following mass assignments.

Table III. Summary of the results of MOCK II fitting program.

δx (μ)	100	50	200	100
X_0 (m)	10	20	10	10
P_{inc} (BeV/c)	150±0.15	150±0.15	150±0.15	10.0±0.15
H ($\mu b/m^2$)	4.0	4.0	4.0	4.0
Diameter (ml)/length (m)	4/8	4/8	4/8	0.4/2
$\delta(MM^2)/m_{\pi^0}^2$	≈ 0.05-0.3	≈0.02-0.1	2-4	0.01-0.05
δp (long.)(MeV/c)	≈ 400	≈ 250	≈ 500	≈ 250
δp(transverse)(MeV/c)	≈ 40	≈ 20	~ 50	≈ 20
χ^2_B	$\tilde{>}$ 100	> 250	> 60	> 600
χ^2_C	$\tilde{>}$ 8-400	13-800	> 5	> 50
χ^2_D	≈ 2-40	4-100	> 2	> 100
χ^2_E	> 50	> 100	> 30	> 200

Table IV. Hypothetical mass assignments tried in the fitting procedure.

	$\pi^+ + p \rightarrow$		
	N^{*++}	+	ρ^0
Hypothesis A (true)	$\pi^+ + p$		$\pi^+ + \pi^-$
B	$p + \pi^+$		$\pi^+ + \pi^-$
C	$\pi^+ + \pi^+$		$p + \pi^-$
D	$\pi^+ + p$		$K^+ + K^-$
E	$\pi^+ + K^+$		$p + K^-$

Columns 1, 2, and 3 (Table III) show the effects of varying the measuring accuracy and the radiation length. For comparison column 4 shows the results with a 2-meter chamber similar to those presently used at much lower incident beam momenta (10 BeV/c).

CONCLUSIONS

These results strongly indicate that kinematic fitting will be a valuable tool in a monster bubble chamber at the 200-BeV accelerator, at least for the subset of four-constraint events. To the extent that gamma rays can be converted and π^0 momenta reconstructed with accuracy comparable to charged tracks, the usefulness of fitting will, of course, be extended.

This and similar programs can be extremely useful in the detailed design of large bubble chambers. Information on the effect of different chamber size, aspect ratio, magnetic field, and measurement accuracy can be readily obtained and easily evaluated. It will probably be particularly useful to simulate the effect of optical resolution, local variations in the density of the liquid, uncertainties in the optical constants, and the effect of large-scale liquid motions if adequately precise approximations can be made to these effects. These checks would, of course, require a considerable but not overwhelming modification of MOCK and possibly more general programs.

References

1. Contact R. J. Plano, Rutgers University.

2. G. H. Trilling, The Use of Hydrogen Bubble Chambers at SLAC, SLAC Report No. 5, Summer 1962.

3. Brookhaven 14-Foot Cryogenic Bubble Chamber Project Final Pre-Title I Report, December 1, 1965.

4. W. Chinowsky, Monster Bubble Chamber Document, UCID-10163, August 25, 1965. M. L. Stevenson, S. L. Adler, N. Cabibbo, Frank Chilton, and John Moriarty, Bubble Chamber Physics at the 200 GeV Accelerator, UCID-10152, 1965.

5. R. L. Gluckstern, Nucl. Instr. Methods 24, 321 (1963).

6. R. J. Plano and D. H. Tycko, A Method for the Spatial Reconstruction of Bubble-Chamber Tracks, Proceedings of the International Conference on Instrumentation for High-Energy Physics, CERN, Geneva, Switzerland, 1962, published in Nucl. Instr. Methods 20, 458 (1963).

7. J. P. Berge, F. T. Solmitz, and H. D. Taft, Rev. Sci. Instr. 32, 538 (1961).

100 M^3 CRYOGENIC BUBBLE CHAMBER – EXTRAPOLATED COST

H. Paul Hernandez

The cost of a 100 m^3 liquid-hydrogen bubble chamber, I believe, is estimated to be in the range of 30 to 50 million dollars.

A cost of $30 million for a 100 m^3 chamber was extrapolated from the Brookhaven 14-ft cryogenic bubble chamber costs (Ref. 1) December 1, 1965. The 30-kG BNL superconducting magnet does not have a steel return path, and the coils are placed in a common vacuum tank with the chamber. The 14-ft chamber has a visible volume of 46 000 liters and a total volume of 68 000 liters.

A cost of $50 million was extrapolated from the ANL 12-ft hydrogen bubble chamber costs (Ref. 2). The 18-kG magnet has a steel core and the superconducting coils have a separate vacuum system. The visible volume is 20 000 liters and the total volume 26 000 liters.

The cost estimate for the 3.5-m diameter CERN bubble chamber is very preliminary and was obtained from R. Florent at CERN. The CERN chamber is similar in arrangement to the BNL chamber; it has a visible volume of 20 m^3 and a total volume of 30 m^3. The magnetic field is 35 kG and the superconducting coils have a separate vacuum system. The magnet core is used for shielding and has the shape of a large cubic room of about 12 m.

The details of the extrapolations are summarized in Table I and are given in detail on the work-sheets of Engineering Note M3810(3). These total costs are for complete installations, but do not include the beam line equipment from the accelerator to the bubble chamber. Escalation was not considered. The costs of cryogenic bubble chambers are plotted on Fig. 1 along with an extrapolated cost for a 100 m^3 bubble chamber. Figure 2 shows how the cost per unit volume decreases with chamber size.

Taking another approach, we see that for 35 million dollars, a bubble chamber can be built that is reasonably close to 100 m^3. There is also a cost optimum between size and quality. The overall optical accuracy of such a chamber is expected to be about the same as today's chambers. The most uncertain problem in a large chamber is assuring that the temperature gradient remains within tolerance over the visible region of the chamber.

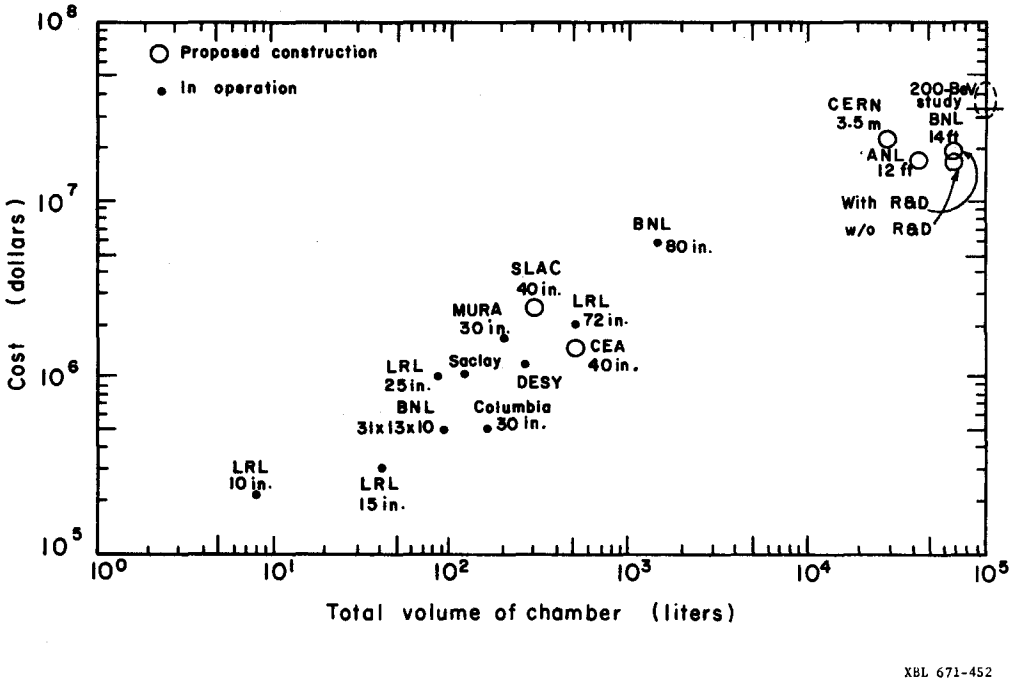

Fig. 1. Total costs of cryogenic bubble chambers as a function of the total volume.

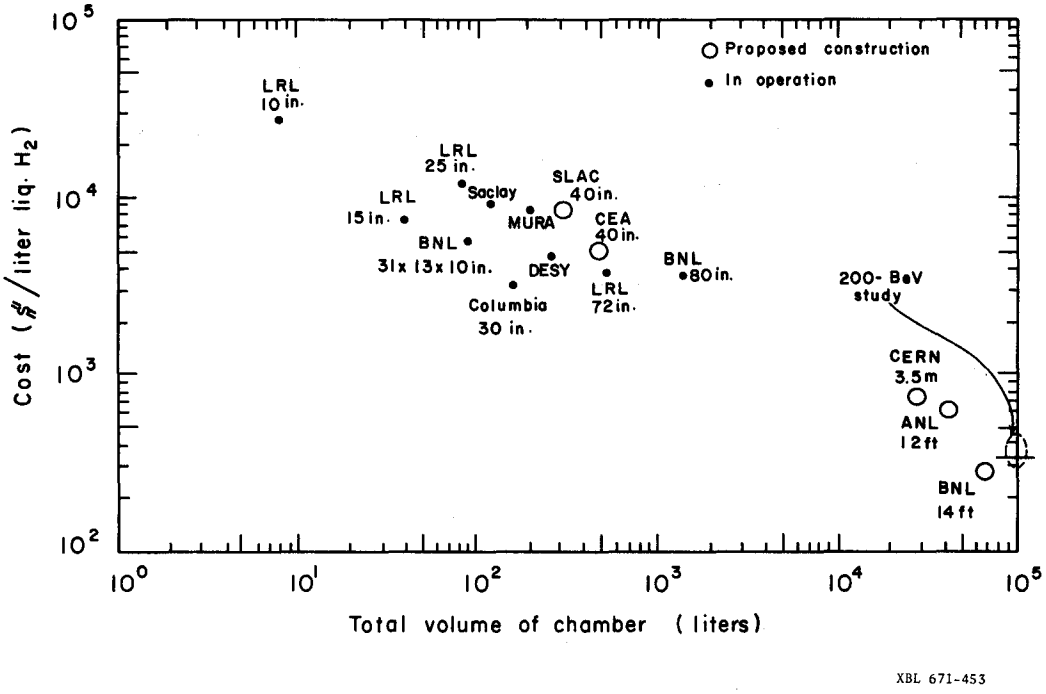

Fig. 2. Cost per unit volume of cryogenic bubble chambers as a function of the total volume.

Table I. Extrapolated costs of liquid-hydrogen bubble chamber for 200-BeV accelerator (summarized from Ref. 3).

	Costs (thousands of dollars)			
	BNL[a] 14 ft	100 m^3 BC	ANL[b] 12 ft	100 m^3 BC
Chamber body	739	1 460	699	2 690
Expansion system	612	1 296	221	850
Optical system	447	1 222	323	1 240
Magnet system	2 860	4 700	1 860	7 160
Vacuum system	1 008	1 860		
Refrigeration	1 336	2 690	3 126	12 000
Instrumentation and safety	280	726	282	804
	7 282	13 954	6 511	24 744
Bldg. and facility	2 920	3 780	2 110	5 170
Total manpower	2 993	4 030	3 384	12 690
Contingency (16.3%)	3 110	3 550	2 040	7 246
	16 305	25 314	14 045	49 850
Research and development (18.2%)	2 990	4 610	---	---
TOTAL	19 295	29 924	14 045	49 850
		(30 000)		(50 000)

a. See Ref. 1.

b. See Ref. 2.

The 1966 Summer Study specified the 100 m^3 chamber generally as a horizontal cylinder of 4-m diameter by about 8 m long and having a vertical magnetic field of 40 kG. The 100 m^3 magnet would almost certainly have superconducting coils. Preliminary studies by R. Yourd and M. Green at LRL in the Summer of 1965 showed that it is more economical to omit the steel flux return path; however, a steel core may be required for magnetic shielding or for improving the field uniformity. To date, bubble-chamber magnetic fields have not had strict uniformity requirements, but the uniformity may have to be controlled to allow more freedom in the design of moving parts of the expansion system.

The 12-ft ANL and the 14-ft BNL bubble chambers should be sufficiently complete before the final design of the 100 m^3 chamber is fixed so that the more accurate extrapolations of quality and costs should be possible in the future.

References

1. Brookhaven 14-Foot Cryogenic Bubble Chamber Project Final Pre-Title I Report, December 1, 1965.
2. ANL 12-Foot Hydrogen Bubble Chamber, July 1966, Title I Report.
3. Extrapolated Costs, 100 M^3 Cryogenic Bubble Chamber, Advanced Accelerator. LRL Engineering Note M3810, H. P. Hernandez, September 12, 1966.

A CONSIDERATION OF SUPERCONDUCTING EXPERIMENTAL MAGNETS FOR USE WITH THE 200 BEV ACCELERATOR

A. Abashian

INTRODUCTION

During the past few years, rapid strides have been made in the development of super-conducting magnets of appreciable size. Quite naturally, the question is raised as to the role they may play in the experimental facilities available at the 200-BeV accelerator. Some of the questions one should consider include the following:

1. For what type of experiments is the super-conducting magnet unique?
2. How do factors such as beam intensity, particle separation, and particle energy affect the choice of type of magnet?
3. What are the relative merits of super-conducting and conventional magnets?

Each of these questions is expanded upon below. The conclusion reached is that it is still too early to decide whether to use super-conducting magnets, conventional magnets, or both. Very little information is currently available on the costs and problems of super-conducting installations.

FACILITIES REQUIRING UNIQUENESS OF SUPER-CONDUCTING DEVICES

Hyperon and Other Very Short-Lived Beams

As already calculated by Longo,[1] the decay length of 100 BeV/c hyperons varies from 6.5 to 23.3 feet. Dekkers et al.[2] have found that at about 20-BeV incident proton energy, almost all K^+ production proceeds via N^* production followed by $K^+ + Y$ decay. This indicates that Λ and Σ production may each occur with an abundance of about one quarter the K^+ production. Therefore, fluxes of the order of 10^5 Λ's or Σ's (per 1% dp/p, 10^{-6} steradian and 10^{13} interacting protons) may be produced at the target. Quite obviously, it is imperative that if hyperon beams of reasonable intensities are to be useful for experiments, the length of the beam transport must be kept small, perferably less than 50 feet in length. This indicates that focal lengths must be typically about 10 feet. Conventional iron magnets are completely incapable of providing sufficient magnet-field gradient to focus a 100-BeV/c beam in such a short distance.

A super-conducting magnet pair of about 10 feet total length comes close to providing the required focussing.

Long-Spill rf Separated Beams

With available fluxes of K and $\bar{p}$ greater than 10^6 per pulse, it becomes important to seek ways of producing separated and enriched beams for counter and spark-chamber experiments. Not only is this desirable from the standpoint of reducing count rates in the counters, but it becomes necessary when electronic techniques fail. At momenta < 50 BeV/c, differential Cerenkov counters may be successfully employed to achieve separation. At momenta > 50 BeV/c, the use of threshold Cerenkov counters is being contemplated. The threshold counters will not always be able to achieve beams of high purity because they are typically hundreds of feet long, and decays of the wanted particles may occur after tagging. For example, a typical beam might have two π threshold counters 300-ft long, followed by a single π + K threshold counter 100 ft long.[3] If a K^+ meson decayed into $\mu^+ + \nu$ in the third counter, the μ^+ meson would simulate a K meson, would enter the detection apparatus, and thereby would give improper results. At 100 BeV/c, approximately 5% of the K-meson beam would be π and μ mesons.

Because of these factors, methods of achieving physical separations of particles is desired. Electrostatic separators of reasonable length are inadequate beyond 20 BeV. The rf cavity technique appears to be most promising at higher energies. Lach has designed a 100-BeV/c rf separated beam for use with a hydrogen bubble chamber.[3] The power required to drive the cavities is of the order of a few megawatts, but the pulse duration is only of the order of few microseconds. The beam is therefore not useful for counter experiments.

Work is currently underway at SLAC to develop superconducting cavities with Q's of the order of 10^8. Such cavities would require only tens of watts to be driven and could therefore have duty factors approximating one. Further, higher frequency rf sources could be employed, thereby reducing the intercavity space and also reducing the need for a long transport system. Should cavities of the sizes needed at these high energies prove to be feasible, they would provide probably the best overall means of particle separation.

Switching and Separating Magnets

One of the features of large synchrotrons has been the ability to use several secondary beams from the same traget. This is easily done because production cross sections remain reasonable out to about 30°. At 200 BeV, about half the particles are emitted within an angle given by $\theta = 0.5/p$, where p is the particle momentum in BeV/c, which for 100 BeV/c corresponds to 5 milliradians. This places rather severe restrictions upon the relative closeness of beams which "look back" at the same target.

If one uses a conventional iron magnet of 20 kG, it would have to be 50 feet

long to achieve a separation between the 100-BeV/c positive and negative beams of about 5 feet. It would be difficult to place quadrupoles downstream from the switching magnet much closer to the incident beam line without running into problems with the incident proton beam striking the quadrupoles. The angle subtended by a 4-in. -diameter quadrupole magnet, placed 50 feet from the production target, is 2 in./600 in. = 3 milliradians. Clearly, the full production angle of 5 milliradians is not being employed in this case and a loss of intensity results.

A super-conducting magnet (or set) 10 feet long with a field of 60 kG would provide a separation of > 7 feet between positive and negative beams at a distance of 30 feet from the production target. The ability to fan out rapidly the secondary beam makes the possibility of using a super-conducting magnet as the switching magnet an attractive one.

PARTICLE-BEAM PARAMETERS AFFECTING CHOICE OF MAGNET

In the design of a particle beam, the main concerns are with particle separation and intensity. They determine the type, quantities, and arrangements of the magnets in the transport system. Listed below are three general classes of beams, along with the primary methods of separating particles.

Bubble-Chamber Beams

Almost all of these beams will be rf separated beams necessitating generally hundreds of meters of drift space between rf cavities.[3] The focal lengths of the focussing quadrupoles are large, and the momentum band accepted is small because of the long focal distances involved. Rarely is intensity an important factor in the design.

Should the circularly polarized cavities become practical, savings in the intercavity spacing can be achieved.[4] This may allow for substantial reduction in the total length of the beam-transport system and make super-conducting magnets more desirable.

Long-Spill Beams Below 50 BeV/c

These beams use differential Cerenkov counters as their main means of separating particles. This unfortunately limits the maximum intensity because of instantaneous pulse rates from unwanted particles jamming the electronics. Intensity is usually a prime factor in the design, and care is usually taken to keep the beam length short so as to reduce decay of unstable particles in flight. Electrostatic separation is unfeasible for all but the lowest energy beams. Current rf separators suffer from the very short duty cycle. If the super-

conducting cavities become feasible, they will probably become the preferred mode of separation.

Long-Spill Beams Above 50 BeV/c

Above 50 BeV/c, the angular separation between Cerenkov radiation from π and from K mesons becomes too small to be useful. Threshold-type Cerenkov counters several hundred feet long can be used. Inflight decays of wanted particles limit the ability to separate particles, and high rejection efficiencies are not easily attainable. Super-conducting rf cavities and methods employing transition radiation which separate particles according to $\gamma^2 = E^2/M^2$ appear to show most promise at this stage.[5]

The motivation for describing the beams above is to point out that for both bubble-chamber beams and counter beams greater than 50 BeV/c, particle separation already dictates that the beam transport must be hundreds of meters long. There is no need for small-focal-length lenses or high dispersing magnets. Below 50 BeV/c, this is not true. The increased decay in flight along with the ability to use short detecting devices would prompt a short-beam design. The lower momentum, however, means less field gradient is needed for focussing, and less magnetic field for dispersing.

The choice between super-conducting or conventional iron magnets for these beams does not appear to depend strongly upon such parameters as beam length, optics, and intensity. Either will fulfill most needs. The decision rests more directly upon considerations of cost, ease of maintenance, and reliability. Some of these items are discussed in the following section.

RELATIVE MERITS OF SUPERCONDUCTING AND CONVENTIONAL IRON MAGNETS

Cost of Building and Operating Magnets

This item is always one of the prime factors considered and is always the most difficult to estimate. One reason is the rapid improvements in cable fabrication and increased competition which lead to lower costs of super-conducting material. Another factor is inexperience in maintaining a large number of super-conducting magnets operative over long periods of time. Because any estimates made today will undoubtedly change by large factors within the next 10 years, no further consideration will be given to the subject currently. One must assume that SC magnets will be somewhat comparable in cost to the conventional iron magnet; otherwise the problem is academic.

Problem of Maintaining Operation

The conventional iron magnet has a very distinct advantage in ease of

operation. This is because it is an inherently simple device and because operational experience has removed many of the bugs. Maintenance to keep the magnet operative is more demanding, primarily because of the need for operating at 4°K. There is, for example, the question of how to supply liquid helium to the magnet. Concerning this problem, it appears that the following techniques might be employed:

1. Have a central liquefaction plant where liquid helium is placed in large dewars. Transport the dewars to the magnet to maintain liquid helium in it. Collect the helium gas in tanks or a line returning to the liquefaction plant.

2. Have a central liquefaction plant and run semi-permanent transfer lines to the magnets. Return cold or hot gas back to the main plant through insulated or non-insulated line.

3. Alongside each magnet place refrigerators which will circulate the helium liquid through the magnet after the magnet has been cooled down. Helium for cool-down would be provided initially from the central liquefaction plant and dewars.

As can be easily seen, prospects 1 and 3 would require a crew of technicians checking periodically on the status of the dewars and refrigerators. The last of prospect 2 could easily become very large, depending upon the cost of very low heat-loss transfer lines which must convey liquid helium over distances of hundreds of meters.

Susceptibility to Unexpected Occurrences

With a conventional iron magnet, the main disturbance to a magnet occurs when the power supply trips out. Nothing serious happens to the magnet and restoration to normal occurs in a matter of minutes. For the super-conducting magnet, the problem of being able to handle large amounts of magnet power in the event of a disaster is a serious one. A suggestion to remove the power-supply leads so as to reduce the heat loss makes it imperative that a safe shunt be provided to handle the current, should the magnet go normal for any reason.

Another problem is that of minimizing the beam heating should particles strike the windings of the magnet and thereby lose large amounts of their energy. Should even 10^{10} particles per pulse lose an average energy of 10 BeV through multiple interactions in the cold part of the magnet, more than 5 watts of power would be developed. If the entire external proton beam were inadvertently diverted into such a magnet, large amounts of liquid helium would be immediately boiled off. Also, the effects of radiation damage to the coils for extended periods may affect the super-conducting properties of the magnet.

Size and Cost of Experimental Areas

For low-momentum beams below 50 BeV/c, and for which separation techniques still exist, the length of a beam may be dictated by the ability of the magnets to focus and to disperse. There is no question that an enclosed building, if economically feasible, is a desirable structure. Crane coverage, ease of obtaining electrical power, and permanence of the experimental floor area are all desirable features. If the average length of many transport systems can be reduced substantially, fewer buildings will be necessary. Or, for the same funds, more experiments and other functions can be carried out in the same space.

SUMMARY AND CONCLUSION

Most of what has been considered herein has been of a very speculative nature. We are still in the infancy of development of large super-conducting magnets. None has yet been built of the type considered here. We have no experience to fall back upon and very few ideas as to the problems on the horizon with super-conducting magnets.

From the physics standpoint, they would be attractive to use because of their ability to do all that the conventional magnet can do and more. As to compelling reasons for going to super-conducting magnets, there appear to be rather few; of these, two are hyperon-beam construction and high-field switching magnets. Usually other factors dictate the magnetic fields required to be those obtainable with conventional magnets of reasonable size.

Generally speaking, one concludes that the time is premature by about two years to consider seriously the possibility of making the experimental magnets super-conducting. A serious evaluation could certainly be made more profitably at that time.

References

1. M. J. Longo, Experiment with Hyperon Beams at the 200 GeV Accelerator, LRL Report, AS/Experimental/02, Sept. 8, 1964.
2. D. Dekkers et al., Phys. Rev. 137, B962 (1965).
3. J. Lach, A High Energy R. F. Separated Beam for the Proposed 200 BeV Accelerator, LRL Report, AS/Experimental/02, March 24, 1966.
4. J. Sandweiss, RF Separated Beam Systems for Use at the 200 BeV Accelerator, see elsewhere in this volume.
5. A. L. Alikhanyan, Transition Radiation and Energy Loss of Fast Particles in Matter, Harvard Loeb Lectures, 1965 (unpublished).

THE POTENTIAL OF SUPERCONDUCTING MAGNETS FOR USE IN THE EXPERIMENTAL AREAS: PRELIMINARY REPORT

Robert B. Meuser

INTRODUCTION

It has been estimated that 164 general-purpose dc magnets, bending magnets and quadrupoles, will be needed by the experimenters three or four years after turn-on.[1] The magnets together with their power supplies and cooling systems will cost $11 million, and the electricity for a 10-year period will cost $5 million.[2] More than 30% of the peak electrical load of the Laboratory is used by these magnets.

Recent advances in superconducting (SC) magnet technology have raised the possibility of replacing all of the dc magnets, except for a few of the smaller ones, by SC magnets. The SC magnets themselves would be quite expensive, and they would require costly refrigeration systems. The savings in the costs of electricity, power supplies, and cooling systems, however, may make the SC magnets cheaper than conventional magnets in the long run. An additional benefit is that SC magnets can produce higher fields,* possibly resulting in shorter beam-path lengths, hence savings in costs of vacuum systems, shielding, and building space. Perhaps the higher fields will permit more experiments to be performed, or better experiments. It is impossible to evaluate such benefits on an economic basis, but at least they should be viewed as a valuable bonus.

The experimenters' magnets will not be needed until the accelerator is completed. Nevertheless, the amount of electric power and cooling capacity required for the experimental areas must be known rather early in the design process. Therefore, a decision about whether to rely heavily on SC magnets must be made early if a costly mismatch is to be avoided.

The ultimate goal of our study is to decide whether to go almost entirely to SC magnets. We are not yet ready to answer that question.

In this report we will discuss various ways of making SC beam-transport elements and various problems related to their use.

---

* Conventional magnets can produce dc fields of over 200 000 G. For beam transport magnets, however, it is not economical to go over 20 000 G. It will be practical to make SC bending magnets that produce 50 000 G or more.

STABILITY AND CURRENT DENSITY

If a SC solenoid is wound from plain SC wire it will not carry as much current, at a given field, as will a short sample of the same material. This phenomenon is called "current degradation," and it is worse in large magnets than in small ones, and worse in split-pairs than in simple solenoids. As the current is increased, the flux penetrates the superconductor in discrete steps, called "flux jumps." Energy is liberated as the flux jumps occur, and local heating results in a small region's losing its superconducting property—it "quenches" or "goes normal." The normal region propagates rapidly throughout the whole coil.

If an attempt has been made to reduce the current degradation, the magnet is said to be "stabilized." The terms "stabilized" or "fully stabilized" have no precise, universally accepted meanings, and most people who use these terms are careful to define them when they use them.

In a sense, a magnet is "stable" if it can achieve the short-sample characteristics of the material. If the current exceeds the short-sample value, however, the magnet will quench, and the current must be reduced to a fraction of its rating for the superconducting property to be regained. The BNL quadrupoles (described in the Appendix) have this kind of stability.

Some magnets have a large quantity of copper bonded to the SC, and very good heat transfer between the conductor and the liquid helium. The normal conductor can carry the full current without the temperature exceeding the critical temperature of the SC. If the current exceeds the short-sample critical current, the current is carried by the copper and a dc voltage appears across the winding. When the current is reduced to the short-sample value, the SC property is regained and the voltage drops to zero. The AVCO magnet (described in the Appendix) has this kind of stability.

All stabilizing methods entail a reduction in the space factor of the coil, and therefore, a reduction in the allowable bulk current density.* The degree of stability that is appropriate for a magnet depends on several factors:

1) The severity of the consequences of accidental quenching,

2) The probability that the current could accidentally exceed the rating,

3) The penalty paid for a low space factor,

4) The existence of factors tending to aggravate the stability problem: large size, split pairs, conductor permitted to move, and so on.

---

* By "bulk current density" we mean the total amp turns divided by the gross cross section occupied by the coil, including superconductor, normal conductor, interleaving material, fluid passages, and the like.

In a large bubble-chamber magnet, all of these factors tend toward a low power density. In a small quadrupole, the coil can quench with nothing more severe happening than a small burp of helium.

For beam-transport magnets, we should strive for high-current densities. The size, weight, cost, and mass to be cooled down will all benefit. With the variety of usage that experimental magnets experience, it is a virtual certainty that sometime, somewhere, when we least expect it, the current in a magnet will exceed its rating. It is absolutely essential that excessive current not endanger personnel, and it would be highly desirable that a moderately excessive current not damage the magnet. There seems to be no reason, however, to demand that the magnet not quench when it exceeds the rating; one should expect to pay some penalty for such a goof. No magnet, however, conventional or SC, can be made completely idiot-proof. An extreme overcurrent will wreck either one. For the largest bending magnet on our list, both Stekly[3] and Laverick[3] have told me they thought 10 000 A/cm^2 would be appropriate. For the smaller magnets and especially the quads (less stored energy for their size), we should be able to go much higher.

MECHANICAL STRESSES

It is quite common to make SC solenoids with no structure to resist the magnetic forces except the conductor itself. In a solenoid the magnetic pressure is uniform and radial and results in simple tension in the coil, analogous to a pressure vessel. With bending magnets, and to a lesser extent with quadrupoles, the magnetic pressure is concentrated, and large bending moments are developed. To resist the bending moments, the AVCO transverse-field magnet (see Appendix) has structural rings 10 inches deep surrounding it. For fields at least as high as 50 000 G, the structural problem is not insurmountable, but it is difficult.

SIZE EFFECT

It is interesting to see how the various magnet parameters vary with the size of the magnet. This variation depends strongly on what we chose to hold constant. We might be tempted to hold the current density constant, but, as we showed earlier, large magnets will probably be limited to much lower current densities than small ones, so to be realistic we should adopt some relationship between current density and size. We can't say with great certainty what the relationship is, but we would probably be more nearly correct if we assume the current density to vary inversely with the characteristic linear dimension, L, of the cross section rather than to assume that it is

independent of L. In the table that follows we show how the magnet parameters vary for both constant current density and current density proportional to 1/L. Furthermore, we compare magnets having geometrically similar cross sections -- the thicknesses of the coil and mechanical structure are proportional to the aperture dimension.

Variation of magnet parameters with magnet size for two cases:
Case A; Constant current density
Case B; Current density proportional to 1/L

	Case A	Case B[a]
Current density, NI/L^2	Constant	1/L
Total current, NI	L^2	L
Field strength, B	L	Constant
Field gradient, B/L	Constant	1/L
Stored energy	L^4	L^2
Mechanical stress	L^2	Constant

a. L is characteristic linear dimension of magnet cross section.

For the constant-current-density case, we see that the field increases as the size increases, which seems to be in direct violation of Murphy's Second Law. We also notice that the mechanical stresses increase drastically with increasing size. For the more realistic 1/L-variation of current density, however, we see that the field and mechanical stresses are both independent of size.

NATURAL VERSUS FORCED CONVECTION

The earliest SC coils were merely dunked into a dewar of liquid helium, and the helium was allowed to permeate the coil.

Heat transfer would be enhanced and therefore stability would be improved if the liquid were forced through the coil. If one scratched his head a little, he could probably figure a way to force the fluid through passages specifically designed to provide an optimum solution to the heat-transfer problem, and this might be hailed as a great improvement over the crude coil-in-a-pot designs that have evolved. But then we would need a circulating pump which must be bought, wired, interlocked, and maintained, and if it failed, or the power to it were shut off, the magnet would quench. Perhaps we will be seeing the decadent coil-in-a-pot design for a while yet.

MAGNET CONFIGURATIONS

There are an infinite number of ways to produce uniform or quadrupole

fields. Some have real advantages, such as reducing the total current required or avoiding saturation effects — others are merely ingenious, or amenable to mathematical manipulation. The ability of the superconducting coil to attain a high current density makes attractive many configurations which, in a conventional magnet, would require unreasonably high quantities of electric power.

When considering various configurations, we must bear in mind that the experimenters will not willingly tolerate a beam-transport magnet which produces a large stray field.

The "picture frame" design can produce uniform fields as high as 20 000 gauss. The largest magnet on our list has an aperture 8 by 16 inches and is 160 inches long. A conventional magnet of this design is shown in Fig. 1. The coil is shown 15 inches wide, about the economic optimum for the expected operating conditions. A SC coil to replace the copper one has to be only 0.8 inch wide for a current density of 10,000 A/cm^2 (Fig. 2). Tension members passing above and below the useful aperture tie the two sides of the coil together. If the 300-ton magnetic force on the coil were allowed to bear directly on the yoke, the heat leak through the supports would be 100 times too high—the forces must be balanced internally. This is true for all magnet configurations.

The iron-yoke design can be pushed as high as 30 to 40 000 G without saturating the iron by using the diamond-shaped apertures recently analyzed by Leeb and Umstatter[4] (Fig. 3). A current sheet in the form of a circular cylinder will produce a uniform field inside it if the current follows a cosine distribution. The uniform field is retained if such a coil is closely surrounded by iron, but then the field is limited to 20 000 G. However, if one desires a higher field, an annulus of sufficient width to reduce the field in the iron to 20 000 G can be placed between the coil and the iron. A real coil cannot have the mathematically infinitesimal thickness of a "current sheet," but a finite thickness can be built up of thin layers, each of which has a cosine distribution.

One arrangement that has become popular is the intersecting-circle cross section shown in Fig. 4. Its chief virtue, it seems, is that its magnetic properties can be mathematically described without the use of calculus. The current density is uniform within the current-carrying region, but it is by no means unique in this respect. Surrounding the coil with iron probably destroys the uniformity of its field, but the boundary of the current-carrying region could be modified to regain it.

A variety of configurations are also available for producing quadrupole fields. One can surround almost any shape of aperture with a suitable distribution of currents, with or without the use of iron.

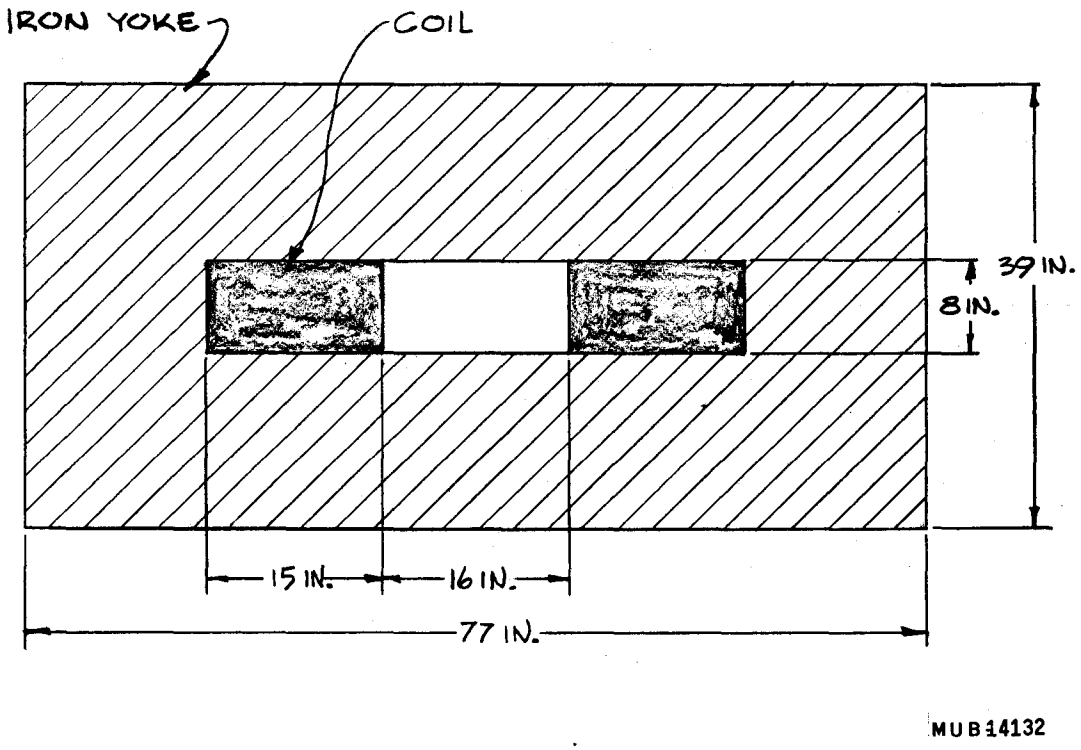

Fig. 1. Conventional picture-frame magnet, capable of about 20,000 G.

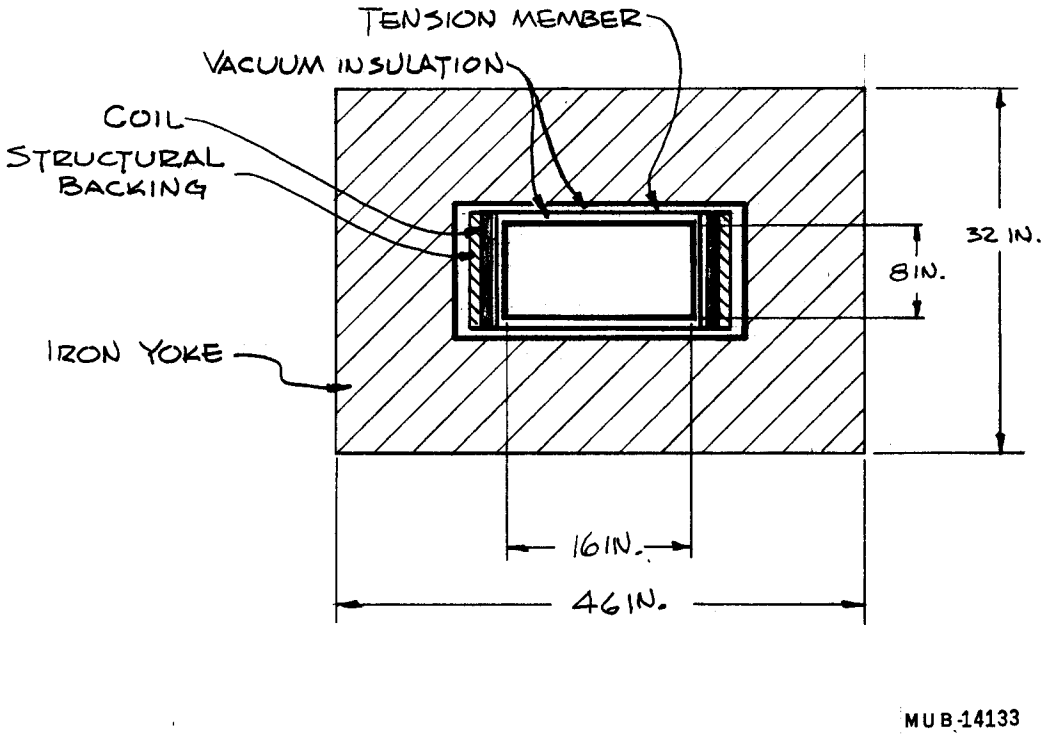

Fig. 2. Superconducting picture-frame magnet having the same useful aperture size and field as that shown in Fig. 1. Current density is 10,000 A/cm^2.

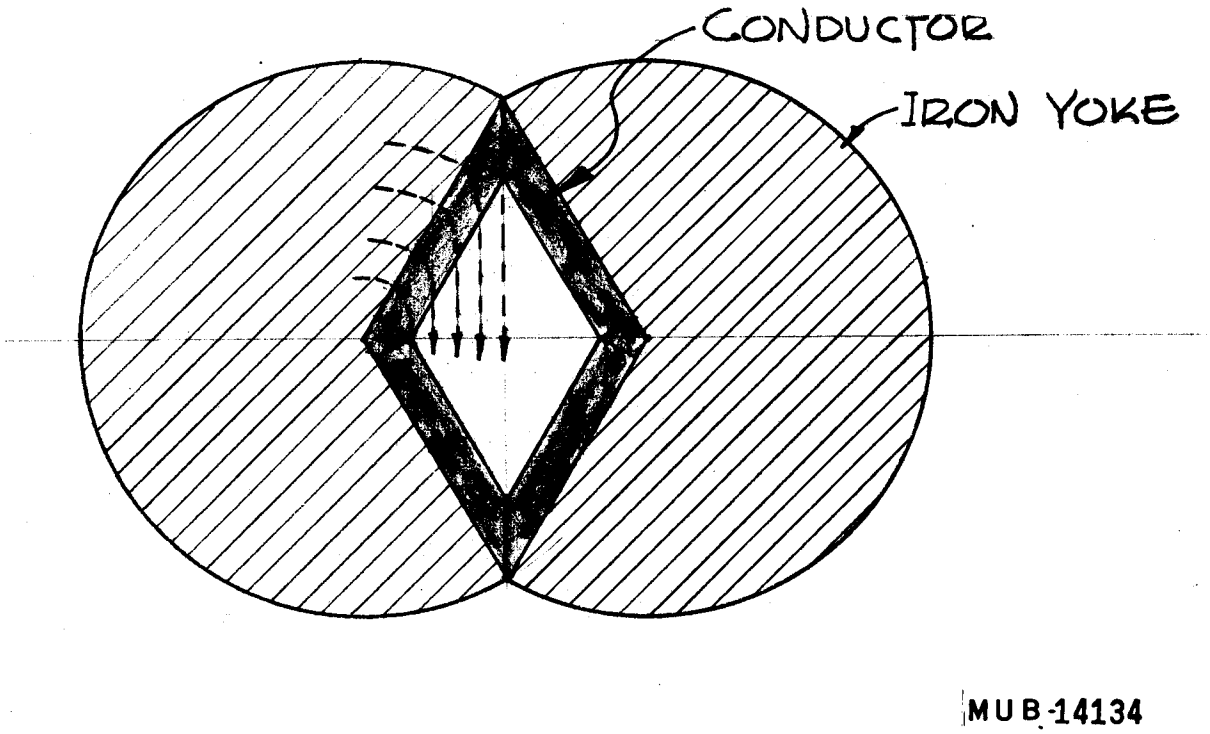

Fig. 3. High-field iron-core magnet design analyzed by Leeb and Umstatter (Ref. 3). For the design shown, the field in the iron is 20,000 G when the field in the aperture is 40,000 G.

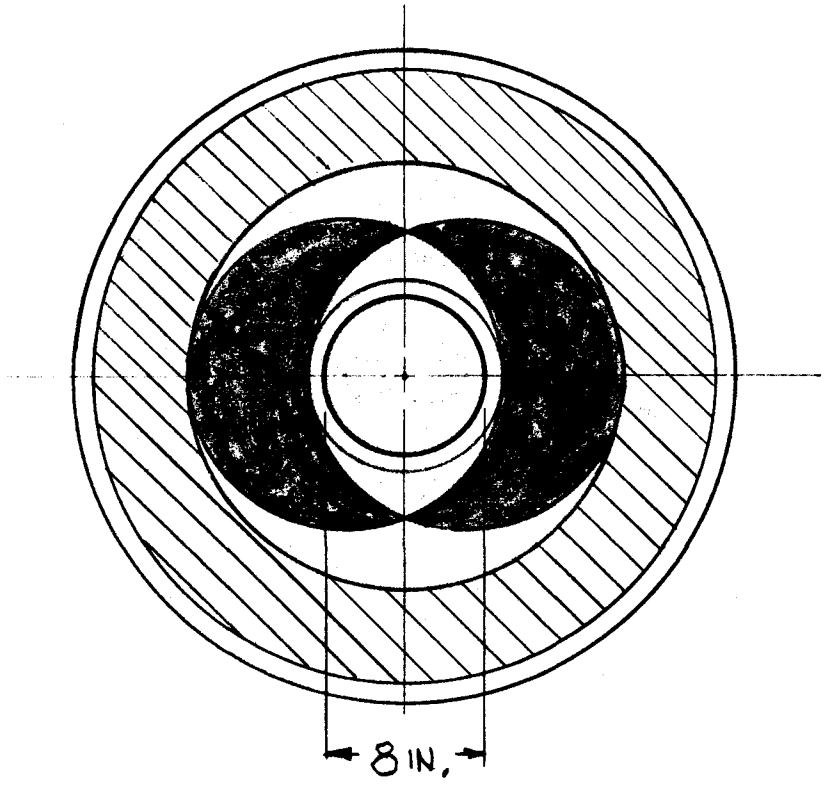

MUB 14135

Fig. 4. Superconducting bending magnet employing intersecting-circle coil cross section; 50,000 G, 5000 A/cm^2.

Of particular interest are the configurations recently investigated mathematically by R. A. Beth.[5] He shows that a current sheet in the form of a circular or elliptical cylinder will produce uniform or multipole fields if the currents have a cosine distribution, with the proper number of cycles. Furthermore, around the first coil and spaced some distance from it, one can place a second coil that exactly cancels the external field produced by the first one. This configuration provides magnetic shielding, admittedly at some extra cost in superconductor, but without the weight and bulk of the iron shielding necessary for a high-field magnet.

REFRIGERATION SYSTEM AND ITS COST

One can invent many schemes for refrigerating the magnets, for example:

a. single refrigerator for each magnet or small cluster of magnets,

b. central refrigerator, with insulated transfer lines to and from each magnet,

c. central liquefier, with distribution of liquid either by transfer lines or by transport dewar; boiled-off gas returned by uninsulated piping. Within each of these classes there can be many variations. The selection of the "best system" is worthy of considerable attention by the best people in the field. We have arranged for the NBS[6] to make a preliminary study of the problem and to produce rough cost estimates. I will not attempt to abstract their report except to say that three of the 12 systems they investigated have 10-year total costs (capital plus operating) of $7.0 to $9.5 million for the refrigeration of the 164 magnets.

SUPERCONDUCTING VERSUS CONVENTIONAL MAGNETS: WHICH ARE LEAST EXPENSIVE IN THE LONG RUN?

That is the question we are trying to answer, but we aren't ready to yet.

A list of superconducting beam transport elements, past, present, and future, is presented in the Appenix.

APPENDIX: LIST OF SC BEAM TRANSPORT ELEMENTS

Brookhaven

W. B. Sampson and R. Britton have built several interesting quadrupoles. The first was a Panofsky square-aperture type. The second, a 3-in. bore cosine-current-distribution magnet, produced 8.5 kG/cm, equivalent to an iron quad with a 32.4-kG pole-tip field. In the shop is a 4-in. bore by 60-cm long quad having a gradient greater than 8.5 kG per cm and intended for use on a beam line.

Argonne

Joseph Peerson at ANL is in the early stages of planning a SC quad.

AVCO

Z. J. J. Stekly et al.,[7] AVCO-Everett Research Laboratories, have built a large magnet of the overlapping-circle cross-section type which, except for the fact that its axis is vertical, would make a passable bending magnet. Its specifications are:

Field strength	40 kG
Useful aperture diameter	12 in.
Outside diam of magnet and structure, not including dewar	33 in.
Effective length	about 6 ft
Current	800 A
Conductor	9 wires imbedded in copper strip
Liquid helium for cooldown	1500 liters $\cong$ \$5000
Current density based on gross coil volume	3000 A/cm^2

Rutherford

M. N. Wilson and Bryan F. Colyer,[8] Science Research Council, Rutherford Laboratory, England, are in the detail-design stage of a bending magnet of the overlapping-circle cross-section type. Pertinent data (very similar to Fig. 4) are:

Field strength	50 kG
Useful aperture diameter	12 cm
Effective length	150 cm
Current	1000 A
Conductor	Cable
Current density based on coil envelope dimensions	5000 A/cm^2

Conductor cost	$ 60 000
Total cost	$100 000
Completion date	Mid 1967

CERN

A. Asner, CERN, is reported by Wilson to be building or planning to build a SC quadrupole.

Siemens (Germany)

Sampson says Siemens is making an iron-core bending magnet.

References

1. 200 BeV Accelerator Design Study Report, UCRL-16000, June 1965, Table XIII-I.

2. R. B. Meuser, Experimenters' Magnets, LRL Engineering Note M3817, September 1966.

3. Z. J. J. Stekly and C. Laverick, private communication.

4. K. Leeb and H. H. Umstatter, Magnets with Iron Yokes and Fields above 20 kG, CERN 66-7, February 1966.

5. R. A. Beth, Brookhaven National Laboratory reports AADD-66, -102, -103, -106, -107, -110, February - May 1966 (the work is continuing).

6. T. R. Strobridge, D. B. Mann, and D. B. Chelton, Preliminary Analysis of Refrigeration Requirements for Superconducting Magnets at the 200 BeV Accelerator, National Bureau of Standards Report No. 9259, October 1966.

7. Z. J. J. Stekly et al., International Institute of Refrigeration, Commission 1 Meeting, Boulder, Colorado, June 1966, Paper No. VI-1.

8. P. F. Smith and M. N. Wilson, International Institute of Refrigeration, Commission 1 Meeting, Boulder, Colorado, June 1966, Paper No. VI-3.

DUTY FACTOR FOR THE dc EXPERIMENTAL MAGNETS

Robert B. Meuser

As an aid to cost estimating and design optimization of the dc experimenters' magnets, one would like to know what their duty factor will be. An early estimate of the total initial-plus-operating cost of these magnets came to 20 million dollars, so it is not a trivial matter. Then, too, we are currently studying the possibility of making those magnets superconducting, and the relative costs will be the major factor in deciding the superconducting vs conventional magnet question.

I made an estimate of the duty factor with the help of Denis Keefe early in the summer. The method involved estimating a number of individual factors which enter in the final "duty factor." Later, when the Summer Study group arrived, I showed it to some of them and urged them to change the numbers as they saw fit. The psychology of this approach was probably all wrong--I should have given them an outline and asked them to fill in the blanks--but I think the end result would not have been much different.

Another approach would have been to rely more heavily on data concerning the experience at other accelerators. Such data are not easily obtained and one would still have to use judgment in applying the data to the 200-BeV machine. We have since obtained some data from the Bevatron and the AGS--no serious disagreements are apparent.

Although the details varied from person to person, the end results were in substantial agreement. The average overall duty factor was 0.197 against my original estimate of 0.235.

Subsequent to the Study Group's departure, some of the people at LRL had expressed the feeling that a factor of 0.9 for f_i [(number of magnets installed) divided by (number owned)] was too high, and that a figure of 0.8 would be more appropriate.

In the numerical work which follows, my original guesses are shown, together with the average of all the estimates (which are shown in [ ]'s).

$\frac{\text{Time accelerator is on}}{\text{Total time}} = f_t$:

Total shifts in one year = 3×365.24	= 1096
Shutdowns; 6 wk/yr×21 shifts/wk	= - 126
Maintenance; 2 shifts/wk×(52 - 6)	= - 92
Accelerator development; 1 shift/wk×(52 - 6)	= - 46
	832

$$f_t = 832 \div 1096 = 0.76 \quad [0.70]$$

$$\frac{\text{No. of magnets installed}}{\text{No. of magnets owned}} = f_i = 0.9 \quad [0.9]$$

$$\frac{\text{No. of magnets under power}}{\text{No. of magnets installed}} \approx \frac{\text{No. of active beam lines}}{\text{Total no. of beam lines}}$$

$$= f_e = 0.7 \quad [0.63]$$

$$\frac{\text{Average power}}{\text{Maximum power used during experiment}} = f_{p1}$$

Let current, i, vary linearly with time, or in sawtooth fashion, between maximum and minimum values I and KI in the time interval T.

$$i = [K + (1 - K)\, t/T]I$$

$$f_{p1} = \bar{P}/P_{max} = \frac{1}{\bar{T}} = \frac{\int_0^T i^2 R dt}{I^2 R} = (1 + K + K^2)/3$$

For K = 0.5; $\quad f_{p1} = 7/12 = 0.58 \quad [0.58]$

$\frac{\text{Max. power used during experiment}}{\text{Max. power rating of magnet}} = f_{p2}$:

$$f_{p2} = \left[\frac{\text{Max. current...}}{\text{Current}}\right]^2 = (0.9)^2 = 0.81 \quad [0.78].$$

When the accelerator is turned off, some of the beam-line magnets remain on for tune-up, because it is too much trouble shutting down and starting up. For this condition, there will be corresponding f values as previously defined:

$$f'_i = 0.9 \quad [0.9]$$
$$f'_e = 0.2 \quad [0.4]$$
$$f'_{p1} = 0.6 \quad [0.6]$$
$$f'_{p2} = 0.8 \quad [0.75]$$

The time fraction associated with this mode of operation is taken as 50% of the accelerator off-time:

$$f'_t = (1 - 0.76) \times 0.5 = 0.12 \quad [0.06].$$

Finally, then, the duty factor is

duty factor = (Energy used in given time) ÷ (Energy that would be used at rated power)

$$= f_t f_i f_e f_{p1} f_{p2} + f'_t f'_i f'_e f'_{p1} f'_{p2}$$

$$= .76 \times .90 \times .70 \times .58 \times .81 + .12 \times .90 \times .20 \times .60 \times .80$$

$$= 0.225 + 0.010$$

$$= 0.235 \quad [0.197]$$

E. THEORY

ELASTIC SHRINKAGE AND POMERANCHUK DOMINANCE

W. Rarita

The shrinking of diffraction peaks has had a curious history. The hypothesis that cross sections are dominated at high energies by the exchange of Regge poles in a cross channel leads to a simple expression for the πN elastic differential cross section:

$$\frac{d\sigma}{dt} \sim \frac{1}{4\pi} \sum_{i,j} \mathrm{Re}(\zeta_i^* \zeta_j)\, \eta_\pi^i \eta_\pi^j (\eta_N^i \eta_N^j + \phi_N^i \phi_N^j) \left(\frac{s}{s_0}\right)^{\alpha_i - 1} \left(\frac{s}{s_0}\right)^{\alpha_j - 1} ,$$

and similar expressions for other cross sections. The sums are carried over all contributing poles, ζ_i is the "signature factor," the η's and ϕ's are analogous to coupling constants, and the α_i's are the Regge trajectories of the exchanged particles. Each of these parameters is only a function of t, the momentum transfer, so that the dependence of $d\sigma/dt$ on s (the energy squared in the c.m. system) is explicit. If one expands $\alpha(t) \approx \alpha(0) + t\,\alpha'(0)$, and then assumes that the energy is so high that only the pole with the largest α is important, he immediately finds that for increasing s, the cross section becomes more and more narrowly limited toward the forward direction. The first indication of this Regge-pole behavior was found in the shrinking of pp elastic scattering (line 4, Table I), but later it was found that the πp scattering had no shrinking (lines 1 and 2, Table I) and that $\bar{p}p$ showed antishrinking! The usual explanation was that in the above cases in which we have several Regge poles contributing, we have no definite shrinking or antishrinking over a limited energy range. Since each pole has several adjustable parameters, it is possible to fit the energy dependence of the elastic scattering.[1]

We now give a simple model to account for the effective Pomeranchuk slope, $\tilde{\alpha}'_P$, also called the "effective one-pole slope" for the several reactions listed in Table I. This parameter is the value needed for α'_P to fit $d\sigma/dt$ in various reactions if a one-pole approximation is used in an attempt to fit the data. In the various reactions, this pole has the quantum numbers of the vacuum, is assumed to have $\alpha_P(0) = 1$, and is designated as the "Pomeranchuk pole."

We assume that the Pomeranchuk (P) trajectory dominates the other Regge poles in the reaction. Alternatively, we may say that the partial contribution, σ_P, due to the Pomeranchuk, P, is large compared with the contributions, $\sigma_{P'}$ and σ_V, due to the next known vacuum trajectory (like P) and the vector meson

Table I. Values of $\bar{\alpha}'_P$ deduced from various experiments.[a]

		Reaction	$\bar{\alpha}'_P$ (BeV/c)$^{-2}$
I	1	$\pi^- p \to \pi^- p$	-0.062 ± 0.068
	2	$\pi^+ p \to \pi^+ p$	0.103 ± 0.074
II	3	$\bar{p}p \to \bar{p}p$	-0.914 ± 0.376
	4	$pp \to pp$	0.685 ± 0.051
III	5	$K^- p \to K^- p$	-0.398 ± 0.322
	6	$K^+ p \to K^+ p$	0.50 ± 0.16

a. Data from S. J. Lindenbaum, Oxford International Conference, Sept. 1965, p. 113.

of largest $\alpha(0)$. The latter includes the ρ for $\pi^\pm p$ and the ω for $\bar{p}p$ and pp. It then turns out that $\bar{\alpha}'_P$ is mainly given by the interference term between P and V. Treating the V contribution as small, one can deduce that the correction to the α'_P in the effective $\bar{\alpha}'_P$ from the V is given by

$$\Delta_V \bar{\alpha}'_P = \pm [\alpha_P(0) - \alpha_V(0)](\sigma_V/\sigma_P)(\tilde{a}_P - \tilde{a}_V) \equiv \alpha_{PV} \ . \qquad (1)$$

Here $\tilde{a}_i$ is the total width of the ith pole and includes an energy-independent part a_i and an energy-dependent term $\alpha'_i \ \ell n \, E$. In Eq. (1) the sign of $\Delta\alpha'_P$ changes as charge conjugation is applied to the incoming particles. We observe that Eq. (1) has only one parameter, $(\tilde{a}_P - \tilde{a}_V)$, which is not fixed by total cross-section information, and determines two experimental numbers. For example, $(\tilde{a}_P - \tilde{a}_V)$ can be determined in $\pi^\pm p$ scattering (I or lines 1 and 2 of the table), so that Eq. (1) gives $\Delta_V \bar{\alpha}'_P = \pm 0.08$. The remainder 0.02 will be discussed in Eq. (2) below. The entries II and III give similar results.

The part of $\bar{\alpha}'_P$ which does not depend on V is given by P alone and the interference of P and P' :

$$\Delta_{P'} \bar{\alpha}'_P = (\alpha_P - \alpha_{P'})(\sigma_{P'}/\sigma_P)(\tilde{a}_P - \tilde{a}_{P'}) \equiv \alpha_{PP'} \qquad (2)$$

$$\bar{\alpha}'_P = \alpha'_P + \Delta_{P'} \bar{\alpha}'_P + \Delta_V \bar{\alpha}'_P \ .$$

As noted above, $\pi^\pm p$ gives $\bar{\alpha}'_P = 0.02$. We see that the data for II (or $\bar{p}p$ and pp) are consistent with $\bar{\alpha}'_P = 0.0$ in Eq. (2) and an effective slope determined entirely by the P-V interference. We may note that as $s \to \infty$, only α'_P remains.

The initial expectation concerning the slopes of Table I based on one-pole theory was that they would all be the same -- roughly about 1. If the interference terms in Eqs. (1) and (2) were small, this expectation would have been

correct. Otherwise stated, α'_P should be much larger than a_{PP} and a_{PV}. This is not the case. In fact, we find that $a_{P'} + a_{PP'} \approx 0$. In addition, α'_P can be given a range of values from 0 to 0.4, and the parameter $(\tilde{a}_P - \tilde{a}_{P'})$ can be adjusted to make up the difference.

The described qualitative features have been tested in detailed calculations performed by Phillips and Rarita.[2]

References

1. A good introduction to Regge poles is given in R. J. N. Phillips, Regge Poles in High Energy Scattering, lecture notes prepared for Erice Summer School, 1966.
2. R. J. N. Phillips and W. Rarita, Phys. Rev. 139, B1336 (1965).

SOME π-N AND N-N REGGE-POLE PREDICTIONS AT HIGH ENERGIES

W. Rarita

The Regge-pole hypothesis has had some success in correlating the known high-energy data (6 to 25 BeV/c).[1,2,3] We have compiled the known measurements, and in this report we provide predictions for other interesting quantities to be measured at present accessible energies as well as at planned energies for future accelerators. In this way the fruitful exchange between theory and experiment will be continued.

The present πN situation is summarized in a recent paper by Chiu, Phillips, and Rarita.[4] There, total cross sections, σ_T, differential cross sections for elastic ($\pi^{\pm}p \to \pi^{\pm}p$) and charge-exchange ($\pi^-p \to \pi^0n$) scattering, $d\sigma/dt$, the ratio of the real to imaginary part of the forward elastic amplitude, Re/Im, and the π^-p elastic polarization were used in the determination of the Regge parameters for the system. These data are from 6 BeV/c upward and refer to momentum-transfer squared $|t| < 1$ (BeV/c)^2.

For the NN system, we have the following data: $d\sigma/dt$ and σ_T for both pp and $\bar{p}p$ scattering, the Berkeley polarization data from 5 to 7 BeV/c, and the ratio Re/Im for pp scattering.

All these data have been analyzed simultaneously. This procedure is a most exacting test of the factorization of Regge poles. First, there is the internal factorization in NN itself, and second, the factorization between the combined πN and NN. A detailed report describing this procedure is forthcoming.[5]

In the accompanying figures (1-20), determinations and predictions for incoming momenta at 10, 25, 70, and 200 BeV/c are given. The first momentum, 10 BeV/c, is in the middle and the second momentum, 25 BeV/c, at about the highest part of the range of present accelerators. The third value, 70 BeV/c, is the designed Russian momentum and the last, 200 BeV/c, is the designed American momentum. We also show some typical curves which indicate the agreement of our calculations with present experimental data. Besides the quantities already measured, we include predictions for C_{NN}, A_{recoil}, and R_{recoil} for pp and $\bar{p}p$ scattering.[6] Also the quantities which have been measured only for pp scattering are extended to $\bar{p}p$ scattering.

The best parameters for the 407 data points used in this analysis lead to a χ^2 of 443. Among the parameters thus determined, the trajectories have

generally been of greatest interest. For these we find $\alpha_P(0) = 1.0$, $\alpha'_P(0) = 0.2$, $\alpha_{P'}(0) = 0.7$, and $\alpha_\omega(0) = 0.2$.

Finally, we note that we are engaged in a similar study to include the KN system as well.

References

1. R. J. N. Phillips, Regge Poles in High Energy Scattering, lecture given at the International School of Physics, "Ettore Majorana," Erice, Italy, 1966 (to be published).

2. M. Gell-Mann, Current Topics in Particle Physics, in Proceedings of the XIIIth International Conference on High-Energy Physics, August 31 through September 7, 1966, Berkeley, California (proceedings to be published by the University of California Press, Berkeley).

3. L. Van Hove, Hadron Collisions at Very High Energies, Rapporteur's talk, Session 13, in Proceedings of the XIIIth International Conference on High-Energy Physics, August 31 through September 7, 1966, Berkeley, California (proceedings to be published by the University of California Press, Berkeley).

4. C. B. Chiu, R. J. N. Phillips, and W. Rarita, πN Polarization and Regge Poles, UCRL-16940, June 29, 1966 (to be published in Phys. Rev.).

5. W. Rarita, R. Riddell, C. B. Chiu, and R. J. N. Phillips, Regge Pole Model for pp and $\bar{p}p$ Scattering (in preparation).

6. R. J. N. Phillips and W. Rarita, High Energy Polarization Experiments and Regge Poles, UCRL-16185, June 10, 1965.

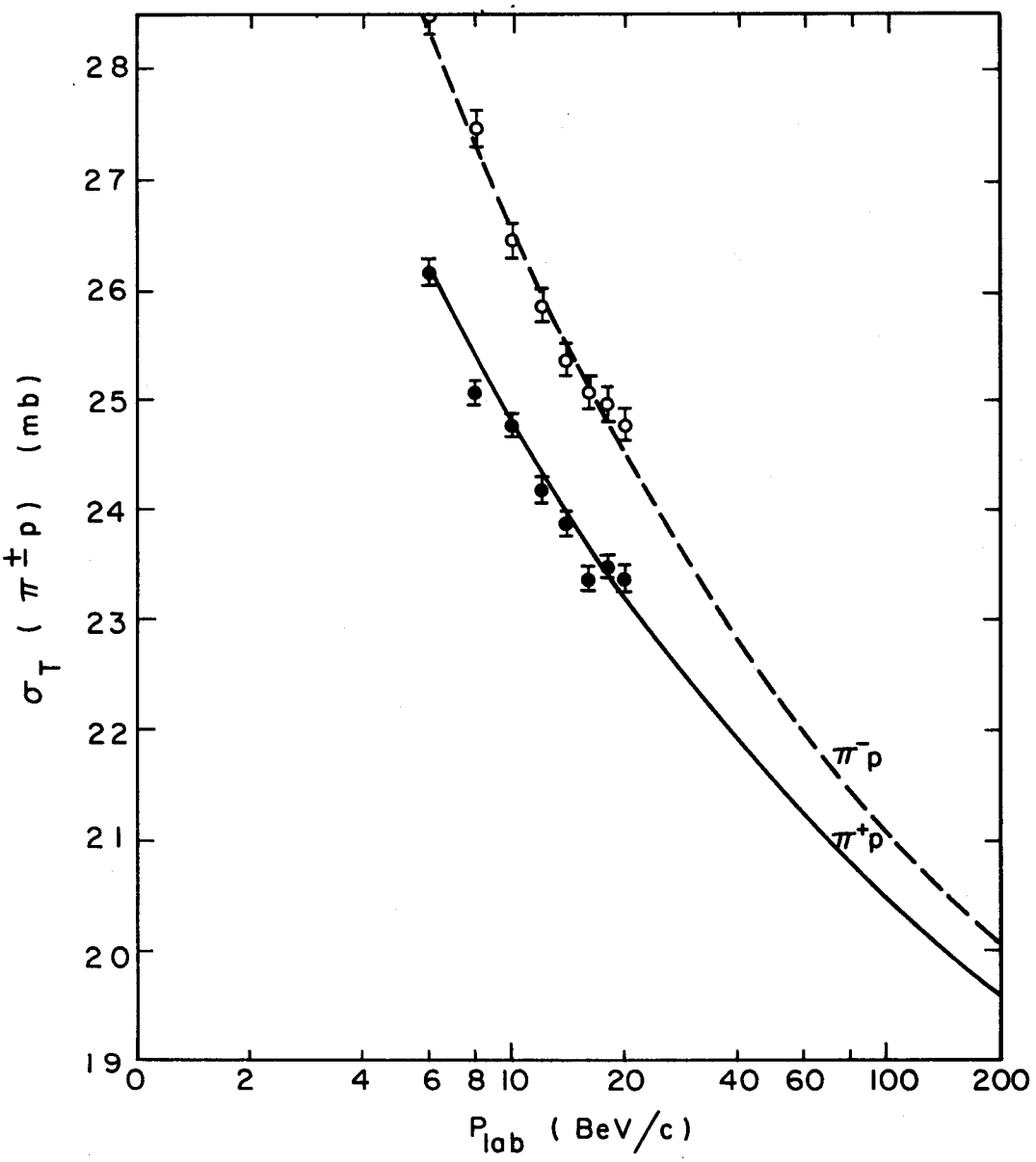

XBL 671-30

Fig. 1. Total cross sections for $\pi^{\pm}$ p.

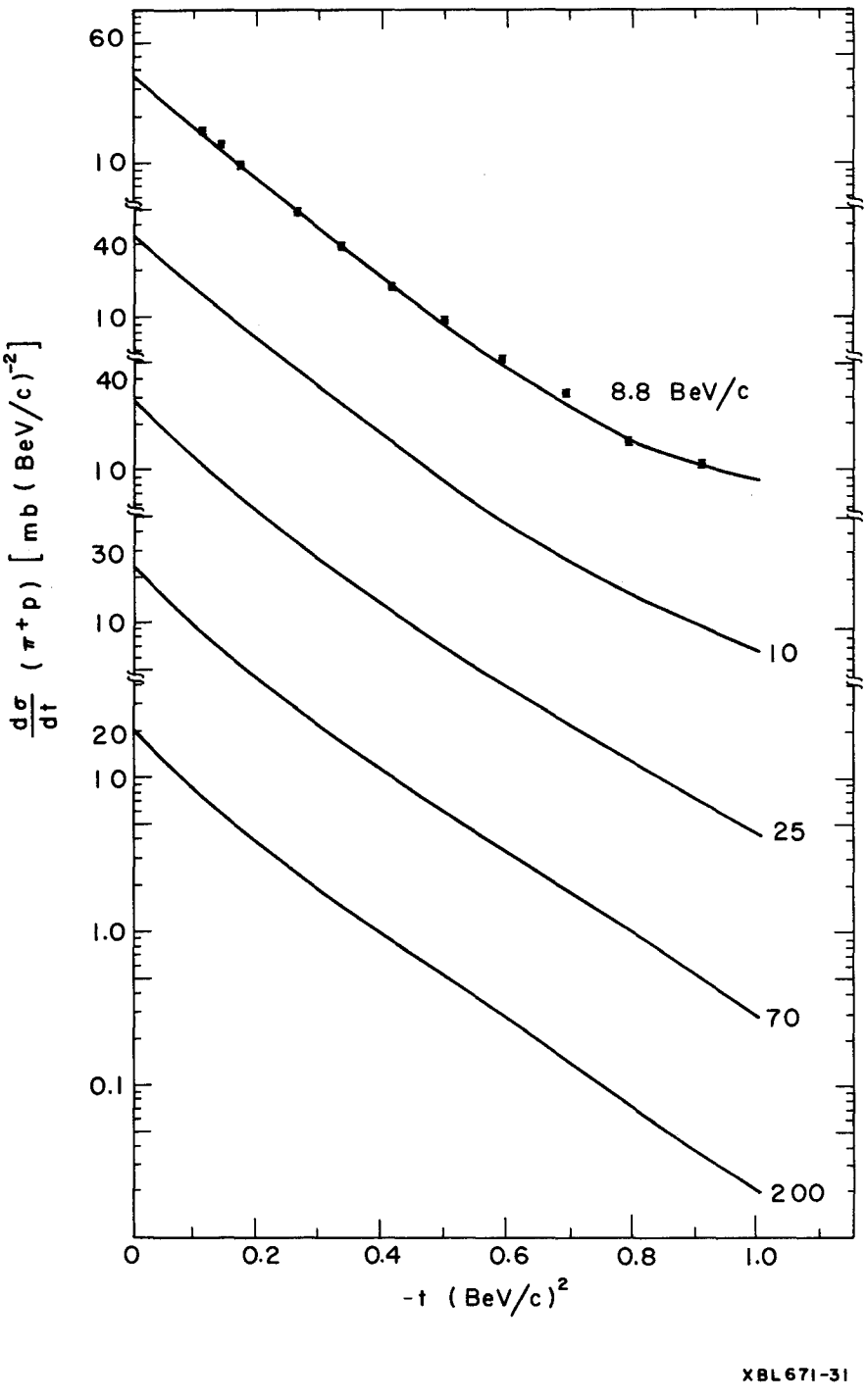

Fig. 2. $\pi^+ p$ Differential cross sections at 8.8, 10, 25, 70, and 200 BeV/c. Successive sets are spaced by a decade.

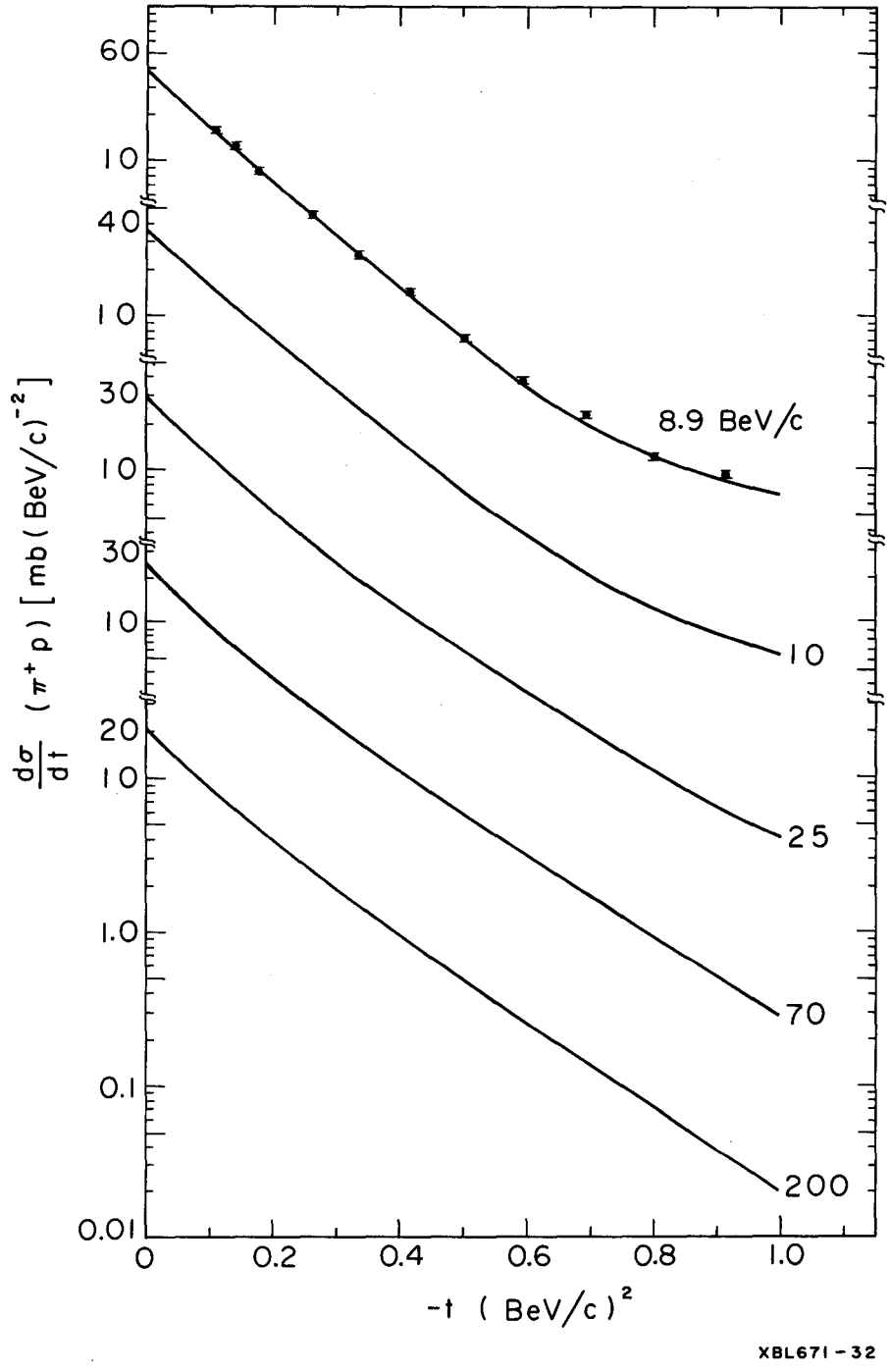

Fig. 3. π^-p Differential cross sections at 8.9, 10, 25, 70, and 200 BeV/c. Successive sets are spaced by a decade.

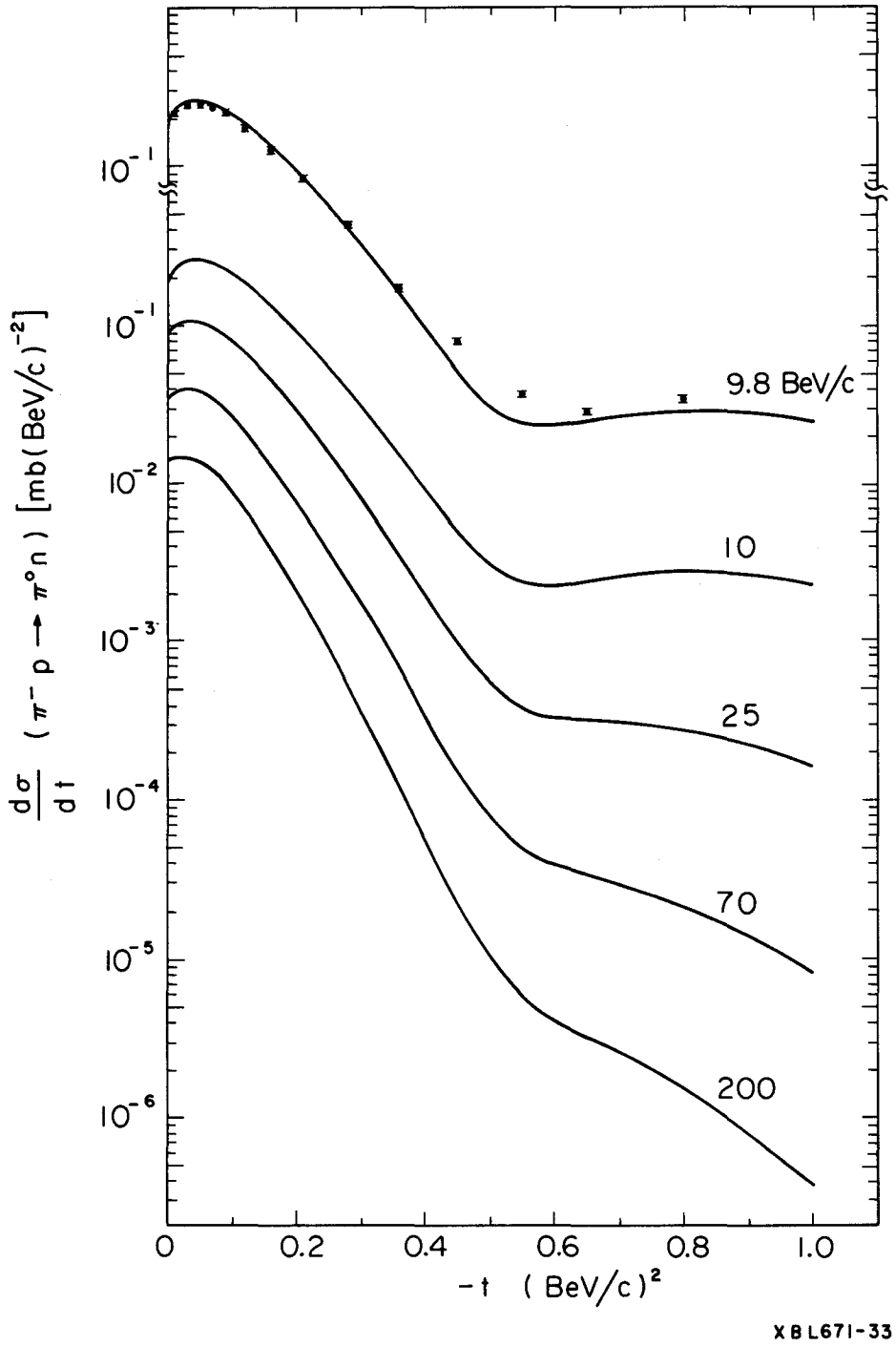

Fig. 4. $\pi^- + p \rightarrow \pi^0 + n$ differential cross sections at 9.8, 10, 25, 70, and 200 BeV/c. Successive sets are spaced by a decade.

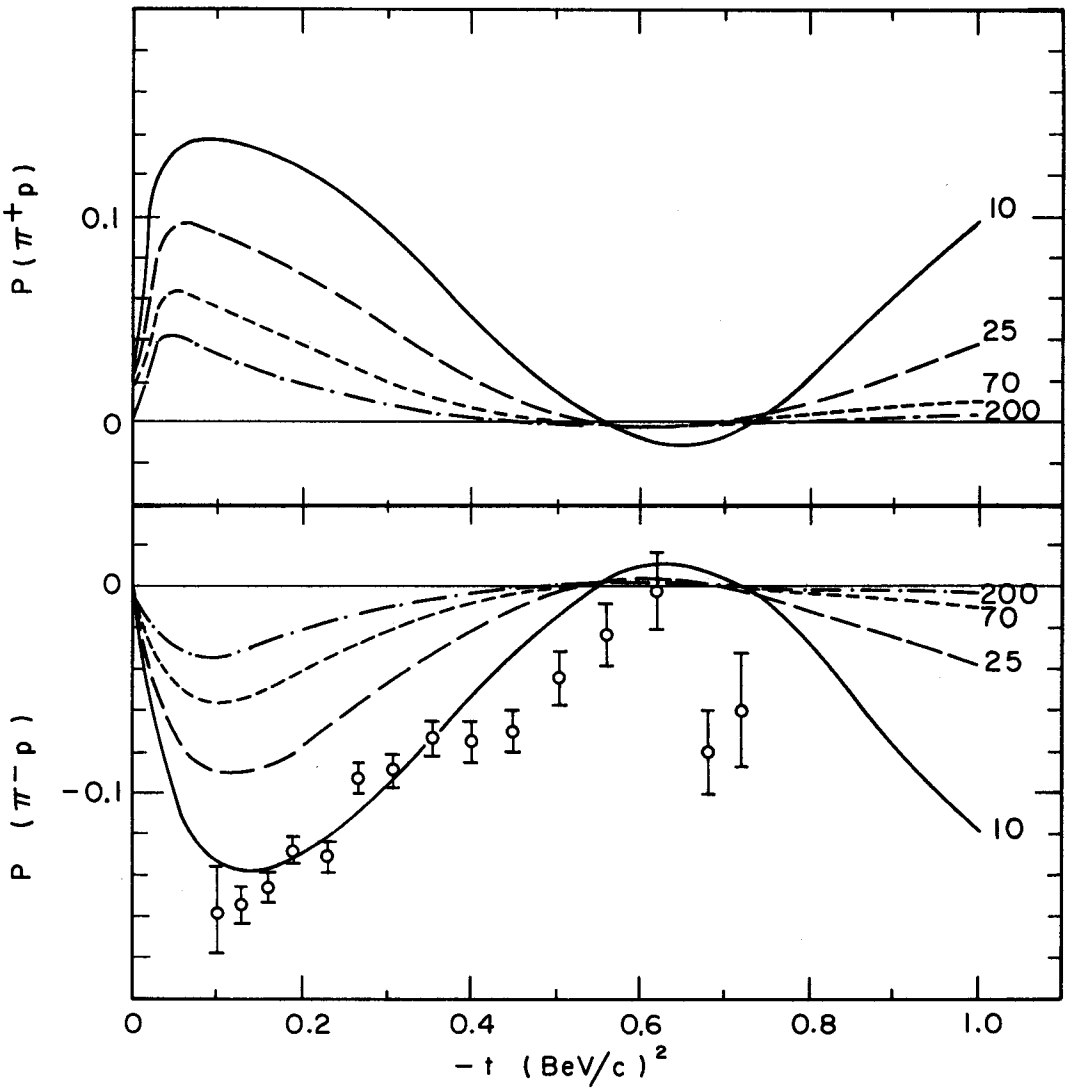

Fig. 6. The ratio of the real to the imaginary part of the forward scattering amplitude for $\pi^{\pm}$p scattering as a function of momentum.

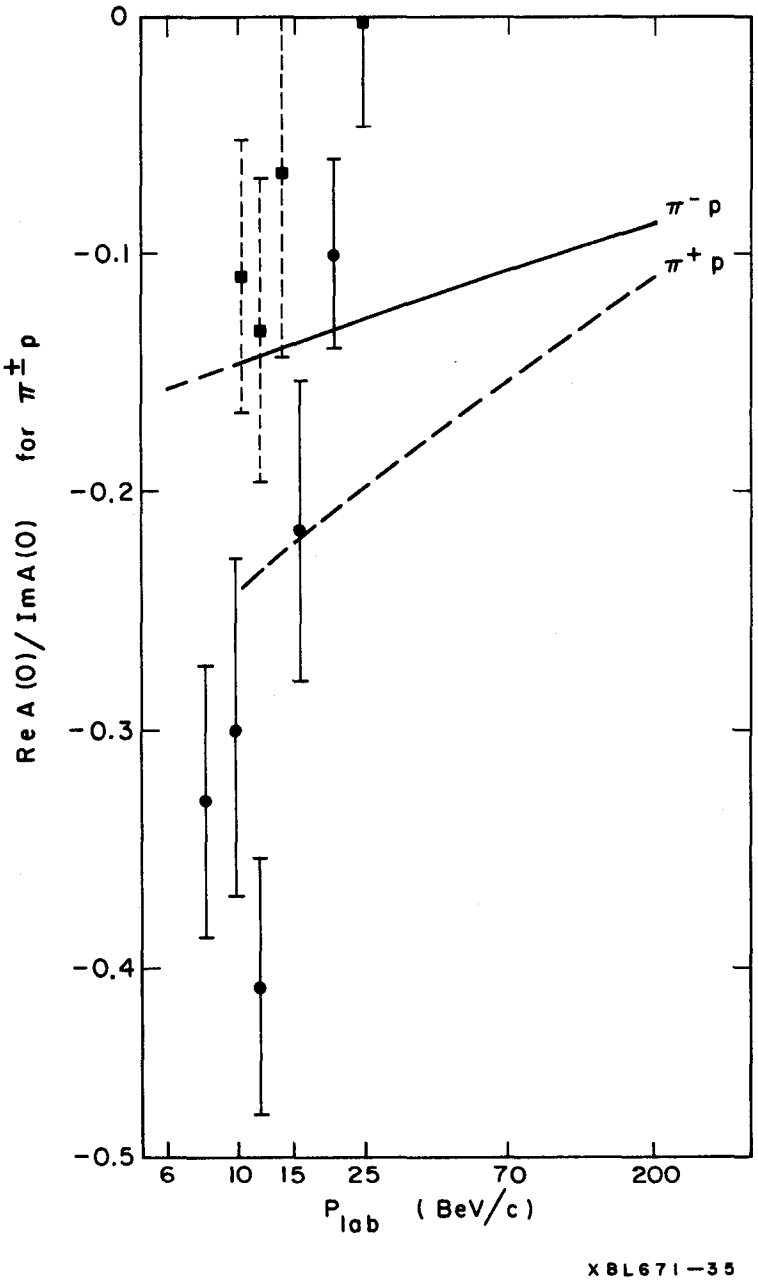

Fig. 5. $\pi^{\pm}$p Polarizations at 10, 25, 70, and 200 BeV/c. The experimental π^-p polarization is shown to indicate the quality of the fit.

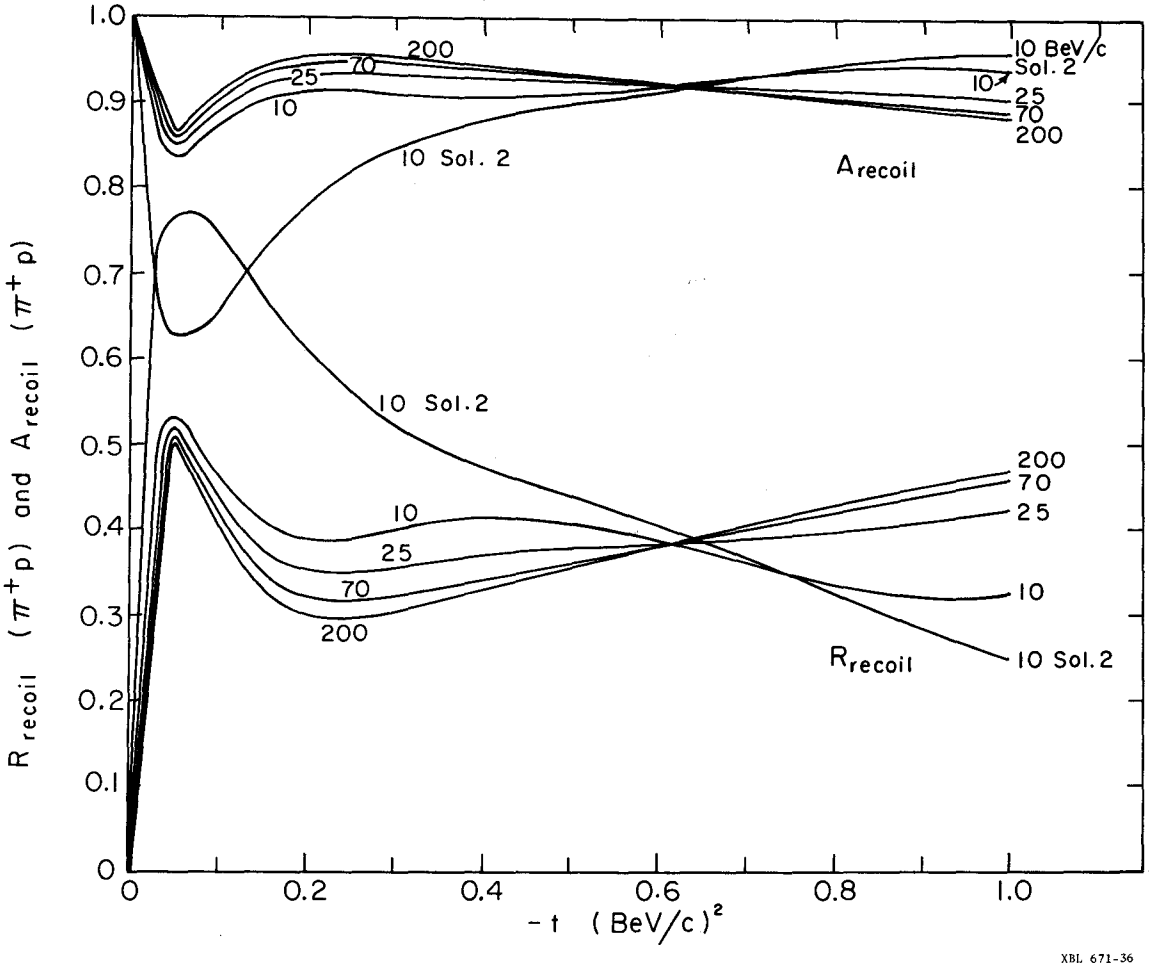

Fig. 7. R_{recoil} and A_{recoil} for π^+p scattering at 10, 25, 70, and 200 BeV/c. Also shown is the 10-BeV/c prediction for Solution 2.

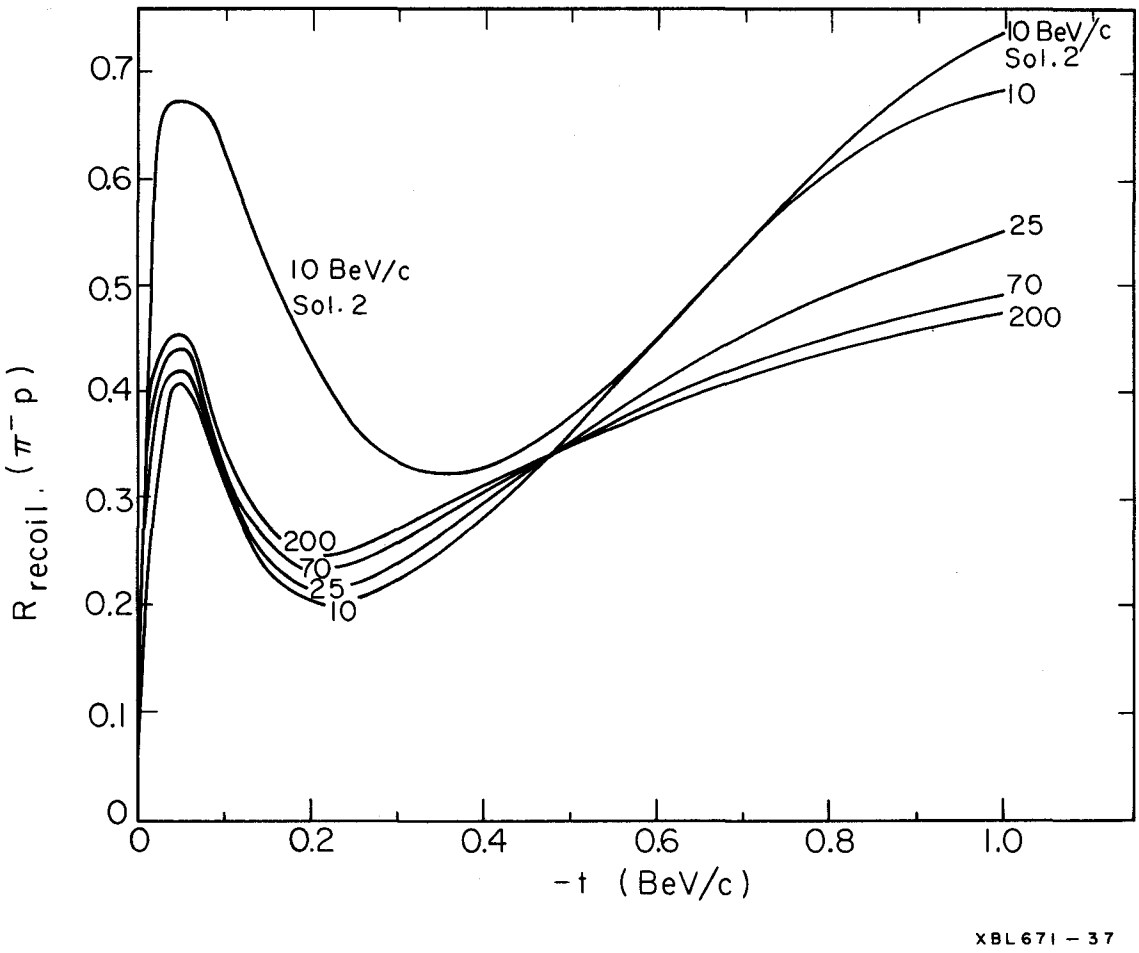

Fig. 8. R_{recoil} for $\pi^- p$ scattering at 10, 25, 70, and 200 BeV/c. The 10-BeV/c prediction for Solution 2 is also given.

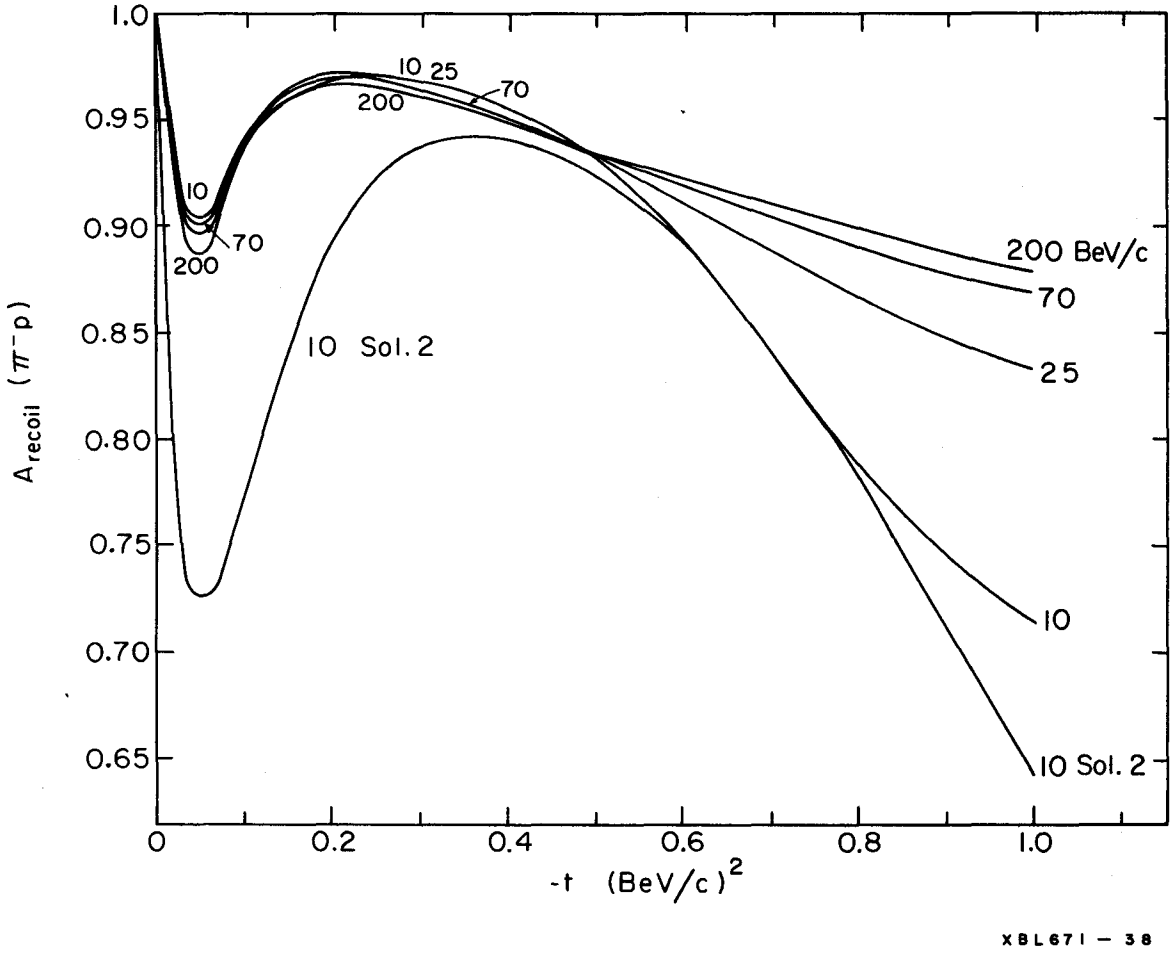

Fig. 9. A_{recoil} for $\pi^- p$ scattering at 10, 25, 70 and 200 BeV/c. The 10-BeV/c prediction for Solution 2 is also given.

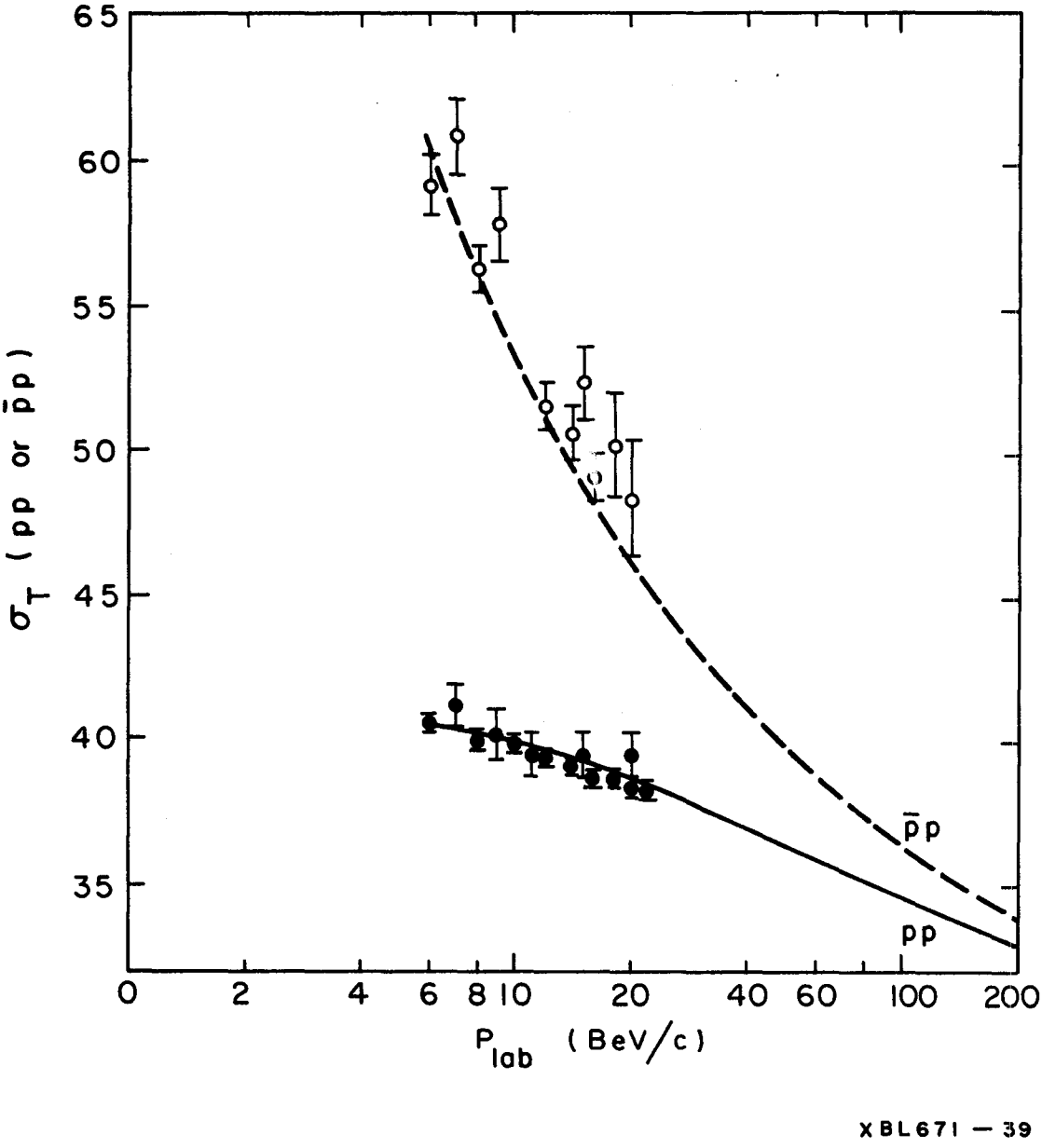

Fig. 10. Total cross section for pp and $\bar{p}p$.

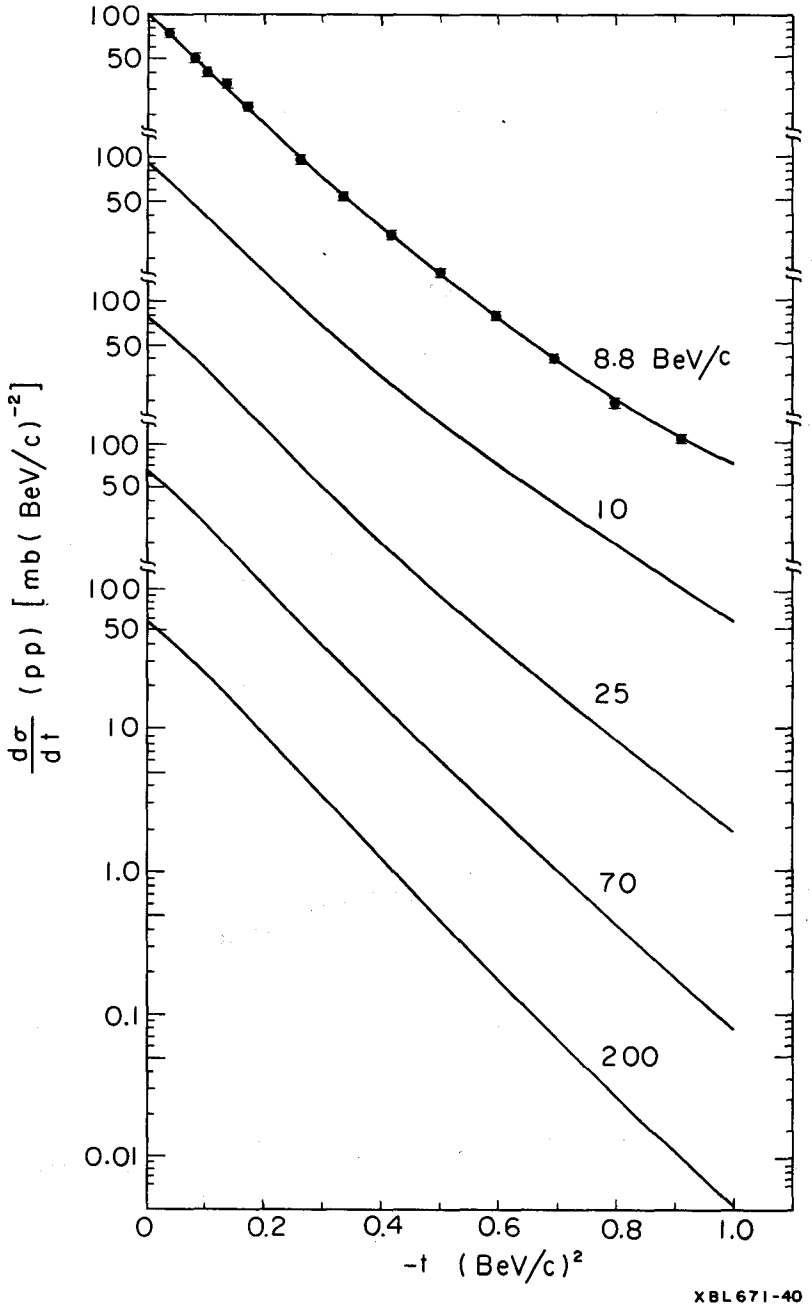

Fig. 11. pp Differential cross sections at 8.8, 10, 25, 70, and 200 BeV/c. Successive sets are spaced by a decade.

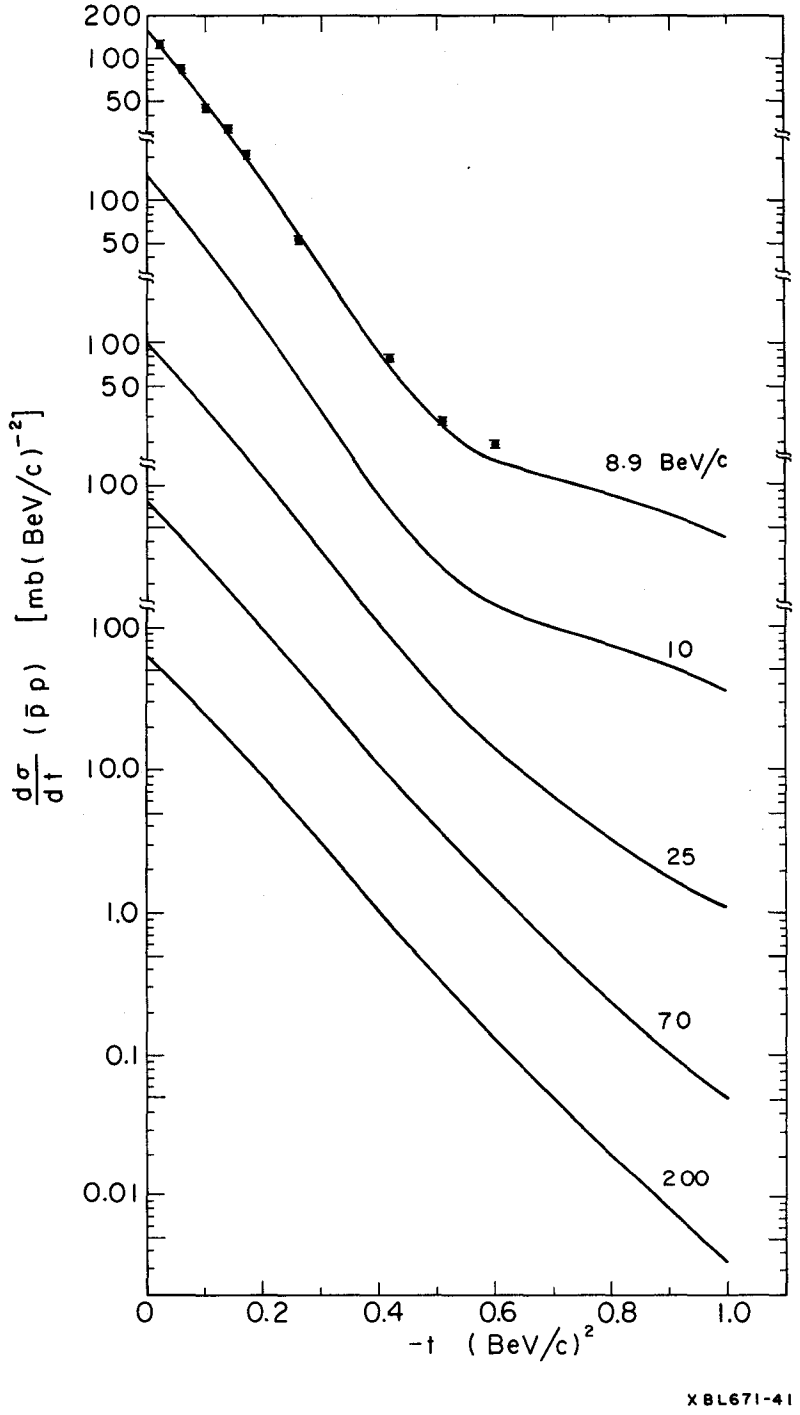

Fig. 12. $\bar{p}p$ Differential cross sections at 8.9, 10, 25, 70, and 200 BeV/c. Successive sets are spaced by a decade.

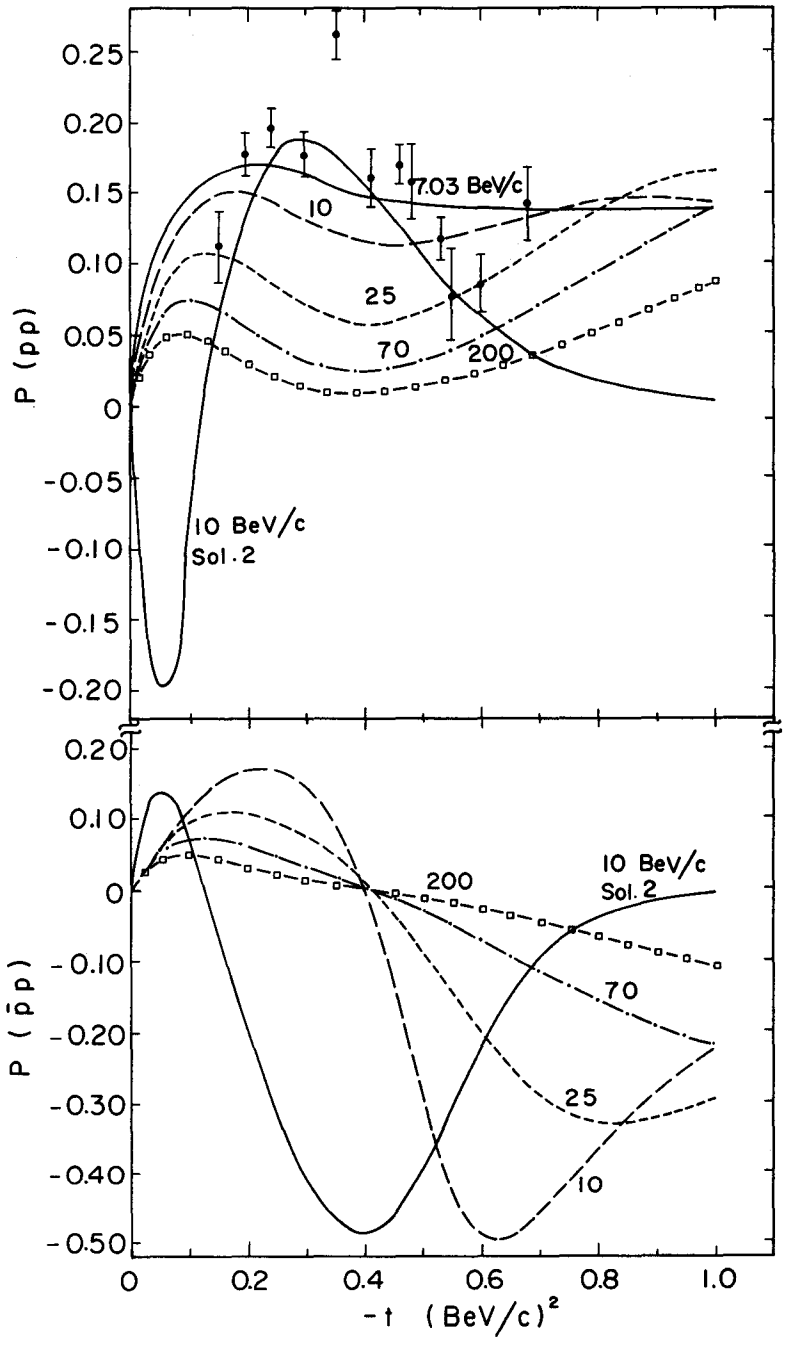

Fig. 13. pp and $\overline{p}p$ Polarizations at 10, 25, 70, and 200 BeV/c. The experimental fit at 7.03 BeV/c for pp is also shown. The prediction at 10-BeV/c for Solution 2 is also given.

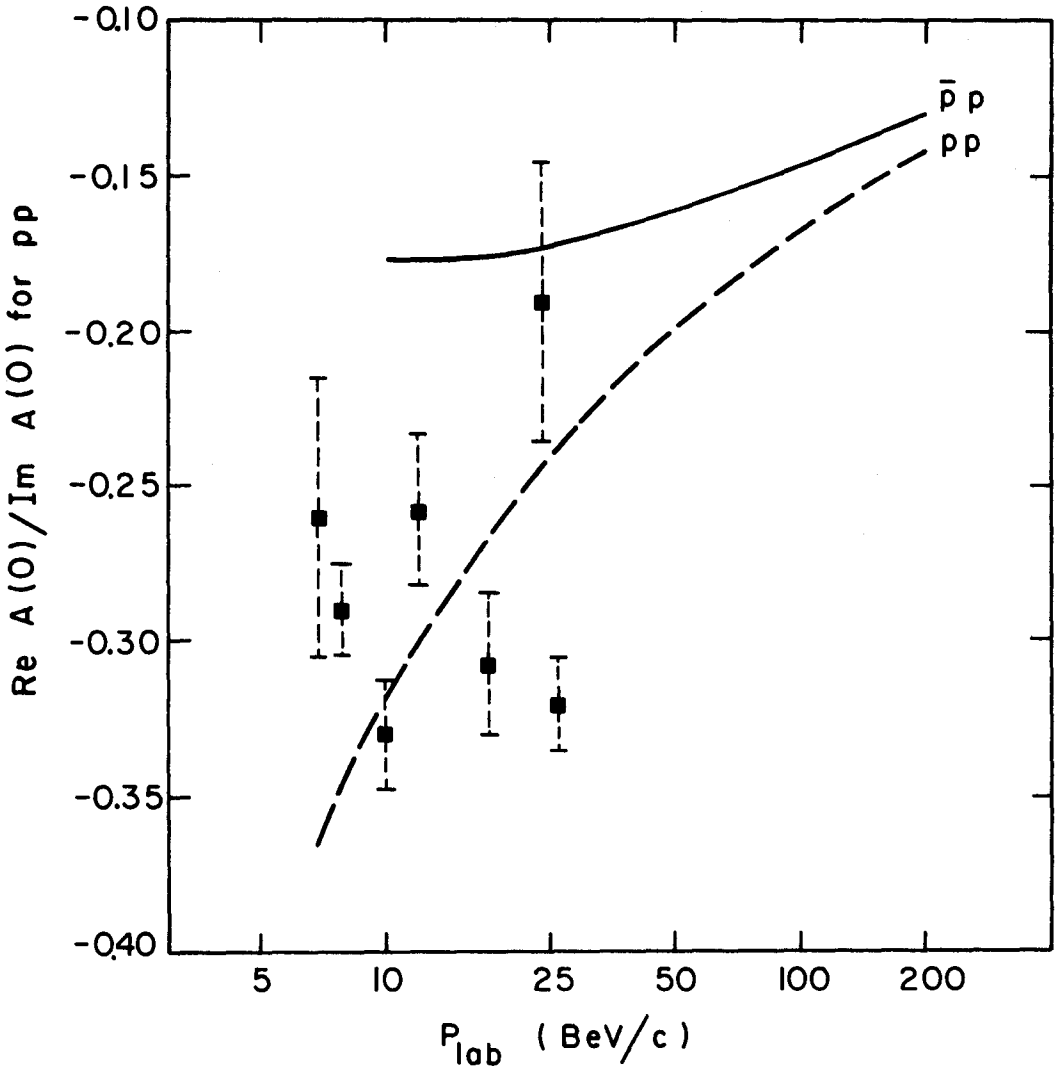

Fig. 14. The ratio of the real to the imaginary part of the forward scattering amplitude for pp and $\bar{p}p$ scattering.

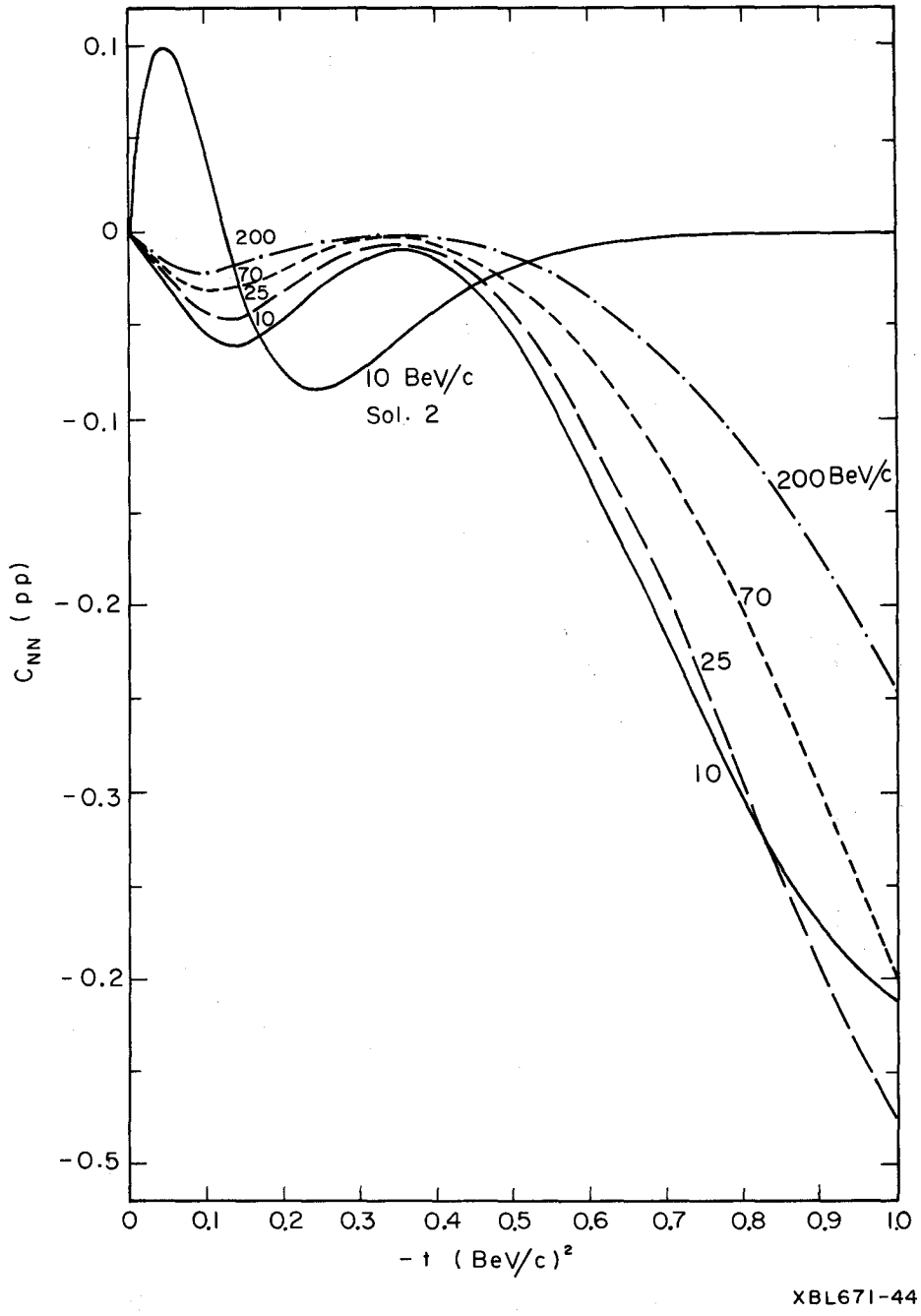

Fig. 15. C_{NN} for pp scattering at 10, 25, 70, and 200 BeV/c. The 10-BeV/c prediction for Solution 2 is given.

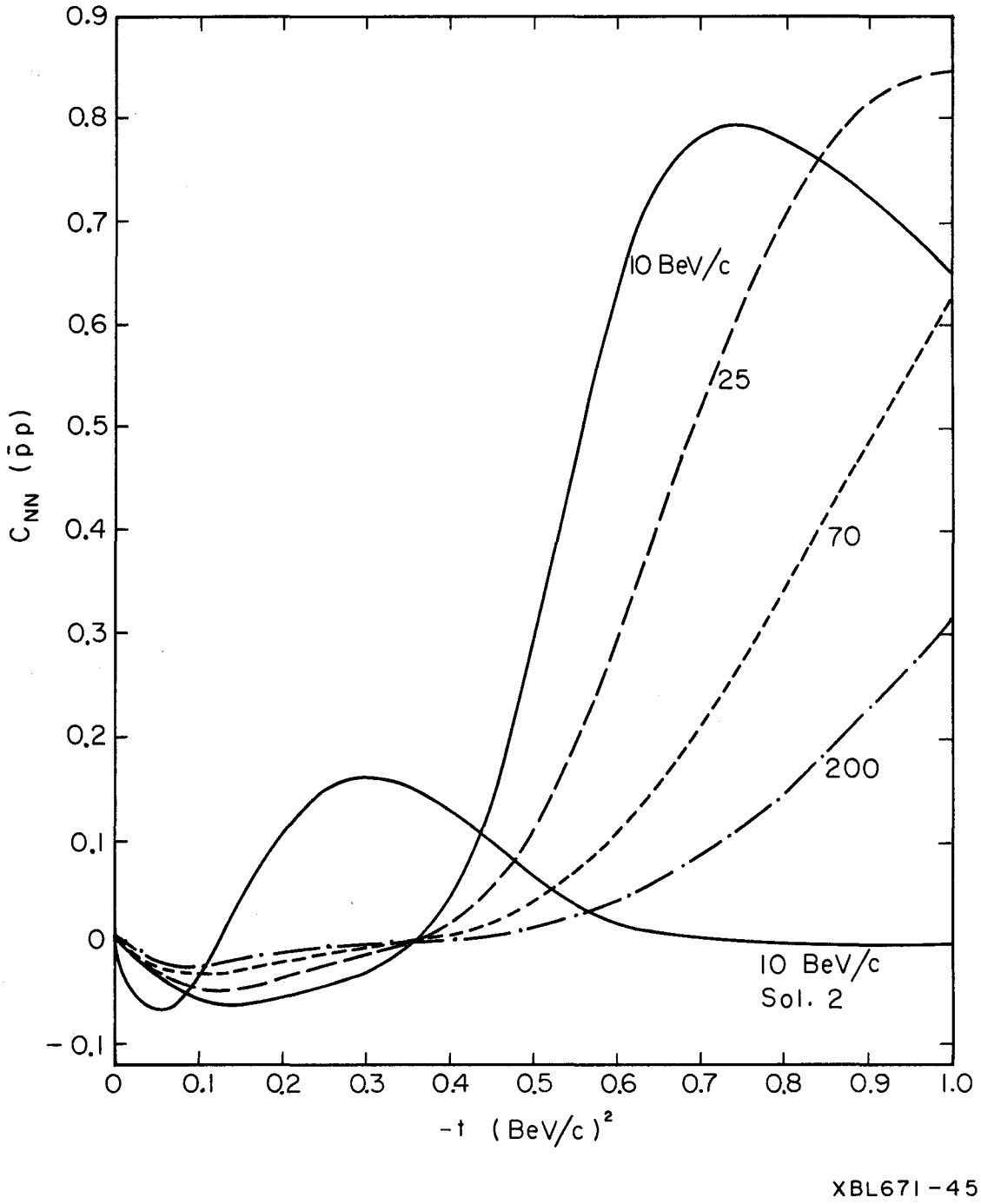

Fig. 16. C_{NN} for $\bar{p}p$ scattering at 10, 25, 70, and 200 BeV/c. The 10-BeV/c prediction for Solution 2 is given.

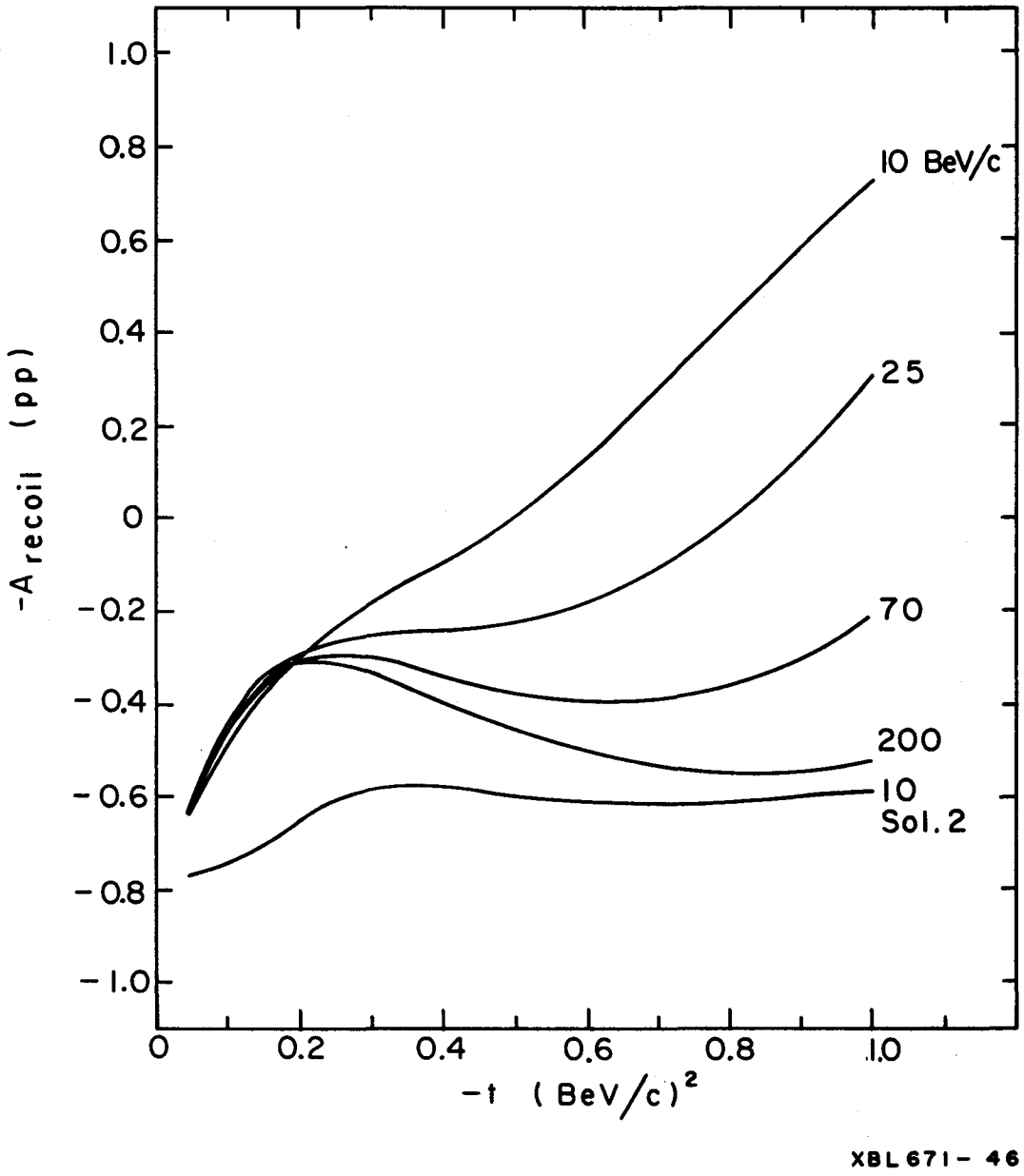

Fig. 17. – A_{recoil} for pp scattering at 10, 25, 70, and 200 BeV/c. The 10-BeV/c prediction for Solution 2 is given.

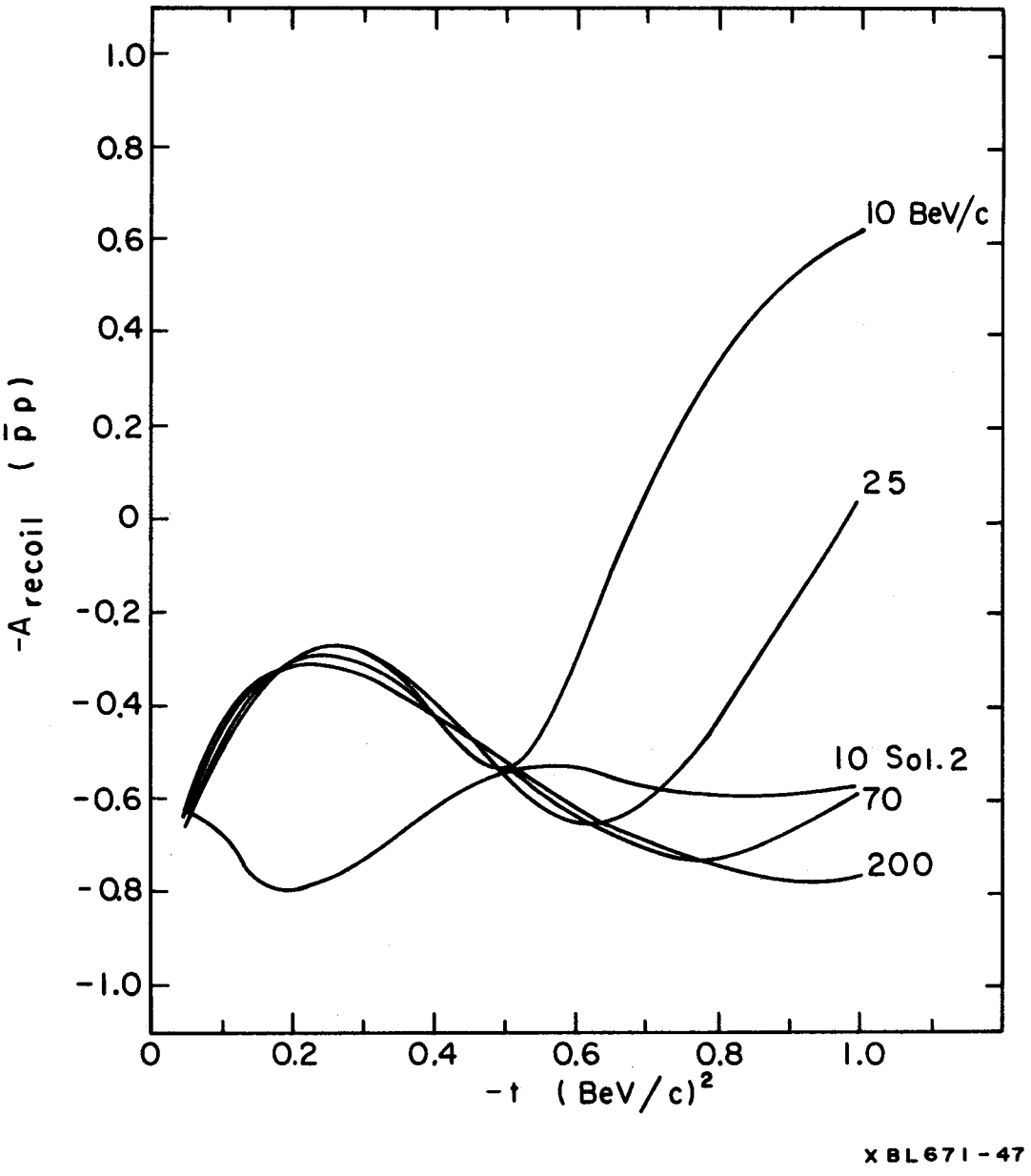

Fig. 18. $-A_{recoil}$ for $\bar{p}p$ scattering at 10, 25, 70, and 200 BeV/c. The 10-BeV/c prediction is given for Solution 2.

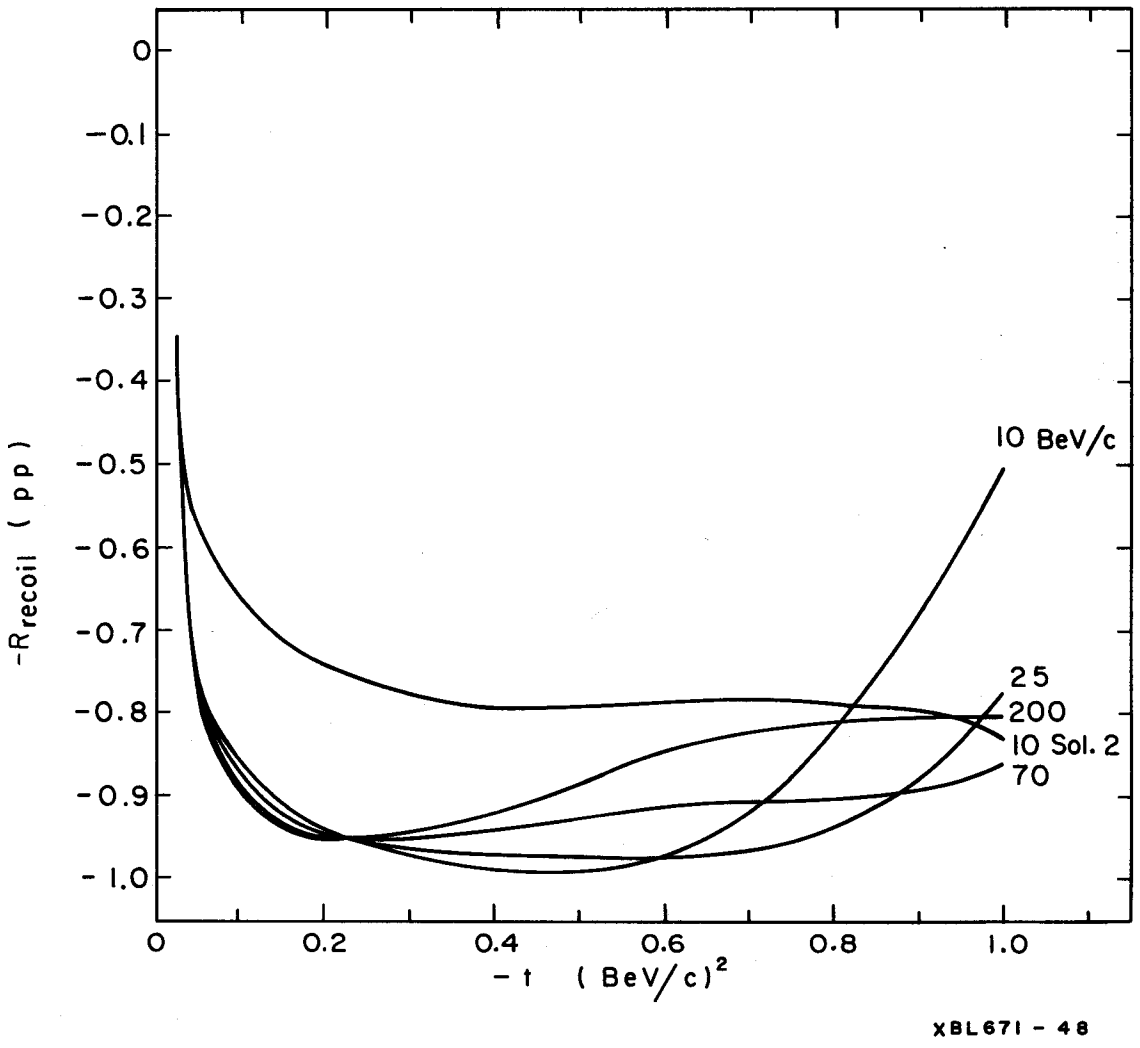

Fig. 19. $-R_{recoil}$ for pp scattering at 10, 25, 70, and 200 BeV/c. The 10-BeV/c prediction is given for Solution 2.

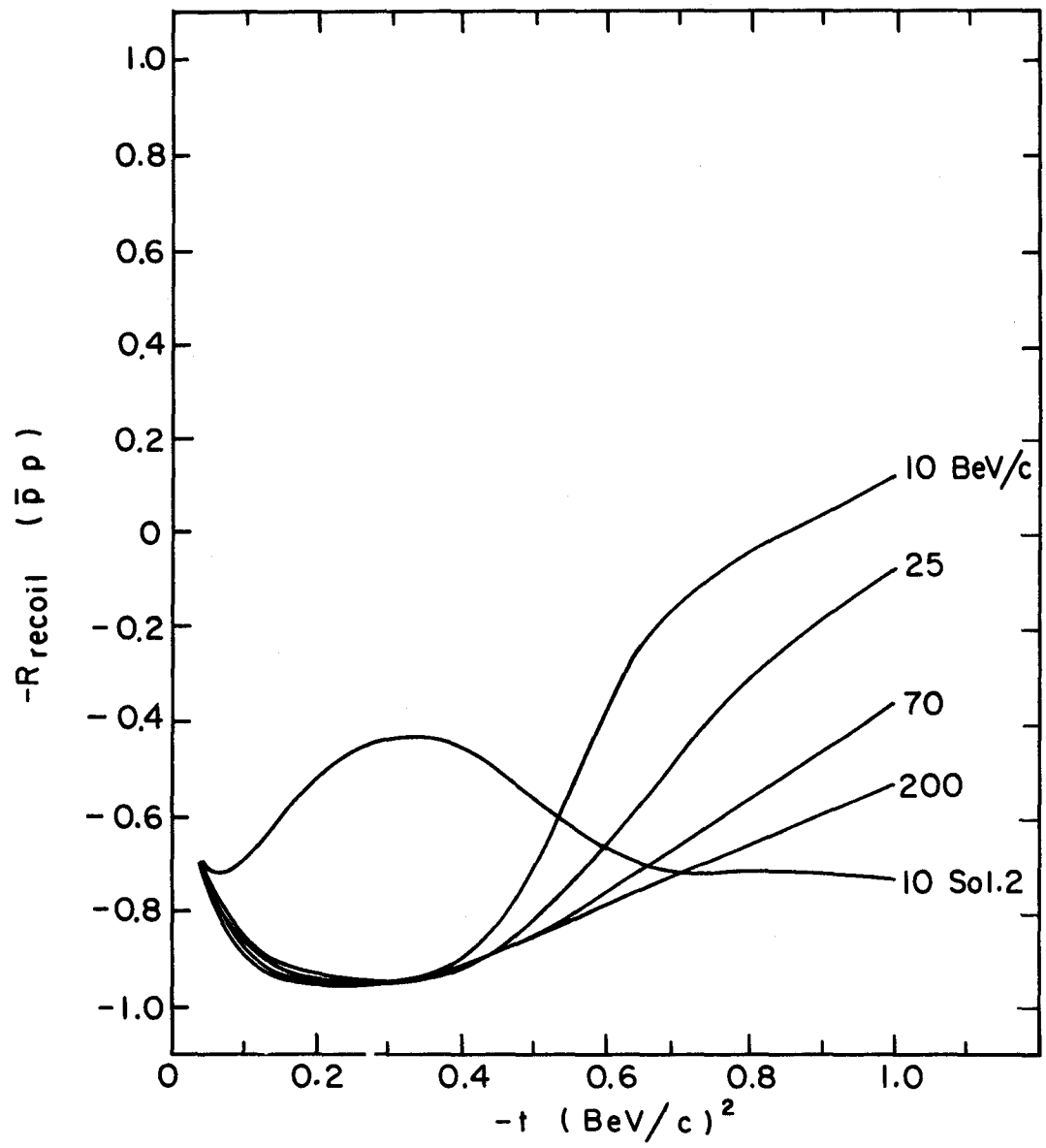

Fig. 20. $-R_{recoil}$ for $\bar{p}p$ scattering at 10, 25, 70, and 200 BeV/c. The prediction at 10 BeV/c for Solution 2 is given.

SPECULATIONS CONCERNING LARGE-ANGLE MESON-NUCLEON SCATTERING AT HIGH ENERGIES*

G. Domokos and R. Karplus

INTRODUCTION

Some time ago Wu and Yang[1] made an interesting conjecture that related the asymptotic behavior of electromagnetic form factors at large-momentum transfers to the behavior of the proton-proton scattering amplitude at large energies and momentum transfers. Roughly speaking, Wu and Yang assumed that as s and t tend to infinity, the pp scattering amplitude becomes

$$A(s,t) \sim s^{\gamma} [G_{Ep}(t)]^2 , \qquad (1)$$

where γ is some fixed power, and G_{Ep} is the electric form factor of the proton.

As a further consequence of their essentially statistical reasoning, Wu and Yang conjectured that the dependence of G on t must be essentially governed by a Boltzmann factor, so that $G(t) \sim \exp(-\beta\sqrt{t})$. It is by now well known that such a form of the amplitude fits the experimental data fairly well. Other theories emphasized either the statistical aspect of the problem,[2,3] or tried to motivate the exponential behavior of the amplitude, starting from different assumptions.[4]

The purpose of the present note is to emphasize and investigate the perhaps most startling features of Eq. (1), namely, that as s, t, and u go to infinity, (a) a scattering amplitude factorizes into a (simple) function of the energy, and (b) the factor depending on the momentum transfer is related to a form factor. For the sake of simplicity, first we consider the scattering of spinless particles and further indicate how the result can be generalized to pion-nucleon scattering. We find that both (a) and (b) are satisfied under some rather specific conditions.

The plan of the paper is the following. In the next section we make it plausible that the factorization property as described above is obtained if the Regge poles of both the t- and u-channels retreat to (at least) $\ell = -1$. Finite contributions come from those poles which go to $\ell = -1$. In the next section we describe the application of our conjecture to pion-nucleon scattering at large

momentum transfers. We guess the form of the equal-time commutator of the pion source and derive a relation for charge-exchange scattering; the elastic differential cross section can be expressed directly in terms of the isoscalar magnetic form factor of the nucleon. We then devise a simple method of comparing measured differential cross sections with asymptotic formulas of the type derived in this paper, and find that experimental data at least do not contradict our predictions (following section). Finally, in the last section we summarize the basic ideas and try to understand them on the basis of a simple intuitive picture.

SINGULARITY OF THE COMMUTATOR OF THE SOURCES AND ASYMPTOTIC BEHAVIOR OF THE SCATTERING AMPLITUDE

Assume that a particle of mass μ and isospin index α is scattered on particle B of mass M, and there emerges the same kind of particle (μ') with isospin index β and particle B' of mass M. The invariant scattering amplitude can be written as the Fourier transform of a retarded commutator of the sources[5]

$$A_{\alpha\beta}(\nu, t) = -2i(2\pi)^3(\underline{p}_B'^2 + M^2)^{1/2}(\underline{p}_B^2 + M^2)^{1/2}\int dz\, e^{iQz}$$

$$\times\, \theta(z^0)\langle B|[j_\alpha(z/2), j_\beta(-z/2)]\,|B'\rangle. \qquad (2)$$

Here ν equals $(4M)^{-1}(s-u)$, and Q equals $1/2(q+q')$, where q, q' are the four-momenta of the particle of mass μ in the initial and final states, respectively.

In the Breit frame (BF), we have with $\underline{p}_B = -\underline{p}_B' \equiv \underline{p}$:

$$Q^0 = \nu;\ \underline{Q}\cdot\underline{p} = 0;\ |\underline{Q}| = (\nu^2 + t/4 + \mu^2)^{1/2};\ \underline{p}^2 = -t/4.$$

Consider now the function

$$F_{\alpha\beta}(\nu, \underline{z}) = \int_{-\infty}^{\infty} dz^0\, \theta(z^0)\langle B|[j_\alpha(z/2),\ j_\beta(-z/2)]|B'\rangle\, e^{i\nu z^0} \qquad (3)$$

with Im $\nu > 0$.

If the equal-time commutator (ETC)

$$\langle B|[j_\alpha(0, \underline{z}/2),\ j_\beta(0, -\underline{z}/2)]\,|B'\rangle$$

is finite, then[6] for $|\nu| \to \infty$ the leading term of F reads as follows:[7]

$$F(\nu, \underline{z}) \sim \frac{1}{i\nu} \langle B | [j_\alpha(0, \underline{z}/2), j_\beta(0, -\underline{z}/2)] | B' \rangle \ . \qquad (4)$$

Covariance and locality of the theory require that the right side of Eq. (4) be proportional to a polynomial in $\delta(\underline{z})$, $\partial_k \delta(\underline{z}), \ldots$ etc. Assuming that the strongest singularity is $\delta(\underline{z})$, we see that Eq. (4) becomes

$$F(\nu, \underline{z}) \sim \frac{1}{i\nu} \ G_{\alpha\beta}(t) \delta(\underline{z}),$$

and inserting (4) into (2)

$$A_{\alpha\beta}(\nu, t) \sim -\frac{2}{\nu}(2\pi)^3 (M^2 - 1/4t) G_{\alpha\beta}(t) \ , \qquad (5)$$

where $G_{\alpha\beta}$ is in general a function of the momentum transfer and antisymmetric in α, β. Equation (5) already shows essentially the desired factorization property of the amplitude. Depending on the form of j_α and j_β, $G_{\alpha\beta}$ is proportional to some kind of a form factor of the particle B.

As a generalization of the previous considerations, it is instructive to consider the following example. The matrix element of the commutator can depend on the invariants: t, z^2, $Q \cdot z$, $p \cdot z$, and $\kappa \cdot z$, where $P = 1/2(p_B + p_{B'})$, and $\kappa = q - q'$. In the BF, of course, $\underline{P} = 0$. Let us now assume that as $z^0 \to 0$, the commutator has a power-type singularity, but otherwise is proportional to $\delta(\underline{z})$:

$$\langle B | [j_\alpha(z/2) j_\beta(-z/2)] | B' \rangle \sim (z^0)^{-\gamma - 1} G_{\alpha\beta}(t) \delta(\underline{z}). \qquad (6)$$

(The power γ may depend on t.) Inserting (6) into Eqs. (3) and (2), and remembering the integral representation of the Γ-function, one finds that

$$A_{\alpha\beta}(\nu, t) \sim \nu^\gamma \Gamma(\gamma) G_{\alpha\beta}(t) \exp(-i\frac{\pi}{2}\gamma)(M^2 - t/4).$$

If γ depends on t, this is a Regge-type behavior as $\nu \to \infty$. (Actually, this example is not as artificial as it might look at first sight: Computing the commutator in the ladder approximation, one obtains a behavior precisely of this type for small relative times.) One obtains a finite ETC for $\gamma = -1$ only, as could have been expected. We are thus led to conjecture that <u>if a scattering amplitude has a Regge-type behavior and the Regge poles retreat to $\ell = -1$ at high-momentum transfers</u>, then <u>asymptotically the scattering amplitude obeys Eq. (5), where $G_{\alpha\beta}$ is computed from an ETC of the sources.</u>

Evidently, such a behavior as described by Eq. (5) can be obtained if the Regge poles of both the t- and u-channel retreat to the negative half of the ℓ-plane so that the leading term in the amplitude is $0(\nu^{-1})$.

Presumably this condition is met if one considers scattering at a fixed angle in the c.m. system (around 90°), so that both t and u go to infinity together with s.

We remark in passing that the amplitude necessarily behaves as ν^{-1} for large energies and momentum transfers if there is an essential singularity in the angular momentum plane at $\ell = -1$, as conjectured by Gribov and Pomeranchuk some time ago.[8] At present, it is not clear whether this is just a coincidence of if both phenomena are connected. Such a connection seems, however, quite plausible; in fact, as the previous example shows, the coefficient of ν^{-1} (i.e., the ETC) gets a finite contribution from Regge poles which go to $\ell = -1$ only. On the other hand, it is unlikely that the exchange of a few Regge poles would describe large-momentum-transfer scattering; one expects rather that an infinite number of poles (plus the residual integral) contribute. This is, however, just the situation described in Ref. 8.

PION-NUCLEON SCATTERING

In order to be able to compare our conjecture with experiments, we have to treat some realistic scattering process. Due to its relative simplicity, we choose pion-nucleon scattering. The reasoning outlined in the preceding section can be repeated step-by-step in this case as well, so the complication is essentially kinematical only. We follow the notation of Chew et al.[9]

Write the invariance amplitude as

$$\mathcal{T} = g^2 \bar{u}(p')(-A + i\gamma Q B)u(p). \tag{7}$$

We can accordingly decompose the matrix element of the retarded commutator:

$$\mathcal{R}(z) \equiv \langle p' | [j_\beta(z/2), j_\alpha(-z/2)] | p \rangle \theta(z^0)$$

$$= \frac{M}{E} \bar{u}(p')[-\tilde{A}(z^2, z\cdot p, z\cdot \kappa, t) + i\gamma z \tilde{B}(z^2, z\cdot p, z\cdot \kappa, t)] u(p) \theta(z^0) \tag{8}$$

with $\kappa = q' - q$, i.e., $t = \kappa^2$; here j_α, j_β are the sources of the incoming and outgoing pion field, respectively, and g^2 is the pion-nucleon coupling constant.

In the BF we find after a short calculation that

$$\int dz\, e^{iQz}\mathcal{R}(z) = \chi_f^\dagger \left\{ -\int dz\, e^{iQz}\theta(z^0)\tilde{A} + \frac{iM}{E\nu}\left[\nu + \frac{i}{M}(\underline{p}\times\underline{\sigma})\cdot\underline{Q}\right]\frac{\partial}{\partial\nu}\int dz\, e^{iQz}\theta(z^0)\tilde{B} \right\}\chi_i \tag{9}$$

and

$$\mathcal{F} = \chi_f^\dagger \left\{ -\frac{E}{M}A(\nu,t) + \left[-\nu - \frac{i}{M}(\underline{p}\times\underline{\sigma})\cdot\underline{Q}\right]B(\nu,t) \right\}\chi_i \ , \tag{10}$$

where $\chi_{i,f}$ are the (two-component) nucleon spinors in the initial and final states, respectively.

On comparing (10) with (9), we obtain

$$A(\nu,t) = \frac{M}{E}\int dz\, e^{iQz}\theta(z^0)\tilde{A}$$

$$B(\nu,t) = -i\frac{M}{E\nu}\frac{\partial}{\partial\nu}\int dz\, e^{iQz}\theta(z^0)\tilde{B} \ .$$

Using this last equation, we finally arrive at the desired relation expressing the matrix element of the retarded commutator through the invariant amplitudes in the BF:

$$\int dz\, e^{iQz}\mathcal{R}(z) = \chi_f^\dagger \left\{ -\frac{E}{M}A(\nu,t) - \left[\nu + \frac{i}{M}(\underline{p}\times\underline{\sigma})\cdot\underline{Q}\right]B(\nu,t) \right\}\chi_i . \tag{11}$$

[We omitted isospin indices in Eq. (11).] Here E is the energy of the nucleon in the BF, i.e., $E = (M^2 - t/4)^{1/2}$. Remembering the dispersion relations satisfied by the even and odd amplitudes,[9] we see that

$$A^{(\pm)}(\nu,t) = \frac{1}{\pi}\int_{\mu+t/4M}^{\infty} d\nu' A_\nu^{(\pm)}(\nu',t)\left(\frac{1}{\nu'-\nu} \pm \frac{1}{\nu'+\nu}\right)$$

$$B^{(\pm)}(\nu,t) = \frac{1}{2M}\left(\frac{1}{\nu_B-\nu} \mp \frac{1}{\nu_B+\nu}\right) + \frac{1}{\pi}\int_{\mu+t/4M}^{\infty} d\nu' B_\nu^{(\pm)}\left(\frac{1}{\nu'-\nu} \mp \frac{1}{\nu'+\nu}\right) ,$$

with

$$\nu_B = \frac{1}{2M}(\mu^2 + \frac{t}{2}) \ .$$

We see that--assuming sufficiently rapid convergence[10]--as $\nu \to \infty$, we have

$$A^{(+)}(\nu,t) = 0(\nu^{-2})$$
$$A^{(-)}(\nu,t) = 0(\nu^{-1})$$
$$B^{(+)}(\nu,t) = 0(\nu^{-1})$$
$$B^{(-)}(\nu,t) = 0(\nu^{-2}) .$$

Thus $B^{(+)}$ and $\frac{E}{M}A^{(-)}+\nu B^{(-)}$ are the possible candidates to be related to an ETC.

We now have to compute the ETC of the sources. Assuming a form $j_a = \frac{1}{2}\bar{\psi}\gamma_5\tau^a\psi$ for the source of pions, one can try to take perturbation theory as a guide to guess the ETC of the pion sources. Various models (quarks coupled to an isosinglet scalar meson, pseudo-scalar meson theory up to fourth order) suggest that we assume the following form of the one-nucleon matrix element of the ETC in the BF:

$$\langle -\underline{p}s'A'|[j_a(0,\underline{z}/2), j_\beta(0-\underline{z}/2)]|\underline{p}sA\rangle = \delta(\underline{z})\epsilon_{a\beta\gamma}\langle -\underline{p}s'A'|V_0^\gamma(0)|\underline{p}sA\rangle + i\frac{Z}{4M}\partial_k\delta(\underline{z})\delta_{a\beta}\langle -\underline{p}s'A'|V_k(0)|\underline{p}sA\rangle . \tag{12}$$

In Eq. (12), V_0^γ is the time-like component of the vector-isovector current; V_k are the space-like components of the vector-isoscalar current; and $\underline{p}, s, A$ stand for the momentum, spin, and isospin indices of the nucleon. The factor Z is model dependent; therefore, it is hard to predict its exact value. One expects, however, that $Z \approx 1$. The first term on the right side of Eq. (12) is what one obtains from the canonical commutation relations; the second term is an "induced" one. We have in the BF

$$\langle p''s''A''|V_0^\gamma(0)|p's'A'\rangle = \chi^\dagger_{s''A''}\frac{1}{2}\tau^\gamma\chi_{s'A'}G_E^1(t) \tag{13}$$

$$\langle p''s''A''|\underline{V}(0)|p's'A'\rangle = -i\frac{1}{M}\chi^\dagger_{s''A''}(\underline{\sigma}\times\underline{p})\chi_{s'A'}G_M^0(t), \tag{14}$$

where the χ's are the spin-isospin wave functions of the nucleon, and $G_{E,M}^{1,0}$ are the isovector, isoscalar, electric, and magnetic Sachs form factors of the nucleon, respectively. Using now Eqs. (11) to (14) and taking into account (5), we find the following asymptotic relations:

$$\sqrt{1-t/4M^2}\;A^{(-)}(\nu,t)+\nu B^{(-)}(\nu,t) \sim \frac{-iG_E^1(t)}{\nu} \tag{15}$$

$$B^{(+)}(\nu,t) \sim -i\frac{Z}{4}\frac{G_M^0(t)}{\nu}$$

$$A^{(+)}(\nu,t) \sim 0(\nu^{-2}) . \tag{16}$$

On writing the scattering amplitude in the c.m. system as

$$f = f_1 + \frac{(\underline{\sigma q}')(\underline{\sigma q})}{|\underline{q}'|\,|\underline{q}|} f_2 ,$$

we find the following relation between the charge-exchange amplitudes:

$$\frac{-iG_E^1(t)}{4\pi} \sim \frac{\nu}{\epsilon+M}[\nu+(W+M)(1-t/4M^2)^{1/2}]f_1^{(-)} + \frac{\nu}{\epsilon-M}[\nu-(W-M)(1-t/4M^2)^{1/2}]f_2^{(-)} \quad . \tag{17}$$

Here ϵ is the energy of the nucleon in the c.m.: $\epsilon \pm M = (2W)^{-1}[(W+M)^2-\mu^2]$, and $W = \sqrt{s}$. Unfortunately Eq. (17) can be tested only if both f_1 and f_2 are known separately, e.g., one measures both the differential cross section and polarization of the charge-exchange scattering.

Equation (16), however, completely determines the differential cross section of the elastic scattering. Neglecting the mass of the pion, we find

$$\frac{d\sigma^{(+)}}{d\Omega} \sim \frac{3}{2}\left(\frac{Z}{4}\right)^2\left(\frac{g^2}{4\pi}\right)^2 \frac{[G_M^0(t)]^2}{[2(s-M^2)+t]^2}\left(1+\frac{M^4}{s^2}+\frac{2}{3}\,\frac{M^2+t}{s}\right). \tag{18}$$

Asymptotically there is no polarization as f_1 is proportional to f_2 with a real coefficient. Our next task is now to compare (18) with the available experimental results.

EVALUATION OF EXPERIMENTAL DATA

Pion-nucleon scattering has a relatively complicated structure due to the many excited states of the nucleon. It is not our purpose to give a detailed analysis of the experimental data (in particular, we shall nowhere compute errors) but rather to propose a simple method of testing Eq. (18) and to illustrate the procedure on some data available in the literature. We use the following fit to the form factor[11]

$$G_M^0(t) = \frac{1}{2}(\mu_p+\mu_n)\exp\left(-\frac{\sqrt{-t}}{0.6M}\right) , \tag{19}$$

which is sufficiently accurate for our purpose; further, we shall put $M = 1$. At $s \approx 25$ ($p_{lab} = 12$ BeV/c), the variation of the rational factor in (18) is negligible up to $-t \approx 7$. Therefore, on inserting $s = 25$ into Eq. (18), we can write in approximate form the equation

$$\frac{d\sigma}{d\Omega} \sim \frac{1}{2}\,\sigma_0 \cdot 10^{-3}\exp(-3.33\sqrt{-t}) ,$$

where

$$\sigma_0 = \frac{3}{2}\left(\frac{g^2}{4\pi}\right)^2\left(\frac{\mu_p+\mu_n}{2}\right)^2\left(\frac{Z}{4}\right)^2 .$$

Inserting $g^2/4\pi \approx 13.5$, and the magnetic moments of the nucleons, we find

$$\frac{d\sigma}{d\Omega} \sim 105\left(\frac{Z}{4}\right)^2 \exp(-3.33\sqrt{-t})(\mu b/sr) .$$

Adopting this formula, we see that $f(t) \equiv \ln\, d\sigma/d\Omega + 3.33\sqrt{-t} \approx$ const. We take the observed values of $d\sigma/d\Omega$ at $p_{lab} = 12$ BeV/c and plot f(t); extrapolating f(t) to $t \to -\infty$ we hope to find the value of Z. As a further test, we can take the difference quotients $\Delta f/\Delta t$ and see if they tend to zero. Using the data of Orear et al.,[12] we arrive at the numbers summarized in Table I. We see that the data are not incompatible with the expression (18) of the differential cross section. In particular, $\Delta f/\Delta t$ (except the first point, which is at too small momentum transfer anyway) seems to decrease monotonously. In order to

Table I. $\pi^- p \to \pi^- p$ at $p_{lab} = 12$ BeV/c.

t[BeV/c]	1.20	1.50	2.0	2.40	3.50
$\left(\frac{d\sigma}{d\Omega}\right)_{exp}\left[\frac{\mu b}{sr}\right]$[a]	21.1	12.1	1.35	0.21	< 0.06
f(t)	6.69	6.56	5.01	4.60	< 3.41
$\frac{\Delta f}{\Delta t}$	0.39	3.10	1.03	< 1.09	

a. Observed cross section, from Ref. 12, Table 1.

determine the constant Z, we make a crude analytical fit to the function f(t):

$$f(t) = a - \frac{b}{t} ,$$

which gives $a \approx 1.85$. Hence, comparing the last expression with the theoretical value $f(\infty) = a = \ln 105(Z/4)^2$, we find $Z \approx 0.96$. We consider this a reasonable agreement, in view of the several experimental and theoretical uncertainties. (Evidently, the exact value of Z should not be taken too seriously. What we mean by saying that there is a "reasonable agreement" between Eq. (18) and the observed cross section, is that Z turns out to be of the order of unity and not, say, 1/100.) A real test would be, of course, to carry out the pro-

cedure described in this section on experimental data at higher energies and momentum transfers, and see if they are consistent with each other and with Eq. (18).

DISCUSSION

To summarize, we emphasize the following points of our previous considerations.

If at high energies and momentum transfers, a scattering amplitude behaves as ν^{-1}, then plausibly the coefficient of $1/\nu$ is an ETC of the sources. Put in another way, the mechanism sketched here may provide a way of measuring equal-time commutators of source densities. Adopting a Regge-pole picture for the amplitude at finite momentum transfers, one can say that the situation described in this paper occurs if none of the Regge poles stays above $\ell = -1$ as $-t \to \infty$ and at least some of them tend to (-1), in order to get a finite contribution. (Evidently, the ghosts at $\ell = -1$ must be killed somehow.) From the experimental point of view, it would be desirable to test the relation (15) [or, equivalently, (17)] for the charge-exchange amplitudes; in a sense, this is the relation which is the "safe" one, viz no model-dependent assumption is needed to its derivation. Nonetheless, we feel somewhat encouraged by the result of the analysis performed in the last section; in our opinion it is unlikely that coupling constants, magnetic moments (i.e., low-energy parameters), and kinematic factors would reproduce an asymptotic cross section "just by accident."

To draw a (necessarily loose) intuitive picture, we can imagine that if both the energy and momentum transfer are large, the meson is re-emitted immediately after being absorbed. By covariance then, the re-emission must take place at the same point where the meson had been absorbed. Thus a meson pair asymptotically probes the local structure of the nucleon, just as a photon does in ep scattering. This intuitive picture is useful in further understanding the conditions of applicability of the present considerations. The mechanism described in this paper can dominate the scattering amplitude if the excitation spectrum in the s-channel is a "mild" one, so that at infinite energy there is no appreciable contribution from "compound" reactions. Our theory thus describes a situation just opposite to the one in which the application of a statistical model is justified.

Roughly speaking, a statistical model assumes that the spectrum in the s-channel is infinitely complicated, i.e., "compound nucleon" formation persists up to the highest energies. Whereas, according to our basic assumption, ours is (if not the best), in a sense, the simplest of all possible worlds. It remains to be seen whether this is indeed the case.

We thank Dr. M. B. Halpern and Professor S. Mandelstam for some interesting remarks. One of the authors (GD) wants to express his thanks to the Physics Department of the University of California for its hospitality.

Footnotes and References

*Research supported in part by the Air Force Office of Scientific Research, Office of Aerospace Research, under grant AF-AFOSR-232-66.

1. T. T. Wu and C. N. Yang, Phys. Rev. 137, B708 (1965).

2. G. Fast, R. Hagedorn, and L. W. Jones, Nuovo Cimento 27, 856 (1963).

3. N. Byers and C. N. Yang, Phys. Rev. 142, 976 (1966).

4. T. Kinoshita, Phys. Rev. Letters 8, 80 (1964); A. Martin, Nuovo Cimento 37, 671 (1965).

5. We omit degenerate terms having a polynomial dependence on ν. This amounts essentially to assuming that the meson is not a "fundamental" particle. We shall discuss this problem in more detail in a forthcoming paper.

6. Cf., A. Erdelyi, Asymptotic Expansions, Dover, New York, 1956.

7. It was apparently Bjorken who realized this for the first time. (J. D. Bjorken, Phys. Rev., to be published).

8. V. N. Gribov and I. Ja. Pomeranchuk, Proc. of the 1962 International Conference on High Energy Physics at CERN (CERN, Geneva, 1962).

9. G. F. Chew, M. L. Goldberger, F. E. Low, and Y. Nambu, Phys. Rev. 106, 1337 (1957).

10. This is certainly consistent with the picture developed in this paper. If the amplitude at $\nu \to \infty$ is described by an asymptotic expansion of the Regge type, then at sufficiently large momentum transfers, the dispersion relations in ν must converge without subtractions.

11. L. H. Chan, K. W. Chen, J. R. Dunning, Jr., N. F. Ramsey, J. K. Walker, and R. Wilson, Phys. Rev. 141, 1298 (1966).

12. J. Orear, R. Rubinstein, D. B. Scarl, D. H. White, A. D. Krisch, W. R. Frisken, A. L. Read, and H. Ruderman, Large Angle Pion-Proton Elastic Scattering at High Energies, preprint, July 1966.

SYMMETRIES AT HIGH ENERGIES

Gino C. Segrè

We shall discuss only strong-interaction processes, considering the relevance to them of certain recent theoretical investigations. To begin with, let us comment that there is no compelling reason for the breaking of SU(3) to decrease with energy, e.g., assuming that the total cross sections of pion-nucleon and kaon-nucleon interactions both tend to a constant; there is no reason why this has to be the same constant. The Pomeranchuk theorem predicts that asymptotically

$$\sigma(K^+p) = \sigma(K^-p) \qquad (1)$$
$$\sigma(\pi^+p) = \sigma(\pi^-p) \ ,$$

and SU(3) symmetry would suggest that asymptotically all four cross sections are equal. This does not seem to be the case, as differences of the order of 10 to 20%, presumably due to SU(3) breaking, appear to persist at high energies.

Several models have been proposed for explaining some of the features of high-energy scattering. We shall discuss only two of them.

QUARK MODEL

This assumes the existence of a fundamental SU(3) triplet of particles with baryon number equal to 1/3, and fractional charges 2/3, -1/3, and -1/3 (Refs. 1 and 2). Let us label this triplet as q_p, q_N, and q_Λ, where the first two form an isotopic-spin doublet and the last is a strange-isospin singlet. Baryons are assumed to be composed of three quarks, and mesons of a quark–antiquark pair.

If we now assume that in some sense the quarks (which must have a mass of several BeV in order to have escaped detection) act as light particles when bound together to form a hadron, hadron-hadron scattering may be treated in the impulse approximation as having a scattering matrix equal to the sum of the quark-quark transition amplitudes. If we further assume that quark-quark and quark–antiquark amplitudes are equal, we arrive at the first and most striking prediction of the model, namely

$$\frac{\sigma(pp)}{\sigma(\pi^+ p)} = 3/2 \ . \qquad (2)$$

This follows immediately from the fact that the incident proton has three quarks, whereas the incident meson has only one quark and one antiquark. Experimentally this relation is well verified.

Let us see what other predictions can be made regarding meson-nucleon scattering; we do not wish to use SU(3) symmetry, however, as it would force $\sigma(\pi p) = \sigma(Kp)$. Let us instead make the following ad hoc assumptions about quark-quark and quark–antiquark scattering within the "quasi-free light quark" model. Asymptotically

i. Deviations from the SU(3) limit are due to the strange quark
ii. Deviations from the Pomeranchuk theorem limit occur only in the isospin-zero channel.

We may then describe the amplitudes by three parameters, which we call P, S, and A. Labeling the q_i-q_j transition amplitude by $(q_i q_j)$, we have

$$(q_p q_n) = (q_{\bar{p}} q_n) = (q_p q_p) = (q_n q_n) \equiv P \qquad (3a)$$

$$(q_\lambda q_p) = (q_\lambda q_n) = (q_{\bar{\lambda}} q_p) = (q_{\bar{\lambda}} q_n) \equiv P\text{-}S \qquad (3b)$$

$$(q_{\bar{p}} q_p) = (q_{\bar{n}} q_n) \equiv P+A \ . \qquad (3c)$$

With these assumptions, we obtain the following additional predictions:

$$\sigma(K^- p) + 2\sigma(\pi^+ p) = \sigma(K^+ p) + 2\sigma(\pi^- p) \qquad (4a)$$

$$\sigma(K^- p) + 2\sigma(K^+ n) = \sigma(K^+ p) + 2\sigma(K^- n) \qquad (4b)$$

$$\sigma(K^+ p) = \sigma(K^+ n), \qquad (4c)$$

all of which are in excellent agreement with experiment.

The results are encouraging, but the justification for the model is, at best, a very weak one. Several attempts to obtain these results without postulating underlying quarks have been made; we shall briefly discuss one of them.

"QUARK CURRENT" REGGE-POLE-RESIDUE MODEL

This model[3] assumes that high-energy scattering is dominated by two nonets of even intrinsic parity Regge trajectories. The nonets of 2^+ and 1^- particles lie on these trajectories; the model further assumes the Pomeranchon, or vacuum trajectory, to also lie on the same trajectory as the unitary singlet 2^+ meson.

The residues of the Regge pole C, lying on the 2^+ trajectory between two states A and B, which we denote by

$$\gamma_C^{AB}(+) ,$$

are then assumed to obey a pattern specified by the commutation relations of scalar and vector integrated quark currents

$$S^i = \int \bar{q}\lambda^i q \, d\vec{x} \tag{5a}$$

$$V^i = \int \bar{q}\gamma_4\lambda^i q \, d\vec{x} , \tag{5b}$$

where the λ^i are three-by-three unitary-spin matrices, and the quarks are three-component spinners in this space. The commutation relations can be computed as

$$[S^i, S^j] = i f^{ijk} V^k \tag{6a}$$

$$[S^i, V^j] = f^{ijk} S^k . \tag{6b}$$

Specifically we require γ_C^{AB} to be given by the matrix elements of S^i between states A and B at rest. The latter are determined by consistency requiring (6a) and (6b) to hold when examined between states.

This scheme has as consequences many of the good results of the first quark model, including Eq. (2); it also makes some predictions that disagree with experiment if we force the Pomeranchon trajectory to have an intercept of 1 at $t = 0$, i.e., $\alpha_0(0) = 1$. To circumvent this difficulty, it has been suggested that the data could be fitted if $\alpha_0(0) \approx 0.925$.

Recapitulating, the usual Regge-pole scheme has two nonets of even-parity trajectories and one unitary singlet, the Pomeranchon, with $\alpha_0(0) = 1$. This scheme drops the singlet from the trajectory, whose recurrence is the 2^+ mesons, replaces it by the Pomeranchon, or vacuum trajectory, and says that $\alpha_0(0) \approx 0.925$. As, asymptotically, total cross sections behave like

$$\sigma \sim s^{\alpha(0)-1} ,$$

this model predicts decreasing total cross sections.

References

1. Quarks: M. Gell-Mann, Phys. Letters 8, 214 (1964), and G. Zweig, unpublished.

2. Model 1: E. M. Levin and L. L. Frankfurt, JETP Letters 2, 65 (1965);

H. J. Lipkin and F. Scheck, Phys. Rev. Letters 16, 71 (1966); and H. J. Lipkin, Lectures at Yalta, USSR, April 1966.

3. Model 2: N. Cabibbo et al. CERN preprints, Th 680 and Th 685.

WEAK INTERACTIONS AT HIGH ENERGIES: NEUTRINO EXPERIMENTS

Gino C. Segrè

Weak interactions may be studied over a wide range of energies with the use of neutrino beams and, despite the experimental difficulties involved, will probably produce interesting new results.[1] Let us begin by discussing purely leptonic processes, e.g.,

$$\nu_\mu + e^- \rightarrow \nu_e + \mu^- . \tag{1}$$

At low energies this is described very well by an effective current-current Lagrangian

$$L = -\left[G/\sqrt{2}\right] J_\Lambda^{(\mu)^+} J_\Lambda^{(e)} + (\text{Herm. conj.}) \tag{2}$$

where J_Λ is the usual V-A current. If we call k and k' the initial and final three momenta in the center-of-momentum frame, and $\cos\theta$ the angle between them, we find the differential cross section for (1) is given by

$$d\sigma = \left[G^2/\pi\right] \frac{k' + \omega_\mu}{\omega_e} k'^2 \, d\left[\cos\theta\right] \tag{3}$$

where

$$\omega_\mu = \sqrt{k'^2 + m_\mu^2}, \quad \omega_e = \sqrt{k^2 + m_e^2} .$$

The scattering occurs through a $J = 0$ state only, and therefore is bounded by the unitarity limit of $\pi/2k^2$. For $k \approx 300$ BeV, this limit is exceeded by Eq. (3), so we may expect deviations from (3) much below 300 BeV; these could be due to an intermediate vector boson, to higher order weak interactions, or to some new mechanism.

For semi-leptonic processes, high-energy neutrino experiments will continue to give tests for the $\Delta S/\Delta Q = 1$ rule, for the absence of neutral currents, and for the suppression of strangeness changing currents due to the Cabibbo angle. In addition, a test of time-reversal invariance can be obtained by looking at the transverse polarization of the final state baryon.

There are also very interesting predictions made by the algebra of current components regarding high-energy-neutrino processes. For example, in the limit of infinite neutrino energy we expect

$$\lim_{E_\nu \to \infty} \left[\frac{d\sigma_{tot}(\bar{\nu}+p)}{dk^2} - \frac{d\sigma_{tot}(\nu+p)}{dk^2} \right] = \frac{G^2}{\pi} (\cos^2\theta_c + 2\sin^2\theta_c) \qquad (4a)$$

$$\lim_{E_\nu \to \infty} \left[\frac{d\sigma_{tot}(\bar{\nu}+n)}{dk^2} - \frac{d\sigma_{tot}(\nu+n)}{dk^2} \right] = \frac{G^2}{\pi} (-\cos^2\theta_c + \sin^2\theta_c) , \qquad (4b)$$

where k^2 equals $(k_\nu - k_e)^2$, G is the constant in (2), and θ_c is the Cabibbo angle. In order to obtain the above relation, it was necessary to derive a sum rule by means of the algebra of current components and an unsubtracted dispersion relation for a given amplitude. Both assumptions are questioned, so a test of the above relations would be of great interest.

References

1. Two excellent talks in the Proceedings of the International Conference on Weak Interactions, Oct. 25-27, 1965, Argonne National Laboratory: S. L. Adler, High-Energy Semi-Leptonic Reactions, p. 285; D. H. Perkins, High-Energy Neutrino Experiments at Accelerators, p. 273.

FURTHER ASPECTS OF WEAK INTERACTIONS

Barbara Barrett

Two other areas of weak-interaction physics may be investigated with high-energy neutrino beams--direct lepton-lepton scattering, and the production of intermediate vector bosons. A search for vector bosons may also be made in strong-interaction processes such as πN and NN collisions.

LEPTON-LEPTON INTERACTIONS

The standard form of the weak current-current Lagrangian

$$L = \frac{G}{\sqrt{2}}\, j_\lambda^* j_\lambda \quad (G \approx 10^{-5}/M_p^2), \tag{1}$$

where

$$j_\lambda = \bar{\psi}_\mu \gamma_\lambda (1+\gamma_5)\, \psi_{\nu_\mu} + \bar{\psi}_e \gamma_\lambda (1+\gamma_5) \psi_{\nu_e} \tag{2}$$

gives rise to direct lepton-lepton scattering processes such as

$$\nu_\mu + e^- \rightarrow \nu_e + \mu^- \tag{3}$$

$$\nu_e + e^- \rightarrow \nu_e + e^- \tag{4}$$

$$\bar{\nu}_e + e^- \rightarrow \bar{\nu}_e + e^- \tag{5}$$

as well as to the observed decay $\mu \rightarrow e + \nu + \bar{\nu}$. For reaction (3), the threshold neutrino energy in the lab system is $E_\nu \approx m_\mu^2/2m_e \approx 10$ BeV. At energies well above threshold, the cross sections for processes (3) and (4) are equal to[1]

$$\sigma = \frac{2G^2 m_e E_\nu}{\pi} = 1.6 \times 10^{-41} E_\nu \text{ (in BeV) cm}^2;$$

the cross section for (5) is one third of this. The process (3) should show up as a very characteristic event: a high-energy μ^- emerging at a very small angle to the ν_μ beam.

The same lepton-lepton interactions may contribute to neutrino scattering off nuclei, i.e., to the process

$$\nu_\mu + Z \rightarrow \nu_\mu + Z + \mu^+ + \mu^- \quad , \qquad (6)$$

shown in Fig. 1, which has been considered by Stanciu[2] and by Czyz et al.[3] For $E_\nu = 10$ BeV, Stanciu obtains $\sigma_{tot} \approx 10^{-41}\text{cm}^2$ on aluminum and $\sigma \approx 3\times 10^{-41}\text{cm}^2$ on copper. These cross sections are considerably smaller than those expected if reaction (6) proceeds via an intermediate vector boson (see below).

If the weak Lagrangian also contains products of neutral leptonic currents, then as pointed out by Wu,[4] the cross section for the reaction

$$\nu_\mu + Z \rightarrow \nu_\mu + Z + e^+ + e^- \qquad (7)$$

is, apart from possible differences in coupling strengths, equal to that for $\nu_e + Z \rightarrow \nu_e + Z + e^+ + e^-$ given by Czyz et al.[3]

W PRODUCTION

We now know that the intermediate vector boson, if it exists, must have a mass $M_W \geq 2$ BeV.[5] Since theoretical estimates of W production involve complicated integrations, computer programs would have to be re-run for values of the W mass and neutrino energy appropriate to future experiments. Here we quote the results for the largest values of M_W and E_ν used in the various calculations mentioned.

W Production by Neutrinos

The reaction

$$\nu_\mu + Z \rightarrow Z + \mu^- + W^+ \quad , \qquad (8)$$

shown in Fig. 2, has been considered by Wu et al.,[6] who discuss much earlier work on this process. For $M_W = 1.5$ BeV, $E = 10$ BeV, they obtain $\sigma \approx 10^{-36}\text{cm}^2$ for an aluminum target, and $\approx 2\times 10^{-36}\text{cm}^2$ for copper.

The reaction

$$\nu_\mu + p \rightarrow \mu^- + p + W^+ \rightarrow \mu^- + p + \nu_\ell + \ell^+ \qquad (9)$$

has been estimated by Dooher and Tausner[7] for larger values of M_W. Taking $\Gamma(W \rightarrow \text{leptons})/\Gamma(W \rightarrow \text{all}) = 0.72$, they obtain $\sigma \approx 10^{-37}\text{cm}^2$ for $M_W = 3$ BeV and $E = 20$ BeV.

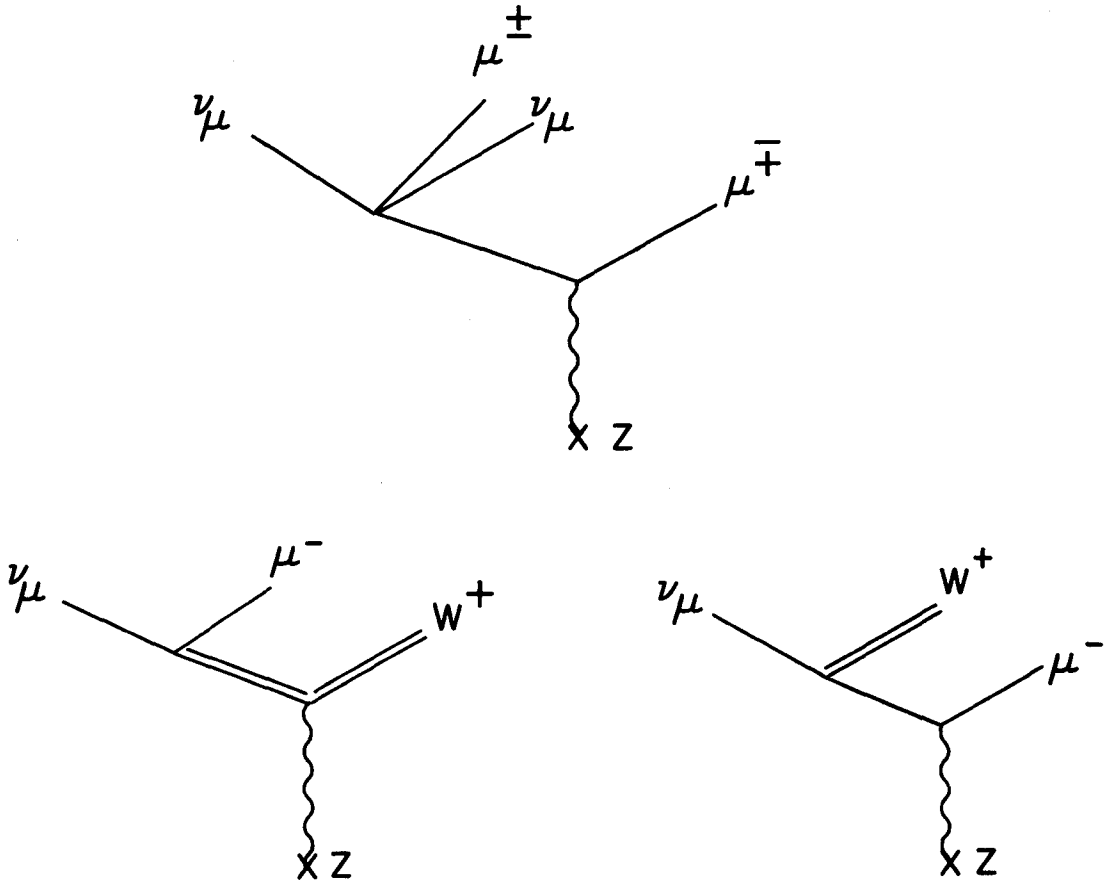

XBL 671-451

Fig. 1. Diagram of the reaction $\nu_\mu + Z \rightarrow \nu_\mu + Z + \mu^+ + \mu^-$ (above).

Fig. 2. Diagrams of the reaction $\nu_\mu + Z \rightarrow Z + \mu^- + W^+$ (below).

W Production in Strong Interactions

Piccioni[8] has described a study for an experiment to detect the W, with mass as high as 6 BeV, by observing the missing-mass spectrum for the reaction

$$p + p \rightarrow d + W^{+}. \qquad (10)$$

He used the value $\sigma \approx 1.5 \times 10^{-33} cm^2$, which is based on theoretical estimates[9] discussed by him.

Chilton et al.[10] have made calculations of the reaction

$$N + N \rightarrow N + N + W \qquad (11)$$

based on a double peripheral model. Their conservative estimates for E = 30 BeV are $\sigma \approx 6 \times 10^{-34} cm^2$ for $M_W = 3$ BeV, and $\sigma \approx 10^{-34} cm^2$ for $M_W = 6$ BeV. For nuclear targets they expect the cross section to increase roughly as A.

Lewis[11] has pointed out that the W should be produced in nucleon-anti-nucleon annihilation, and estimates that the production cross section would show a resonance with natural width $\Gamma \geq 50$ keV and integrated area $\int \sigma \, dE \approx 3 \times 10^{-29} cm^2$ MeV.

Bernstein and Feinberg[12] calculated the cross section for

$$\pi + p \rightarrow W + p \qquad (12)$$

via one-pion exchange; at the high energies presently under consideration, their results should be modified by corrections for absorption.

Other Methods

For completeness we note that estimates of W production in $e^{+}e^{-}$ collisions[13] and photoproduction[14] have been made.

References

1. See, for example, T. D. Lee and C. S. Wu, Ann. Rev. Nucl. Sci. 381 (1965).
2. G. N. Stanciu, Phys. Rev. Letters 13, 288 (1964).
3. W. Czyz, G. C. Sheppey, and J. D. Walecka, Nuovo Cimento 34, 404 (1964).
4. T. T. Wu, Phys. Rev. 147, 1033 (1966).
5. R. Burns et al., Phys. Rev. Letters 15, 42 (1965); M. M. Block et al., Phys. Letters 12, 281 (1964); G. Bernardini et al., Phys. Letters 13, 86 (1964).

6. A. C. T. Wu, C.-P. Yang, K. Fuchel, and S. Heller, Phys. Rev. Letters 12, 57 (1964).

7. J. Dooher and M. Tausner, Phys. Rev. 142, 1018 (1966).

8. O. Piccioni, Proceedings of the CERN Informal Conference on Experimental Neutrino Physics, 1965, CERN 65-32, p. 181.

9. J. Bernstein, Phys. Rev. 129, 2323 (1963); J. Nearing, Phys. Rev. 132, 2323 (1963); M. Le Bellac, F. M. Renard, D. Schiff, and J. Tran Thanh Van, Nuovo Cimento 34, 1096 (1964).

10. F. Chilton, A. M. Saperstein, and E. Schrauner, Phys. Rev. 148, 1380 (1966).

11. R. R. Lewis, Phys. Rev. 137, B164 (1965).

12. J. Bernstein and G. Feinberg, Phys. Rev. 125, 1741 (1962).

13. Y. S. Tsai and A. C. Hearn, Phys. Rev. 140, B721 (1965), and references given there.

14. H. R. Reiss and M. H. Cha, Phys. Rev. Letters 14, 399 (1965); S. M. Berman and Y. S. Tsai, Phys. Rev. Letters 11, 483 (1963); A. C. T. Wu, T. T. Wu, and K. Fuchel, Phys. Rev. Letters 11, 390 (1963).